Université de Montréal

Spectroscopie Raman de fibres électrofilées : Développement de méthodes et application aux fibres individuelles

par Marie Richard-Lacroix

Département de chimie
Faculté des Arts et Sciences

Thèse présentée à la Faculté des études supérieures et postdoctorales
en vue de l'obtention du grade de Philosophiae Doctor (Ph.D.)
en chimie

Mars 2016

Résumé

L'électrofilage est une technique de mise en œuvre efficace et versatile qui permet la production de fibres continues d'un diamètre typique de quelques centaines de nanomètres à partir de l'application d'un haut voltage sur une solution concentrée de polymères enchevêtrés. L'évaporation extrêmement rapide du solvant et les forces d'élongation impliquées dans la formation de ces fibres leur confèrent des propriétés hors du commun et très intéressantes pour plusieurs types d'applications, mais dont on commence seulement à effleurer la surface. À cause de leur petite taille, ces matériaux ont longtemps été étudiés uniquement sous forme d'amas de milliers de fibres avec les techniques conventionnelles telles que la spectroscopie infrarouge ou la diffraction des rayons X. Nos connaissances de leur comportement proviennent donc toujours de la convolution des propriétés de l'amas de fibres et des caractéristiques spécifiques de chacune des fibres qui le compose. Les études récentes à l'échelle de la fibre individuelle ont mis en lumière des comportements inhabituels, particulièrement l'augmentation exponentielle du module avec la réduction du diamètre. L'orientation et, de manière plus générale, la structure moléculaire des fibres sont susceptibles d'être à l'origine de ces propriétés, mais d'une manière encore incomprise. L'établissement de relations structure/propriétés claires et l'identification des paramètres qui les influencent représentent des défis d'importance capitale en vue de tirer profit des caractéristiques très particulières des fibres électrofilées. Pour ce faire, il est nécessaire de développer des méthodes plus accessibles et permettant des analyses structurales rapides et approfondies sur une grande quantité de fibres individuelles présentant une large gamme de diamètre.

Dans cette thèse, la spectroscopie Raman confocale est utilisée pour l'étude des caractéristiques structurales, telles que l'orientation moléculaire, la cristallinité et le désenchevêtrement, de fibres électrofilées individuelles. En premier lieu, une nouvelle méthodologie de quantification de l'orientation moléculaire par spectroscopie Raman est développée théoriquement dans le but de réduire la complexité expérimentale de la mesure, d'étendre la gamme de matériaux pour lesquels ces analyses sont possibles et d'éliminer les risques d'erreurs par rapport à la méthode conventionnelle. La validité et la portée de cette nouvelle méthode, appelée MPD, est ensuite démontrée expérimentalement. Par la suite, une

méthodologie efficace permettant l'étude de caractéristiques structurales à l'échelle de la fibre individuelle par spectroscopie Raman est présentée en utilisant le poly(éthylène téréphtalate) comme système modèle. Les limites de la technique sont exposées et des stratégies expérimentales pour les contourner sont mises de l'avant. Les résultats révèlent une grande variabilité de l'orientation et de la conformation d'une fibre à l'autre, alors que le taux de cristallinité demeure systématiquement faible, démontrant l'importance et la pertinence des études statistiques de fibres individuelles.

La présence de chaînes montrant un degré d'enchevêtrement plus faible dans les fibres électrofilées que dans la masse est ensuite démontrée expérimentalement pour la première fois par spectroscopie infrarouge sur des amas de fibres de polystyrène. Les conditions d'électrofilage favorisant ce phénomène structural, qui est soupçonné d'influencer grandement les propriétés des fibres, sont identifiées. Finalement, l'ensemble des méthodologies développées sont appliquées sur des fibres individuelles de polystyrène pour l'étude approfondie de l'orientation et du désenchevêtrement sur une large gamme de diamètres et pour une grande quantité de fibres. Cette dernière étude permet l'établissement de la première relation structure/propriétés de ces matériaux, à l'échelle individuelle, en montrant clairement le lien entre l'orientation moléculaire, le désenchevêtrement et le module d'élasticité des fibres.

Mots-clés : Électrofilage, Fibres, Spectroscopie Raman, Orientation moléculaire, Désenchevêtrement, Relations structure/propriétés.

Abstract

Electrospinning is an efficient and versatile technique to produce continuous fibers of typical diameter of a few hundred nanometers from the application of a high voltage on a concentrated and entangled polymer solution. The rapid solvent evaporation and the significant elongational forces involved in the fiber formation process give rise to unusual properties that are interesting for various types of applications, but that are yet to be fully explored. Due to their small size, these materials have been, for a long time, studied into bundles composed of thousands of fibers using conventional techniques such as infrared spectroscopy and X-ray diffraction. Our current understanding of their behavior thus relies on a convolution of the properties of the mat and the specific characteristics of each fiber composing it. Recent studies at the individual fiber level have revealed unusual properties, particularly an exponential increase of the modulus with the diameter reduction. The orientation and the molecular structure within the fibers are suspected to be at the origin of these properties, but in a way that is still far from being understood. Establishing clear structure/properties relationships and identifying the parameters that influence them represent significant challenges. However, they are of tremendous importance to fully take advantage of the specific characteristics of electrospun fibers. A key step toward this goal is to develop methodologies that enable fast and in-depth structural analysis on large quantities of individual fibers with a large diameter range.

In this thesis, confocal Raman spectroscopy is used to probe structural characteristics of individual fibers such as their molecular orientation, crystallinity and disentanglement. A new methodology for orientation quantification is first demonstrated theoretically with the objectives of reducing the experimental complexity of the Raman measurements, of extending the variety of materials that can be analysed, and of eliminating recurrent errors brought by the use of the conventional method. The experimental validity and applicability of this new method, referred to as MDP, is then demonstrated. Following this, an efficient protocol enabling the structural study of individual electrospun fibers by confocal Raman spectroscopy is presented, using poly(ethylene therephthalate) as a model system. The limitations of the technique are exposed and experimental strategies to circumvent them are highlighted. Results

reveal the large variability of the orientation and of chain conformation from fiber to fiber, showing the importance and the relevance of statistical studies of individual fibers.

Following this, the presence of chains showing a level of entanglement lower in electrospun fibers than in the bulk is demonstrated experimentally for the first time using infrared spectroscopy on bundles of polystyrene fibers. The principal electrospinning conditions promoting this structural phenomenon, which is suspected to influence greatly the properties of the fibers, are identified. Finally, the various methodologies developed in the thesis are combined for an in-depth study of orientation and disentanglement on large quantities of individual polystyrene fibers covering a large diameter range. This last study enables establishing the first structure/properties relationships for these materials, at the individual fiber scale, by clearly exposing the link between orientation, disentanglement and the elastic modulus of the fibers.

Keywords : Electrospinning, Fibers, Raman spectroscopy, Molecular orientation, Disentanglement, Structure/properties relationships.

Table des matières

Résumé i

Abstract iii

Table des matières v

Liste des figures ix

Liste des abréviations xv

Remerciements xix

Chapitre 1 1

1.1. Introduction 1

1.2. Contenu de la thèse 4

1.3. Références 7

Chapitre 2. Molecular orientation in electrospun fibers: from mats to single fibers 9

2.1. Abstract 9

2.2. Introduction: electrospinning and orientation 10

2.3. Orientation studies at the mat level 14

2.3.1. Impact of the collector on molecular orientation 14

2.3.2. Orientation and polymorph formation 18

2.3.3. Effect of orientation on the mechanical properties of mats 21

2.4. Mechanical properties of single fibers 24

2.4.1. Experimental studies of the mechanical properties of single fibers 24

2.4.2 Why does the modulus of electrospun nanofibers vary with their diameter? 29

2.4.3. What is the role of the electrospinning conditions? 37

2.5. Thermal properties of single fibers 40

2.5.1. Melting and crystallization temperatures 40

2.5.2. Glass transition temperature 43

2.6. Molecular orientation studies at the single nanofiber scale 44

2.7. Other properties and applications of electrospun fibers related to orientation 50

2.8. Conclusion and outlook 55
2.9. Acknowledgements 57
2.10. References 57
Chapitre 3. Novel method for quantifying molecular orientation by polarized Raman spectroscopy: a comparative simulations study 67
3.1. Abstract 67
3.2. Introduction 68
3.3. Theoretical section 70
3.3.1. Orientation distribution function 70
3.2.2. Orientation quantification by Raman spectroscopy 73
3.4. Results and discussion 76
3.4.1. Simulations of the MPD method for parallel orientations 76
3.4.2. Simulations of the MPD and DC methods for perpendicular orientations 87
3.5. Conclusion 92
3.6. Acknowledgments 93
3.7. References 93
3.8. Supporting information 95
Chapitre 4. Accurate new method for molecular orientation quantification using polarized Raman spectroscopy 106
4.1. Abstract 106
4.2. Introduction 107
4.3. Theoretical section 109
4.3.1. Depol constant (DC) method 110
4.3.2. Most probable distribution (MPD) method 111
4.4. Experimental section 114
4.5. Results and discussion 115
4.6. Conclusion 127
4.7. Acknowledgements 128
4.8. References 128
4.9. Supporting information 131

Chapitre 5. Orientation and structure of single electrospun nanofibers of poly(ethylene terephthalate) by confocal Raman spectroscopy 132
5.1. Abstract 132
5.2. Introduction 133
5.3. Theoretical section 134
5.4. Experimental section 137
5.5. Results and discussion 138
5.5.1. Orientation quantification at the single nanofiber level 138
5.5.2. Structural analysis at the single nanofiber level 145
5.6. Conclusion 150
5.7. Acknowledgments 151
5.8. References 151
Chapitre 6. Partial disentanglement in continuous polystyrene electrospun fibers 154
6.1. Abstract 154
6.2. Introduction 155
6.3. Experimental section 157
6.4. Results and discussion 158
6.5. Conclusion 169
6.6. Acknowledgements 169
6.7. References 170
6.8. Supporting information 173
Chapitre 7. Orientation and partial disentanglement in individual electrospun fibers: diameter dependence and correlation with mechanical properties 174
7.1. Abstract 174
7.2. Introduction 175
7.3. Experimental 177
7.4. Results and discussion 178
7.4.1. Diameter dependence of orientation in individual PS fibers 178
7.4.2. Partial disentanglement in individual polystyrene fibers 184
7.4.3. Schematic representation of chains organization in PS fibers 191

7.5. Conclusion 195
7.6. Acknowledgments 196
7.7. References 196
7.8. Supporting information 199
8. Conclusions et perspectives 204
8.1. Conclusion 204
8.2. Perspectives 210
8.2.1. Études fondamentales sur les fibres électrofilées individuelles par spectroscopie Raman confocale 210
8.2.2. Caractérisation des fibres électrofilées à l'aide de méthodes spectroscopiques émergentes 223
8.3. Références 229

Liste des figures

Figure 2.1. Scheme of a typical electrospinning setup…….…….. 11

Figure 2.2. SEM images of PEO nanofibers collected using **A)** an aluminum foil, **B)** a two-rods collector, and **C)** a rotating mandrel at a velocity of 1700 rpm. **D-F)** Polarized IR spectra recorded for mats 16

Figure 2.3. In-situ characterization of the deformation of a PVA mat. **A)** 2D-SAXS patterns recorded at different elongations, **B)** 2D-WAXD patterns measured in the same conditions, and **C)** Schematic representation of the evolution of the fiber alignment and crystalline orientation based on the SAXS and WAXD results 22

Figure 2.4. A) Typical experiment for the tensile testing of a single electrospun nanofiber using an AFM tip. Typical setup for a three point bending test of a single fiber: **B)** AFM image (contact mode) of a suspended single fiber and **C)** Scheme of the deflection of the nanofiber induced by the AFM tip. **D)** Typical setup for a shear modulation force microscopy (SMFM) experiment..... 26

Figure 2.5. Relative Young modulus of nylon-6,6 electrospun nanofibers as a function of their diameter 29

Figure 2.6. Proposed model for explaining the modulus increase with decreasing fiber diameter based on the orientation of polymer chains in nanofibers. **A)** Thin fiber with correlated oriented surfaces. **B)** Thicker fiber with uncorrelated oriented surfaces. **C)** Composite fiber with additional oriented surfaces. **D)** Relative modulus of PS fibers with different molecular weights as a function of their radius scaled with Rg..... 31

Figure 2.7. A) AFM phase contrast imaging of the cross-section of a PVA fiber, prepared using a focused ion beam, that shows a core-shell morphology. **B)** Shell thickness of PVA nanofibers with different diameters 33

Figure 2.8. Schematic representation of the internal microstructure of electrospun nanofibers consisting of orientation-correlated, ellipsoid-like, supramolecular structures dispersed in a matrix of amorphous chains **A)** Longitudinal section and **B)** Cross-section of the nanofiber. 34

Figure 2.9. Polymer concentration profiles across the electrospinning jet for a 5 % PEO aqueous solution at different distances from the nozzle. 36

Figure 2.10. Evolution of the melting temperature (Tm) of PEO nanofibers, determined by AFM nanoindentation, as a function of their diameter and compared to a cast film representing the bulk value. 41

Figure 2.11. Characterization of the molecular orientation in individual PE fibers with different diameters. Bright field TEM images and the corresponding SAED patterns for representative fibers with decreasing diameters, and schematic representation of their structure..... 46

Figure 2.12. Characterization of individual PET fibers by confocal Raman spectroscopy. **A)** Set of 4 polarized Raman spectra required for orientation quantification of a single PET nanofiber. **B)** Evolution of the crystallinity degree and gauche and trans fractions as a function of the orientation parameter ($<P_2>$) quantified 49

Figure 2.13. Non-linear optical activity of poly(γ-benzyl α,L-glutamate) fibers. **A)** α-helical structure of PBLG. **B)** X-ray diffraction pattern of electrospun nanofibers and drawn PBLG fibers. **C)** Second harmonic generation microscopy images of electrospun and drawn PBLG nanofibers..... 54

Figure 3.1. a) $<P_2><P_4>$ diagram defining four regions with distinct orientation distribution functions (ODF). 73

Figure 3.2. Correlation between the $<P_2>_{MPD}$ and $<P_2>_{set}$ values in the positive region of the $<P_2><P_4>$ diagram. 79

Figure 3.3. a) Variation of the $<P_2>_{DC}$ values calculated by the DC method induced by an incorrect ρ value. **b)** Variation of $<P_4>_{DC}$ induced by an incorrect ρ value in the conditions described in a). **c)** ODF resulting from the ($<P_2>_{DC}<P_4>_{DC}$) couples calculated for different Δρ for initial ρ_{set} of 0.1, 0.4 and 0.7 83

Figure 3.4. Evolution of *a* with respect to ρ..... 86

Figure 3.5. Correlation between the $<P_2>_{MPD}$ and $<P_2>_{set}$ values in the negative region of the $<P_2><P_4>$ diagram 89

Figure 3.6. a) Variation of the $<P_2>_{DC}$ values calculated by the DC method induced by an incorrect ρ value. **b)** Variation of the $<P_4>_{DC}$ induced by an incorrect ρ value in the conditions described in a). **c)** ODF resulting from the ($<P_2>_{DC}$,$<P_4>_{DC}$) couples calculated for different Δρ for initial ρ_{set} of 0.1, 0.4 and 0.7 91

Figure 3.S1. a) $\langle P_2 \rangle \langle P_4 \rangle$ diagram defining four regions with distinct orientation distribution functions (ODF). **b)** ODFs associated with $\langle P_2 \rangle$ = -0.2 for different values of $\langle P_4 \rangle$..... 95
Figure 3.S2 a) Variation of the $\langle P_2 \rangle_{DC}$ values calculated by the DC method induced by an incorrect ρ value. **b)** Variation of the $\langle P_4 \rangle_{DC}$ in the conditions described in a). **c)** Variation of the $\langle P_2 \rangle_{DC}$ values calculated by the DC method induced by an incorrect ρ value as described in a) **d)** Variation of the $\langle P_4 \rangle$ values in the conditions described in c). 97
Figure 3.S3. a) Variation of the $\langle P_2 \rangle_{DC}$ values calculated by the DC method induced by an incorrect ρ value. **b)** Variation of $\langle P_4 \rangle_{DC}$ in the conditions described in a). **c)** Variation of the $\langle P_2 \rangle_{DC}$ values calculated by the DC method induced by an incorrect ρ value. **d)** Variation of $\langle P_4 \rangle_{DC}$ in the conditions described in c)..... 98
Figure 3.S4. a) Variation of the $\langle P_2 \rangle_{DC}$ values calculated by the DC method induced by an incorrect ρ value. **b)** Variation of the $\langle P_4 \rangle_{DC}$ in the conditions described in a). **c)** Variation of the $\langle P_2 \rangle_{DC}$ values calculated by the DC method induced by an incorrect ρ value. **d)** Variation of the $\langle P_4 \rangle_{DC}$ in the conditions described in c). 99
Figure 3.S5. a) Variation of the $\langle P_2 \rangle_{DC}$ values calculated by the DC method induced by an incorrect ρ value. **b)** Variation of the $\langle P_4 \rangle_{DC}$ in the conditions described in a). **c)** Variation of the $\langle P_2 \rangle_{DC}$ values calculated by the DC method induced by an incorrect ρ value as described in a) **d)** Variation of the $\langle P_4 \rangle_{DC}$ values in the conditions described in c). 100
Figure 3.S6. a) Variation of the $\langle P_2 \rangle_{DC}$ values calculated by the DC method induced by an incorrect ρ value. **b)** Variation of the $\langle P_4 \rangle_{DC}$ in the conditions described in a). **c)** Variation of the $\langle P_2 \rangle_{DC}$ values calculated by the DC method induced by an incorrect ρ value as described in a) **d)** Variation of the $\langle P_4 \rangle_{DC}$ values in the conditions described in c). 101
Figure 3.S7. a) Variation of the $\langle P_2 \rangle_{DC}$ values calculated by the DC method induced by an incorrect ρ value. **b)** Variation of the $\langle P_4 \rangle_{DC}$ in the conditions described in a). **c)** Variation of the $\langle P_2 \rangle_{DC}$ values calculated by the DC method induced by an incorrect ρ value as described in a) **d)** Variation of the $\langle P_4 \rangle_{DC}$ values in the conditions described in c). 102
Figure 3.S8. Evolution of *a* with respect to ρ 104
Figure 4.1. $\langle P_2 \rangle \langle P_4 \rangle$ diagram and a schematic representation of different possible ODFs associated with$\langle P_2 \rangle$ = 0 and with $\langle P_2 \rangle$ = 0.6 113
Figure 4.2. A) Polarized Raman spectra of an oriented HDPE sample. **B)** Orientation of HDPE samples quantified with the MPD and DC methods compared to the calibration curve

using the *complete method*. **C)** Localization in the $<P_2><P_4>$ diagram of the $<P_2>$,$<P_4>$ couples quantified using the DC method. 116

Figure 4.3. A) Polarized Raman spectra and **B)** Polarized IR spectra recorded on the same PET film. 120

Figure 4.4. A) Comparison of the $<P_2>$ values quantified by Raman with the MPD and DC methods with those obtained by polarized IR spectroscopy on the same PET films. **B)** $<P_2>$ values for the *trans* conformers compared with the global $<P_2>$ values obtained by IR spectroscopy. 121

Figure 4.5. A) Comparison of the $<P_2>$ values of a series of PS films quantified by Raman with the MPD method and DC method as a function of the $<P_2>$ values determined by IR spectroscopy on the same films. **B)** Simulation of the impact of the variation of the depolarization ratio on the $<P_2>$ value quantified using the DC method 125

Figure 4.S1. Evolution of the crystallinity degree and *gauche* and *trans* fractions as a function of $<P_2>$ quantified by IR spectroscopy on PET films 131

Figure 4.S2. A) Polarized IR spectra and **B)** Polarized Raman spectra recorded on the same PS film 131

Figure 5.1. Polarized Raman spectra for three representative individual electrospun PET fibers in the 1580-1780 cm^{-1} spectral region 139

Figure 5.2. Polarized Raman spectra of single electrospun PET fibers in the 675-1175 cm^{-1} spectral region 141

Figure 5.3. Most probable orientation distribution function determined for three single electrospun PET nanofibers 142

Figure 5.4. Calibration curve relating the 1616/705 cm^{-1} intensity ratio in the ZZ spectra to the $<P_2>$ and $<P_4>$ orientation parameters 144

Figure 5.5. Evolution of the *gauche* and *trans* fractions as function of $<P_2>$ in electrospun PET fibers. 147

Figure 5.6. Evolution of the degree of crystallinity of PET nanofibers as function of their $<P_2>$ 149

Figure 6.1. IR spectra of a solvent-cast PS film produced from a 10% chloroform solution **(a)** and of fibers electrospun from the same solution without **(b)** and with **(c)** additional bands

associated to a conformation made possible by partial disentanglement of the polymer chains. **d)** IR spectrum of fibers electrospun from an 8% solution. 159

Figure 6.2. A) Temperature-controlled infrared spectra of electrospun fibers, collected from a 10% chloroform solution, during a heating ramp at 1 °C/min. **B)** Temperature evolution of the normalized absorbance of the 1262 cm^{-1} band for electrospun fibers and for a highly oriented film ($<P_2> = 0.22$) 161

Figure 6.3. A) Representative IR spectra of fibers produced from a 10% chloroform solution and collected for different electrospinning times. **B)** Evolution of the 1262/3026 cm^{-1} absorbance ratio as a function of the collection time for PS fibers electrospun from 10, 12.5 and 15% chloroform solutions 164

Figure 6.4. A) SEM pictures of PS fibers electrospun from 10, 12.5 and 15% chloroform solutions and schematic representation of a core-shell morphology as a function of the average fiber diameter. Schematic representations of the electrospinning process **(B)** and of the solvent evaporation from the fibers core for short **(C)** and long **(D)** collection times. 166

Figure 6.5. SEM pictures of PS fibers electrospun from a 10% chloroform solution showing the presence of elongated pores on the surface 168

Figure 7.1. Representative sets of four polarized Raman spectra recorded for individual PS electrospun fibers with a diameter of ~3 μm and 700 nm showing no orientation ($<P_2> = 0.01$) and a high level of orientation ($<P_2> = 0.21$) 179

Figure 7.2. A) Exponential dependence of molecular orientation ($<P_2>$) as a function of the fiber diameter for PS electrospun fibers. **B)** Demonstration of the direct correlation between the diameter dependence of relative modulus and molecular orientation. 182

Figure 7.3. Comparison of the parallel-polarized Raman spectra of an electrospun PS fiber of 500 nm ($<P_2>= 0.17$) with those of an oriented PS film ($<P_2>= 0.20$) 184

Figure 7.4. A) Radial Raman mapping of the Excess of isotropic Intensity of the 1295 cm^{-1} band associated to partial Disentanglement of the chains (EID) for a fiber showing a wrinkled morphology on the micrometer scale. **B)** Parallel-polarized Raman spectra recorded at the similarly-colored mapping positions shown in panel A. **C)** Raman mapping of the EID of an elongated bead showing a core-shell morphology. **D)** Longitudinal Raman mapping of a fiber showing a wrinkled morphology. 187

Figure 7.5. A) Diameter dependence of the Excess of isotropic Intensity of the 1295 cm^{-1} band associated to partial Disentanglement of the chains (EID). **B)** Orientation dependence of the EID values..... 189
Scheme 7.1. Schematic representation of the chain organization in PS electrospun fibers showing a core-shell morphology with a constant shell thickness. 192
Figure 7.S1. Calibration curve linking the $<P_2>$ value to the 1450/620 cm^{-1} band ratio of the ZZ spectra for fibers and films covering the accessible orientation range for PS samples 199
Figure 7.S2. Calibration curve relating the orientation parameter ($<P_2>$) to the ratio of the parallel-polarized spectra (XX/ZZ) of the 620 cm^{-1} band for oriented films and electrospun fibers. 200
Figure 7.S3. Representative series of the four polarized Raman spectra recorded for PS electrospun fibers with similar diameters (~800 and 700 nm)..... 200
Figure 7.S4. SEM images of polystyrene fibers produced from 10, 12.5 and 15 % w/v solutions in chloroform. 201
Figure 7.S5. Isotropic intensity of the 1295 cm^{-1} quantified according to Equation 1 for PS films showing a wide range of orientation..... 201

Liste des abréviations

ρ	Ratio de dépolarisation
χ	Paramètre d'interaction
$<P_l>$	Paramètre d'ordre
$<P_2>$	Second paramètre d'ordre
$<P_4>$	Quatrième paramètre d'ordre
AFAM	Microscopie atomique à force acoustique
AFM	Microscopie à force atomique
ATR	Réflexion totale atténuée
BaF_2	Fluorure de barium
CNT	Nanotube de carbone
DC	Dépolarisation constante
DMF	N,N-Diméthylformamide
DMSO	Diméthylsulfoxyde
DSC	Calorimétrie différentielle à balayage
EID	Excès d'intensité isotrope d'une bande associée au désenchevêtrement
FIB	Faisceau d'ions focalisé
GIXD	Diffraction des rayons X à angle rasant
HDPE	Poly(éthylène) haute densité
HFIP	Hexafluoropropan-2-ol
IR	Infrarouge
IR-*s*-SNOM	Microscopie en champ proche à sonde diffusante dans l'IR
MEK	Butan-2-one
MEH-PPV	Poly(2-méthoxy-5-(2-éthylhexyloxy)-1,4-phénylènevinylène)
MNA	2-Méthyle-4-nitroaniline
MPD	Distribution la plus probable
MWCNT	Nanotube de carbone multiparois
NA	Ouverture numérique
NLO	Optique non linéaire
ODF	Fonction de distribution d'orientation

OFET	Transistor organique à effet de champ
P3HT	Poly(3-hexylthiophène)
PA 6(3)T	Poly(triméthyle hexaméthylène téréphthalamide)
PAIRS	Spectroscopie infrarouge à matrice à plan focal
PAN	Polyacrylonitrile
PBLG	Poly(γ-benzyl α,L-glutamate)
PCL	Poly(ε-caprolactone)
PBT	Poly(butylène téréphtalate)
PEO	Poly(oxyde d'éthylène)
PEVA	Poly(éthylène-co-acétate de vinyle)
PET	Poly(éthylène téréphtalate)
PHBHx	Poly[(R)-3-hydroxybutyrate-co-(R)-3-hydroxyhexanoate]
PLED	Diode à polymère électroluminescent
PLLA	Acide poly-L-lactique
PM-IRLD	Dichroïsme linéaire infrarouge avec modulation de polarisation
PMMA	Poly(méthacrylate de méthyle)
POM	Poly(oxyméthylène)
PPL	Poly(pivalolactone)
PPO	Poly(2,6-diméthyl-1,4-phénylène oxide)
PS	Polystyrène
PVA	Poly(vinyle alcool)
PVC	Poly(chlorure de vinyle)
PVDF	Poly(fluorure de vinylidène)
PVME	Poly(vinyl méthyl éther)
PVP	Poly(vinylpyrrolidone)
Rg	Rayon de gyration
SAED	Diffraction électronique par aire sélectionnée
SANS	Diffusion des neutrons aux petits angles
SAXS	Diffusion des rayons X aux petits angles
SEM	Microscopie électronique à balayage
SERS	Diffusion Raman exaltée de surface

SNOM	Microscopie en champ proche à sonde diffusante
SMFM	Microscopie à modulation de force de cisaillement
SWCNT	Nanotube de carbone à parois unique
TFA	Acide trifluoroacétique
THF	Tétrahydrofurane
Tg	Température de transition vitreuse
Tm	Température de fusion
TEM	Microscopie électronique à transmission
TERS	Spectroscopie Raman à effet de pointe
WAXD	Diffraction des rayons X aux grands angles

Un peintre apprenti demandait à son maître « Quand dois-je considérer que mon tableau est fini? » Et le maître répondit : « Quand tu pourras le regarder avec surprise en te disant : C'est moi qui ai fait ça? » - Sartre

Remerciements

Je souhaite tout d'abord remercier mon directeur de recherche Christian Pellerin. Il est particulièrement difficile de résumé adéquatement une relation qui s'étend sur une aussi longue période et qui a traversé autant d'événements. Le cliché veut que je le remercie de m'avoir accueilli dans son groupe de recherche pour mes stages et mon doctorat. La vérité est qu'il ne m'a jamais « accueilli » dans son labo : il m'y a emmené et m'a entraîné dans sa vision du meilleur chemin possible pour moi. Sur l'échelle d'une vie, je crois sincèrement qu'on rencontre peu de gens qui nous change d'une manière aussi profonde. Il a modelé ma manière de réfléchir et surtout, ma perception de mes propres limites professionnelles et personnelles. Au-delà de tous les aspects scientifiques, il m'a appris à voir beaucoup plus loin et plus grand pour moi-même et m'a poussé à réussir d'une manière que je n'aurais jamais envisagée possible à une autre époque de ma vie. Christian : merci d'avoir cru en moi beaucoup plus que moi-même, d'avoir été mon mentor et d'avoir fait de moi la scientifique que je suis devenue.

Je veux aussi remercier C. Geraldine Bazuin, Antonella Badia, Robert E. Prud'homme, avec qui j'ai eu l'occasion d'étroitement collaborer sur des projets qui ne sont pas inclus de cette thèse, mais qui sont tout aussi chers à mon cœur. D'un point de vue professionnel, vous avez grandement enrichi mon registre de connaissances et j'ai beaucoup appris de vos visions respectives. C'est en travaillant sur vos projets que j'ai compris le chemin scientifique que je souhaite prendre dans le futur. D'un point de vue personnel, je tiens à souligner vos encouragements constants, sur toute la durée de mes études. Chacun à votre manière, vous avez cru en mes capacités, m'avez fait confiance et m'avez traité comme si j'étais un membre de vos groupes de recherche respectifs. J'en ai eu besoin et je l'ai apprécié bien au-delà de ce que vous pouvez réaliser. Pr. Prud'homme, merci également pour toutes ces années de lettres de recommandation d'une efficacité redoutable!

Je voudrais aussi remercier les employés de soutien qui ont croisé ma route, tout particulièrement Sylvain Essiembre, Pierre Ménard-Tremblay, Francine Bélanger et les gens de l'atelier, en particulier Yves Teasdale et Jean-François Myre. Je n'ai jamais eu une idée technique trop difficile ou impossible à réaliser. Sylvain, Yves et Jean-François : vous m'avez

appris que tout se répare, tout peut se construire et tout s'améliore avec un peu (souvent beaucoup) de travail et une bonne dose d'imagination. Merci pour votre soutien, votre disponibilité et surtout, votre enthousiasme, chaque fois que j'en ai eu besoin.

Je veux remercier chaleureusement les étudiants avec qui j'ai travaillé et/ou dont j'ai supervisé les travaux au fil du temps : Frédéric Byette, Anna Gittsegrad, Katia Borozenko et tous les stagiaires, qui sont trop nombreux pour être énumérés. J'ai beaucoup appris de vous tous. Fred : merci pour ta présence calme et rassurante quand les choses n'allaient vraiment pas pour moi.

Je veux aussi souligner l'impact positif sur moi des étudiants de B.Sc. à qui j'ai enseigné au fil du temps. Dans les bons jours, leurs regards illuminés m'ont donné l'impression d'être au bon endroit, au bon moment et de faire la bonne chose. Les gens qui me connaissent savent que je n'éprouve pas souvent de certitudes aussi fortes. Les étudiants croient souvent qu'on les aide, mais c'est parfois (et même souvent) l'inverse.

Je veux remercier tous les organismes qui ont financé mes projets et récompensé mes efforts pendant toute la durée de mon doctorat : le CRSNG, le FQRNT, le Coblentz, le FACSS et le MSED. Les réussites ne sont jamais un abri contre l'échec (et/ou les sentiments d'échec). Chaque prix et chaque bourse est un renouveau d'énergie, un grand encouragement pour faire plus et mieux et surtout, un rayon de soleil dans les journées plus difficiles.

Finalement, je souhaite remercier chaleureusement le comité d'évaluation de cette thèse : les professeurs Julian X. Zhu, D. Bruce Chase, Robert E. Prud'homme pour leur lecture attentive, leurs commentaires pertinents et positifs et leur intérêt évident pour mon travail des dernières années. Grâce à vous, je quitte l'université de Montréal avec le sentiment du devoir accompli et une plus grande confiance en mon futur.

Chapitre 1

1.1. Introduction

Les fibres polymères, synthétiques ou naturelles, sont partout dans nos vies. Selon la nature du polymère qui les compose, les techniques de mise en œuvre utilisées pour les former et la manière dont elles sont tissées (ou assemblées les unes par rapport aux autres), ces fibres confèrent aux objets « macroscopiques » de notre quotidien des propriétés complètement différentes. La plupart des fibres commerciales composées de polymères synthétiques sont produites par extrusion, où un fondu ou une solution visqueuse du polymère passe par une buse de taille variable, sous l'effet d'une pression, et mène à la formation d'un jet qui prend la forme d'une fibre et se solidifie par abaissement de la température, par évaporation du solvant ou par coagulation dans un non solvant.[1-3] La fibre est souvent étirée à des taux d'élongation et à des vitesses d'étirement exceptionnelles, soit pendant la phase finale de solidification ou suite à la solidification, dans l'optique d'induire une orientation préférentielle,[4] une cristallisation[2] et même parfois un désenchevêtrement[5] des chaînes polymères et ainsi d'optimiser les propriétés de la fibre selon son axe principal. De manière générale, la morphologie des fibres et leurs relations structure/propriétés sont d'un intérêt crucial,[6-9] et dépendent fortement de la méthode de mise en œuvre utilisée.[10]

Le diamètre inférieur atteignable des fibres extrudées dépend de plusieurs facteurs, notamment de la taille de l'orifice et de l'étirement subséquent, mais demeure typiquement de plusieurs micromètres.[11] Plusieurs problèmes sont en effet rencontrés avec les méthodes d'extrusion conventionnelles lorsque l'on tente de réduire le diamètre, tels que des instabilités lorsque la pression appliquée est trop élevée ou la cassure des fibres lorsqu'elles sont trop étirées.[12] Historiquement, l'électrofilage a été développé comme une alternative de mise en œuvre intéressante et versatile permettant de réduire le diamètre. Dans ce cas, les fibres sont produites en appliquant un voltage élevé sur l'aiguille d'une seringue contenant un fondu ou une solution de chaînes polymères enchevêtrées dans un solvant volatil. Lorsque les forces électrostatiques répulsives dépassent la tension de surface, la goutte au bout de l'aiguille prend la forme d'un cône de Taylor et un jet fin est éjecté vers un collecteur qui agit à titre de contre-

électrode (voir Fig. 2.1). D'un point de vue théorique, les forces d'élongation associées au jet sous l'action du champ électrique dépassent de loin les valeurs accessibles pour les fibres extrudées[13,14] puisque le diamètre typique des fibres résultantes va de quelques dizaines de nm à quelques micromètres.[13] L'imposant ratio aire/volume qui en résulte ainsi que la porosité des amas de fibres collectés en ont d'abord fait des candidates pour des applications telles que la filtration, où l'optimisation de l'aire de surface est essentielle.[15-17] Elles ont également été utilisées en ingénierie tissulaire où, en plus de ces caractéristiques, l'alignement des fibres ainsi que leurs propriétés mécaniques prennent une importance plus grande.[18-20] Plus récemment, elles ont été intégrées dans divers dispositifs où l'organisation moléculaire des chaînes polymères qui composent les fibres joue un rôle capital.[21-23]

Un principe de base s'applique pour toutes les applications pratiques impliquant des amas de fibres : le macroscopique et le microscopique sont intrinsèquement reliés. L'un ne va pas sans l'autre, mais les questions doivent être posées dans un ordre précis qui est d'une logique implacable. Ce principe peut être compris par l'analogie de la couturière qui souhaite fabriquer un vêtement : elle choisit d'abord le type de fil qui définit, par exemple, l'extensibilité du vêtement, sa résistance aux déchirures ou sa texture. Ensuite, elle détermine la bonne manière de tisser les fils pour obtenir le résultat final souhaité. En termes de chimie des matériaux, on se pose fréquemment les mêmes questions fondamentales, mais en ajoutant une étape préalable incontournable : pour un type de fil (fibre) donné, quels sont les paramètres de mise en œuvre susceptibles d'influencer les relations structure/propriétés et jusqu'à quelle limite peut-on optimiser une propriété en ajustant ces paramètres? En dernier lieu seulement viennent les questionnements sur la meilleure manière d'assembler macroscopiquement ces fils. Sans qu'on en prenne réellement conscience, les fibres naturelles sont elles-mêmes soumises à cette étape préliminaire. Depuis plusieurs millénaires, les vers à soie, par exemple, optimisent et adaptent leur technique de mise en œuvre pour produire des matériaux plus résistants, qui augmentent leurs chances de survie et permettent la pérennité de l'espèce.

Pour des applications telles que les vestes pare-balles, chaque fibre doit présenter un module élevé dans l'axe de la fibre, couplé à une haute résistance à la rupture et ce, tout en demeurant légère. Les fibres extrudées de kevlar[24] ou des composites de polyéthylène de haute

densité[25] sont particulièrement reconnues pour ce type d'application. Évidemment, les propriétés des fibres individuelles elles-mêmes ne sont pas seules à entrer en ligne de compte : une veste pare-balles protégeant de manière unidirectionnelle serait d'une efficacité douteuse, selon l'angle du projectile. L'organisation macroscopique des fibres en couches perpendiculaires les unes par rapport aux autres et tissées serré assure donc une protection plus uniforme.[26] On peut également penser aux fils de toiles d'araignée, composés de protéines organisées sous la forme de feuillets bêta et d'hélices alpha orientés dans l'axe de la fibre[27,28] et assemblés macroscopiquement par les araignées de manière à former une toile résistante à l'impact, où les insectes venant de toutes les directions sont finalement faits prisonniers.

Dans le domaine des fibres électrofilées, ces questions se sont souvent posées dans le désordre. De par leur petite taille, elles ont longtemps été pratiquement impossibles à étudier, en termes de caractéristiques structurales, à l'échelle individuelle. Historiquement, elles ont d'abord été étudiées sous forme d'amas de milliers de fibres, pour en extraire les propriétés, puis intégrées dans divers types de dispositifs. Finalement, devant les performances intéressantes et même parfois surprenantes qui ont été observées, on s'est intéressé aux fibres individuelles, à leurs caractéristiques particulières et à leurs relations structure/propriétés, encore très largement incomprises et méconnues.

De manière générale, l'orientation moléculaire d'une fibre est un paramètre critique puisqu'elle améliore fortement plusieurs propriétés, tel que le module dans l'axe de la fibre. Les études d'orientation sur les fibres de polymères peuvent s'avérer un défi expérimental important. La diffraction des rayons X aux grands angles (WAXD) est très utilisée pour ce type d'étude.[29-33] Cette technique est toutefois limitée aux phases cristallines et/ou aux mésophases (états pré-cristallins organisés) et nécessite souvent des amas de fibres (même dans le cas de fibres extrudées de plusieurs micromètres de diamètre) pour obtenir un ratio signal sur bruit satisfaisant.

Pour une fibre individuelle, la spectroscopie Raman est une technique très populaire pour évaluer l'orientation et la structure moléculaire des fibres extrudées.[27,34-37] Comme toute technique de spectroscopie vibrationnelle, elle donne accès à une riche variété d'information pour tous les types de phases présentes dans le matériau et permet donc une analyse fine d'une

plus large gamme de polymères que les techniques de diffraction. Pour tirer pleinement profit de la résolution spatiale théoriquement accessible de quelques centaines de nm associée aux longueurs d'onde du visible, la spectroscopie Raman confocale, issue du couplage entre la spectroscopie Raman et la microscopie optique confocale, peut être utilisée. Cette technique a été largement appliquée, par exemple, pour étudier en profondeur l'orientation et les aspects structuraux des soies d'araignées d'un diamètre typique de 3 à 5 µm.[27,28] Dans le cas des fibres électrofilées dont le diamètre est souvent proche de la limite de résolution spatiale de la technique, le défi expérimental est immense. Les tentatives antérieures à cette thèse d'effectuer de telles études ont donné lieu à des valeurs d'orientation hors des limites théoriques suite à la mesure de spectres polarisés montrant un ratio signal sur bruit extrêmement faible.[38]

Il n'en reste pas moins que le domaine des fibres électrofilées souffre grandement d'un manque de compréhension des facteurs qui influencent les propriétés de ces matériaux et la solution réside dans la multiplication des études structurales à l'échelle de la fibre individuelle. La spectroscopie Raman, de par son accessibilité et par la richesse de l'information structurale à laquelle elle donne accès, apparaît comme un outil de choix. L'objectif principal de cette thèse était donc le développement de méthodologies rendant possible l'étude des relations structure/propriétés à l'échelle de la fibre individuelle et permettant un meilleur contrôle de leurs propriétés.

1.2. Contenu de la thèse

Cette thèse débutera au Chapitre 2 par une revue de la littérature publiée dans *Macromolecules* (M. Richard-Lacroix, C. Pellerin, *Macromolecules*, **2013**, 46, *24*, 9473-9493) qui énoncera également les perspectives et défis futurs dans le domaine de l'orientation moléculaire des fibres électrofilées. Suite à une courte revue de l'histoire de l'électrofilage et des caractéristiques spécifiques du jet, la Section 2.3.1 présente les premières et principales études d'orientation moléculaire sur des amas de fibres, souvent associées aux types de collecteurs, à l'aide de techniques telles que la spectroscopie infrarouge et la diffraction des rayons X. Par la suite, la Section 2.3.2 traite des paramètres spécifiques à l'électrofilage qui encouragent la formation de phases cristallines polymorphes normalement observées

uniquement lorsqu'un matériau est sous contrainte et/ou formé par une trempe. Les corrélations entre l'orientation moléculaire et les propriétés mécaniques des amas de fibres sont finalement survolées à la Section 2.3.3.

La Section 2.4 revisite les études des propriétés mécaniques à l'échelle de la fibre individuelle qui ont récemment bouleversé notre compréhension de ces matériaux en montrant une augmentation inhabituelle du module avec la diminution du diamètre des fibres. Elle décrit également les différents modèles proposés pour justifier une telle évolution en mettant de l'avant les similitudes et incohérences entre ces différentes propositions, ainsi que les questions soulevées par les études effectuées à ce jour. La Section 2.5 couvre également l'influence de l'orientation et du diamètre sur les propriétés thermiques et sur le taux de cristallinité des fibres par rapport au comportement massique.

Peu d'études d'orientation ont été effectuées à l'échelle de la fibre individuelle et ce, principalement à cause de leur faible diamètre et des limites de résolution spatiale de la plupart des techniques de caractérisation conventionnelles. Ces quelques études existant au moment de la publication de cette perspective sont donc mises de l'avant à la Section 2.6, ainsi que le potentiel d'utilisation de ces techniques en vue de répondre à plusieurs questions soulevées. La section suivante (2.7) traite de propriétés (autres que le module) des fibres électrofilées soupçonnées d'être influencées par l'orientation moléculaire ainsi que de plusieurs applications pour lesquelles une forte orientation peut mener à (ou justifier) un accroissement significatif des performances des dispositifs dans lesquels les fibres sont intégrées. Cette revue de la littérature se conclut en soulevant des questions toujours sans réponse, en indiquant des points litigieux d'intérêt et en offrant des pistes de solution.

La spectroscopie Raman confocale est la technique au centre de la plupart des chapitres présentés dans cette thèse puisqu'elle donne accès à une résolution spatiale de l'ordre du diamètre typique des fibres électrofilées, soit quelques centaines de nanomètres. Ses désavantages sont principalement la complexité de la mesure expérimentale ainsi que certaines limites théoriques associées à la méthode de quantification de l'orientation, qui entraîne fréquemment des erreurs. Dans l'optique d'optimiser l'applicabilité de la spectroscopie Raman polarisée pour l'étude des fibres électrofilées, mais également pour tout autre type de

matériaux, le Chapitre 3, publié dans *Applied Spectroscopy* (M. Richard-Lacroix, C. Pellerin, *Applied Spectroscopy*, **2013**, 47, *4*, 409-419) présente le développement des équations d'une nouvelle méthode de quantification de l'orientation moléculaire par spectroscopie Raman, démontre son efficacité par simulation et expose clairement les limites de la procédure conventionnelle. Le Chapitre 4, publié dans *Macromolecules* (M. Richard-Lacroix, C. Pellerin, *Macromolecules*, **2013**, 46, *14*, 5561-5569), illustre ensuite l'applicabilité expérimentale de la méthode développée au Chapitre 3 sur des matériaux polymères ainsi que son efficacité par rapport à la méthode conventionnelle.

L'objectif suivant était d'établir un protocole clair et simple permettant l'étude de l'orientation et de la structure moléculaire à l'échelle de la fibre électrofilée individuelle. Le Chapitre 5, publié dans *Macromolecules* (M. Richard-Lacroix, C. Pellerin, *Macromolecules*, **2012**, 45, *4*, 1946-1953), présente la procédure établie, ses limites ainsi que des stratégies expérimentales pour les surpasser en utilisant le poly(éthylène téréphtalate) comme système modèle, puisque son spectre Raman est bien compris. La somme de l'information structurale pouvant être extraite de ces matériaux par spectroscopie Raman est également exposée.

Au Chapitre 6, publié dans *Macromolecules* (M. Richard-Lacroix, C. Pellerin, *Macromolecules*, **2015**, *48*, 1, 37-42), c'est la spectroscopie infrarouge sur des amas de fibres de polystyrène qui est utilisée pour démontrer expérimentalement un aspect structural important des nanofibres, soupçonné d'influencer grandement leurs propriétés, soit le degré d'enchevêtrement plus faible dans les fibres que dans la masse. Les paramètres d'électrofilage qui influencent l'apparition du phénomène sont également identifiés. Finalement, au Chapitre 7, également publié dans *Macromolecules* (M. Richard-Lacroix, C. Pellerin, *Macromolecules*, **2015**, *48*, 13, 4511-4519), la puissance de l'ensemble des méthodologies Raman préalablement développées est exploitée dans l'optique d'établir la première relation directe structure/propriétés, à l'échelle de la fibre électrofilée individuelle, par l'étude de l'orientation moléculaire et du désenchevêtrement en fonction du diamètre de fibres de polystyrène. Ces paramètres sont mis en corrélation avec les propriétés mécaniques et étudiés sur une quantité significative et statistiquement représentative de fibres uniques. Finalement, une synthèse des résultats principaux de cette thèse sera présentée, ainsi qu'une proposition de 6 projets biens définis décrivant comment les techniques émergentes de spectroscopie vibrationnelle

permettront éventuellement d'aller encore plus loin dans l'étude détaillée de la structure moléculaire caractéristique de ces matériaux.

1.3. Références

1. Wilding, M. A. In *Chemistry of the Textiles Industry*; Carr, C. M., Ed.; Springer Netherlands: Dordrecht, 1995, p 1-45.
2. Black, W. B. *Annu. Revi. Mater. Sci.* **1980**, *10*, 311-362.
3. Wang, Y.-X.; Wang, C.-G.; Yu, M.-J. *J. Appl. Polym. Sci.* **2007**, *104*, 3723-3729.
4. Hoogsteen, W.; Hooft, R. J.; Postema, A. R.; Brinke, G.; Pennings, A. J. *J. Mater. Sci.* **1988**, *23*, 3459-3466.
5. Schaller, R.; Feldman, K.; Smith, P.; Tervoort, T. A. *Macromolecules* **2015**, *48*, 8877-8884.
6. Black, W. B. *Annu. Rev. Mater. Sci.* **1980**, *10*, 311-362.
7. Li, S. F. Y.; McGhie, A. J.; Tang, S. L. *Polymer* **1993**, *34*, 4573-4575.
8. Graham, J. F.; McCague, C.; Warren, O. L.; Norton, P. R. *Polymer* **2000**, *41*, 4761-4764.
9. Sprague, B. S. *J. Macromol. Sci. B* **1973**, *8*, 157-187.
10. Gupta, B.; Revagade, N.; Hilborn, J. *Prog. Polym. Sci.* **2007**, *32*, 455-482.
11. Postema, A. R.; Luiten, A. H.; Oostra, H.; Pennings, A. J. *J. Appl. Polym. Sci.* **1990**, *39*, 1275-1288.
12. Larrondo, L.; St John Manley, R. *J. Polym. Sci.: Polym. Phys.* **1981**, *19*, 909-920.
13. Greiner, A.; Wendorff, J. H. *Angew. Chem. Int. Ed.* **2007**, *46*, 5670-5703.
14. Reneker, D. H.; Kataphinan, W.; Theron, A.; Zussman, E.; Yarin, A. L. *Polymer* **2002**, *43*, 6785-6794.
15. Bhardwaj, N.; Kundu, S. C. *Biotechnol. Adv.* **2010**, *28*, 325-347.
16. Feng, C.; Khulbe, K.; Matsuura, T. *J. Appl. Polym. Sci.* **2010**, *115*, 756-776.
17. Liu, Y.; Wang, R.; Ma, H.; Hsiao, B. S.; Chu, B. *Polymer* **2013**, *54*, 548-556.
18. Li, W. J.; Laurencin, C. T.; Caterson, E. J.; Tuan, R. S.; Ko, F. K. *J. Biomed. Mater. Res.* **2002**, *60*, 613-621.
19. Pham, Q. P.; Sharma, U.; Mikos, A. G. *Tissue Eng.* **2006**, *12*, 1197-1211.

20. Kai, D.; Prabhakaran, M. P.; Jin, G.; Ramakrishna, S. *J. Biomed. Mater. Res. B* **2011**, *98*, 379-386.
21. Bedford, N. M.; Dickerson, M. B.; Drummy, L. F.; Koerner, H.; Singh, K. M.; Vasudev, M. C.; Durstock, M. F.; Naik, R. R.; Steckl, A. J. *Adv. Energy Mater.* **2012**, *2*, 1136-1144.
22. Pagliara, S.; Camposeo, A.; Polini, A.; Cingolani, R.; Pisignano, D. *Lab. Chip.* **2009**, *9*, 2851-2856.
23. Chen, J.-Y.; Kuo, C.-C.; Lai, C.-S.; Chen, W.-C.; Chen, H.-L. *Macromolecules* **2011**, *44*, 2883-2892.
24. Wilfong, R.; Zimmerman, J. *J. Appl. Polym. Sci.* **1977**, *31*, 1-21.
25. Lee, B. L.; Song, J. W.; Ward, J. E. *J. Comp. Mater.* **1994**, *28*, 1202-1226.
26. Grujicic, M.; Arakere, G.; He, T.; Bell, W. C.; Cheeseman, B. A.; Yen, C. F.; Scott, B. *Mater. Sci. Eng.* **2008**, *498*, 231-241.
27. Lefèvre, T.; Paquet-Mercier, F.; Rioux-Dube, J. F.; Pézolet, M. *Biopolymers* **2012**, *97*, 322-336.
28. Rousseau, M. E.; Lefèvre, T.; Beaulieu, L.; Asakura, T.; Pézolet, M. *Biomacromolecules* **2004**, *5*, 2247-2257.
29. Grubb, D. T.; Prasad, K. *Macromolecules* **1992**, *25*, 4575-4582.
30. Eling, B.; Gogolewski, S.; Pennings, A. J. *Polymer* **1982**, *23*, 1587-1593.
31. Zhou, G.; Shao, Z.; Knight, D. P.; Yan, J.; Chen, X. *Adv. Mater.* **2009**, *21*, 366-370.
32. Iwata, T.; Aoyagi, Y.; Fujita, M.; Yamane, H.; Doi, Y.; Suzuki, Y.; Takeuchi, A.; Uesugi, K. *Macromol. Rapid Comm.* **2004**, *25*, 1100-1104.
33. Kolb, R.; Seifert, S.; Stribeck, N.; Zachmann, H. G. *Polymer* **2000**, *41*, 2931-2935.
34. Adar, F.; Noether, H. *Polymer* **1985**, *26*, 1935-1943.
35. Pigeon, M.; Prud'homme, R. E.; Pézolet, M. *Macromolecules* **1991**, *24*, 5687-5694.
36. Frisk, S.; Ikeda, R. M.; Chase, D. B.; Kennedy, A.; Rabolt, J. F. *Macromolecules* **2004**, *37*, 6027-6036.
37. Yang, S.; Michielsen, S. *Macromolecules* **2003**, *36*, 6484-6492.
38. Bellan, L. M.; Craighead, H. G. *Polymer* **2008**, *49*, 3125-3129.

Chapitre 2. Molecular orientation in electrospun fibers: from mats to single fibers

2.1. Abstract

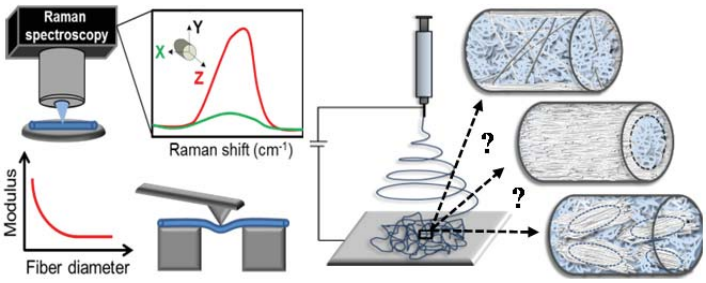

Electrospinning is the most versatile and popular technique for preparing nanofibers from a very broad range of polymer systems. In spite of more than 20 years of studies, our understanding of the relationships between the microstructure and the properties of these fibers, and how they are influenced by the electrospinning conditions, remains fragmentary. This is especially true for molecular orientation, a critical parameter that is often invoked to explain the properties of fibers but that is challenging to quantify properly. Recently, the emergence of characterization techniques enabling studies at the single fiber level, including their orientation, has propelled the field in new directions and provided a wealth of new knowledge. In this perspective, we review and discuss our current understanding of the structure and properties of electrospun nanofibers with a particular emphasis on their molecular orientation. We first describe how studies at the mat level have provided crucial knowledge about the impact of orientation, but also revealed the difficulties associated with its measurement. In the following sections, we present and critically review the most important findings originating from studies of the mechanical and thermal properties of individual fibers. We focus in particular on important models proposed in the literature to explain the variation of the modulus with fiber diameter. We then describe the latest advances in the microstructural characterization of individual fibers. Finally, we show the importance of controlling molecular orientation for some of the most exciting new applications of electrospun nanofibers.[1]

---

[1] Publié comme Perspectives dans *Macromolecules*, **2013**, 46, *24*, 9473-9493 par Marie Richard-Lacroix et Christian Pellerin

2.2. Introduction: electrospinning and orientation

Electrospinning has emerged in the last two decades as a uniquely convenient technique for producing continuous nanofibers. Its experimental accessibility and versatility have enabled the preparation of 1-D nanomaterials from a remarkably broad class of macromolecules-based systems. Electrospun nanofibers find applications in various domains such as tissue engineering and drug delivery,[1] energy storage, conversion and electronic devices,[2] and sensors and filtration membranes,[3] leading to an increased industrial interest for these materials.[4]

Figure 2.1 shows a typical setup used for preparing mats of electrospun nanofibers. Essentially, electrospinning involves applying a high voltage (typically 5-30 kV) on the needle of a syringe filled with a concentrated or semi-diluted entangled polymer solution. The liquid is forced out of the syringe at a constant flow rate by a pump in order to maintain a stable droplet at the tip of the needle. The droplet adopts the shape of a Taylor cone when the electrostatic repulsion, caused by charge formation and migration, overcomes the surface tension of the solution. A solution jet is then ejected and accelerated towards a metallic collector, typically a few cm away, which acts as a counter electrode. The jet rapidly thins and solidifies due to the strong, electrically-driven elongational forces and the extremely fast solvent evaporation.[5, 6] Reneker's group,[7-12] Rutledge and coworkers,[13] Joo and coworkers,[14] and others,[15] have thoroughly investigated, both theoretically and experimentally, the jet formation mechanism and the instabilities it experiences on its way to the collector. Briefly, the jet initially follows a straight trajectory but, as it gets thinner, it rapidly bends due to mutual repulsion of the excess charges it carries.[7] This leads to a looping trajectory, called the whipping motion, in which the jet makes the shape of an envelope cone until reaching the collector.[9]

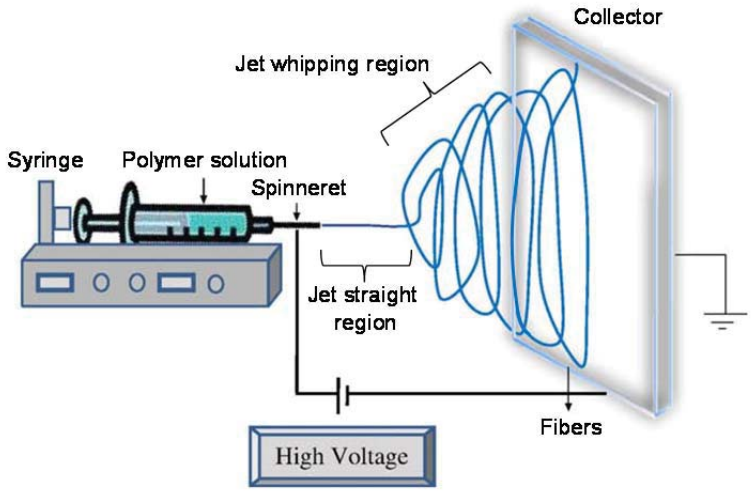

Figure 2.1. Scheme of a typical electrospinning setup. Adapted from Bhardwaj and Kundu.[6]

Despite the apparent simplicity of the process, electrospun nanofibers are complex materials. Their morphology and internal microstructure are affected by numerous experimental parameters, such as the applied voltage, the nature of the collector and the working distance, as well as by a wide range of solution properties, such as its concentration, conductivity, viscosity, surface tension, and the volatility of the solvent. A wealth of studies has provided us with rules that allow tuning the macroscopic morphological features of electrospun fibers.[5, 12, 16] It is now often possible to control, for instance, their diameter from tens of nanometers to a few micrometers, the presence of surface pores, and their relative alignment. In contrast, our ability to predict and control the microstructure of electrospun fibers and, as a consequence, their properties, is much more limited. In particular, understanding and optimizing their molecular orientation is a key challenge in view of their widespread and larger scale application. Indeed, it is well known that orientation can strongly affect the mechanical, thermal, electrical and optical properties of polymeric material, thereby directing their performance in various types of devices. In this *Perspective*, to avoid confusion, the term *orientation* will always refer to the molecular orientation of polymer chains within a fiber, while *alignment* will be used to describe the macroscopic organization of the fibers in a mat.

Several studies have used particles tracing and/or orientation measurements to demonstrate the large elongational forces experienced by the solution in the straight jet section, for instance using high-speed imaging,[11, 17] birefringence,[9, 11] Raman spectroscopy[18] and, most recently, X-ray phase contrast imaging,[19, 20]. Depending on the electrospinning conditions, a draw ratio of approximately 1000 and strain rates ranging from 100 to 1000 s^{-1} have been estimated.[7, 10] The strain rate would increase back to approximately 1000 s^{-1} when the jet enters the whipping region, followed by a gradual decrease due to the increasing viscosity of the solution as the solvent evaporates. The total draw ratio would reach extremely high values on the order of 25 000.[7, 11]

In spite of these very large draw ratios and strain rates, electrospun nanofibers have long been considered to present negligible orientation.[21] The orientation at the end of any deformation process is dictated by the competition between the extensional forces, which orient polymer chains along the deformation direction, and orientation relaxation, which promotes a return to the isotropic state due to the entropic cost of extending chains beyond their equilibrium dimensions. The relaxation times depend on several factors such as the flexibility of the polymer, its molecular weight, and its concentration in solution, just to mention a few.[11] The evaporation of the solvent during fiber formation leads to a gradual increase of the relaxation times of the polymer, as well as to an increase of its effective glass transition temperature (Tg) since the solvent acted as a plasticizer. The system can therefore be locked in an out-of-equilibrium oriented state if the polymer becomes vitrified (if its Tg is below the electrospinning temperature) and/or if crystallization occurs in the jet. An additional complicating phenomenon is the possible loss of entanglements in solution, due to the high strain rate extensional flow, which could promote faster orientation relaxation.[22]

It has been reported that chain orientation is significant in the early part of the straight jet section[20] but that relaxation dominates downstream.[10] Nonetheless, the orientation and microstructure of electrospun nanofibers are necessarily modified, if not largely determined, by the events occurring in the whipping region. Unfortunately, it is extremely challenging to study the jet in this zone due to its small size and to its rapid large-amplitude motion.[9, 11, 18] In addition, the presence of residual solvent in the collected fibers may allow further processes to

occur after electrospinning is completed, in particular orientation relaxation and crystallization.

Conventional techniques used for studying molecular orientation, such as wide-angle X-ray diffraction (WAXD) and infrared (IR) spectroscopy, both require large quantities of well-aligned fibers. Their results are a convolution of molecular orientation and fiber alignment. As a consequence, studying electrospun fibers deposited as a random mat on a foil collector systematically leads to the apparent absence of orientation which, in fact, is due to the lack of alignment. The design, in the early 2000s, of collectors capable of inducing a high level of fiber alignment allowed revealing that a significant level of molecular orientation can be reached in electrospun nanofibers. In spite of more than two decades of extensive investigations, we have only grazed at the surface of the unique properties of electrospun nanofibers, which are still far from being well understood. The factors that determine the level of orientation in electrospun fibers and the spatial distribution of oriented chains within the fiber remain subject to controversy.

In this *Perspective*, we review the salient observations regarding the microstructure and properties of electrospun nanofibers. We also discuss the current challenges and the new opportunities created by advanced techniques providing information at the single fiber scale. The first section provides a critical review of important studies that were conducted at the scale of fibers mats. We first consider the impact of collectors on orientation and their major drawback: their possible influence on the microstructure of fibers. We then review the formation of polymorphic crystalline forms in electrospun fibers and its relation with molecular orientation. Finally, we very briefly consider studies of mechanical properties conducted on mats that were interpreted in terms of molecular orientation.

The four following sections deal specifically with recent studies of individual fibers that have completely modified our understanding of these unique materials. In Section 2.4, we describe the impressive advances made possible by the development of new methods, most often based on atomic force microscopy (AFM), to study mechanical properties of single fibers. We highlight the unusual properties of electrospun nanofibers, especially their size-dependent modulus, and then critically discuss the foremost models proposed to explain this

phenomenon, which all involve orientation. In the third part, we review the intriguing, but conflicting, results that have emerged from thermal studies of individual nanofibers. It is our belief that a complete understanding of the mechanical and thermal properties of electrospun fibers will only stem from more detailed structural studies at the single fiber scale. We therefore explore in Section 2.6 the early results provided by selected area electron diffraction (SAED) and confocal Raman spectroscopy on individual fibers. Finally, the last section presents examples of the significant influence of molecular orientation on some of the most exciting emergent applications of electrospun nanofibers.

2.3. Orientation studies at the mat level

2.3.1. Impact of the collector on molecular orientation

Most early studies of electrospun nanofibers have concluded that their orientation was small and that their crystal organization was poorly developed.[21, 23-25] These studies were conducted on collections of fibers and were therefore complicated by the convolution of orientation and fiber alignment. Based on the premise that nanofibers should be anisotropic, much effort has been put in developing collectors to enable their preparation and characterization as well-aligned bundles and, possibly, to increase their level of orientation.

To the best of our knowledge, Fenessey and Farris[21] were the first to show that using a rotating collector induces increased orientation in nanofibers. They prepared polyacrylonitrile (PAN) nanofibers which, when collected on a stationary collector, did not show any birefringence or crystallinity. In contrast, orientation and crystallinity both increased when the fibers were collected at progressively higher speeds on a rotating mandrel, until a plateau was reached. The absence of orientation in fibers prepared on the static collector was partially attributed to presence of residual dimethyl formamide (DMF) solvent due to its high boiling point. The chains may have oriented during the electrospinning process but they had the opportunity to relax. The authors hypothesised that the orientation observed for samples collected at high rotation speeds was not induced by the electrospinning process itself but rather appeared at the last stage of the fiber formation, when reaching the collector. This was supported by the parallel reduction of the fibers' diameter that suggested additional stretching.

The orientations values, quantified by WAXD and IR, were quite low. Nevertheless, this study has provided one of the first evidence for orientation in electrospun nanofibers. Several studies have later led to similar conclusions for several other polymer systems and using various types of rotating collectors.[26-29] Recently, Rungswang et al.[30] have shown that the orientation of block copolymer microdomains can also be adjusted by the rotator velocity.

In 2003, Li et al.[31] have proposed using two charged metallic plates separated by a short air gap (a "two-rods collector") to improve the fibers' alignment. Kakade et al.[32] were among the first to show that the orientation of electrospun fibers can, in fact, be extremely high for poly(ethylene oxide) (PEO) fibers collected using this type of device. They compared the results with fibers collected on an aluminum foil and on a rotating mandrel. The scanning electron microscopy (SEM) pictures of Figure 2.2A-C show that a random mat was produced on the aluminum foil, while the fibers were macroscopically aligned with the two-rods collector and the rotating mandrel. All fibers showed an equivalent diameter distribution (from 100 to 400 nm), leading the authors to conclude that the collectors caused no additional stretching under these conditions. Polarized IR spectroscopy was then used to determine the orientation of PEO in the various samples (Figure 2.2D-F). As an aside, we want to warn the reader that several studies in the literature have over-interpreted distorted IR spectra of fiber mats showing derivative-shaped bands due to the anomalous dispersion of the refractive index. This is not the case for the high quality spectra of Figure 2.2. The two polarized spectra were equivalent for fibers collected on the aluminum foil (Figure 2.2D), showing the absence of orientation which may, in fact, be simply due the lack of fiber alignment. In contrast, the two polarized spectra showed completely different absorbance values for fibers collected between the two rods (Figure 2.2E), indicating their very high level of orientation. The dichroic ratio was much lower for fibers collected on the rotating mandrel (Figure 2.2F), even though their macroscopic alignment was reported as being comparable. Kakade et al. hypothesized that the high level of orientation of PEO was related to the orientation of the solvent (water) molecules in the electric field and to the similarity of the relaxation time for water and the PEO backbone. The rapid deposition of the fibers between the negatively charged rods would also prevent relaxation from occurring, in contrast to the situation when using a grounded rotating collector.

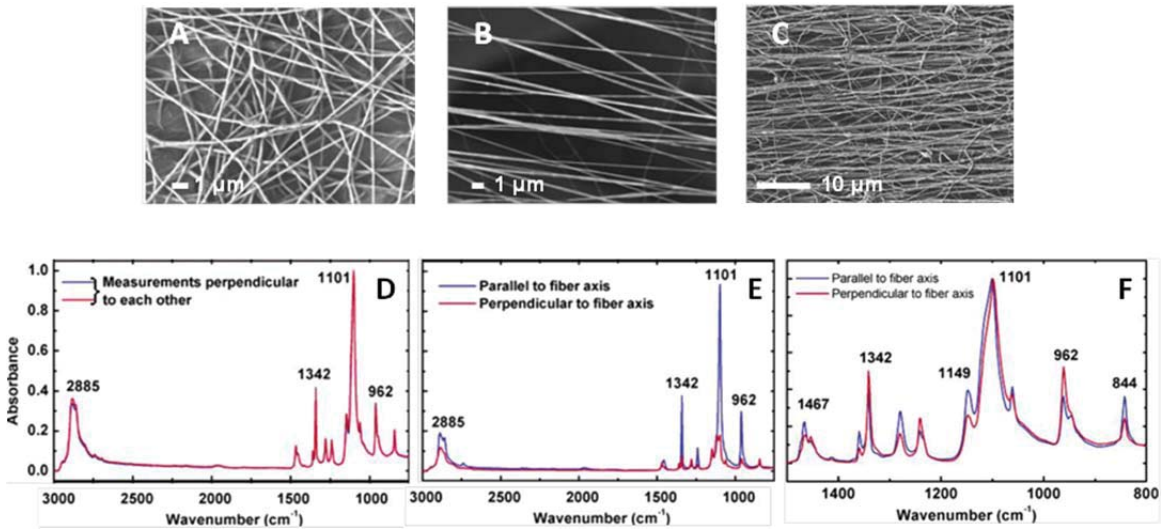

Figure 2.2. SEM images of PEO nanofibers collected using **A)** an aluminum foil, **B)** a two-rods collector, and **C)** a rotating mandrel at a velocity of 1700 rpm. **D-F)** Polarized IR spectra recorded for mats corresponding to panels A-C, respectively. Adapted from Kakade et al.[32]

In the same period, our group has shown that electrospun fibers of the α form of the PEO complex with urea also show an extremely high level of orientation when collected between two metallic rods.[33] These fibers were produced from methanol solutions, suggesting that the high level of orientation could be due to the collector but not to the solvent relaxation time. In this complex, the PEO chains are confined in an extended conformation in narrow channels of urea. This initially led us to believe that the channels orient in the electric field because of their large aspect ratio, by analogy to the high orientation observed for multi-walled carbon nanotubes (MWCNT) in electrospun PAN fibers.[34] However, a similarly high orientation was later found for other PEO complexes that do not form channel structures,[35, 36] and for pure poly(oxymethylene) (POM) fibers collected on a rotating disk.[37] A common feature of all these systems is their high crystallinity and fast crystallization kinetics. Based on this observation, we now believe that molecular ordering in these nanofibers is strongly driven by the crystallization process through the formation of oriented nuclei that can grow at a rate at least comparable to the timescale of the electrospinning process. Once formed, these crystals would hinder relaxation of the chains in fibers. In this context, the collection method

would mainly influence the macroscopic alignment of the fibers rather than their microstructure development.

The situation is obviously more complex for fibers composed of lower crystallinity polymers, for which crystal development is partially hindered during electrospinning due to their slower growth rate. In bulk samples, such as films, these polymers are usually more sensitive to the cooling rate and to cold drawing, so we can speculate that their microstructure will also be more affected by the solvent properties and the additional stretching induced by the collector. For totally amorphous polymers, the ability to preserve the orientation imposed by the high strain rate during electrospinning relies on their Tg. Everything else being equal, a polymer with a higher Tg is expected to be more oriented, regardless of the collection method. While they would not form fibers on their own, amorphous polymers with a Tg below room temperature would become completely isotropic due to their chain mobility even when the solvent is removed. In the context of semi-crystalline polymers, such as PEO and PAN, the Tg has less effect on the residual orientation.

Numerous other collection methods have been proposed, either to induce higher levels of macroscopic alignment of fibers, to better control their deposition, or to modify their microstructure and improve their properties in view of specific applications.[38, 39, 40] However, their impact on the orientation and microstructure of the fibers is extremely difficult to determine when working with bundles because one has to average over fibers that are not equally well aligned and that can show broader or narrower morphological distributions. The alignment is unavoidably imperfect and the orientation is therefore systematically underestimated.

In this context, Edwards et al.[28] have proposed using the Legendre addition theorem to take into account the alignment of the fibers when quantifying orientation from measurements on bundles. They have shown that the alignment increases rapidly at low rotation speed and reaches a plateau when the tangential velocity of the collector reaches the speed of fiber deposition, while the orientation of the crystals measured by WAXD continued to increase. At higher velocity, alignment decreased due to the breakage of fibers and the orientation reached a plateau.[28] Mohan et al.[29] have studied the level of orientation of polystyrene (PS) nanofibers

collected at different rotation speeds by small angle neutron scattering (SANS) using a similar strategy. Interestingly, fibers collected at high tangential velocities were much more oriented than those collected between two rods, in contrast with the results of Kakade et al. on PEO fibers.[32]

The Legendre addition theorem is an interesting approach to correct the orientation parameters determined on bundles and to help understanding the real impact of the collector, which is still subject to debate. However, the method leads to increasingly larger errors for lower fiber alignment and is useless for random mats. The only way to perfectly dissociate the effects of the electrospinning conditions and of the collector on the microstructure of nanofibers is to study individual fibers, as will be described in Section 2.6.

2.3.2. Orientation and polymorph formation

A particular feature of electrospun fibers that has attracted much attention is their distinct crystallization behavior as compared to bulk materials. The strong elongational forces acting on the jet and its extremely rapid solidification, which can be compared to an extraordinarily fast quenching process, sometimes lead to the formation of metastable phases or crystalline polymorphs. One of the first systems for which this phenomenon was observed is nylon-6. This polymer normally crystallizes in the thermodynamically stable α phase but the metastable γ phase was found to be predominant in electrospun nanofibers,[24, 27, 41] as previously observed for fibers melt-spun at high take-up speeds.[42] Kongkhlang et al.[37] later demonstrated that the morphology and orientation of POM fibers can also be controlled by the electrospinning conditions. This polymer forms standard folded chain crystals in quiescent conditions and extended chain crystals (ECC) upon drawing.[43] The authors showed that electrospinning leads preferentially to the formation of the ECC polymorph, even on a stationary collector, and that both the ECC fraction and their orientation along the fiber axis increase with the rotation speed of the collector.

In the same period, Yee et al.[44, 45] have observed a similar phenomenon in nanofibers of poly(vinylidene fluoride) (PVDF), a polymer that can form at least five different crystalline polymorphs depending on the processing conditions. The most common ones are the non-polar α and polar γ phases, which are obtained by melt crystallization or solvent casting, and

the polar β phase, which can be formed through several post-treatments including mechanical drawing.[44, 45] The β phase has an all-trans conformation and is, by far, the most deeply studied phase because of its strong piezoelectric and ferroelectric activities. The electrospun PVDF fibers were composed of a blend of α and β crystals with a ratio unaffected by the rotation speed of the collector or by the DMF/acetone solvent composition. In contrast, spin-coated PVDF films were composed of a mixture of α and γ crystals.[44] Knowing that spin-coating also implies a very fast solvent evaporation, it was concluded that the stretching of the jet plays a key role in the formation of the β phase. In fact, this all-trans polymorph became dominant when adding an organic salt to increase the electrical conductivity of the solution, confirming the importance of the large columbic forces.[44] In addition, the level of orientation was always much higher for the β phase than for the α phase, providing additional support to this hypothesis. In a subsequent study, Zheng et al.[46] have shown that the α/β/γ ratio in PVDF fibers can in fact be tuned by varying the nature of the solvent and temperature. These studies strongly suggest that the formation of the β crystalline phase is closely related to the level of orientation and that its fraction is representative of the stress experienced by the fiber. They also reinforce the link between orientation and ECC formation suggested for POM fibers by Kongkhlang et al.[37]

The case of nylon-6 fibers, briefly mentioned above, is more complex. In contrast to the cases of POM and PVDF, it is the helical γ structure that is promoted by electrospinning and not the extended stable α conformation.[47] Giller et al.[48] have studied the effect of the solvent evaporation kinetics on the α/γ ratio for nylon-6 nanofibers. Samples were prepared by electrospinning in an environmental chamber that allowed controlling the solvent vapor pressure to slow down the evaporation process. Their results indicated that the fraction of the α phase increases gradually for slower evaporation rates. In contrast, exposing the fibers to solvent vapor after spinning had limited effect. It was concluded that the fast solidification of the jet favors the formation of the metastable γ phase due to its fast crystallization rate and that it is detrimental to the formation of the α phase that crystallizes more slowly. By slowing down the solvent evaporation rate, the thermodynamically stable α phase becomes dominant.

In the same vein, Cho et al.[49] have shown that fibers formed by melt electrospinning (that implies an extremely fast solidification) are composed exclusively of the metastable γ crystals.

In spite of the fact that the solvent plays the most critical role in forming the metastable polymorph for nylon-6, the conclusion reached for PVDF and POM, i.e. that the more extended structure is favored by the elongational forces that lead to molecular orientation during electrospinning, still holds for nylon-6. Indeed, Kimura et al.[50] have probed the effect of the gap size between the electrodes of a two-rods collector and observed that larger gaps lead to a higher level of orientation and to a higher content of the all-trans α phase. Lee et al.[27] also observed a similar increase of the α phase when increasing the speed of their rotating collector.

From a practical point of view, controlling the crystallization of electrospun nanofibers represents a great challenge for several applications because polymorphs often show completely different properties. As exposed in this section, polymorph formation depends on a fine balance between the solvent evaporation rate and the large stretching of the jet, but it may also be affected by other factors that have not been explored yet. The examples presented in this section are all polymorphs that can only convert to their thermodynamically stable form by melt recrystallization. In this context, the crystalline state is frozen by the rapid solidification of the jet. In contrast, polymorphs undergoing solid–solid transitions have not been reported in electrospun nanofibers, to the best of our knowledge. PEO is an example of a polymer that can experience a stress-induced solid-solid transition, in stretched films, from the thermodynamically favorable 7/2 helical conformation to the all-trans conformation.[51] This extended structure has never been observed for electrospun PEO nanofibers, in spite of their impressively large orientation.[32] We believe that such stress-induced polymorphic structures may form during the electrospinning process but that our capability to observe it is limited by the kinetics of its reconversion to the thermodynamically stable form.

Another important aspect that has not been studied yet is the spatial distribution of the polymorphs in nanofibers. For instance, are the polymorphs uniformly distributed throughout the fiber or are there longitudinal heterogeneities due to inhomogeneous stretching? As will be presented in Section 2.4, different models also propose that the organization of the chains is

heterogeneous across the section of the fiber, so that a radial distribution of polymorphs is also possible. Probing polymorph distribution in single fibers might be an interesting way of corroborating these hypotheses. Unfortunately, very few techniques provide the necessary spatial resolution and phase selectivity, but emergent techniques such as nanofocus X-ray diffraction and tip-enhanced Raman spectroscopy (TERS) could be powerful approaches for this purpose.

2.3.3. Effect of orientation on the mechanical properties of mats

Understanding and controlling the mechanical properties of electrospun fibers is important because they govern their suitability for most applications, such as in tissue engineering, membranes and optoelectronic devices. Several studies performed on mats have shown that electrospun nanofibers have interesting mechanical properties, such as an increased Young modulus as compared to bulk materials,[21, 52, 53, 54] while a few others have not shown this effect.[55] The mechanical properties of mats depend, at a small scale, on the microstructure of each individual fiber and, at a larger scale, on the mat porosity, the presence and density of bonding sites between fibers, and on the alignment of the fibers.[54, 56] These factors lead to a heterogeneous stress distribution and interfere with the accurate determination of the properties of the fibers.

Numerous studies have demonstrated the enhancement of the modulus with the alignment of the fibers prepared using a rotating collector.[25, 53, 56, 57] For instance, Mathew et al.[57] have shown that the Young modulus and the strength of poly(butylene terephthalate) (PBT) mats, quantified using a conventional tensile tester, increased by a factor of four when the velocity of the rotating collector was increased from 4.3 to 17.5 m/s. Unsurprisingly, mediocre properties were found when stretching the mat perpendicular to its main direction. Pedicini and Farris[53] have proposed that the mechanical properties of polyurethane differ in fiber mats and in bulk films because, at least in part, of the molecular orientation in the electrospun fibers.

Yano et al.[58] have recently provided a deeper analysis of the microstructure development during the stretching of mats of poly(vinyl alcohol) (PVA) fibers by conducting in-situ small angle X-ray scattering (SAXS), WAXD, and IR measurements. Figure 2.3A shows the two-

dimensional SAXS patterns obtained for different elongations. Due to the size of the nanofibers, the scattering is dominated by the electron density contrast between the fibers and the air gaps. The equivalent intensity for all azimuthal angles, before elongation, is characteristic of the isotropic fiber alignment in the nonwoven mat. The scattering pattern becomes highly anisotropic at 50% elongation and plateaus beyond 100% elongation. The 2D-WAXD patterns presented in Figure 2.3B, on the other hand, give information on the orientation of crystals in the mat. No orientation is observed before stretching, as expected since the fibers were randomly aligned. Crystal orientation gradually increases during elongation and, interestingly, continues to grow beyond 100% elongation instead of plateauing as for the fiber alignment. Figure 2.3C shows schematically the deformation process. The authors have hypothesized that the crystals were already partially oriented along the fiber axis prior to stretching since a direct measurement was not possible on the random mat. Their orientation increases during elongation due to fiber alignment (up to 100%) and to the cold-drawing of the fibers once they are well aligned. This study is very interesting from two opposing perspectives since it demonstrates the power of combining deformation studies with in-situ structural characterization at different length scales, while simultaneously revealing the limits of studying mats for a full description of the structure within the fiber.

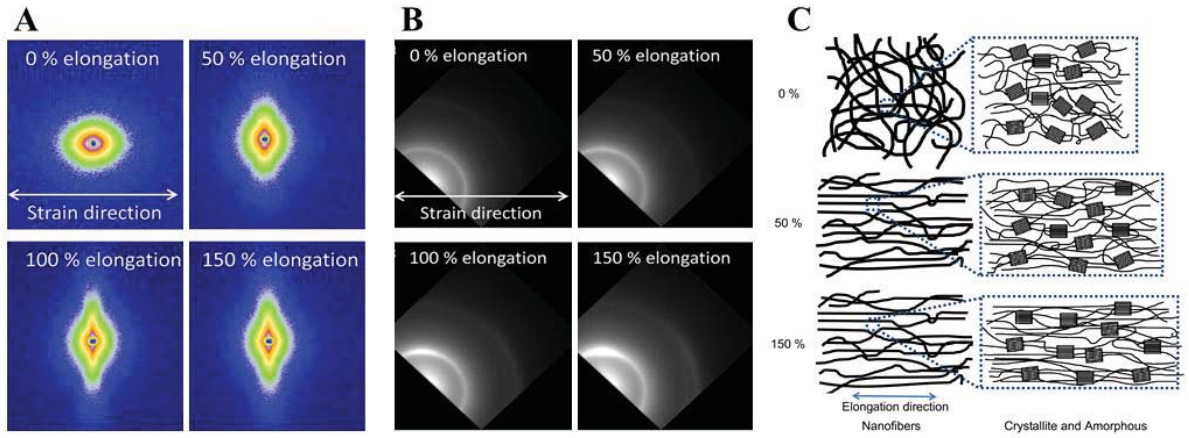

Figure 2.3. In-situ characterization of the deformation of a PVA mat. **A)** 2D-SAXS patterns recorded at different elongations, **B)** 2D-WAXD patterns measured in the same conditions, and **C)** Schematic representation of the evolution of the fiber alignment (left) and crystalline orientation (right) based on the SAXS and WAXD results, respectively. Reproduced from Yano et al.[58]

The correlation between the molecular orientation and the mechanical properties of nanofibers has been established more clearly for polymer nanocomposites, which have been extensively studied in the past 10 years. In particular, composites of carbon nanotubes (CNT) in different polymer matrices have attracted much attention due to their excellent electrical conductivity and their capability to act as efficient reinforcing agents. In fact, studies of composites have largely contributed to demonstrating the capability of electrospinning to produce highly ordered fibers, in particular its ability to orient fillers along the fiber axis. Most of the fillers can be directly imaged by transmission electron microscopy (TEM) thanks to their electronic contrast with the polymer matrix. This technique therefore provides a clear and direct proof of their high level of orientation. WAXD, IR or Raman spectroscopy must be used in parallel to conclude on the orientation of the polymer matrix. For instance, Dror et al.[59] have proposed different strategiesto disperse MWCNTs in a solution of PEO and used TEM imaging to show their good dispersion in electrospun nanofibers and their high orientation. However, WAXD measurements showed that the orientation of the PEO crystals was lowered by the addition of the MWCNT.[59, 60] McCullen et al.[61] have later shown that the Young modulus and electrical conductivity of random mats of PEO fibers containing only 1% of MWCNT were 3 and 10^{12} times higher, respectively, than for pure PEO nanofibers. Su et al.[62] have recently shown that the tensile strength and modulus were significantly improved for aligned PEO/MWCNT fibers collected with a modified rotating drum when compared to random mats.

MWCNT or single-walled carbon nanotubes (SWCNT) have been successfully dispersed in electrospun fibers of a variety of other matrices such as silk,[63] poly(methyl methacrylate) (PMMA),[64] PAN,[34, 65] polyurethane,[66] polyimine,[67] and poly(ethylene terephthalate) (PET),[68] just to mention a few examples. Several other types of fillers that can act as reinforcing agents, such as cellulose nanocrystals,[69] polyhedral oligomeric silsesquioxane,[70] organonanoclays,[71] gold nanorods,[72] etc., have also been studied. A significant increase of the modulus was observed in most cases and was attributed to the high level of orientation of the filler. The possible impact of fillers on the orientation/crystallization of the polymer chains has also been investigated, but the conclusions vary from system to system.

It is critical to measure and understand the properties of electrospun fibers at the scale of the mat since this is how they will be used in most applications. However, the properties of mats are influenced by both the macroscopic organization of the fibers and by their internal microstructure. As will be underlined in Section 2.6, these measurements cannot give a direct and accurate indication of the properties of the fibers themselves even if a perfectly aligned bundle is produced. Characterizing mechanical properties at the single fiber level is therefore a necessary step towards controlling and optimizing these critical properties at the microscopic and macroscopic scales.

2.4. Mechanical properties of single fibers

2.4.1. Experimental studies of the mechanical properties of single fibers

As exposed in the previous section, studying the mechanical properties of electrospun nanofibers using most conventional techniques requires bundles composed of hundreds, if not thousands, of fibers that may each show distinct intrinsic properties. The nature and fraction of the phases, their respective level of orientation, and their distribution through the cross-section of the fibers are all examples of fundamental factors that can affect the mechanical properties of nanofibers in a way that is still poorly understood. Establishing accurate structure/properties relationships is challenging for any material, but it is even more difficult for electrospun nanofibers since it requires using techniques that enable probing very small forces.

AFM has rapidly emerged as a natural characterization tool for this purpose. In 1996, Jaeger et al.[73] have first used it to image the chain packing at the surface of PEO nanofibers. Although noisy, these images have shown the extremely high organization of the polymer chains at the nanometer scale at a time when electrospun fibers were usually considered as completely disordered materials. At the beginning of the century, the development of methods to effectively probe the tensile properties of individual nanoobjects using AFM,[74] often coupled with SEM or TEM imaging,[75] provided a means to study single electrospun nanofibers.[76] The work of Tan et al., in the middle of the 2000s, has largely contributed to the establishment of these experimental methods.[77, 78, 79, 80] There are four main approaches:

tensile testing using a nanotensile apparatus or an AFM, bending testing, nanoindentation, and shear modulation force microscopy (SMFM).

Nanotensile instruments allow measuring complete stress-strain curves, as conventional tensile testers, but at the single fiber level.[79, 81] In its AFM analog, one end of the fiber is bonded to the tip and pulled by a wire while its elongation and breakage are simultaneously imaged by SEM or optical microscopy (Figure 2.4A). The deflection of the cantilever (δ) is used to quantify the force as a function of the elongation of the fiber.[80-82] Bending testing, on the other hand, is experimentally simpler but it only enables probing the modulus at the single fiber scale. Figure 2.4B-C gives an example of the experimental setup for a typical three point bending test. The fiber is suspended on a micro/nano grid and its morphology, position and diameter are first evaluated by AFM imaging (Figure 2.4B). The three point bending test (Figure 2.4C) is then performed by impinging the tip into the fiber to induce a small deflection (δ). The Young modulus is calculated by applying bending theory, assuming that the deformation is purely elastic and that the shear forces acting between the fiber and the grid surface are negligible. A more exhaustive theoretical and experimental description of these procedures is beyond the scope of this *Perspective* and can be found elsewhere.[79, 83]

Nanoindentation and SMFM are also used to study the mechanical properties of individual fibers, but they specifically probe their surface modulus. Essentially, a normal force is applied with the AFM tip to produce a small indentation at the surface of the fiber. In SMFM, as schematized Figure 2.4D, an additional small oscillation of the tip is imposed parallel to the sample axis. The amplitude of the lateral deflection is then used to calculate the apparent modulus based on the Hertz model and on the approximation of a totally elastic deformation.[85]

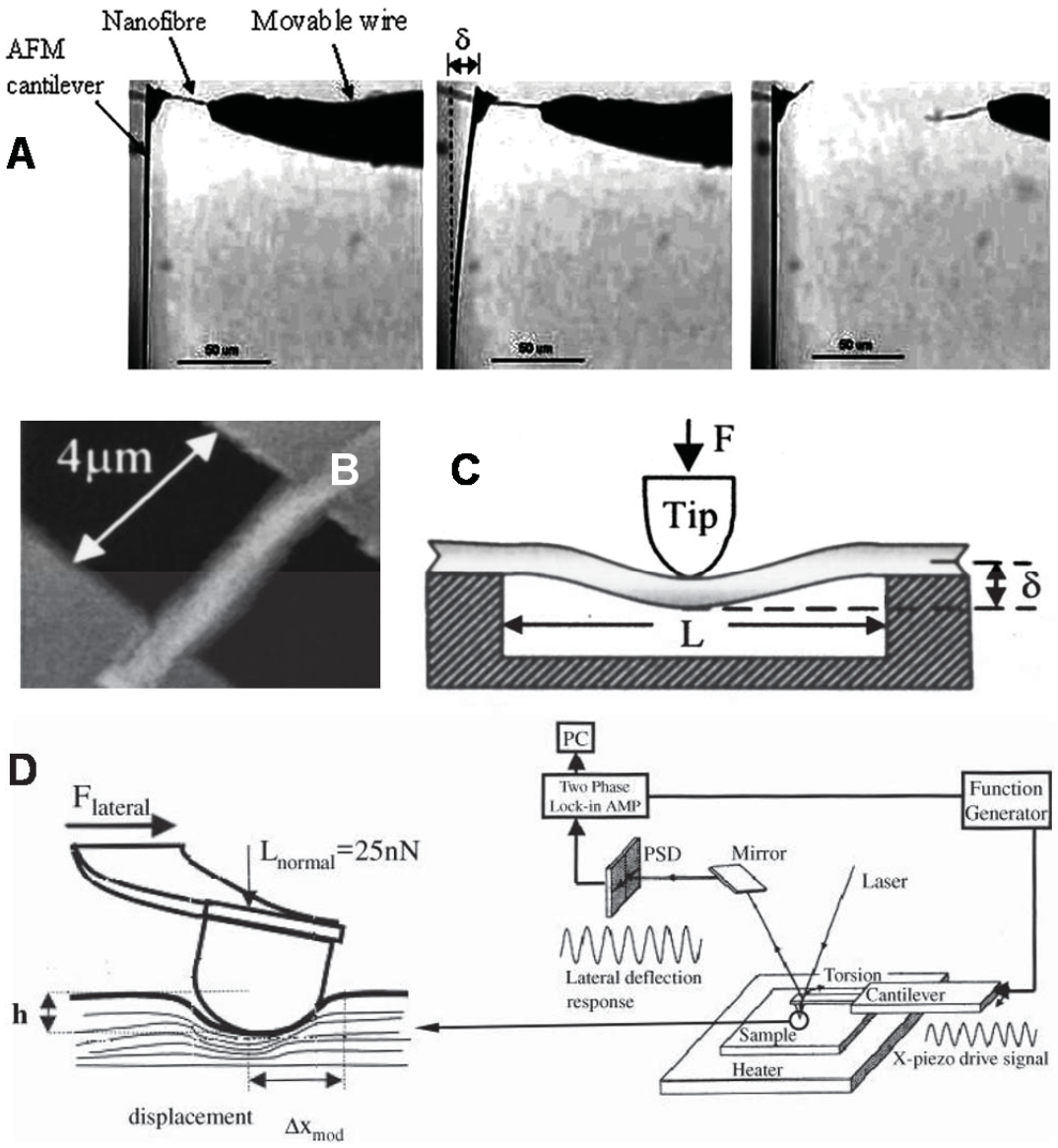

Figure 2.4. A) Typical experiment for the tensile testing of a single electrospun nanofiber using an AFM tip. The scale bar represents 50 μm. Reproduced from Bazbouz et al.[83] Typical setup for a three point bending test of a single fiber: **B)** AFM image (contact mode) of a suspended single fiber and **C)** Scheme of the deflection of the nanofiber induced by the AFM tip. Reproduced from Tan et al.[77] **D)** Typical setup for a shear modulation force microscopy (SMFM) experiment. Reproduced from Ji et al.[84]

A few aspects affecting the mechanical properties of electrospun nanofibers that were previously studied at the scale of the mat have been revisited in recent years, using these procedures, to probe their impact on single fibers. They can be grouped into the impacts of: i) adding reinforcing agents, ii) using specific collectors, and iii) changing the fiber diameter. Studies at the single fiber level on several composites such as PAN/SWCNT,[86]

PMMA/CNT,[87] PVA/cellulose nanowhiskers,[88] polycaprolactone (PCL) with hydroxyapatite,[89] PS/clay,[84] and PS/MWCNT,[90] just to mention a few, have confirmed the significant modulus improvement with the addition of a nanoscaled filler, as observed previously on aligned mats. This modulus increase is usually partially attributed to the orientation of the fillers in these nanofibers, as mentioned in Section 2.3.

Fewer studies have dealt with the impact of the collector on the mechanical properties of individual fibers. Zussman et al.[91] showed that the modulus and strength of nylon-6,6 nanofibers increase when formed on a rotating collector at increasing velocities. They related this enhancement to a larger orientation of the crystalline phase, as determined by WAXD on mats. Zhang et al.[92] and Chan et al.[93] have drawn similar conclusions for poly(L-lactic acid) (PLLA) and poly[(R)-3-hydroxybutyrate-co-(R)-3-hydroxyvalerate] nanofibers, respectively. It is worth noting that the crystallinity of PLLA nanofibers gradually increased with the rotator velocity, while poly[(R)-3-hydroxybutyrate-co-(R)-3-hydroxyvalerate] nanofibers exhibited a crystal modification from the folded chain to the extended chain structure. These structural changes most likely also contribute to the modification of mechanical properties.

In sharp contrast, Thomas et al.[94] have observed a decrease of the Young modulus of PCL fibers as a function of the rotator speed, as determined by nanoindentation. They attributed this result to a gradual decrease of the fibers' crystallinity. On the other hand, their tensile measurements on mats revealed the opposite trend, a discrepancy that they explained by a higher fiber alignment and a lower porosity when increasing the rotation speed. Efforts have been made to reconcile the mechanical properties of mats with those of single fibers,[95] but very few studies have probed both parameters simultaneously. More work is therefore needed to establish a full understanding of these relationships.

In the last few years, several groups have studied the dependence of the mechanical properties of electrospun fibers with their diameter. In doing so, they have contributed to the discovery of one of the most interesting characteristics of electrospun nanofibers. In 2004, Tan et al.[77] have first evidenced that the Young modulus of PLLA nanofibers increased significantly when their diameter was lower than 350 nm. In 2006, Shin et al.[96] have studied poly(2-acrylamido-2-methyl-1-propanesulfonic acid), an electroactive polymer with poor

mechanical properties in the bulk, and demonstrated that the modulus of electrospun fibers increased exponentially from 0.3 to 2.1 GPa when decreasing the diameter from 110 to 55 nm. Importantly, these fibers were all recovered from the same sample, so that their electrospinning conditions were identical. The authors hypothesized that the smaller fibers were subjected to a higher strain rate that led to a higher level of molecular orientation, although this hypothesis was not corroborated by experimental measurements. These studies highlighted a pitfall faced when relating the mechanical properties of single fibers with structural information obtained from macroscopic measurements: mats always contain nanofibers with a distribution of diameters (whose breadth varies with conditions) and of structural characteristics (see Section 2.6). The sharp change of modulus with the fiber diameter also adds to the complexity of studying the impact of the collector or of the addition of fillers, since they often induce a change of the fibers diameter.

The same exponential dependence of the modulus with diameter was later observed for several other amorphous and semi-crystalline polymers, either by preparing fibers from solutions with different polymer concentrations or by varying the applied voltage.[38, 40, 89, 91, 96-102] It is now well accepted as a general phenomenon for electrospun nanofibers. A typical example of such modulus variation with diameter is given in Figure 2.5 for nylon-6,6 nanofibers, where the modulus has been normalized with respect to the bulk value.[97] Overall, this series of studies has completely modified our understanding of the nanofibers' properties and triggered a reexamination of our vision of these materials.

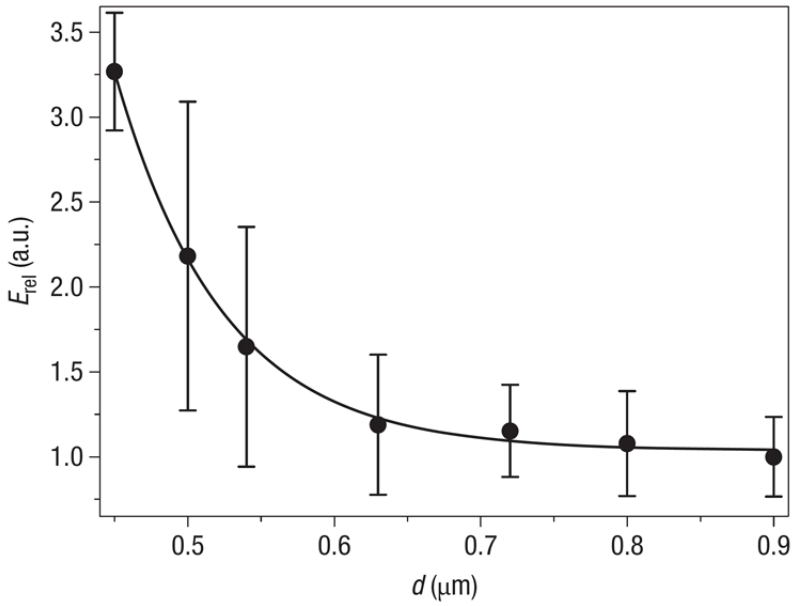

Figure 2.5. Relative Young modulus ($E_{rel} = E_{fiber}/E_{bulk}$) of nylon-6,6 electrospun nanofibers as a function of their diameter. Reproduced from Arinstein et al.[97]

2.4.2 Why does the modulus of electrospun nanofibers vary with their diameter?

2.4.2.1 Description of the principal models

There is not yet a general agreement on the origin of the sharp increase of the modulus with decreasing fiber diameter. Most authors have suggested that it is related to a higher level of molecular orientation in thinner fibers. In the simplest scenario, the orientation may be homogeneously higher throughout the entire fiber.[98] However, more elaborate models have been proposed in which the orientation is not uniform. This section summarizes the three models that have raised the most interest in the literature.

1. Surface oriented layer

Ji et al.[84] were among the first to observe the exponential increase of the modulus for electrospun nanofibers. They have first investigated by SMFM the surface modulus of PS and PS/clay nanofibers over a large diameter range from 4 μm to 150 nm. The same modulus dependence was observed in both cases, although the values were higher when adding

nanoclay.[84] They later studied single fibers of PS with different molecular weights and covering a large diameter range by three point bending and SMFM.[90] The modulus quantified by these two procedures agreed quite well, suggesting that its sharp increase originates from the whole fiber. They proposed a model in which a thin layer of highly oriented polymer chains would be present at the surface of the fibers, due to the large forces experienced during the electrospinning process and to the effect of surface tension. As the diameter of the fiber decreases, the opposing surfaces would become physically coupled, resulting in the reinforcement of the fiber as illustrated in Figure 2.6A. For larger fibers, the surface layers are no longer correlated and their mechanical properties become gradually closer to those of the bulk (Figure 2.6B). In this context, the authors suggested that the modulus dependence with diameter should scale with the radius of gyration (Rg). Figure 2.6D shows the relative modulus (normalized with respect to the bulk value) for a series of PS fibers of different molecular weights as a function of their radius (normalized by their respective Rg). All series show the same exponential dependence with an onset radius of approximately 20 Rg.[90] A similar phenomenon was also observed for PS/MWCNT and PS/clay composite nanofibers. The modulus increase when adding a filler would be due to the formation of layers of oriented chains at these additional interfaces, as schematized in Figure 2.6C.

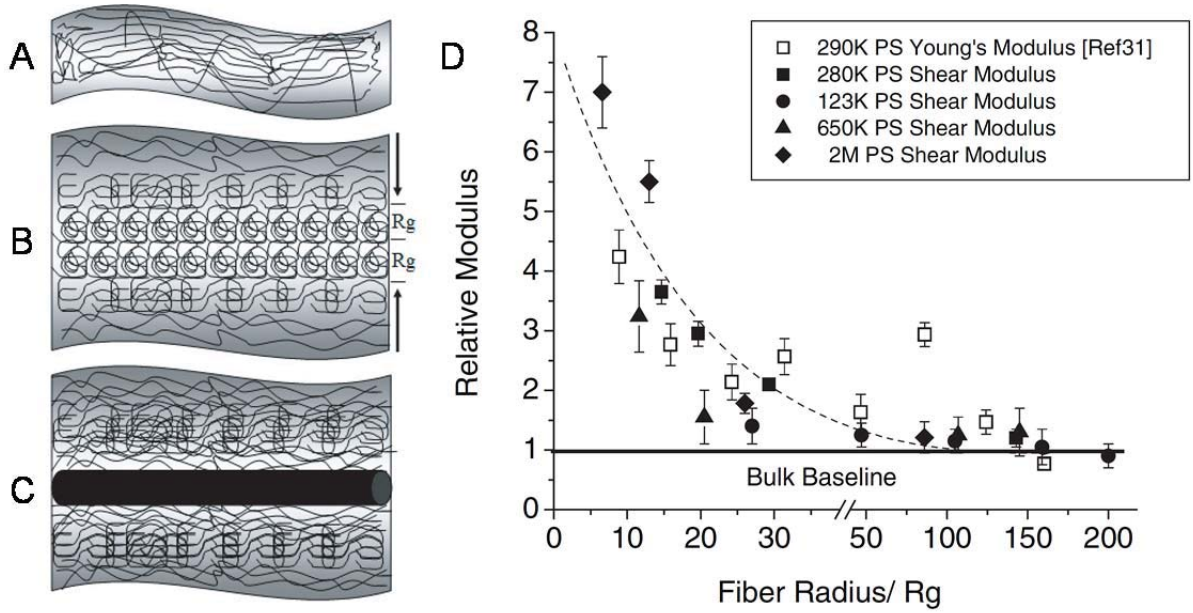

Figure 2.6. Proposed model for explaining the modulus increase with decreasing fiber diameter based on the orientation of polymer chains in nanofibers. **A)** Thin fiber with correlated oriented surfaces. **B)** Thicker fiber with uncorrelated oriented surfaces. **C)** Composite fiber with additional oriented surfaces. **D)** Relative modulus of PS fibers with different molecular weights as a function of their radius scaled with Rg. Reproduced from Ji et al.[90]

2. Core-shell morphology

The second model, which we will call the core-shell morphology, is based on several experimental observations and theoretical considerations. It is increasingly considered as describing adequately the size-dependent behavior of electrospun nanofibers. Reneker and coworkers[11, 17] were the first to report that the birefringence is always higher in the outer region of the electrospinning jet. They proposed that this leads to a core-shell fiber morphology. The formation of a densely packed shell would be caused, among other factors, by the faster solvent evaporation at the surface of the jet. The larger electric stretching force acting at the surface, due to excess charges, combined with a longer relaxation time than in the core, due to the higher polymer concentration, would both result in a higher molecular orientation at the surface. Experimental evidence for the formation of a core-shell morphology has been extensively reported for multiple polymer/solvent systems. The most extreme cases are the so-called "ribbon-like" fibers, which consist of a collapsed tubular or hollow

morphology. Ribbon-like fibers are most often observed when electrospinning highly concentrated polymer solutions in a solvent with a very low boiling point.[103]

Guenthner et al.[104] have simulated the process of nanofiber formation to elucidate the conditions leading to different morphologies. They confirmed the presence of a polymer density profile across the jet: the outer boundaries are highly enriched in polymer, while the solvent fraction rapidly increases in the core. The final morphology of the fiber depends on the competition between the rates of solvent evaporation and diffusion from the solvent-rich core to the polymer-rich shell. For very fast evaporation rates, the skin solidifies quickly and hinders the solvent diffusion by acting as a barrier. Hollow fibers with an intact shell are formed in these conditions. At the other extreme, if the evaporation rate is sufficiently low, the shell becomes diffuse and the density gradient completely disappears, leading to cylindrical fibers. In between, "normal" fibers with a core-shell morphology would be formed. Pai et al.[105] and Wang et al.[106] have associated the buckling observed in nanofibers, formed under various conditions, to skin formation and relaxation of the core as a result of the inhomogeneous solvent evaporation kinetics. Arinstein and Zussman[107] later provided experimental evidence for the presence of residual solvent in the core of tubular fibers and investigated the mechanism and kinetics of its evaporation after the electrospinning. While they selected extreme conditions to enable direct experimental observations, their conclusions should also be applicable core-shell fibers. The presence of residual solvent would therefore allow post-process reorganization, such as orientation relaxation and crystallization, in particular in the core region.

Stachewicz et al.[108] have recently presented strong experimental support for the core-shell model. They prepared cross-sections of PVA fibers using a focused ion beam (FIB) and observed them by AFM phase contrast imaging, a technique that is sensitive to the stiffness of the sample. A representative example is shown in Figure 2.7A, where the presence of a stiffer shell is clearly observable. Figure 2.7B shows that the shell thickness was approximately constant over the investigated diameter range. The mechanical properties of single fibers were quantified by AFM three point bending and showed the usual exponential increase when decreasing the fiber diameter. Accordingly, the authors explained the modulus enhancement by the formation of a highly oriented, rigid, and densely packed shell that would surround an

essentially isotropic core. They proposed a "two phase" model in which the overall modulus depends on the volume fractions of the core and the shell: the properties of fibers become increasingly dominated by the shell when decreasing their diameter.

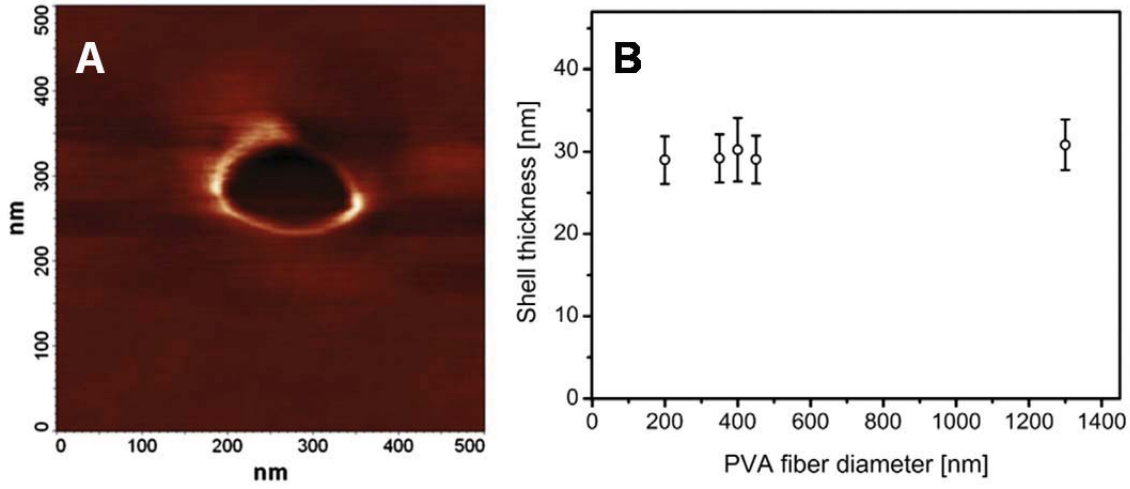

Figure 2.7. A) AFM phase contrast imaging of the cross-section of a PVA fiber, prepared using a focused ion beam, that shows a core-shell morphology. **B)** Shell thickness of PVA nanofibers with different diameters. Reproduced from Stachewicz et al.[108]

3. Formation of supramolecular oriented amorphous structures

The third model is based on a study by Arinstein et al.[97] of nylon-6,6 electrospun nanofibers in 2007. They proposed that the size-dependent properties are due to the formation of supramolecular structures composed of densely packed orientation-correlated amorphous chains. These structures would form due to the extremely high forces acting during the fiber formation. When very thin fibers are prepared, their diameter eventually reaches the same order of magnitude as the correlation length of the supramolecular structures, which therefore become constrained by a confinement effect and lead to the increase in modulus.

This model has drawn much attention in the last few years, but it remained unclearly defined until it was recently illustrated by Arinstein.[109] As schematized in Figure 2.8, the supramolecular structures are assumed to take the shape of anisotropic, ellipsoid-like particles, whose long axis is partially oriented along the fiber axis. These ordered structural elements would be separated by amorphous and essentially isotropic layers. Nanofibers could thus be described as composites containing a large fraction of particles with anisotropic mechanical

properties. When the fiber is submitted to a longitudinal stress, these structures would rotate and decrease their tilt angle with respect to the fiber axis. The confinement effect originates from the partially hindered rotation of the particles at the surface of the fiber that would act as a wall. This model is based on rheological arguments of grains formation in polymer melts under high deformation rates[110] and shear-induced phase separation under continuous shear flow.[111] The model was shown to fit reasonably well not only the increase of the modulus below a critical diameter, but also the molecular weight dependence reported by Ji et al.[90] for PS fibers.

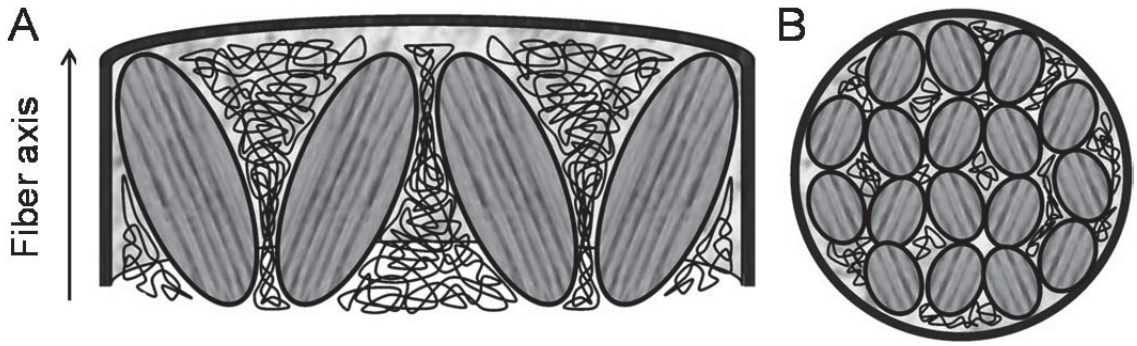

Figure 2.8. Schematic representation of the internal microstructure of electrospun nanofibers consisting of orientation-correlated, ellipsoid-like, supramolecular structures dispersed in a matrix of amorphous chains, as described by Arinstein.[109] **A)** Longitudinal section and **B)** Cross-section of the nanofiber.

2.4.2.2. Consistencies and contradictions between models

The models 1 and 2 are both based on surface effects, in particular on the existence of a highly oriented surface layer. They are nevertheless in complete experimental contradiction. The suggestion by Ji et al.[90] that oriented surfaces become coupled for thin fibers is justified by the agreement between the surface and fiber moduli quantified by SMFM and three point bending, respectively. In contrast, the core-shell model implies the presence of a stiffer shell that should lead to a surface modulus higher than that of the overall fiber. This rigid shell model is supported by the imaging study by Stachewicz et al.[108] In contrast, the Arinstein et al. concept of confined supramolecular oriented structures is not directly related to the surface of the fiber. It is quite interesting but lacks of direct experimental support. In fact, the experimental demonstration of this concept would undeniably be complex, since the contrast between regions of the fiber may not be sufficiently high to be probed by SAXS or SANS

studies. Arinstein[109] has recently concluded that his theory is in line with the observations of Stachewicz et al.[108], since it also predicts an heterogeneous distribution of the polymer density across the fiber cross-section and the formation of densely packed oriented structures. AFM studies may therefore allow observing such density variations in fiber sections.

A recent study by Liu et al.[100] has added to the debate and further complicated the story. Using a strategy similar to that of Ji et al.,[90] they have investigated the modulus dependence with diameter of poly(ethylene-co-vinyl acetate) (PEVA) fibers using SMFM and atomic force acoustic microscopy (AFAM) to probe the properties of the surface and of the entire fiber, respectively. The moduli agreed well but, interestingly, the onset for the modulus increase appeared at a diameter of approximately 10 μm, much larger than in previous studies. It is unlikely that thin surface layers composed of oriented chains would propagate and couple through the interior of such large fibers, as suggested in the first model. However, the correspondence of the moduli measured by SMFM and AFAM does not match the core-shell model either. In a similar manner, the concept of composite fibers composed of ellipsoid-like anisotropic structures (third model) is unlikely to be applicable since the correlation length of the supramolecular structures would need to be enormous for them to be confined in fibers of such diameter.

Greenfeld et al.[19, 20] recently studied the straight part of the electrospinning jet by high resolution X-ray phase-contrast imaging and brought new arguments that could help reconcile conflicting results. Among other parameters, they have studied the heterogeneity of the relative polymer concentration ($\Delta c_p/c$) as a function of the radial distance from the jet center (r/a_0, where a_0 is the internal radius of the nozzle). A representative example is shown in Figure 2.9 for a 5 % PEO aqueous solution at different positions along the length of the jet. In agreement with the simulations of Guenthner et al.[104] and the results of Stachewicz et al.[108], a clear rise in polymer concentration rapidly occurs at the boundaries of the jet due to the extremely rapid solvent evaporation, supporting the hypothesis of the formation of a densely packed skin in electrospun fibers.

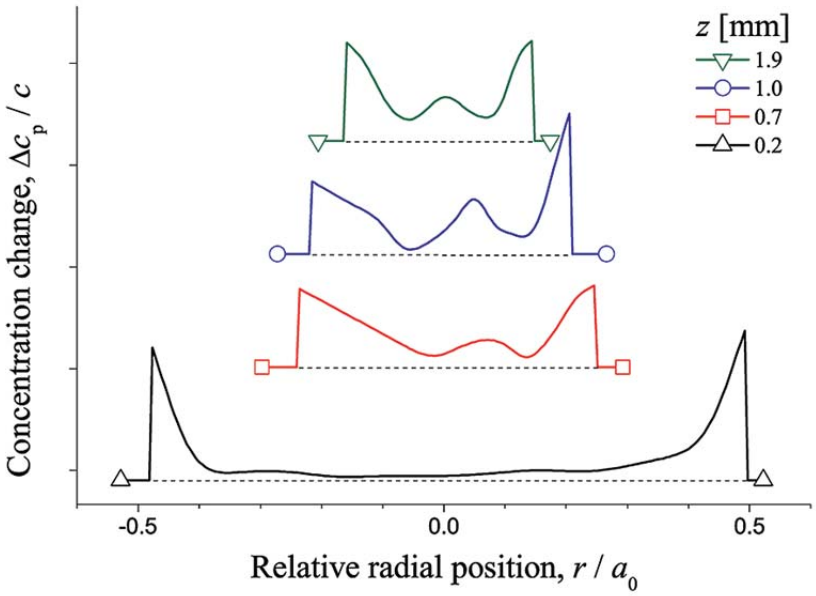

Figure 2.9. Polymer concentration profiles across the electrospinning jet for a 5 % PEO aqueous solution at different distances (z) from the nozzle. The profiles were deduced from X-ray phase-contrast imaging measurements. Reproduced from Greenfeld et al.[20]

Interestingly, the formation of a skin is rapidly followed by a second concentration rise at the center of the jet. This rise would be due to the contraction of the entangled polymer network when submitted to extremely high longitudinal stretching.[20] The relative concentration rise between the core and the boundaries is determined by the balance between stretching of the jet and solvent evaporation, which are competing factors. They would both affect the final density gradient across the fiber and, therefore, its specific microstructure.[19, 20] A disadvantage of X-ray phase-contrast imaging, as for most techniques used to investigate the electrospinning jet, is that it only provides information on the first few mm of the straight section. It does not allow studying the whipping region, where the larger elongation forces may redistribute the polymer and affect the final state of the fiber. If this heterogeneous density distribution in the core of the fiber survives, instead of merging into a smooth homogeneous morphology, it may be observable by AFM phase contrast imaging, although it was not the case in the specific conditions studied by Stachewicz et al.[108]

In fact, none of these three models appears capable of fully justifying all the observed experimental results. We believe that a proper description of the microstructure of electrospun nanofibers could involve a combination of these models. In particular, the second rise of

density in the core of the fiber may reconcile the core-shell model with the results of Ji et al.[90] and of Liu et al.[100] that showed identical moduli at the surface and through the entire fiber thickness. Furthermore, knowing that the thickness of the shell strongly depends on factors such as the solvent volatility, the model of mechanically coupled oriented surfaces may represent an extreme case of diffuse shell. One could further suggest that both a densely packed shell and supramolecular anisotropic particles, confined in its core, could coexist. The shell itself could in fact be composed of such structures and see its properties affected by confinement if the shell/core interface is sufficiently sharp to prevent rotation of the structures. Further investigations by X-ray phase-contrast imaging correlated with mechanical properties and orientation studies at the single fiber level would definitely be beneficial to our understanding of the size-dependent properties of electrospun nanofibers.

2.4.3. What is the role of the electrospinning conditions?

The models presented in Section 2.2 all involve a high level of organization in the amorphous phase but they do not explicitly take into account the crystalline phase. This is mainly based on the argument that a similar exponential increase of the modulus with decreasing fiber diameter was observed for a wide variety of polymer systems that include totally amorphous ones such as PS,[84, 90] and poly(trimethyl hexamethyleneterephthalamide) (PA 6(3)T),[98] as well as several semi-crystalline polymers such as nylon-6,6,[97] PAN[38] and PCL.[99] This is in fact counterintuitive since the crystallinity degree, the orientation and the morphology of the crystals are likely to have a large impact on the modulus of the fibers and, furthermore, to change when decreasing their diameter. It is also worth emphasizing that the highest levels of orientation reported up to now in the electrospinning literature were all for fibers of very highly crystalline polymers such as POM, PEO, and PEO complexes with urea and thiourea.[10, 32, 33, 35] It is very unlikely that the amorphous phase, which only constitutes a small volume fraction in these materials, would entirely determine their mechanical properties. Furthermore, it is well known that the orientation relaxation is much faster in the amorphous phase so that the overall orientation in electrospun nanofibers should be dominated by crystalline or mesophase orientation.

Arinstein et al.,[97] in particular, have based their model on the absence of a correlation between the exponential increase of the modulus and the crystallinity degree, the orientation of the crystalline phase, and even the orientation of the amorphous phase, which were all found to increase monotonically when decreasing the diameter of nylon-6,6 nanofibers. In sharp contrast, Papkov et al.[112] have recently reported a decrease of the crystallinity that approximately followed the drastic increase of the modulus when reducing the diameter of PAN nanofibers. Interestingly, they observed a simultaneous improvement of rigidity and of toughness, which are parameters that usually evolve in opposing directions. They attributed this unusual behavior to a gradual increase of molecular orientation, which would justify the larger modulus, concurrently with a reduction of crystallinity (due to the faster solvent evaporation for thinner jets) which would increase the toughness. In the same vein, Pai et al.[98] have observed an exponential increase of molecular orientation in totally amorphous PA 6(3)T nanofibers that followed the same trend as their Young modulus.

These structural studies were conducted by WAXD or IR spectroscopy measurements, which require large quantities of well-aligned fibers and do not account for the heterogeneity of the characteristics found in a typical bundle. The breadth of the diameter distribution, the unavoidable presence of defects in mats, and the imperfect macroscopic alignment of the fibers (and their variation when adjusting conditions to produce fibers with different average diameters) can all lead to quantification errors and can mask the real evolution of the structural parameters with diameter. These studies nevertheless underline the significant differences in the evolution of the orientation and crystallinity that can be observed for different systems despite the apparent similarity of their modulus dependence with diameter.

Furthermore, some studies have reported conflicting evolutions of the modulus with diameter or different critical onset diameters. For instance, Papkov et al.[112] and Naraghi et al.[101] have both studied the mechanical properties of single PAN nanofibers and observed the usual exponential increase of the modulus with diameter. However, the first have reported an onset diameter of approximately 150-200 nm, while the second found 500-600 nm for fibers collected at a large working distance and using a high voltage. Intriguingly, the effect of diameter on the modulus was barely observable for fibers collected at shorter distances and lower voltage (but maintaining a constant electric field), leading to the conclusion that the

electrospinning conditions have a significant influence on the phenomenon.[101] In the same vein, Lim et al.[99] have reported the usual exponential modulus increase for PCL nanofibers with an onset diameter of approximately 500 nm. Tan et al.[77], on the other hand, have also investigated PCL nanofibers in a diameter range of approximately 425 to 275 nm and reported only a jump of the modulus for fibers smaller than 350 nm.

It is also noteworthy that size-dependent properties have been reported for very small fibers of a few tens of nanometers as well as for much larger ones of a few micrometers. Consequently, the size of the fiber itself is perhaps not the critical parameter. Do fibers of a given diameter, for a given polymer, possess some intrinsic characteristics regardless of the conditions used to reach this diameter? Or rather, are the diameter and the observed characteristics only the associated outcomes of the specific conditions used to produce increasingly smaller fibers? Based on the arguments and results presented in this section, we expect that the diameter at which the mechanical properties of the fibers start to differ from those of the bulk, as well as the specific shape of their evolution, strongly depends on the electrospinning conditions and on the properties of the electrospun solution. For instance, the nature of the solvent, which is virtually unexplored, is expected to modify the crystallization behavior and the level of residual orientation in nanofibers, in addition to enabling (or not) the formation of a core-shell morphology. If so, one could eventually tune separately the properties and the diameter of nanofibers in view of their intended application.

Our understanding of the specific structure/processing/properties relationships of electrospun nanofibers has made a huge progress thanks, in part, to the studies cited in this section, but it is still partial. Some questions that remain open include: why is the same shape often observed for the modulus dependence of fibers composed of totally amorphous, low- and high-crystallinity polymers? and What is the origin of the differences observed for fibers of the same polymer produced in different conditions? We believe that a better comprehension will come from directly correlating mechanical, thermal, and microstructural properties probed at the scale of single nanofibers.

2.5. Thermal properties of single fibers

As in the case of mechanical properties, our understanding of the thermal properties of electrospun nanofibers, such as their melting temperature (Tm) and Tg, has greatly evolved in the past few years. Molecular orientation is, once again, expected to play a major role in determining these properties, but their evolution with fiber diameter and with electrospinning conditions still remains less than clear. The availability of new characterization tools now allows revisiting thermal properties at the single fiber level. In particular, their evolution could be rationalized in the context of the models presented in Section 2.4.2 to support or refute some of their premises.

2.5.1. Melting and crystallization temperatures

Most early thermal studies conducted on mats, typically using differential scanning calorimetry (DSC), have reported a decrease of Tm and of the crystallinity degree for electrospun nanofibers when compared to the bulk material.[112, 113, 114] In general, this has been attributed to the rapid solidification of the jet that prevents the development of a well-ordered crystalline structure. Recent studies at the single fiber level have shown that the melting point is, in fact, strongly dependent on the diameter of the nanofibers.

Wang and Barber[114] have used AFM nanoindentation to probe the melting point of individual PEO nanofibers. Their results, presented in Figure 2.10, reveal a significant decrease of Tm when decreasing the fiber diameter. The crystallinity degree, quantified from DSC measurements on mats, also decreased abruptly, from 62 % for fibers with a diameter greater than 800 nm to 32 % for 68 nm fibers. Their results were well fitted (black curve of Figure 2.10) using a model derived from the Gibbs-Thompson equation that describes the decrease of Tm when reducing the crystal thickness due to the additional interfacial energy, but adapted by Jiang et al.[115] to consider an additional decrease when dealing with small to mesoscale materials. Their hypothesis to justify the simultaneous decrease of Tm and of crystallinity was that amorphous chains with a higher mobility are present at the surface of the fibers and that their volume fraction increases for thinner fibers. This effect would dominate over orientation, which would be expected to induce the opposite trend.

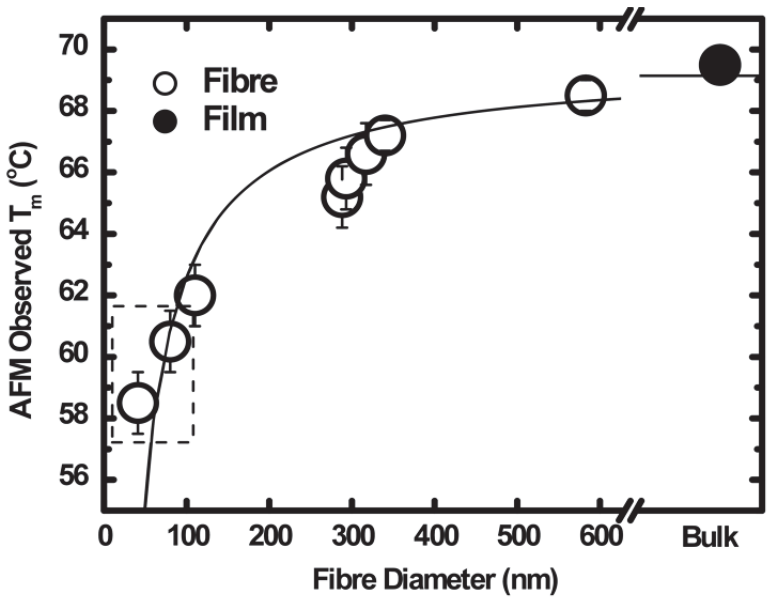

Figure 2.10. Evolution of the melting temperature (Tm) of PEO nanofibers, determined by AFM nanoindentation, as a function of their diameter and compared to a cast film representing the bulk value. Reproduced from Wang and Barber.[114]

In fact, this decreasing trend of Tm could also have been more directly interpreted in terms of a reduction of the size of the crystals when decreasing the fiber diameter. Several studies have, indeed, evidenced by WAXD (with the Scherrer equation) that crystals are smaller in electrospun nanofibers than in the bulk,[10, 37, 116] and that their size is influenced by the processing conditions.[37] One could expect that smaller fibers will contain crystals of reduced size, assuming that their solvent evaporation rate is higher. Indeed, solvent removal leads to an increased jet viscosity and therefore to a smaller crystal growth rate. If the evaporation rate is not uniform through the thickness of the fiber, leading to a core-shell morphology, a radial distribution of crystal sizes may also be expected. Surprisingly, to the best of our knowledge, no studies have been conducted to evaluate directly the evolution of the crystal size with fiber diameter.

Liu et al.[117] have later studied PEVA fibers by SMFM and also observed an important reduction of Tm when decreasing the diameter below 15 μm. The same behavior was observed for a series of PEVA fibers covering a large diameter range with different comonomer ratios.[100] Based on these data, Arinstein et al.[118, 119] have proposed that the drop of Tm is due to an additional melting entropy term. Their theory is based on the hypothesis that an

important difference between thicker and thinner fibers is their entanglement density, which would be much lower in thin fibers than in the bulk due to the rapid solvent evaporation and the important forces acting during the fiber formation. The entanglement density in electrospun fibers would be frozen in a non-equilibrium state that depends on the initial concentration of the solution. When crystallization occurs, the relaxation of the polymer network toward its equilibrium state (more densely entangled) is hindered because tie chains are included in both the amorphous and crystalline phases. As a consequence, crystal melting would be promoted by the additional entropy gained by the system when reaching its equilibrium entanglement density. This additional entropy term would gradually increase as the solutions are diluted to produce smaller fibers, thereby explaining their lower Tm.

A significant level of organization in the amorphous phase, as suggested by the three models presented in Section 2.4.2, should also influence the crystallization behavior, especially for low crystallinity polymers. It has been shown, for instance that the cold crystallization peak occurs 20 °C lower for PLLA nanofibers than for melt spun samples and that it overlaps with Tg due to the preorganization of the amorphous chains.[120] Zhang et al.[92] have also observed the phenomenon for PLLA nanofibers of different molecular weights and showed that the cold crystallization peak gradually decreased as the rotation velocity of the collector increased. They associated this behavior to a higher level of orientation in the amorphous phase that facilitates cold crystallization by reducing its free energy barrier. A mechanism for this transformation, involving a highly oriented mesophase, has recently been proposed.[121] The amplitude and temperature of the cold crystallization peak was dependent on the solution conductivity, which may also influence the degree of orientation.[122]

Another interesting example is the case of nylon-6 nanofibers produced from high concentration or high temperature solutions. Fibers produced in such conditions show an additional melting peak as much as 15 °C higher (depending on the electrospinning conditions) than the Tm of α crystals in bulk samples.[123, 124] Based on a detailed WAXD, SAXS, and IR study, Wang et al.[124] have concluded that this high temperature melting peak is associated to the crystallization, upon annealing, of thick α crystals formed from highly oriented chains. The authors speculated that the coexistence, upon annealing, of these two

types of α crystals was possible due to the core-shell morphology of the fibers. The high melting temperature phase would be exclusively formed in the shell due to the presence of highly oriented chains. Knowing that the stretching of the fiber is quite inhomogeneous during its formation, these two types of crystals could also, arguably, be distributed along the fiber length. These two possibilities could be discriminated, for example, by temperature-controlled confocal Raman spectroscopy studies at the single fiber level. This method would also be applicable to systems for which the coexistence of polymorphs has been observed.

2.5.2. Glass transition temperature

The evolution of the Tg of electrospun nanofibers with their diameter and with the electrospinning conditions is probably as complex as that of Tm. Ji et al.[84] were the first to study the evolution of Tg with the diameter of single fibers by using SMFM to quantify the modulus as a function of temperature. They did not observe any change of Tg for PS nanofibers when decreasing their diameter down to 620 nm. They also reported that the modulus of nanofibers decreased gradually with temperature and recovered its bulk value at Tg. Their hypothesis was that this phenomenon is caused by the gradual loss of the molecular orientation of the chains with temperature until reaching equilibrium at Tg.[84]

In contrast, Wang and Barber[125] have recently observed, using indentation and three point bending testing, a notable Tg decrease of 7 °C when decreasing the diameter of single PVA nanofibers from 600 to 100 nm. They successfully fitted this trend with a model proposed by Forrest and Mattsson[126] for thin films that is based on the hypothesis of a surface layer with a higher mobility. Accordingly, they concluded that this Tg decrease should be related to confinement effects. In fact, this Tg drop could also be explained using the above-mentioned arguments of Arinstein et al.[118] regarding the Tm decrease with diameter. Indeed, a lower entanglement density in smaller nanofibers would also lead to a diminution of Tg, as reported at the surface of thin films.[127] If this is the case, one could expect Tg to vary for fibers with identical diameters but prepared under different conditions, for instance in solvents with different boiling points.

Adding to the complexity of this parameter, Baji et al.[128] have recently reported an increase of Tg when decreasing the average diameter of polyamide-6,6 nanofibers. They

attributed this behavior to a higher level of orientation in smaller nanofibers due to the higher extensional forces that they experienced during their formation. It should be specified that these Tg values were determined by dynamic mechanical analysis on mats and not on individual fibers.

The results presented in this section clearly reveal that more work, in particular at the single fiber level, is required to explain the dependence of Tg, Tm, and of the degree of crystallinity with the fiber diameter and with the processing conditions. The melting temperature, for instance, is believed to depend on the relative rates of crystallization and of orientation relaxation of the amorphous chains, which both depend on the nature of the polymer and on the specific conditions. In fact, the discrepancies between the results for different systems, or even for the same polymer prepared under different conditions, corroborate the hypothesis that the thermal (and mechanical) properties of electrospun nanofibers result from several competing and interacting factors and cannot be predicted based on a single model or a single parameter such as their diameter. Molecular orientation, in particular, is expected to profoundly influence the properties of both amorphous and semi-crystalline polymers and is often invoked as a driving mechanism. Our understanding of the thermal properties of electrospun fibers will benefit from experimental investigations of microstructure at the single fiber level. The next section will highlight the recent progresses in this field which, we believe, will lead to a better control of nanofibers' properties.

2.6. Molecular orientation studies at the single nanofiber scale

The development of techniques to probe the mechanical and thermal properties of individual electrospun nanofibers has led to numerous discoveries, including their significant variation with the fiber diameter and with the specific formation conditions. However, as highlighted in Sections 2.3 and 2.4, our current understanding of the origin of these properties is limited by a lack of detailed structural information. Until recently, most microstructural studies have been conducted by averaging over large bundles that often contain fibers with different sizes and morphologies that are now expected to show different individual properties. Moreover, larger fibers and defects (such as beads) unavoidably contribute more to the averaged signal than thinner fibers, possibly hiding important information. From this

perspective, an increasing attention has been paid in recent years on the development and application of efficient tools to characterize the orientation and microstructure at the single nanofiber level.

Selected area electron diffraction (SAED) has rapidly emerged as a particularly efficient technique for this purpose. To the best of our knowledge, SAED has been used for the first time for the study of single electrospun nanofibers as early as in 2003 by Dror et al.[59] and by Dersch et al.[24] The latter have revealed the longitudinal heterogeneity of the orientation in a 50 nm thick polyamide-6 nanofiber. They concluded that orientation was either small or absent, depending on the specific location along a 600 nm long section of the fiber. They attributed this orientation variability to the instabilities experienced by the jet during the electrospinning process that also cause a diameter gradient in the resulting fiber. In 2006, Huang et al.[129] have produced ultrathin nylon-4,6 fibers as random mats on TEM copper grids and evidenced their extremely high level of orientation using SAED. These results revealed for the first time that fibers in random mats can, indeed, be highly oriented.

Yoshioka et al.[130, 131] have later investigated more deeply the impact of the morphology and size of polyethylene fibers on their level of molecular orientation. They highlighted the substantial distribution of diameter and morphology in samples produced under the same conditions from hot p-xylene solutions. Fibers ranging from 150 nm to a few micrometers of diameter were analyzed individually by SAED and categorized into three groups, presented in Figure 2.11. Fibers with a diameter larger than 1 μm were isotropic, as revealed by a uniform intensity at all azimuthal angles (group i). In contrast, the fibers with a diameter between 400 nm and 1 μm showed an intermediate level of orientation (group ii) and the smallest fibers were very highly oriented (group iii). Careful SEM and TEM analysis indicated that fibers from groups ii and iii had a stacked-lamellar or shish-kebab crystal morphology, as illustrated in Figures 2.11b'' and c'', while some of the thinnest fibers rather showed a fibrillar morphology. Beads and ribbon-like fibers were also present in their samples. Beads were composed of an unoriented crystalline phase while ribbon-like fibers were very highly oriented with a uniplanar uniaxial orientation rather than a fiber texture. To the best of our knowledge, this was the first report proving directly the link between the reduction of the fiber diameter and the enhancement of molecular orientation. As mentioned in Sections 2.3 and 2.4,

it is often invoked that smaller fibers experience more stretching during electrospinning and, thus, present a higher level of orientation, but a direct demonstration was lacking.

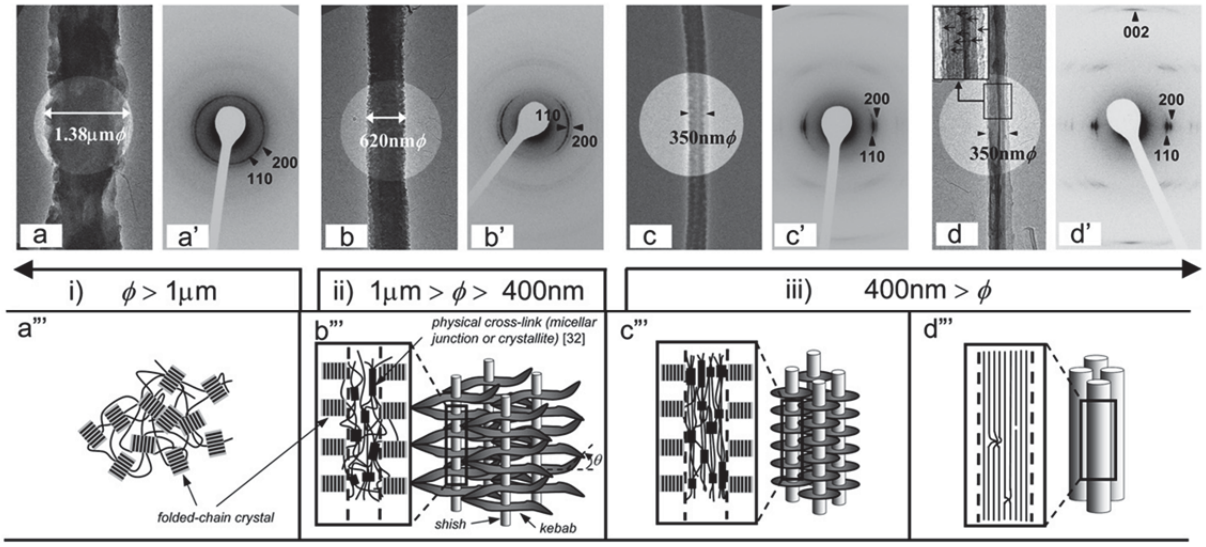

Figure 2.11. Characterization of the molecular orientation in individual PE fibers with different diameters. Bright field TEM images (a to d) and the corresponding SAED patterns (a' to d') for representative fibers with decreasing diameters, and schematic representation of their structure (a'' to d''). Reproduced from Yoshioka et al.[130]

Ma et al.[132] recently studied, at the single fiber level, the impact of using a two-rods collector on the level of orientation of PVDF fibers. Their SAED study showed that fibers collected in the air gap between the two metallic plates, directly on the rods, or even on an aluminum foil, were all molecularly oriented. In contrast, IR spectroscopy measurements only showed orientation for samples collected in the gap since the method is highly sensitive to the fiber alignment in the mat, emphasizing the importance of studies at the single fiber level. When comparing individual fibers with the same diameter, they observed a significantly higher level of orientation for those collected in the air gap, suggesting that the collector does truly modify the nanofibers microstructure. Since orientation originates from a balance between deformation and relaxation, it can be rationalized that deformation induced by the collector at the latest stage of the fiber formation is critical. Due to solvent evaporation, the polymer concentration is higher than earlier in whipping region (and much higher than in the straight jet section), increasing its relaxation time. Furthermore, the possible additional

elongation of the jet provided by the collector simultaneously promotes solvent evaporation by increasing the surface/volume ratio of the fiber, further limiting the relaxation.

Obviously, much more work at the single fiber level is needed to fully understand the effects of the solution properties, of the nature of the polymer (and its propensity to crystallize) and of the electrospinning conditions on the orientation of nanofibers. One of the major limitations of SAED to reach such understanding is that it is restricted to the analysis of the crystalline phase and, therefore, to highly crystalline polymers. This is a significant issue for three main raisons: 1) most electrospun fibers are composed of polymers with lower cristallinity than those that have been studied by SAED; 2) the electrospinning process often hinders crystallization due to the rapid jet solidification that can be compared to a fast quench; and 3) as highlighted in the previous sections, the currently proposed models to explain the unique characteristics of electrospun nanofibers, such as their exceptional mechanical properties as compared to bulk materials, are expected to depend on the orientation of the amorphous phase.

Recent SAED studies attempted to circumvent part of these problems by annealing the nanofibers (allowing their crystallization in different conditions) to extract information on their previous organization. For instance Tosaka et al.[133] have used this strategy to study isotactic PS nanofibers produced by hot solution electrospinning. Chloroform solutions led to ribbon-like fibers with small surface pores that disappeared upon annealing above Tg, indicating a significant mobility of the chains that could have led to complete orientation relaxation. Instead, the annealing led to the formation of highly oriented crystals. The authors proposed a mechanism in which, upon annealing, the highly oriented amorphous chains situated at the surface would partially preserve their original orientation. These chains would act as nuclei that can grow to form highly oriented shish-kebab-like structures. It is noteworthy that these results correlate well with the proposed core-shell morphology of nanofibers presented in Section 2.4.2.

Cheng et al.[134] have used a similar strategy to study syndiotactic PS fibers produced from hot solution electrospinning. IR spectroscopy and SAED at the single fiber level indicated that the as-spun fibers were amorphous. Upon annealing at temperatures lower than

the melting point, the order parameter (<P_2>) of the crystalline phase, reached as high as 0.98, extremely close to its maximum value of 1. This was, again, attributed to the prealignment of amorphous chains that allows them to rapidly undergo crystallization prior to relaxation, as suggested by their IR spectroscopy analysis. Kawahara et al.[135] have observed a similar behavior for bundles of poly(heptamethylene terephthalate) nanofibers upon annealing, although it should be noted that oriented crystals were already present in the as-spun fibers.

While these annealing studies only provide indirect evidence about the structure of the amorphous phase, the alternatives to SAED to get deeper and more direct information at the single fiber level are unfortunately quite limited. Kolbuk et al.[136] have proposed using polarized interference microscopy, but the procedure is limited to a two-phase model (which assumes a single crystalline structure and no "intermediate phases" such as mesophases) and it is based on the approximation that both phases possess the same degree of orientation, which is very unlikely. It additionally requires knowledge of the crystallinity degree, which is generally quantified by averaging over bundles by DSC or WAXD.

Bellan and Craighead[137] were the first to propose using polarized confocal Raman spectromicroscopy, a technique which gives access to molecular-level information similar to IR spectroscopy but with a submicrometer spatial resolution that enables probing single fibers. Accordingly, this technique should provide the orientation of the crystalline and amorphous phases, as well as information on possible polymorphs or mesophases. Their spectra of nylon-6 nanofibers indicated a significant level of orientation but were extremely noisy, leading to some <P_2> values out of the theoretically acceptable range and showing the experimental difficulty of studying individual nanofibers.

In a recent study, we have established an experimental protocol allowing recording high quality polarized Raman spectra in a short acquisition time and, furthermore, demonstrated the accuracy of the quantification procedure on electrospun fibers with diameters down to 500 nm.[138] A typical series of spectra recorded on an individual PET fiber is shown in Figure 2.12A. Careful analysis of the spectra also provided quantitative structural information on the crystallinity degree and the chain conformation of individual fibers, as presented in Figure 2.12B. The $\langle P_2 \rangle$ order parameter varied significantly from fiber to fiber and even along the

length of a single fiber, although they had approximately the same size. The orientation could be directly correlated to an increase in the fraction of trans conformers. Furthermore, some of these fibers showed a remarkably high level of orientation even if their crystallinity degree was quite low, always below 10%. The high trans fraction in oriented fibers was therefore associated to a highly anisotropic mesophase which could not be observed by WAXD when averaging over bundles. These results demonstrate directly and unequivocally the possibility of forming highly ordered nanofibers from non-crystalline polymers.

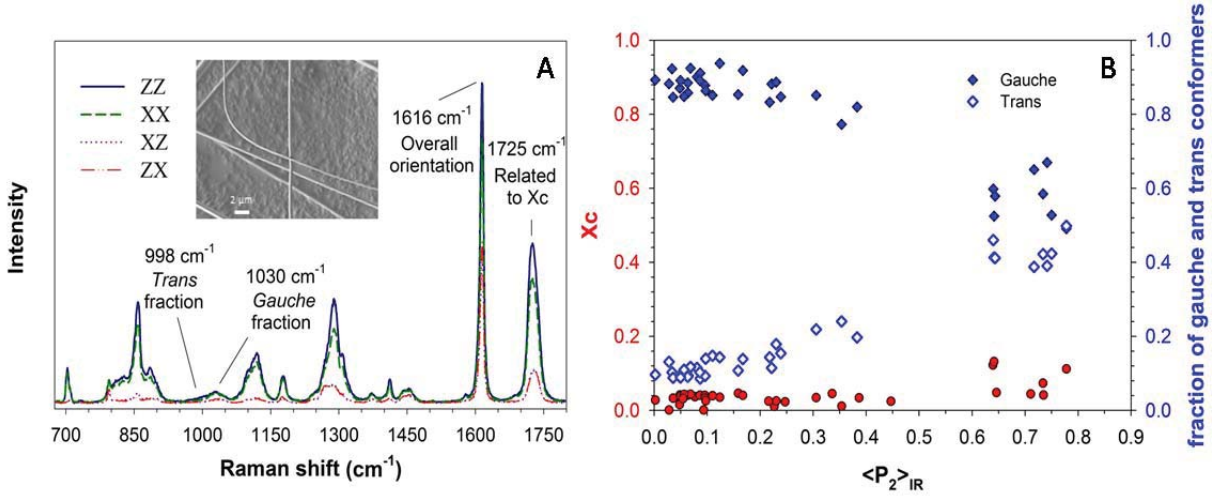

Figure 2.12. Characterization of individual PET fibers by confocal Raman spectroscopy. **A)** Set of 4 polarized Raman spectra required for orientation quantification of a single PET nanofiber. The inset presents an SEM image of a few isolated 500 nm nanofibers on which the Raman spectra were recorded. **B)** Evolution of the crystallinity degree and gauche and trans fractions as a function of the orientation parameter ($\langle P_2 \rangle$) quantified. Adapted from Richard-Lacroix and Pellerin.[138]

Confocal Raman spectromicroscopy is currently, to our knowledge, the only technique that enables quantifying directly the orientation of the amorphous and crystalline phases at the single fiber level. In addition to the currently available suite of SAED, Raman spectroscopy, imaging techniques, and AFM-based methods, other techniques will likely emerge as powerful new tools to study individual electrospun fibers. An IR spectroscopy method based on photothermal detection by an AFM tip (AFM-IR) has recently shown promising developments, including the possibility of recording polarized IR spectra of an individual PVDF fiber.[139] Tip-enhanced Raman spectroscopy may also provide qualitative information about the structure of individual fibers, including at various positions along their cross-section.

Scanning transmission X-ray microscopy and nanofocus X-ray diffraction are also techniques amenable to quantification of the orientation of single fibers.[140] The application of these techniques may lead to several developments in our understanding of the structure of electrospun nanofibers and of the experimental factors that enable controlling their properties.

2.7. Other properties and applications of electrospun fibers related to orientation

The ability of electrospinning to form highly ordered 1D nanomaterials with a tunable morphology has raised an interest for the investigation of several other properties of nanofibers in view of a wide range of applications. The photoconductivity, hole and electron conductivity, nonlinear optical activity, piezoelectricity, etc., have all been shown to be significantly enhanced in nanofibers when compared to thin films. As a consequence, electrospun nanofibers have recently been integrated in a broad variety of devices showing superior performances. This improvement has been, at least in part, attributed to a preferential molecular orientation in electrospun nanofibers. This section presents a brief overview of some of these properties and applications that would benefit from a deeper understanding of the factors that govern orientation in electrospun fibers.

Nanofibers of light-emitting and conductive polymers have recently gained remarkable popularity.[141] However, the backbone rigidity of conjugated polymers is detrimental to achieving the required level of entanglements in solution to allow the production of continuous nanofibers. Two main strategies have enabled the electrospinning of such conjugated polymers (and, more generally, of polyelectrolytes or small molecules that do not entangle in solution): 1) blending with an easily electrospinnable polymer such as PCL; and 2) preparing coaxial fibers composed of the conjugated polymer in the core and surrounded by a flexible polymer that forms a sacrificial shell. The potential application of these nanofibers in photonic and optoelectronic devices, such as organic light-emitting diodes, organic photovoltaics, and field-effect transistors, has been detailed in recent reviews.[141, 142]

The level of anisotropy of the light emission or electron conduction is critical for some of these applications.[143] Highly polarized emission has been reported for well-aligned bundles

of nanofibers of conjugated systems such as 1,1′-diethyl-2,2′-cyanine bromide embedded in a PVA matrix,[144] and poly(2-methoxy-5-(2-ethylhexyloxy)-1,4-phenylenevinylene) (MEH-PPV) or poly(3-hexylthiophene) (P3HT) in composite fibers with PEO,[145] due to the orientation of the emission dipole moment. As for thin films, bundles of randomly aligned fibers show a much smaller polarization ratio, underlying the importance of controlling the macroscopic deposition of fibers when studying bundles. However, Ishii et al.[146] have evidenced that photon re-absorption and scattering influence the luminescence spectra when averaging over a large number of aligned fibers in a bundle, even if each individual fiber has the same spectral characteristics. They concluded that the specific organization of the fluorophores must be deduced from measurements at the single fiber level.

Up to now, only a few polymers, such as poly[(9,9-dioctylfluorenyl-2,7-diyl)-co-(1,4-benzo-1,2'-3-thiadiazole)] (F8BT), PPV and MEH-PPV, have been directly studied at the scale of the single fiber. Their polarization ratios have been demonstrated to be highly sensitive to the preparation conditions.[147-149] Pagliara et al.[147], for instance, have shown that the emission wavelength and anisotropy of F8BT nanofibers were ruled by the nature of the solvent. The emission anisotropy was much higher and red-shifted when using THF as a solvent instead of a mixture of THF and DMSO due to a higher molecular orientation, as proven by IR and Raman spectroscopy, and π-electron delocalization. In a very recent work, the same group has shown that pure fibers of blue-emitting poly[(9,9-dioctylfluorenyl-2,7-diyl)-co-(N,N'-diphenyl)-N,N'-di(pbutyl-oxy-phenyl)-1,4-diaminobenzene)] could be prepared in a good solvent by adding an organic salt. The salt had no detrimental effect on the photoluminescence and waveguiding properties of the fiber while helping to decrease their diameter and to reduce defects.[150]

Pagliara et al.[151] have also proposed integrating MEH-PPV electrospun nanofibers in a microfluidic lab on a chip device in which they acted as a light source. Their highly polarized emission was shown to facilitate the decoupling of the signals originating from the analyte emission and from the excitation source, therefore enhancing significantly the detection sensitivity.[151] The polarization ratio can also be critical for polymer light-emitting diode (PLED) applications, but it is unfortunately not high enough in most nanofibers studied to date.[143] Room-temperature nanoimprinting lithography has recently been proposed as an

interesting approach to enhance the emission polarization efficiency of electrospun fibers by a factor of 2.4 and in a much shorter time (a few minutes compared to several hours) than for thin films due to the specific organization of the chains in nanofibers.[152]

Electrospun nanofibers composed of semi-conducting polymers have also been successfully integrated in organic field-effect transistor (OFET) devices for which the performance was shown to be strongly dependent on the level of molecular orientation. For instance, Tu et al.[149] have evidenced a substantial improvement, by one order of magnitude, of the hole mobility of MEH-PPV nanofibers when compared to films of the same thickness due to the orientation of the chains that would induce a quasi 1D conduction. Similar results were also observed for PPV nanofibers.[148] Devices made of P3HT and poly{[2′,5″-5,5‴di(2-ethylhexyl)-3′;5′,2″;4″2‴]quaterthiophene-*alt*-3,6-dithien-2-yl-2,5-di(2-ethylhexyl)-pyrrolo[3,4-c]pyrrole-1,4-dione-5′,5″-diyl]} (P4TDPP) nanofibers also showed a high efficiency.[153] This was attributed to the high level of orientation as well as to the enhancement of the π-stacking and crystallinity degree, which were all shown to be strongly dependent on the fiber formation conditions and annealing temperature. Most of these studies have been performed on thin mats of more or less aligned fibers deposited on a conducting substrate and the orientation of the chains was evaluated by emission polarization ratio measurements. As for mechanical properties and emission polarization, the macroscopic alignment of the fibers has been shown to affect considerably the fibers' conductivity.[154] Recently, a similar improvement was reported by measuring electron mobility at the single fiber level, showing the potential of these fibers for applications in nanodevices.[155]

In the same mindset, Bedford et al.[156] have recently prepared nanofibers composed of poly(3-hexylthiophene):phenyl-C_{61}-butyric acid methyl ester (P3HT:PCBM) as an electron donor:acceptor pair, using a coaxial electrospinning process with PCL acting as a sacrificial sheath, and integrated these fibers in bulk heterojunction organic photovoltaic devices. The electrospinning process led to a more uniform phase separation of the donor and acceptor moieties and to a higher level of in-plane orientation of the polymer chains when compared to the thin film geometry, confirmed by glancing incidence X-ray diffraction (GIXD) quantification of the orientation parameters. As a consequence, the photon absorption was

improved in the fiber-based device, which led to an increased exciton formation and, thus, to a larger amount of photogenerated carriers.

Another field that is currently explored is the formation electrospun nanofibers with non-linear optical (NLO) or piezoelectric activity for applications in nanosensors or nanogenerator devices. NLO and piezoelectric activity both rely on a noncentrosymmetric distribution of the electrons at the scale of the fiber. Isakov et al.[157] have produced fibers containing 2-methyl-4-nitroaniline (MNA), a small molecule exhibiting a very large second harmonic generation, embedded in a PLLA matrix. They showed that the net transition dipole moment of MNA molecules was preferentially oriented parallel to the fiber axis. Uniaxially aligned MNA/PLLA nanofiber mats showed a strong polarization dependence of the second harmonic generation signal.

In line with this, Farrar et al.[158] have produced nanofibers composed of poly(γ-benzyl α,L-glutamate) (PBLG), an α-helical polypeptide stabilized by aligned intramolecular hydrogen bonds that lead to a large net dipole along the helix axis, as schematized in Figure 2.13A. Figure 2.13B compares the 2D X-ray diffraction pattern of electrospun nanofibers with the one recorded for conventional fibers drawn from a highly concentrated solution. Both patterns confirmed the formation of highly oriented α-helices along the fiber axis. The permanent polarity of both materials was analyzed by second harmonic generation microscopy. As shown in Figure 2.13C, a strong signal is observed for the electrospun nanofibers while only a weak signal, located at the surface, is observed for the drawn fibers. It was concluded that the large dipole of the α-helices coupled with the electric field during electrospinning and that their orientation relaxation was partially hindered due to the fast solvent evaporation, leading to highly oriented materials with a permanent polarity. In contrast, conventional drawing produced fibers in which the helices are organized in an antiparallel way. The high thermal stability of the piezoelectricity allowed producing transparent films by fusing these electrospun fibers without inducing relaxation.[159] A preferential molecular orientation of the dipoles, leading to a high piezoelectric response, was also shown in poly(vinylidene fluoride-trifluoroethylene) nanofibers.[160]

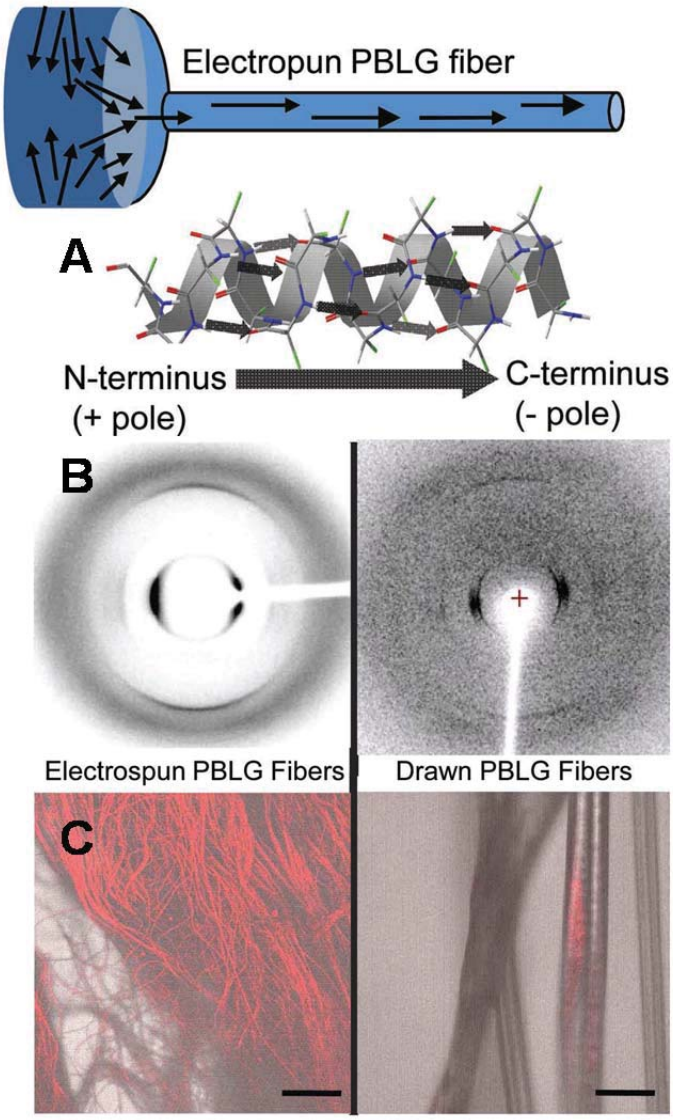

Figure 2.13. Non-linear optical activity of poly(γ-benzyl α,L-glutamate) fibers. **A)** α-helical structure of PBLG. The small arrows in the helix are individual hydrogen bonds while the long arrow under the helix represents its macroscopic dipole. The arrows in the needle tip area represent the orientation of the helices dipoles during the electrospinning process. **B)** X-ray diffraction pattern of electrospun nanofibers and drawn PBLG fibers. **C)** Second harmonic generation microscopy images of electrospun and drawn PBLG nanofibers. The scale bar is 100 μm. Reproduced from Farrar et al.[158]

2.8. Conclusion and outlook

In this Perspective, we have reviewed and highlighted the current challenges related to electrospun nanofibers' internal structure, with a particular emphasis on their molecular orientation since it is believed to be closely related to most of their properties. Over the last twenty years, studies performed on mats have provided useful information on several key aspects of nanofibers microstructure. The studies of the electrospinning jet and the development of collectors enabling a better control of the fibers deposition have revealed the possibility of preparing highly ordered materials and to tune the properties of the mats. They have also underlined the possibility of readily forming different crystal polymorphs that can often hardly be obtained by conventional techniques, as well as to control their formation by tuning electrospinning conditions. The mechanical properties of nanofibers mats, especially their modulus, have been shown to be improved when compared to bulk materials for several polymer systems. However, we have reached a point where studies on bundles using conventional characterization techniques, while still useful, are not sufficient for solving the remaining mysteries concerning the microstructural organization and the properties of electrospun fibers. Indeed, studies on bundles are often inappropriate due to the averaging over thousands of nanofibers whose individual characteristics are inextricably convoluted with the macroscopic properties of the mats.

The recent development of methods for characterizing mechanical and thermal properties at the single fiber level has lifted the veil on behaviors that had never been suspected when working on bundles, such as the exponential modulus dependence with diameter, leading to a renewed understanding and interest for these materials. Different models involving a highly oriented amorphous phase have been proposed to explain such distinctive behavior. These models nevertheless still lack a complete experimental validation and do not yet provide a description that encompasses all the observed behaviors. Among the major aspects that remain unclear are the roles of the crystalline phase and or molecular orientation in determining the mechanical and thermal properties of nanofibers. In fact, most of the parameters affecting the fibers properties must now be revisited at the single fiber level to gain a deeper understanding.

The use of SAED to probe individual fibers has, in recent years, highlighted the heterogeneity of the crystalline characteristics in bundles and even along a single fiber, as well as the extraordinarily high level of orientation that can be reached for some systems. It has also provided clues about the amorphous phase organization but the limitation of this technique to the study of the crystalline phase greatly restricts the information that can be obtained for several systems. Confocal Raman spectroscopy has recently revealed its efficiency to probe simultaneously the orientation of the amorphous, crystalline and intermediate (meso) phases in single electrospun nanofibers. Other techniques, such as AFM-IR and nanofocus X-ray diffraction, may arise as powerful new tools in the coming years.

In parallel, an increasingly large number of applications in different fields have emerged in recent years for electrospun nanofibers. In many cases, a high level of orientation has been assumed to be mainly responsible for the enhanced performance of the devices in which they are integrated when compared to thin films. However, the precise control and optimization of these performances require a better understanding of the factors that determine the nanofibers microstructure.

The studies performed to date leave us with a series of open questions, including: How can the orientation be improved and controlled in electrospun nanofibers? What is the real influence of the collector on their microstructure? How are crystal polymorphs distributed and what parameters really affect their formation? How does the orientation affect the nanofibers properties and their performance in various devices? Does orientation alone explain, for instance, the enhanced conductivity observed in electrospun fibers when compared to thin films or does their specific internal structure also play a role, as suspected for mechanical properties? Does the modulus really always show an exponential increase with decreasing fiber diameter or can this dependence be tuned by varying the electrospinning conditions? How are Tg and Tm affected by orientation and microstructure in nanofibers? Can the microstructural organization in electrospun nanofibers be explained by a single comprehensive model?

By answering these interrogations, the most important question summarizing all aspects discussed in this Perspective will reveal itself: how far can we push our control of the structure

of electrospun nanofibers to reach the desired properties for specific applications? We believe that achieving this ultimate goal relies on a much better fundamental understanding of these materials. The recent development of characterization tools that enable structural studies at the single fiber level will open the door, in the near future, to exciting new developments in this field and will contribute to the widespread exploitation of electrospun nanofibers up to their full potential.

2.9. Acknowledgements

The authors acknowledge the financial support of the Natural Sciences and Engineering Research Council of Canada (NSERC).

2.10. References

1. Pillay, V.; Dott, C.; Choonara, Y.E.; Tyagi, C.; Tomar, L.; Kumar, P.; du Toit, L.C.; Ndesendo, V.M.K. *J. Nanomater.* **2013,** *2013*, 1-22; Nisbet, D.R.; Forsythe, J.S.; Shen, W.; Finkelstein, D.I.; Horne, M.K. *J. Biomater. Appl.* **2009,** *24*, 7-29; Cui, W.; Zhou, Y.; Chang, J. *Sci. Technol. Adv. Mat.* **2010,** *11*, 014108; Agarwal, S.; Wendorff, J.H.; Greiner, A. *Adv. Mater.* **2009,** *21*, 3343-3351.
2. Laudenslager, M.J.; Scheffler, R.H.; Sigmund, W.M. *Pure Appl. Chem.* **2010,** *82*, 2137-2156; Miao, J.; Miyauchi, M.; Simmons, T.J.; Dordick, J.S.; Linhardt, R.J. *J. Nanosci. Nanotechno.* **2010,** *10*, 5507-5519; Dong, Z.; Kennedy, S.J.; Wu, Y. *J. Power Sources* **2011,** *196*, 4886-4904.
3. Chigome, S.; Torto, N. *Anal. Chim. Acta.* **2011,** *706*, 25-36; Ding, B.; Wang, M.; Yu, J.; Sun, G. *Sensors (Basel)* **2009,** *9*, 1609-1624; Ding, B.; Wang, M.; Wang, X.; Yu, J.; Sun, G. *Mater. Today* **2010,** *13*, 16-27; Botes, M.; Cloete, T.E. *Crit. Rev. Microbiol.* **2010,** *36*, 68-81.
4. He, J.H.; Liu, Y.; Xu, L. *Mater. Sci. Technol.* **2010,** *26*, 1275-1287; Luo, C.J.; Stoyanov, S.D.; Stride, E.; Pelan, E.; Edirisinghe, M. *Chem. Soc. Rev.* **2012,** *41*, 4708-4735.
5. Greiner, A.; Wendorff, J.H. *Angew. Chem. Int. Ed.* **2007,** *46*, 5670-5703.
6. Bhardwaj, N.; Kundu, S.C. *Biotechnol. Adv.* **2010,** *28*, 325-347.

7. Reneker, D.H.; Yarin, A.L.; Fong, H.; Koombhongse, S. *J. Appl. Phys.* **2000,** *87*, 4531-4547.
8. Reneker, D.H.; Kataphinan, W.; Theron, A.; Zussman, E.; Yarin, A.L. *Polymer* **2002,** *43*, 6785-6794.
9. Yarin, A.L.; Koombhongse, S.; Reneker, D.H. *J. Appl. Phys.* **2001,** *89*, 3018.
10. Kongkhlang, T.; Kotaki, M.; Kousaka, Y.; Umemura, T.; Nakaya, D.; Chirachanchai, S. *Macromolecules* **2008,** *41*, 4746-4752.
11. Reneker, D.H.; Yarin, A.L.; Zussman, E.; Xu, H., Electrospinning of Nanofibers from Polymer Solutions and Melts. In *Advances in Applied Mechanics*, Hassan, A.; Erik van der, G., Eds. Elsevier: 2007; Vol. Volume 41, pp 43-346.
12. Thompson, C.J.; Chase, G.G.; Yarin, A.L.; Reneker, D.H. *Polymer* **2007,** *48*, 6913-6922; Reneker, D.H.; Yarin, A.L. *Polymer* **2008,** *49*, 2387-2425.
13. Hohman, M.M.; Shin, M.; Rutledge, G.; Brenner, M.P. *Phys. Fluids* **2001,** *13*, 2201-2220; Hohman, M.M.; Shin, M.; Rutledge, G.; Brenner, M.P. *Phys. Fluids* **2001,** *13*, 2221-2236.
14. Carroll, C.P.; Joo, Y.L. *Phys. Fluids* **2006,** *18*, 053102-053114; Carroll, C.P.; Joo, Y.L. *Phys. Fluids* **2009,** *21*, 103101-103110; Zhmayev, E.; Zhou, H.; Joo, Y.L. *J. Non-Newton. Fluid* **2008,** *153*, 95-108.
15. Feng, J.J. *Phys. Fluids* **2002,** *14*, 3912-3926.
16. Gupta, P.; Elkins, C.; Long, T.E.; Wilkes, G.L. *Polymer* **2005,** *46*, 4799-4810; Dayal, P.; Liu, J.; Kumar, S.; Kyu, T. *Macromolecules* **2007,** *40*, 7689-7694; Casper, C.L.; Stephens, J.S.; Tassi, N.G.; Chase, D.B.; Rabolt, J.F. *Macromolecules* **2004,** *37*, 573-578.
17. Xu, H. Formation and characterization of polymer jets in electrospinning. Ph.D., The University of Akron, United States -- Ohio, 2003.
18. Gururajan, G.; Giller, C.B.; Snively, C.M.; Chase, D.B.; Rabolt, J.F. *Appl. Spectrosc.* **2011,** *65*, 858-865.
19. Greenfeld, I.; Arinstein, A.; Fezzaa, K.; Rafailovich, M.H.; Zussman, E. *Phys. Rev. E* **2011,** *84*, 041806.
20. Greenfeld, I.; Fezzaa, K.; Rafailovich, M.H.; Zussman, E. *Macromolecules* **2012,** *45*, 3616-3626.

21. Fennessey, S.F.; Farris, R.J. *Polymer* **2004,** *45*, 4217-4225.
22. Greenfeld, I.; Zussman, E. *J. Polym. Sci. B: Polym. Phys.* **2013,** *51*, 1377-1391.
23. Deitzel, J. *Polymer* **2001,** *42*, 8163-8170.
24. Dersch, R.; Liu, T.; Schaper, A.K.; Greiner, A.; Wendorff, J.H. *J. Polym. Sci., Part A: Polym. Chem.* **2003,** *41*, 545-553.
25. Lee, K.H.; Kim, H.Y.; Khil, M.S.; Ra, Y.M.; Lee, D.R. *Polymer* **2003,** *44*, 1287-1294.
26. Moon, S.; Choi, J.; Farris, R.J. *J. Appl. Polym. Sci.* **2008,** *109*, 691-694.
27. Lee, K.-H.; Kim, K.-W.; Pesapane, A.; Kim, H.-Y.; Rabolt, J.F. *Macromolecules* **2008,** *41*, 1494-1498.
28. Edwards, M.D.; Mitchell, G.R.; Mohan, S.D.; Olley, R.H. *Eur. Polym. J.* **2010,** *46*, 1175-1183.
29. Mohan, S.D.; Mitchell, G.R.; Davis, F.J. *Soft Matter* **2011,** *7*, 4397-4404.
30. Rungswang, W.; Kotaki, M.; Shimojima, T.; Kimura, G.; Sakurai, S.; Chirachanchai, S. *Macromolecules* **2011,** *44*, 9276-9285; Rungswang, W.; Kotaki, M.; Shimojima, T.; Kimura, G.; Sakurai, S.; Chirachanchai, S. *Polymer* **2011,** *52*, 844-853.
31. Li, D.; Wang, Y.; Xia, Y. *Nano Lett.* **2003,** *3*, 1167-1171.
32. Kakade, M.V.; Givens, S.; Gardner, K.; Lee, K.H.; Chase, D.B.; Rabolt, J.F. *J. Am. Chem. Soc.* **2007,** *129*, 2777-2782.
33. Liu, Y.; Pellerin, C. *Macromolecules* **2006,** *39*, 8886-8888.
34. Ge, J.J.; Hou, H.; Li, Q.; Graham, M.J.; Greiner, A.; Reneker, D.H.; Harris, F.W.; Cheng, S.Z. *J. Am. Chem. Soc.* **2004,** *126*, 15754-15761.
35. Liu, Y.; Antaya, H.; Pellerin, C. *J. Polym. Sci. B: Polym. Phys.* **2008,** *46*, 1903-1913; Liu, Y.; Antaya, H.; Pellerin, C. *J. Phys. Chem. B* **2010,** *114*, 2373-2378.
36. Richard-Lacroix, M.; Pellerin, C. *Sci. China Chem.* **2013,** *56*, 24-32.
37. Kongkhlang, T.; Tashiro, K.; Kotaki, M.; Chirachanchai, S. *J. Am. Chem. Soc.* **2008,** *130*, 15460-15466.
38. Liao, C.-C.; Wang, C.-C.; Chen, C.-Y.; Lai, W.-J. *Polymer* **2011,** *52*, 2263-2275.
39. Kim, G.H.; Yoon, H. *Appl. Phys. Lett.* **2008,** *93*, 023127; Katta, P.; Alessandro, M.; Ramsier, R.D.; Chase, G.G. *Nano Lett.* **2004,** *4*, 2215-2218; Lee, H.; Yoon, H.; Kim, G. *Appl. Phys. A* **2009,** *97*, 559-565; Teo, W.E.; Ramakrishna, S. *Nanotechnology* **2006,** *17*, R89-R106; Ner, Y.; Asemota, C.; Olson, J.R.; Sotzing, G.A. *ACS Appl. Mater. Inter.*

2009, *1*, 2093-2097; Hellmann, C.; Belardi, J.; Dersch, R.; Greiner, A.; Wendorff, J.H.; Bahnmueller, S. *Polymer* **2009,** *50*, 1197-1205; Edmondson, D.; Cooper, A.; Jana, S.; Wood, D.; Zhang, M. *J. Mater. Chem.* **2012,** *22*, 18646; Sun, D.; Chang, C.; Li, S.; Lin, L. *Nano Lett.* **2006,** *6*, 839-842; Teo, W.-E.; Inai, R.; Ramakrishna, S. *Sci. Technol. Adv. Mat.* **2011,** *12*, 013002.

40. Liao, C.-C.; Wang, C.-C.; Shih, K.-C.; Chen, C.-Y. *Eur. Polym. J.* **2011,** *47*, 911-924.
41. Fong, H. *Polymer* **2002,** *43*, 775-780; Stephens, J.S.; Chase, D.B.; Rabolt, J.F. *Macromolecules* **2004,** *37*, 877-881; Liu, Y.; Cui, L.; Guan, F.; Gao, Y.; Hedin, N.E.; Zhu, L.; Fong, H. *Macromolecules* **2007,** *40*, 6283-6290.
42. Samon, J.M.; Schultz, J.M.; Wu, J.; Hsiao, B.; Yeh, F.; Kolb, R. *J. Polym. Sci. B: Polym. Phys.* **1999,** *37*, 1277-1287.
43. Kobayashi, M.; Sakashita, M. *J. Chem. Phys.* **1992,** *96*, 748-760.
44. Yee, W.A.; Kotaki, M.; Liu, Y.; Lu, X. *Polymer* **2007,** *48*, 512-521.
45. Yee, W.A.; Nguyen, A.C.; Lee, P.S.; Kotaki, M.; Liu, Y.; Tan, B.T.; Mhaisalkar, S.; Lu, X. *Polymer* **2008,** *49*, 4196-4203.
46. Zheng, J.; He, A.; Li, J.; Han, C.C. *Macromol. Rapid Comm.* **2007,** *28*, 2159-2162.
47. Okada, A.; Kawasumi, M.; Tajima, I.; Kurauchi, T.; Kamigaito, O. *J. Appl. Polym. Sci.* **1989,** *37*, 1363-1371.
48. Giller, C.B.; Chase, D.B.; Rabolt, J.F.; Snively, C.M. *Polymer* **2010,** *51*, 4225-4230.
49. Cho, D.; Zhmayev, E.; Joo, Y.L. *Polymer* **2011,** *52*, 4600-4609.
50. Kimura, N.; Kim, H.-K.; Kim, B.-S.; Lee, K.-H.; Kim, I.-S. *Macromol. Mater. Eng.* **2010,** *295*, 1090-1096.
51. Takahashi, Y.; Sumita, I.; Tadokoro, H. *J. Polym. Sci.: Polym. Phys. Ed.* **1973,** *11*, 2113-2122.
52. Lu, J.-W.; Zhang, Z.-P.; Ren, X.-Z.; Chen, Y.-Z.; Yu, J.; Guo, Z.-X. *Macromolecules* **2008,** *41*, 3762-3764; Huang, C.; Chen, S.; Reneker, D.H.; Lai, C.; Hou, H. *Adv. Mater.* **2006,** *18*, 668-671.
53. Pedicini, A.; Farris, R.J. *Polymer* **2003,** *44*, 6857-6862.
54. Cheng, M.-L.; Chen, P.-Y.; Lan, C.-H.; Sun, Y.-M. *Polymer* **2011,** *52*, 1391-1401.
55. Carrizales, C.; Pelfrey, S.; Rincon, R.; Eubanks, T.M.; Kuang, A.; McClure, M.J.; Bowlin, G.L.; Macossay, J. *Polym. Adv. Technol.* **2008,** *19*, 124-130; Subbiah, T.; Bhat,

G.S.; Tock, R.W.; Parameswaran, S.; Ramkumar, S.S. *J. Appl. Polym. Sci.* **2005,** *96*, 557-569.

56. Kim, K.W.; Lee, K.H.; Khil, M.S.; Ho, Y.S.; Kim, H.Y. *Fibers Polym.* **2004,** *5*, 122-127; Lee, K.H.; Kim, H.Y.; La, Y.M.; Lee, D.R.; Sung, N.H. *J. Polym. Sci. B: Polym. Phys.* **2002,** *40*, 2259-2268.
57. Mathew, G.; Hong, J.P.; Rhee, J.M.; Leo, D.J.; Nah, C. *J. Appl. Polym. Sci.* **2006,** *101*, 2017-2021.
58. Yano, T.; Higaki, Y.; Tao, D.; Murakami, D.; Kobayashi, M.; Ohta, N.; Koike, J.-i.; Horigome, M.; Masunaga, H.; Ogawa, H.; Ikemoto, Y.; Moriwaki, T.; Takahara, A. *Polymer* **2012,** *53*, 4702-4708.
59. Dror, Y.; Salalha, W.; Khalfin, R.L.; Cohen, Y.; Yarin, A.L.; Zussman, E. *Langmuir* **2003,** *19*, 7012-7020.
60. Salalha, W.; Dror, Y.; Khalfin, R.L.; Cohen, Y.; Yarin, A.L.; Zussman, E. *Langmuir* **2004,** *20*, 9852-9855.
61. McCullen, S.D.; Stevens, D.R.; Roberts, W.A.; Ojha, S.S.; Clarke, L.I.; Gorga, R.E. *Macromolecules* **2007,** *40*, 997-1003.
62. Su, Z.; Li, J.; Li, Q.; Ni, T.; Wei, G. *Carbon* **2012,** *50*, 5605-5617.
63. Ayutsede, J.; Gandhi, M.; Sukigara, S.; Ye, H.; Hsu, C.M.; Gogotsi, Y.; Ko, F. *Biomacromolecules* **2006,** *7*, 208-214.
64. Sung, J.H.; Kim, H.S.; Jin, H.-J.; Choi, H.J.; Chin, I.-J. *Macromolecules* **2004,** *37*, 9899-9902.
65. Sreekumar, T.V.; Liu, T.; Min, B.G.; Guo, H.; Kumar, S.; Hauge, R.H.; Smalley, R.E. *Adv. Mater.* **2004,** *16*, 58-61; Hou, H.; Ge, J.J.; Zeng, J.; Li, Q.; Reneker, D.H.; Greiner, A.; Cheng, S.Z.D. *Chem. Mat.* **2005,** *17*, 967-973.
66. Sen, R.; Zhao, B.; Perea, D.; Itkis, M.E.; Hu, H.; Love, J.; Bekyarova, E.; Haddon, R.C. *Nano Lett.* **2004,** *4*, 459-464; Tijing, L.D.; Park, C.-H.; Choi, W.L.; Ruelo, M.T.G.; Amarjargal, A.; Pant, H.R.; Im, I.-T.; Kim, C.S. *Compos. Part B-Eng.* **2013,** *44*, 613-619.
67. Chen, D.; Liu, T.; Zhou, X.; Tjiu, W.C.; Hou, H. *J. Phys. Chem. B* **2009,** *113*, 9741-9748.
68. Mazinani, S.; Ajji, A.; Dubois, C. *J. Polym. Sci. B: Polym. Phys.* **2010,** *48*, 2052-2064.

69. Peresin, M.S.; Habibi, Y.; Zoppe, J.O.; Pawlak, J.J.; Rojas, O.J. *Biomacromolecules* **2010,** *11*, 674-681; Zoppe, J.O.; Peresin, M.S.; Habibi, Y.; Venditti, R.A.; Rojas, O.J. *ACS Appl. Mater. Inter.* **2009,** *1*, 1996-2004; Zhou, C.; Chu, R.; Wu, R.; Wu, Q. *Biomacromolecules* **2011,** *12*, 2617-2625.
70. Cozza, E.S.; Ma, Q.; Monticelli, O.; Cebe, P. *Eur. Polym. J.* **2013,** *49*, 33-40.
71. Wang, Y.; Li, M.; Rong, J.; Nie, G.; Qiao, J.; Wang, H.; Wu, D.; Su, Z.; Niu, Z.; Huang, Y. *Colloid. Polym. Sci.* **2013,** *291*, 1541-1546.
72. Roskov, K.E.; Kozek, K.A.; Wu, W.C.; Chhetri, R.K.; Oldenburg, A.L.; Spontak, R.J.; Tracy, J.B. *Langmuir* **2011,** *27*, 13965-13969; Zhang, C.L.; Lv, K.P.; Cong, H.P.; Yu, S.H. *Small* **2012,** *8*, 647-653.
73. Jaeger, R.; Schönherr, H.; Vancso, G.J. *Macromolecules* **1996,** *29*, 7634-7636.
74. Tombler, T.W.; Zhou, C.; Alexseyev, L.; Kong, J.; Dai, H.; Liu, L.; Jayanthi, C.S.; Tang, M.; Wu, S.Y. *Nature* **2000,** *405*, 769-772.
75. Yu, M.F.; Lourie, O.; Dyer, M.J.; Moloni, K.; Kelly, T.F.; Ruoff, R.S. *Science* **2000,** *287*, 637-640.
76. Huang, Z.-M.; Zhang, Y.Z.; Kotaki, M.; Ramakrishna, S. *Comp. Sci. technol.* **2003,** *63*, 2223-2253.
77. Tan, E.P.S.; Lim, C.T. *Appl. Phys. Lett.* **2004,** *84*, 1603-1605.
78. Tan, E.P.S.; Lim, C.T. *Rev. Sci. Instrum.* **2004,** *75*, 2581-2585; Tan, E.P.S.; Ng, S.Y.; Lim, C.T. *Biomaterials* **2005,** *26*, 1453-1456.
79. Tan, E.P.S.; Lim, C.T. *Comp. Sci. technol.* **2006,** *66*, 1102-1111.
80. Tan, E.P.S.; Goh, C.N.; Sow, C.H.; Lim, C.T. *Appl. Phys. Lett.* **2005,** *86*, 073115.
81. Hang, F.; Lu, D.; Bailey, R.J.; Jimenez-Palomar, I.; Stachewicz, U.; Cortes-Ballesteros, B.; Davies, M.; Zech, M.; Bodefeld, C.; Barber, A.H. *Nanotechnology* **2011,** *22*, 365708.
82. Hwang, K.Y.; Kim, S.-D.; Kim, Y.-W.; Yu, W.-R. *Polym. Test.* **2010,** *29*, 375-380.
83. Bazbouz, M.B.; Stylios, G.K. *J. Polym. Sci. B: Polym. Phys.* **2010,** *48*, 1719-1731.
84. Ji, Y.; Li, B.; Ge, S.; Sokolov, J.C.; Rafailovich, M.H. *Langmuir* **2006,** *22*, 1321-1328.
85. Ge, S.; Pu, Y.; Zhang, W.; Rafailovich, M.; Sokolov, J.; Buenviaje, C.; Buckmaster, R.; Overney, R.M. *Phys. Rev. Lett.* **2000,** *85*, 2340-2343.
86. Ko, F.; Gogotsi, Y.; Ali, A.; Naguib, N.; Ye, H.; Yang, G.L.; Li, C.; Willis, P. *Adv. Mater.* **2003,** *15*, 1161-1165.

87. Liu, L.Q.; Tasis, D.; Prato, M.; Wagner, H.D. *Adv. Mater.* **2007,** *19*, 1228-1233.
88. Lee, J.; Deng, Y. *Polym. Bull.* **2012,** *70*, 1205-1219.
89. Wong, S.-C.; Baji, A.; Leng, S. *Polymer* **2008,** *49*, 4713-4722.
90. Ji, Y.; Li, C.; Wang, G.; Koo, J.; Ge, S.; Li, B.; Jiang, J.; Herzberg, B.; Klein, T.; Chen, S.; Sokolov, J.C.; Rafailovich, M.H. *Europhys. Lett.* **2008,** *84*, 56002.
91. Zussman, E.; Burman, M.; Yarin, A.L.; Khalfin, R.; Cohen, Y. *J. Polym. Sci. B: Polym. Phys.* **2006,** *44*, 1482-1489.
92. Zhang, X.; Nakagawa, R.; Chan, K.H.K.; Kotaki, M. *Macromolecules* **2012,** *45*, 5494-5500.
93. Chan, K.H.; Wong, S.Y.; Li, X.; Zhang, Y.Z.; Lim, P.C.; Lim, C.T.; Kotaki, M.; He, C.B. *J. Phys. Chem. B* **2009,** *113*, 13179-13185.
94. Thomas, V.; Jose, M.V.; Chowdhury, S.; Sullivan, J.F.; Dean, D.R.; Vohra, Y.K. *J. Biomater. Sci. Polym. Ed.* **2006,** *17*, 969-984.
95. Silberstein, M.N.; Pai, C.-L.; Rutledge, G.C.; Boyce, M.C. *J. Mech. Phys. Solids* **2012,** *60*, 295-318; Pai, C.-L.; Boyce, M.C.; Rutledge, G.C. *Polymer* **2011,** *52*, 6126-6133.
96. Shin, M.K.; Kim, S.I.; Kim, S.J.; Kim, S.-K.; Lee, H.; Spinks, G.M. *Appl. Phys. Lett.* **2006,** *89*, 231929-231923.
97. Arinstein, A.; Burman, M.; Gendelman, O.; Zussman, E. *Nat. Nanotechnol.* **2007,** *2*, 59-62.
98. Pai, C.-L.; Boyce, M.C.; Rutledge, G.C. *Polymer* **2011,** *52*, 2295-2301.
99. Lim, C.T.; Tan, E.P.S.; Ng, S.Y. *Appl. Phys. Lett.* **2008,** *92*, 141908.
100. Liu, Y.; Chen, S.; Zussman, E.; Korach, C.S.; Zhao, W.; Rafailovich, M. *Macromolecules* **2011,** *44*, 4439-4444.
101. Naraghi, M.; Arshad, S.N.; Chasiotis, I. *Polymer* **2011,** *52*, 1612-1618.
102. Chew, S.Y.; Hufnagel, T.C.; Lim, C.T.; Leong, K.W. *Nanotechnology* **2006,** *17*, 3880-3891.
103. Koombhongse, S.; Liu, W.; Reneker, D.H. *J. Polym. Sci. B: Polym. Phys.* **2001,** *39*, 2598-2606; Jarusuwannapoom, T.; Hongrojjanawiwat, W.; Jitjaicham, S.; Wannatong, L.; Nithitanakul, M.; Pattamaprom, C.; Koombhongse, P.; Rangkupan, R.; Supaphol, P. *Eur. Polym. J.* **2005,** *41*, 409-421; Megelski, S.; Stephens, J.S.; Chase, D.B.; Rabolt, J.F. *Macromolecules* **2002,** *35*, 8456-8466.

104. Guenthner, A.J.; Khombhongse, S.; Liu, W.; Dayal, P.; Reneker, D.H.; Kyu, T. *Macromol. Theory Simul.* **2006,** *15*, 87-93.
105. Pai, C.-L.; Boyce, M.C.; Rutledge, G.C. *Macromolecules* **2009,** *42*, 2102-2114.
106. Wang, L.; Pai, C.-L.; Boyce, M.C.; Rutledge, G.C. *Appl. Phys. Lett.* **2009,** *94*, 151916-151916-151913.
107. Arinstein, A.; Zussman, E. *Phys. Rev. E* **2007,** *76*, 056303.
108. Stachewicz, U.; Bailey, R.J.; Wang, W.; Barber, A.H. *Polymer* **2012,** *53*, 5132-5137.
109. Arinstein, A. *J. Polym. Sci. B: Polym. Phys.* **2013,** *51*, 756-763.
110. Malkin, A.Y.; Semakov, A.V.; Kulichikhin, V.G. *Rheol. Acta* **2011,** *50*, 485-489.
111. Saito, S.; Matsuzaka, K.; Hashimoto, T. *Macromolecules* **1999,** *32*, 4879-4888.
112. Papkov, D.; Zou, Y.; Andalib, M.N.; Goponenko, A.; Cheng, S.Z.; Dzenis, Y.A. *ACS Nano* **2013,** *7*, 3324-3331.
113. Wang, W.; Bushby, A.J.; Barber, A.H. *Appl. Phys. Lett.* **2008,** *93*, 1-3; Wang, W.; Peijs, T.; Barber, A.H. *Nanotechnology* **2010,** *21*, 035705.
114. Wang, W.; Barber, A.H. *Nanotechnology* **2010,** *21*, 225701.
115. Jiang, Q.; Yang, C.C.; Li, J.C. *Macromol. Theory Simul.* **2003,** *12*, 57-60.
116. Lai, C.; Zhong, G.; Yue, Z.; Chen, G.; Zhang, L.; Vakili, A.; Wang, Y.; Zhu, L.; Liu, J.; Fong, H. *Polymer* **2011,** *52*, 519-528; Liu, S.; Liang, Y.; Quan, Y.; Dai, K.; Zheng, G.; Liu, C.; Chen, J.; Shen, C. *Polymer* **2013,** *54*, 3117-3123.
117. Liu, Y.; Li, C.; Chen, S.; Wachtel, E.; Koga, T.; Sokolov, J.C.; Rafailovich, M.H. *J. Polym. Sci. B: Polym. Phys.* **2009,** *47*, 2501-2508.
118. Arinstein, A.; Liu, Y.; Rafailovich, M.; Zussman, E. *Europhys. Lett.* **2011,** *93*, 46001.
119. Arinstein, A.; Zussman, E. *J. Polym. Sci. B: Polym. Phys.* **2011,** *49*, 691-707.
120. Tsuji, H.; Nakano, M.; Hashimoto, M.; Takashima, K.; Katsura, S.; Mizuno, A. *Biomacromolecules* **2006,** *7*, 3316-3320.
121. Ma, Q.; Pyda, M.; Mao, B.; Cebe, P. *Polymer* **2013,** *54*, 2544-2554.
122. Inai, R.; Kotaki, M.; Ramakrishna, S. *Nanotechnology* **2005,** *16*, 208-213.
123. Tsou, S.-Y.; Lin, H.-S.; Wang, C. *Polymer* **2011,** *52*, 3127-3136.
124. Wang, C.; Tsou, S.-Y.; Lin, H.-S. *Colloid. Polym. Sci.* **2012,** *290*, 1799-1809.
125. Wang, W.; Barber, A.H. *J. Polym. Sci. B: Polym. Phys.* **2012,** *50*, 546-551.
126. Forrest, J.A.; Mattsson, J. *Phys. Rev. E* **2000,** *61*, R53-56.

127. Brown, H.R.; Russell, T.P. *Macromolecules* **1996,** *29*, 798-800.
128. Baji, A.; Mai, Y.-W.; Wong, S.-C. *Mater. Sci. Eng. A-Struct.* **2011,** *528*, 6565-6572.
129. Huang, C.B.; Chen, S.L.; Lai, C.L.; Reneker, D.H.; Qiu, H.; Ye, Y.; Hou, H.Q. *Nanotechnology* **2006,** *17*, 1558-1563.
130. Yoshioka, T.; Dersch, R.; Tsuji, M.; Schaper, A.K. *Polymer* **2010,** *51*, 2383-2389.
131. Yoshioka, T.; Dersch, R.; Greiner, A.; Tsuji, M.; Schaper, A.K. *Macromol. Mater. Eng.* **2010,** *295*, 1082-1089.
132. Ma, X.; Liu, J.; Ni, C.; Martin, D.C.; Chase, D.B.; Rabolt, J.F. *ACS Macro Letters* **2012,** *1*, 428-431.
133. Tosaka, M.; Yamaguchi, K.; Tsuji, M. *Polymer* **2010,** *51*, 547-553.
134. Cheng, Y.-W.; Lu, H.-A.; Wang, Y.-C.; Thierry, A.; Lotz, B.; Wang, C. *Macromolecules* **2010,** *43*, 2371-2376.
135. Kawahara, Y.; Naruko, S.; Nakayama, A.; Wu, M.-C.; Woo, E.M.; Tsuji, M. *J. Mater. Sci.* **2009,** *44*, 2137-2142.
136. Kołbuk, D.; Sajkiewicz, P.; Kowalewski, T.A. *Eur. Polym. J.* **2012,** *48*, 275-283.
137. Bellan, L.M.; Craighead, H.G. *Polymer* **2008,** *49*, 3125-3129.
138. Richard-Lacroix, M.; Pellerin, C. *Macromolecules* **2012,** *45*, 1946-1953.
139. Dazzi, A.; Prater, C.B.; Hu, Q.; Chase, D.B.; Rabolt, J.F.; Marcott, C. *Appl. Spectrosc.* **2012,** *66*, 1365-1384.
140. Rousseau, M.E.; Hernandez Cruz, D.; West, M.M.; Hitchcock, A.P.; Pézolet, M. *J. Am. Chem. Soc.* **2007,** *129*, 3897-3905.
141. Cho, H.; Min, S.-Y.; Lee, T.-W. *Macromol. Mater. Eng.* **2013,** *298*, 475-486.
142. Camposeo, A.; Persano, L.; Pisignano, D. *Macromol. Mater. Eng.* **2013,** *298*, 487-503.
143. Grell, M.; Bradley, D.D.C. *Adv. Mater.* **1999,** *11*, 895-905.
144. Demir, M.M.; Ozen, B.; Ozcelik, S. *J. Phys. Chem. B* **2009,** *113*, 11568-11573.
145. Yin, K.; Zhang, L.; Lai, C.; Zhong, L.; Smith, S.; Fong, H.; Zhu, Z. *J. Mater. Chem.* **2011,** *21*, 444; Campoy-Quiles, M.; Ishii, Y.; Sakai, H.; Murata, H. *Appl. Phys. Lett.* **2008,** *92*, 213305.
146. Ishii, Y.; Murata, H. *J. Mater. Chem.* **2012,** *22*, 4695.
147. Pagliara, S.; Vitiello, M.S.; Camposeo, A.; Polini, A.; Cingolani, R.; Scamarcio, G.; Pisignano, D. *J. Phys. Chem. C* **2011,** *115*, 20399-20405.

148. Xin, Y.; Ling, Z.; Li, S.; Lin, T.; Liu, G. *Mater. Sci. Eng. B-Adv* **2012,** *177*, 1094-1097.
149. Tu, D.; Pagliara, S.; Camposeo, A.; Persano, L.; Cingolani, R.; Pisignano, D. *Nanoscale* **2010,** *2*, 2217-2222.
150. Fasano, V.; Polini, A.; Morello, G.; Moffa, M.; Camposeo, A.; Pisignano, D. *Macromolecules* **2013**, 130716092133006.
151. Pagliara, S.; Camposeo, A.; Polini, A.; Cingolani, R.; Pisignano, D. *Lab Chip* **2009,** *9*, 2851-2856.
152. Pagliara, S.; Camposeo, A.; Mele, E.; Persano, L.; Cingolani, R.; Pisignano, D. *Nanotechnology* **2010,** *21*, 215304; Di Benedetto, F.; Camposeo, A.; Pagliara, S.; Mele, E.; Persano, L.; Stabile, R.; Cingolani, R.; Pisignano, D. *Nat. Nanotechnol.* **2008,** *3*, 614-619.
153. Chen, J.-Y.; Kuo, C.-C.; Lai, C.-S.; Chen, W.-C.; Chen, H.-L. *Macromolecules* **2011,** *44*, 2883-2892; Lin, C.J.; Hsu, J.C.; Tsai, J.H.; Kuo, C.C.; Lee, W.Y.; Chen, W.C. *Macromol. Chem. Phys.* **2011,** *212*, 2452-2458.
154. Zhang, Y.; Rutledge, G.C. *Macromolecules* **2012,** *45*, 4238-4246.
155. Canesi, E.V.; Luzio, A.; Saglio, B.; Bianco, A.; Caironi, M.; Bertarelli, C. *ACS Macro Letters* **2012,** *1*, 366-369.
156. Bedford, N.M.; Dickerson, M.B.; Drummy, L.F.; Koerner, H.; Singh, K.M.; Vasudev, M.C.; Durstock, M.F.; Naik, R.R.; Steckl, A.J. *Adv. Energy Mater.* **2012,** *2*, 1136-1144.
157. Isakov, D.V.; de Matos Gomes, E.; Vieira, L.G.; Dekola, T.; Belsley, M.S.; Almeida, B.G. *ACS Nano* **2011,** *5*, 73-78.
158. Farrar, D.; Ren, K.; Cheng, D.; Kim, S.; Moon, W.; Wilson, W.L.; West, J.E.; Yu, S.M. *Adv. Mater.* **2011,** *23*, 3954-3958.
159. Ren, K.; Wilson, W.L.; West, J.E.; Zhang, Q.M.; Yu, S.M. *Appl. Phys. A* **2012,** *107*, 639-646.
160. Mandal, D.; Yoon, S.; Kim, K.J. *Macromol. Rapid Comm.* **2011,** *32*, 831-837.

Chapitre 3. Novel method for quantifying molecular orientation by polarized Raman spectroscopy: a comparative simulations study

3.1. Abstract

Polarized Raman spectroscopy is widely used to quantify the level of molecular orientation of various types of materials using a simplified procedure that we will call the *depol constant* (DC) method since it assumes that the depolarization ratio is a constant. However, our ability to quantify orientation using the DC method is often limited by the requirement of having access to a completely isotropic sample showing the same chemical and phase composition as the oriented sample of interest to obtain information on the depolarization ratio. In this publication, we propose a new method for orientation quantification, the *most probable distribution* (MPD) method, that is based on the hypothesis that the population distribution is the most probable one. In contrast with the conventional DC procedure, this new method does not require knowledge of the depolarization ratio and eliminates the assumption that it does not evolve upon orientation. Simulations show the wide applicability of the MPD method for large sections of the $\langle P_2 \rangle \langle P_4 \rangle$ diagram, especially for coordinates that are most likely to be observed in experimental conditions. They also highlight the significant inaccuracies produced by the conventional DC method due to errors on the depolarization ratio.[2]

---

[2] Publié comme article complet dans *Applied Spectroscopy*, **2013**, 67, *4*, 409-419 par Marie Richard-Lacroix et Christian Pellerin

3.2. Introduction

Molecular orientation is, along with crystallinity and molecular interactions, a parameter of critical importance in the characterization of most materials. Orientation strongly impacts a wide variety of their characteristics such as their mechanical, optical and electronic properties, and therefore greatly influences their potential applications.[1] The most commonly used techniques to characterize the degree of order are X-ray diffraction (XRD) and infrared spectroscopy (IR). XRD has the significant advantage of providing directly the orientation distribution function (ODF) but it is essentially limited to the characterization of the crystalline phase. IR spectroscopy is particularly useful for the analysis of amorphous, semi-crystalline or multicomponent systems, such as blends and copolymers. While it is less often used, polarized Raman spectroscopy offers substantial advantages over these two techniques. In particular, confocal Raman spectroscopy provides the same molecular level specificity as IR spectroscopy and allows detailed localized analysis at the submicron level. This enables the characterization of individual objects, such as electrospun nanofibers, which must otherwise be characterized as bundles using XRD or IR spectroscopy to obtain a satisfying signal-to-noise ratio.[2] It has been used, for example, for the fine analysis of the molecular structure and orientation of spider silk fibers,[3] holographic diffraction gratings[4] and tendons under tension.[5]

One of the main drawbacks of polarized Raman spectroscopy is the relative complexity of the quantification procedure, both from the experimental and theoretical points of view. Indeed, the *complete method* for orientation quantification, developed in the 1970s by Bower, involves recording 12 polarized spectra in 3 different experimental geometries.[6-9] This method has the advantage of not requiring any approximation (except uniaxial symmetry) but it is inapplicable for most samples, extremely time consuming, and subject to large errors due to polarization scrambling and birefringence effects.[6, 8] To this date, only a few research groups have applied this procedure to films and fibers of poly(propylene terephthalate),[6] poly(ethylene terephthalate),[8, 10] high density polyethylene[7, 9] and polystyrene.[11]

Most Raman orientation measurements have relied on a simplified procedure, called $a_1=a_2$ by Frisk *et al.*[6], which is based on the assumption that the Raman tensor is cylindrical and that its shape is unaffected by orientation. In this paper, we will refer to this procedure as

the *depol constant* (DC) method to emphasize the fact that the depolarization ratio must be determined experimentally and that its value must be assumed to be constant, independent of the orientation and molecular structure. These approximations reduce the number of unknowns and enable the quantification of the order parameters, $\langle P_2 \rangle$ and $\langle P_4 \rangle$, using a single experimental geometry.[6] The DC method is particularly useful for micro-spectroscopy since only the backscattering geometry is accessible. It nevertheless requires knowledge about the form of the Raman tensor of the vibrational mode through its depolarization ratio. The measurement of this parameter requires a completely isotropic sample with exactly the same chemical and phase composition as the oriented samples of interest, conditions which are often difficult or even impossible to meet.

The DC method has been severely questioned by Lesko et al.[8], Frisk et al.[6] and later by Soto et al.[12] These authors have shown that, for many vibrational modes, the tensor is not cylindrical and that its form can greatly evolve upon orientation. For polymers, these changes can originate from stress–induced crystallization, formation of a mesophase, or conversion to a polymorph that only exists under tension. The impact on the calculated order parameters of such unpredictable errors on the depolarization ratio can be significant. Furthermore, the access to a completely isotropic sample at the length scale of the measurement can also be problematic, for instance in the cases of large spherulites or single crystals. To our knowledge, these difficulties have not been overcome yet.

In this publication, we propose a new procedure for orientation calculation, called the *most probable distribution* (MPD) method, that is based on the DC method but that eliminates the prerequisite knowledge of the depolarization ratio. Rather, we propose replacing it by the more probable assumption that the $\langle P_4 \rangle$ parameter takes its most probable value associated with the $\langle P_2 \rangle$ of the sample. This publication is divided into four sections. We first expose the theoretical background behind this new method. In the second part, we demonstrate its validity by simulating the results of the MPD over the complete range of possible $\langle P_2 \rangle$ and $\langle P_4 \rangle$ values and for different depolarization ratios. We confirm that the MPD method converges to satisfactory $\langle P_2 \rangle$ results for large regions of the $\langle P_2 \rangle \langle P_4 \rangle$ diagram and, most importantly, for those where most real samples are situated. In the third section, we expose the weaknesses of the DC method by investigating the errors on the orientation parameters and on the ODF

induced by uncertainties or evolution upon orientation of the depolarization ratio. Finally, the last section treats specifically the case of perpendicular orientation for both methods.

3.3. Theoretical section

3.3.1. Orientation distribution function

For a system showing uniaxial symmetry, the orientation distribution function (ODF), N(θ), can be expressed as an infinite expansion of even Legendre polynomials, $P_l(cos\theta)$.

$$N(\theta) = \sum_{l}^{even} \left(l + \frac{1}{2}\right) \langle P_l \rangle \, P_l(cos\theta) \tag{3.1}$$

The $\langle P_l \rangle$ coefficients, often called order parameters, are the averaged values of the l^{th} Legendre polynomials over the ODF and are determined experimentally. The first coefficient, $\langle P_0 \rangle$, is equal to 1. Polarized Raman gives access to the second and fourth coefficients of the series, $\langle P_2 \rangle$ and $\langle P_4 \rangle$.

$$\langle P_2 \rangle = \frac{1}{2} \langle 3cos^2\theta - 1 \rangle \tag{3.2}$$

$$\langle P_4 \rangle = \frac{1}{8} \langle 35cos^4\theta - 30cos^2\theta + 3 \rangle \tag{3.3}$$

The limiting values of $\langle P_2 \rangle$ are 0 for an isotropic distribution, 1 for a perfect orientation of the units along the macroscopic long axis of the sample (Z), and -0.5 for a perfect alignment perpendicular to the long axis (X).

With knowledge of $\langle P_2 \rangle$ and $\langle P_4 \rangle$, one can estimate the most probable orientation distribution, $N(\theta)_{mp}$, which is the smoothest possible ODF and is therefore the most likely to represent the orientation of a given sample. $N(\theta)_{mp}$ can be obtained by maximizing the entropy of orientation of the distribution, S(N(θ)):

$$S(N(\theta)) = -\int_0^{\pi} N(\theta) \ln\big(N(\theta)\big) \, sin\theta d\theta \tag{3.4}$$

This procedure implies that the ODF is Gaussian, that it increases (or decreases) smoothly and monotonically with θ,[13, 14] and that it respects the constraints expressed by Eqs. 3.5a-c, which

specify that the ODF is a normalized probability and that it must be consistent with the experimental $\langle P_2 \rangle$ and $\langle P_4 \rangle$ values.

$$N(\theta) \geq 0 \tag{3.5a}$$

$$\int_0^\pi N(\theta) sin\theta d\theta = 1 \tag{3.5b}$$

$$\langle P_l \rangle = \int_0^\pi P_l\,(cos\theta) N(\theta) sin\theta d\theta \tag{3.5c}$$

Introducing the Lagrange multipliers, λ_l, for l = 2 and 4, and maximizing the entropy leads to:

$$\int_0^\pi [lnN(\theta) - \lambda_2 P_2(cos\theta) - \lambda_4 P_4(cos\theta)] \delta N(\theta) sin\theta d\theta = 0 \tag{3.6}$$

The most probable distribution, $N(\theta)_{mp}$, can be expressed as:[13]

$$N(\theta)_{mp} = \frac{exp[\lambda_2 P_2(cos\theta) + \lambda_4 P_4(cos\theta)]}{\int_0^\pi exp[\lambda_2 P_2(cos\theta) + \lambda_4 P_4(cos\theta)] sin\theta d\theta} \tag{3.7}$$

With knowledge of the experimental $\langle P_2 \rangle$ and $\langle P_4 \rangle$ values, the λ_l can finally be evaluated such that the constraint of Eq. 3.5c is respected.

Nomura et al.[15, 16] have shown that the limiting values of $\langle P_4 \rangle$ depend on the $\langle P_2 \rangle$ value, using the Schwarz inequalities:

$$\langle P_4 \rangle_{min} = \frac{1}{18}(35\langle P_2 \rangle^2 - 10\langle P_2 \rangle - 7) \leq \langle P_4 \rangle \leq \frac{1}{12}(5\langle P_2 \rangle + 7) = \langle P_4 \rangle_{max} \tag{3.8}$$

$\langle P_4 \rangle_{max}$ is associated to an infinitely narrow bimodal orientation distribution at angles of 0° and 90°, and $\langle P_4 \rangle_{min}$ to an infinitely narrow unimodal distribution at an angle θ_0 given by:[17]

$$\theta_0 = arccos\sqrt{\frac{2\langle P_2 \rangle + 1}{3}} \tag{3.9}$$

For all other intermediate $\langle P_4 \rangle$ values, the extrema of N(θ) can be situated at 0°, 90° and at an angle θ_3, that can be determined from the Lagrange multipliers:[13, 14]

$$cos^2\theta_3 = \frac{15\lambda_4 - 6\lambda_2}{35\lambda_4} \tag{3.10}$$

Bower[18] has defined four regions in the $\langle P_2 \rangle \langle P_4 \rangle$ plane, presented in Figure 3.1a, that delimit the different possible shapes of the orientation distribution function. The analytical expressions for the curves delineating these regions have been published by Park et al.[19] The

regions I and II define the combinations of $\langle P_2 \rangle$ and $\langle P_4 \rangle$ for which $N(\theta)_{mp}$ shows a monotonic decrease or increase with θ, respectively. A typical ODF in region I is represented by the green curve of Figure 3.1b for $\langle P_2 \rangle = 0.3$ (the exact coordinates are indicated by the green X mark in Figure 3.1a). In region III, the shape of the ODF associated with the same $\langle P_2 \rangle$ value of 0.3 is no longer monotonic and shows at least a maximum at θ_3, as revealed by the light blue and pink curves of Figure 3.1b. The shift and broadening of the ODF can be noted with decreasing $\langle P_4 \rangle$ values in section III. Similarly, the dark blue and red curves show typical ODFs from region IV, where the distributions are bimodal and show at least a minimum at θ_3. At the lower limit of this region, the ODF is broad (dark blue curve) and the maxima at 0 and 90° are small. In contrast, a much narrower ODF with sharply increasing population at 0° and 90° is observed for the upper limit (red curve), close to $\langle P_4 \rangle_{max}$. Analogous ODF curves for perpendicular orientations (negative $\langle P_2 \rangle$ values) are shown in Figure 3.S1 of the Supporting information.

Bower[18], and later Pottel et al.,[13] defined the most probable $\langle P_4 \rangle$ value, $\langle P_4 \rangle_{mp}$, associated with each $\langle P_2 \rangle$ value, by maximizing the information entropy of the distribution. These conditions are fulfilled for particular $\langle P_2 \rangle$ and $\langle P_4 \rangle$ couples for which λ_4 is equal to 0. Lagugné-Labarthet et al.[14] have approximated analytical equations describing these curves for the positive and negative $\langle P_2 \rangle$ regions as Eqs. 3.11 a and b, respectively. These curves are shown in Figure 3.1a as dashed lines.

$$\langle P_4 \rangle_{mp} = -0.083\langle P_2 \rangle + 1.366\langle P_2 \rangle^2 - 1.899\langle P_2 \rangle^3 + 1.616\langle P_2 \rangle^4 \quad (3.11a)$$

$$\langle P_4 \rangle_{mp} = 0.052\langle P_2 \rangle + 1.574\langle P_2 \rangle^2 + 3.968\langle P_2 \rangle^3 + 8.058\langle P_2 \rangle^4 \quad (3.11b)$$

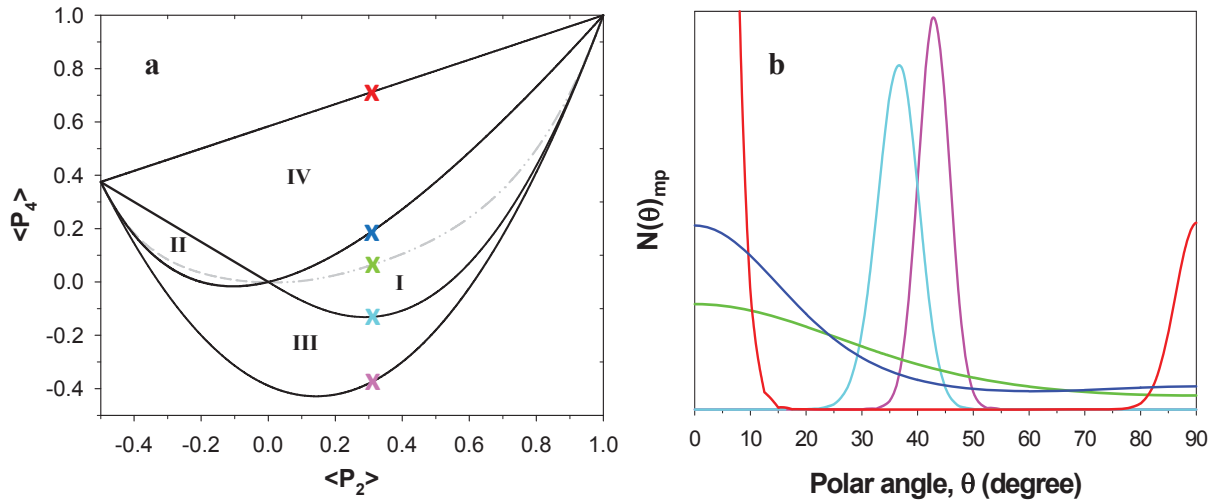

Figure 3.1. a) $\langle P_2 \rangle \langle P_4 \rangle$ diagram defining four regions with distinct orientation distribution functions (ODF). The maximum and minimum $\langle P_4 \rangle$ curves were plotted according to Eq. 3.8 and represent narrow bimodal ODFs with maxima at 0 and 90°, and narrow unimodal ODFs with a maximum at θ_0 (Eq. 3.9), respectively. The curves defining sections I and II were plotted according to Park et al.[19] and delimit the regions where the ODFs show a monotonic decrease or increase with θ, respectively. The dashed grey curves were plotted according to Eq. 3.11 and represent the most probable $\langle P_4 \rangle_{mp}$ associated with each $\langle P_2 \rangle$ value. **b)** ODFs associated with $\langle P_2 \rangle$ = 0.3 and the different values of $\langle P_4 \rangle$ indicated by the X marks of the same color in panel a.

3.2.2. Orientation quantification by Raman spectroscopy

Bower[20] has developed the theory for orientation quantification using polarized Raman intensities, I_s, which are related to quadratic summations of the Raman tensor components, α_{ij}:

$$I_s = I_0 \langle \sum_{i,j} \left(l_i' l_j \alpha_{ij} \right)^2 \rangle \qquad (3.12)$$

where I_0 combines the constant terms of the equation, such as the laser power, and l_i' and l_j define the direction cosines of the incident and scattered light, respectively, with respect to the tensor principal axes. These $\langle (\alpha_{ij})^2 \rangle$ terms are directly related to the orientation parameters, $\langle P_2 \rangle$ and $\langle P_4 \rangle$, and to the shape of the polarizability variation ellipsoid, which can be described by a second rank tensor with its principal components, α_1, α_2 and α_3:

$$\alpha = \begin{pmatrix} \alpha_1 & & \\ & \alpha_2 & \\ & & \alpha_3 \end{pmatrix} = \alpha_3 \begin{pmatrix} a_1 & & \\ & a_2 & \\ & & 1 \end{pmatrix} \quad (3.13)$$

The *complete method* for orientation quantification has been described by several authors.[7-9] For systems with uniaxial symmetry, there are only 5 independent and nonzero equations that contain the 5 unknown parameters ($\langle P_2 \rangle$, $\langle P_4 \rangle$, a_1, a_2, and a constant b combining α_3 and I_0). These unknowns can be determined by measuring 12 spectra in 3 distinct geometries, namely backscattering, right angle scattering, and either right angle scattering or backscattering with the sample tilted at 45°. The 7 supplementary spectra are used for normalization with respect to several theoretical equalities. The necessity of these three experimental geometries makes the *complete method* extremely time consuming, problematic for most samples, and inapplicable for micro-spectroscopy.

3.2.2.1. "Depol constant" (DC) method

In the last decade, most Raman orientation studies have been performed using the simplified DC method, described by Frisk et al.[6] as the $a_1 = a_2$ method. The DC method reduces the number of unknowns from five to four with the approximation of a cylindrical Raman tensor, which means that $a_1 = a_2 = a$, whose shape stays constant upon orientation. This enables eliminating the fifth equation of the *complete method* that required the sample to be tilted at 45° and that was, therefore, subject to large errors due to birefringence. The four remaining equations describing the $\langle (\alpha_{ij})^2 \rangle$ terms can now be expressed as:[3]

$$\langle (\alpha_{ZZ})^2 \rangle = b\left(\frac{1}{15}(3 + 4a + 8a^2) + \frac{4}{21}(3 + a - 4a^2)\langle P_2 \rangle + \frac{8}{35}(1 - a)^2\langle P_4 \rangle\right) \quad (3.14a)$$

$$\langle (\alpha_{XX})^2 \rangle = b\left(\frac{1}{15}(3 + 4a + 8a^2) - \frac{2}{21}(3 + a - 4a^2)\langle P_2 \rangle + \frac{3}{35}(1 - a)^2\langle P_4 \rangle\right) \quad (3.14b)$$

$$\langle (\alpha_{XZ})^2 \rangle = \langle (\alpha_{ZX})^2 \rangle = \langle (\alpha_{ZY})^2 \rangle = b(1 - a)^2\left(\frac{1}{15} + \frac{1}{21}\langle P_2 \rangle - \frac{4}{35}\langle P_4 \rangle\right) \quad (3.14c)$$

$$\langle (\alpha_{XY})^2 \rangle = b(1 - a)^2\left(\frac{1}{15} - \frac{2}{21}\langle P_2 \rangle + \frac{1}{35}\langle P_4 \rangle\right) \quad (3.14d)$$

The backscattering geometry gives access to two parallel-polarized (ZZ and XX) and two cross-polarized (ZX and XZ) spectra which are used to solve the equations 3.14 through the spectral ratios R_1 and R_2 that eliminate the constant b.

$$R_1 = \frac{I_{ZX}}{I_{ZZ}} = \frac{A\langle(\alpha_{ZX})^2\rangle + B\langle(\alpha_{ZY})^2\rangle}{A\langle(\alpha_{ZZ})^2\rangle + B\langle(\alpha_{ZY})^2\rangle} \quad (3.15a)$$

$$R_2 = \frac{I_{XZ}}{I_{XX}} = \frac{A\langle(\alpha_{XZ})^2\rangle + B\langle(\alpha_{XY})^2\rangle}{A\langle(\alpha_{XX})^2\rangle + B\langle(\alpha_{XY})^2\rangle} \quad (3.15b)$$

The A and B constants in Eqs. 3.15 have been introduced by Turrell[21] to take into account the out-of-plane contribution to the polarized Raman signal when using a high numerical aperture (NA) objective in confocal Raman microscopy. They can be determined analytically for each objective according to Eqs. 3.16, where θ_m is the half-aperture angle.[3]

$$A = \pi^2\left(\frac{4}{3} - cos\theta_m - \frac{1}{3}cos^3\theta_m\right) \quad (3.16a)$$

$$B = 2\pi^2\left(\frac{2}{3} - cos\theta_m + \frac{1}{3}cos^3\theta_m\right) \quad (3.16b)$$

The "*a*" parameter of Eqs. 3.14 must finally be determined independently on a completely isotropic sample (for which $\langle P_2\rangle = \langle P_4\rangle = 0$ and therefore $R_1 = R_2$) from the depolarization ratio, ρ, where the positive root has to be selected.

$$\rho = R_1 = R_2 = \frac{(A+B)(1-a)^2}{A\,(8a^2+4a+3)+B\,(1-a)^2} \quad (3.17)$$

3.2.2.2. "Most probable distribution" (MPD) method

The new method proposed in this publication to quantify the orientation by Raman spectroscopy is a variation of the DC method. Indeed, instead of using the depolarization ratio to obtain the parameter "*a*" and fixing it as a constant, we propose to eliminate Eq. 3.17 and to replace it with Eq. 3.11, which defines the most probable $\langle P_4\rangle$. In this context, the shape of the Raman tensor does not have to be known and/or to be considered constant upon orientation. The system of equations to be solved then consists of the two unchanged Eqs. 3.15 and the appropriate Eq. 3.11 (3.11a and 3.11b for parallel and perpendicular orientations, respectively), with the unknowns $\langle P_2\rangle$, $\langle P_4\rangle$ and "*a*". In this method, $\langle P_4\rangle$ necessarily converges to $\langle P_4\rangle_{mp}$ and is therefore meaningless. The loss of information usually provided by $\langle P_4\rangle$ is counterbalanced by the elimination of the errors on $\langle P_2\rangle$ and $\langle P_4\rangle$ induced by the approximations associated with the use of Eq. 3.17, and the implicit experimental complications underlying its use.

3.4. Results and discussion

3.4.1. Simulations of the MPD method for parallel orientations

3.4.1.1. Correlation between the MPD and DC methods in the $\langle P_2 \rangle \langle P_4 \rangle$ diagram

The validity of the MPD method and the range of $\langle P_2 \rangle$ and $\langle P_4 \rangle$ values for which it is applicable was first analyzed. Our objective was to compare the $\langle P_2 \rangle$ values obtained by the MPD and DC methods for all possible experimental situations, i.e., for all the combinations of $\langle P_2 \rangle$, $\langle P_4 \rangle$ and ρ that could theoretically be encountered when measuring the four polarized Raman spectra required for orientation quantification. The easiest way to cover all these possibilities is to use the DC method in a reversed mode: that is, to set a selected ρ (ρ_{set}) and to calculate the spectral ratios R_1 and R_2, using Eqs. 3.14 and 3.15, that would have been determined experimentally for all theoretically possible $\langle P_2 \rangle_{set}$ and $\langle P_4 \rangle_{set}$ couples as shown in Figure 3.1a. The ratios are then used as input parameters for simulating the MPD results, $\langle P_2 \rangle_{MPD}$ and $\langle P_4 \rangle_{MPD}$, by simultaneously solving Eqs. 3.15 and 3.11 using Mathematica. The same process is then repeated for each ρ_{set} in the theoretical limits of 0 to 0.75. The values of A and B in Eq. 3.15 were chosen to correspond to a 100X objective with a numerical aperture of 0.9, because this new method is expected to be particularly useful in Raman micro-spectroscopy.

In this approach, the fixed $\langle P_2 \rangle_{set}$ and $\langle P_4 \rangle_{set}$ couples at the basis of the simulations can be considered as simulated DC values and be compared with the values calculated using the MPD method. In fact, only the $\langle P_2 \rangle$ values should be considered when using the MPD method since it assumes that $\langle P_4 \rangle$ takes the most probable value associated with the $\langle P_2 \rangle_{MPD}$ to which the calculation converged. It should be emphasized that the $\langle P_2 \rangle_{MPD}$ values are determined using the simulated ratios R_1 and R_2 but disregarding ρ_{set}, since knowledge of the depolarization ratio is not required when using the new method.

Before describing the simulation results of Figure 3.2, it must be specified that the MPD method does not lead to a single solution because of the interdependence of $\langle P_2 \rangle$ and $\langle P_4 \rangle$. Nevertheless, a unique solution can be obtained with carefully established selection rules. Most aberrant solutions are easily eliminated by imposing appropriate boundaries for $\langle P_2 \rangle$

values (between -0.05 and 1 for the positive part of the diagram), and for the "*a*" parameter (-0.36 ≤ *a* ≤ 0.75 as imposed by Eq. 3.17). The system can still sometimes generate two "theoretically acceptable" solutions but it was observed that the less consistent solution was the one for which the $\langle P_2 \rangle_{MPD}$ and ρ couples were highest (ρ ≥ 0.60) and was therefore systematically excluded.

With careful respect of these criteria, the unique solution from the MPD method can be compared with the true $\langle P_2 \rangle_{set}$ value. Their concordance, expressed as their absolute difference $\Delta\langle P_2 \rangle$, is shown in Figure 3.2 for the positive part of the diagram and in Figure 3.5 for the negative part. The green circles, blue diamonds and red triangles are associated, respectively, with an excellent agreement ($\Delta\langle P_2 \rangle \leq 0.05$), an intermediate convergence ($0.05 < \Delta\langle P_2 \rangle < 0.1$), and a larger disagreement of the orientation results ($\Delta\langle P_2 \rangle > 0.1$). Figure 3.2b illustrates a typical comparison diagram, for a fixed ρ_{set} of 0.1. A clear pattern can be observed when scanning vertically the diagram from the higher to the lower $\langle P_4 \rangle_{set}$ values. For example, for true $\langle P_2 \rangle_{set}$ and $\langle P_4 \rangle_{set}$ of 0.30 and 0.05, respectively, the MPD method converges exactly to a $\langle P_2 \rangle$ of 0.30, therefore represented by a green symbol on the diagram. This perfect agreement was expected since the ($\langle P_2 \rangle_{set}$, $\langle P_4 \rangle_{set}$) coordinates are directly located on the theoretical curve for the most probable $\langle P_4 \rangle$. As shown by the green curve in Figure 3.1b, the orientation distribution function associated with the most probable $\langle P_4 \rangle$ is smooth and presents a monotonic decrease with θ. Keeping $\langle P_2 \rangle_{set}$ constant at 0.30, but increasing the $\langle P_4 \rangle_{set}$ value to 0.15, directly on the curve delimiting regions I and IV, the MPD methods yields a $\langle P_2 \rangle_{MPD}$ of 0.32 that correlates very well with the expected result ($\Delta\langle P_2 \rangle = 0.02$), even if this point is relatively far from the most probable curve. The ODF for this second scenario is illustrated by the dark blue curve of Figure 3.1b, which is much more abrupt than the most probable one and starts to show a bimodal pattern with a small population at a polar angle of 90° and a minimum at an angle $\theta_3 = 67°$. A similar situation is observed when keeping the $\langle P_2 \rangle_{set}$ constant and decreasing the $\langle P_4 \rangle_{set}$ to a value of -0.15, on the curve delimiting regions I and III. The calculated $\langle P_2 \rangle_{MPD}$ is in good agreement with $\langle P_2 \rangle_{set}$ and is only slightly underestimated with a value of 0.26. The ODF associated with these coordinates is very far from the most probable one, as represented by the light blue curve on Figure 1b that clearly shows a maximum at $\theta_3 \approx 38°$.

When reaching the lowest part of the diagram, at a $\langle P_4 \rangle_{set}$ of -0.35, very close to its minimum value, the calculated $\langle P_2 \rangle_{MPD}$ of 0.22 diverges more significantly from the expected value (blue symbol). This scenario is represented by the pink curve of Figure 3.1b, which shows a unimodal ODF with a narrow maximum at $\theta_3 \approx 43°$. This corresponds to a highly improbable distribution in terms of maximization of the entropy of orientation and it is therefore unlikely to be observed in experimental samples under normal circumstances. At the other extreme, for the maximum $\langle P_4 \rangle_{set}$ of 0.6, the value of $\langle P_2 \rangle_{MPD}$ diverges considerably from the expected one with a value of 0.89, represented on the diagram by a red triangle. This ODF, shown as the red curve of Figure 3.1b, presents a sharp bimodal population distribution which is again statistically highly improbable.

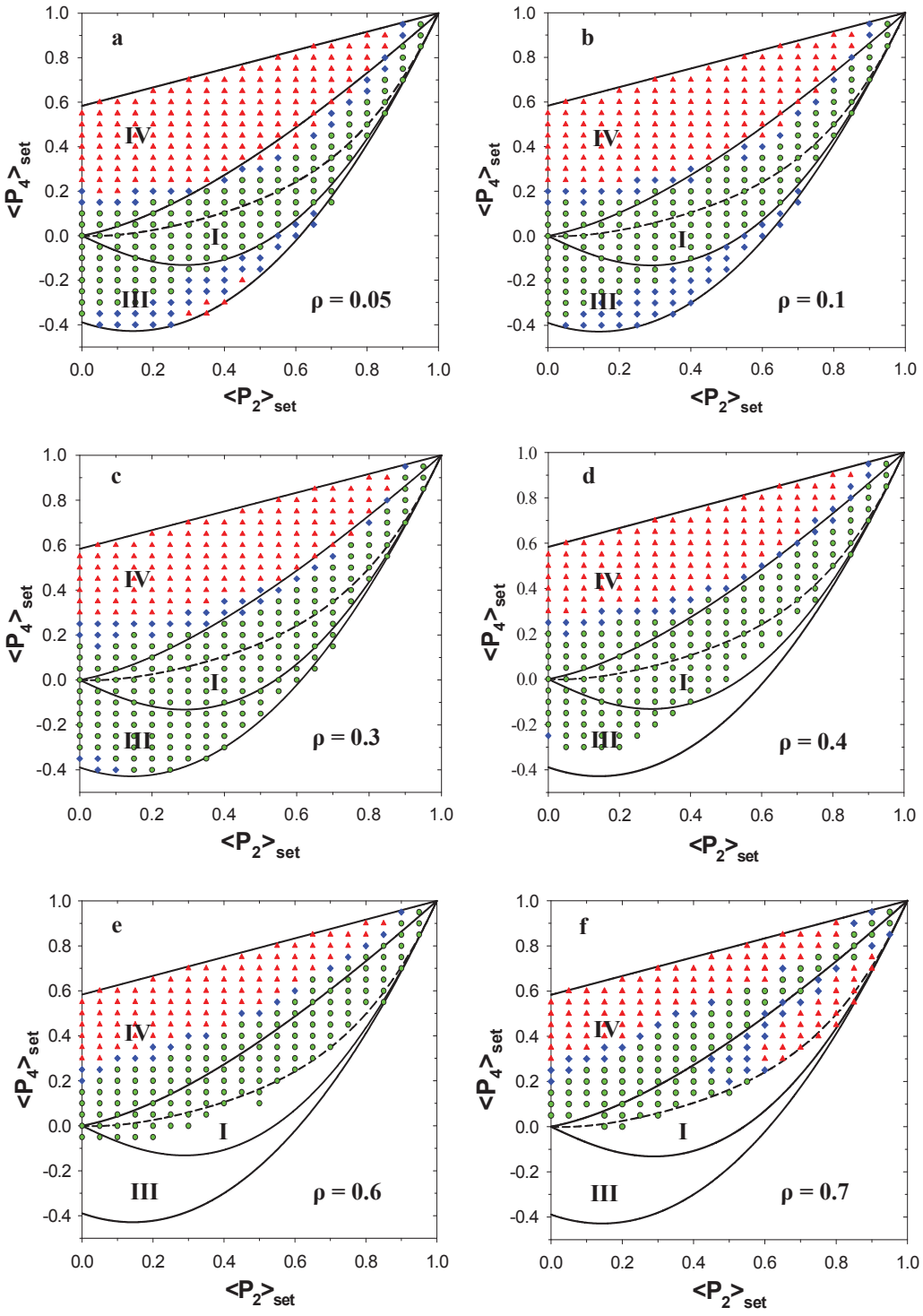

Figure 3.2. Correlation between the $\langle P_2 \rangle_{MPD}$ and $\langle P_2 \rangle_{set}$ values in the positive region of the $\langle P_2 \rangle \langle P_4 \rangle$ diagram. Panels a-f show results for depolarization ratios of 0.05, 0.1, 0.3, 0.4, 0.6 and 0.7, respectively. Red triangles, blue diamonds and green circles are associated with $\Delta\langle P_2 \rangle > 0.1$, $0.05 < \Delta\langle P_2 \rangle < 0.1$ and $\Delta\langle P_2 \rangle \leq 0.05$, respectively. The absence of symbols indicates that the MPD method did not converge to a solution.

More generally, when one scans the diagram of Figure 3.2b vertically from the upper to the lower $\langle P_4 \rangle_{set}$ values for any fixed $\langle P_2 \rangle_{set}$, the $\langle P_2 \rangle_{MPD}$ is first largely overestimated but it decreases rapidly until the curve delimiting regions I and IV is reached. From this point, it starts almost plateauing around the expected $\langle P_2 \rangle_{set}$ value until the lowest part of the diagram, where the values are either slightly underestimated or absent (the program does not converge). Overall, the MPD method converges to acceptable $\langle P_2 \rangle$ values for a surprisingly large portion of the $\langle P_2 \rangle \langle P_4 \rangle$ diagram that, importantly, completely covers the critical region I. Indeed, as previously illustrated in Figure 3.1b, the further away from the most probable curve, the smaller is the probability for a sample to show the corresponding ODF.[13, 18] The same argument is applicable for the regions III and IV, for their respective types of orientation distributions, since their ODFs become increasingly more abrupt when approaching the extreme $\langle P_4 \rangle$ values. The probability of finding such distribution in a real sample is exceedingly small unless very special processing treatments were applied. The excellent convergence of the results, especially in region I, suggests the widespread applicability of the MPD method in real experimental situations. This will be demonstrated unambiguously in an upcoming paper by applying the MPD method to experimental results on several polymer systems.

Figure 3.2a-f shows similar correlation diagrams for different values of ρ_{set}. A tendency similar to the one described for $\rho_{set} = 0.1$ is observed over a large range of ρ from 0.05 to 0.5 (Figure 3.2a-d). The MPD method is therefore directly applicable for a broad range of depolarization ratios covering most experimental situations. For $\rho_{set} = 0.6$, the MPD calculation method does not converge to any solution for a large section below the most probable curve but it remains applicable for most of the experimental cases that should be encountered. However, the method is clearly less efficient when reaching the upper limit of the depolarization ratio for $\rho_{set} = 0.7$, as shown in Figure 3.2f. Indeed, only a small section of region I is covered by acceptable $\langle P_2 \rangle_{MPD}$ for low $\langle P_2 \rangle_{set}$ values. In fact, the MPD method converges to the anticipated values for all ($\langle P_2 \rangle_{set}$, $\langle P_4 \rangle_{set}$) couples that are precisely situated on the most probable curve, but some of these acceptable results were voluntarily discarded based on the selection criteria established to eliminate multiple solutions. These few points are

the only cases where the selection of the solution with the largest $\langle P_2 \rangle_{MPD}$ and ρ couple would have been judicious.

The disagreement of the MPD method with the set values for the particular case of both a high level of orientation ($\langle P_2 \rangle$ larger than 0.6) and a very high ρ (≥ 0.7) does not critically affect the general applicability of the MPD method. Indeed, the limiting values of ρ, 0 and 0.75, are associated with totally symmetric and anti-symmetric vibrational modes,[22] respectively. In contrast, Raman bands of complex molecules such as polymers are usually due to a combination of vibrational modes so it is highly probable that a band used for orientation quantification will present an intermediate ρ value rather than an extreme one. A second attenuating factor is that the main axis of the Raman tensor of most bands is tilted at some angle with respect to the main chain. The orientation parameters of the vibration itself are therefore proportionally smaller. As an example, a band with its tensor tilted at 25° from the main chain axis cannot yield a $\langle P_2 \rangle$ value larger than 0.73 even if the main chain is perfectly oriented, a situation that is very rarely observed since real samples always show a minimal degree of imperfection. Consequently, the MPD method can be conveniently used even for vibrational modes with a large depolarization ratio as long as the orientation of the sample is not unusually high.

From an experimental point of view, the probability for a sample to be situated in the red areas of region IV is small, but the divergence of the results of the MPD method in this region could still induce errors. Indeed, it is challenging to predict an unexpected behavior caused by special processing of the material. Since the $\langle P_4 \rangle_{MPD}$ values associated with these erroneous $\langle P_2 \rangle_{MPD}$ are, by definition, the most probable ones, a sample truly in region IV would be incorrectly interpreted as a very highly oriented sample with a Gaussian ODF. Fortunately, it is possible to provide an objective discrimination procedure by observing the evolution of the "*a*" parameter generated by the MPD method, as described in detail in the Supporting information.

3.4.2.2. Limitations of the DC method

The previous section has addressed in detail the applicability and limitations of the MPD method. Its results were compared with the expected $\langle P_2 \rangle_{set}$ orientation parameters that were

calculated by reversing the DC method assuming a perfect knowledge of ρ. However, in real experimental situations, the results of the DC method will be affected by the error on the ρ value, in addition to the uncertainties associated with the measurement of the spectral ratios R_1 and R_2. As highlighted in the introduction, having access to an isotropic sample with the same phase composition as the oriented ones often limits the possibility of quantifying orientation. In addition, the use of a fixed ρ for samples showing different degrees of orientation can be problematic since the form of the Raman tensor has been shown to be sensitive to orientation and to the associated phase changes.[8, 10, 12, 23] Our objective in this section is therefore to evaluate the impact of these errors on the accuracy of the $\langle P_2 \rangle_{DC}$ and $\langle P_4 \rangle_{DC}$ orientation parameters using the DC method.

Let us consider a sample with an intermediate level of orientation ($\langle P_2 \rangle_{set}$ = 0.3 and $\langle P_4 \rangle_{set}$ = 0.05) showing a Gaussian ODF that corresponds of the most probable curve (green curve of Figure 1b). We will first consider the case where the true depolarization ratio for the band is ρ_{set} = 0.4. The R_1 and R_2 values that would have been determined experimentally from polarized Raman measurements for this sample can be calculated using Eqs. 3.14, 3.15 and 3.17. These ratios are then kept constant and used as input parameters for the simulations. The impact of an erroneous value of ρ can now be investigated by varying it by small increments and observing the evolution of the simulated $\langle P_2 \rangle_{DC}$ and $\langle P_4 \rangle_{DC}$.

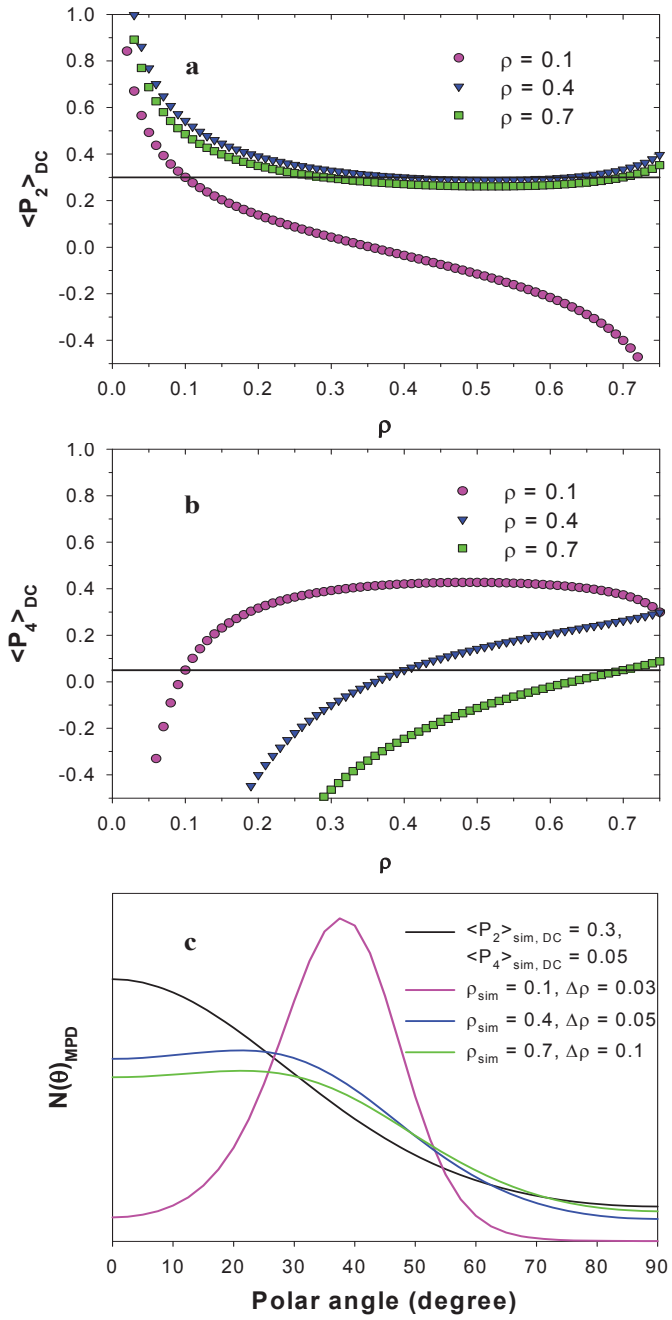

Figure 3.3. a) Variation of the $\langle P_2 \rangle_{DC}$ values calculated by the DC method induced by an incorrect ρ value. The plots were calculated for a fixed ($\langle P_2 \rangle_{set}$, $\langle P_4 \rangle_{set}$) couple of (0.3, 0.05) and with ρ_{set} values of 0.1 (pink circles), 0.4 (blue triangles) and 0.7 (green squares). The black line indicates the expected $\langle P_2 \rangle$ value. **b)** Variation of $\langle P_4 \rangle_{DC}$ induced by an incorrect ρ value in the conditions described in a). **c)** ODF resulting from the ($\langle P_2 \rangle_{DC}$, $\langle P_4 \rangle_{DC}$) couples calculated for different Δρ for initial ρ_{set} of 0.1 (pink curve), 0.4 (blue curve) and 0.7 (green curve). The ($\langle P_2 \rangle_{DC}$, $\langle P_4 \rangle_{DC}$) values corresponding to these scenarios are given in the text. The black curve represents the true ODF associated with the ($\langle P_2 \rangle_{set}$, $\langle P_4 \rangle_{set}$) couple of (0.3, 0.05).

The blue triangles of Figure 3.3a and b illustrate the variation of $\langle P_2 \rangle_{DC}$ and $\langle P_4 \rangle_{DC}$, respectively, for this particular example. The black lines indicate the true values of $\langle P_2 \rangle_{set}$ and $\langle P_4 \rangle_{set}$ that would have been obtained with perfect knowledge of ρ. The absence of symbols implies that $\langle P_2 \rangle_{DC}$ or $\langle P_4 \rangle_{DC}$ fall out of the acceptable range as defined in the theoretical section. While the errors are largest when ρ values strongly depart from the true ρ_{set}, the emphasis of the discussion will be placed on the variation of $\langle P_2 \rangle_{DC}$ and $\langle P_4 \rangle_{DC}$ for ρ values reasonably close to ρ_{set} because it better represents realistic experimental errors. By definition, the true values are obtained if $\rho = \rho_{set} = 0.4$. The simulated $\langle P_2 \rangle_{DC}$ values remain close to $\langle P_2 \rangle_{set} = 0.3$ for ρ values ranging from 0.2 to as far from ρ_{set} as 0.7, showing that large errors on the experimental determination of ρ would not significantly affect the quantification of $\langle P_2 \rangle$.

In sharp contrast, the variation of $\langle P_4 \rangle_{DC}$ is much more abrupt in Figure 3.3b. If, for example, ρ is erroneously determined experimentally as being 0.35 instead of 0.40 ($\Delta\rho = 0.05$), the $\langle P_2 \rangle_{DC}$ value only changes from 0.30 to 0.31, a negligible overestimation, but $\langle P_4 \rangle_{DC}$ varies significantly from 0.05 to -0.014. Figure 3.3c illustrates the large difference between the true ODF associated with the ($\langle P_2 \rangle_{set}$, $\langle P_4 \rangle_{set}$) couple (black curve) and the ODF of the ($\langle P_2 \rangle_{DC}$, $\langle P_4 \rangle_{DC}$) couple (blue curve) calculated using the incorrect $\rho = 0.35$. This slight error converts the ODF from the most probable distribution, as described in the Theoretical Section, into a unimodal ODF with a maximum at $\theta_3 \approx 23°$, an improbable distribution in terms of entropy of orientation. This comparison illustrates well the discrepancy generated by the error on $\langle P_4 \rangle$ due to an incorrect determination of the depolarization ratio when using the DC method.

It should be emphasized that such small experimental errors on ρ are likely to occur even if a perfectly isotropic sample is available. They can originate from various sources of minor experimental uncertainty such as noise in the spectra, imperfect optics of the microscope objective (that would slightly modify the A and B constants), imperfect polarization of the incident and scattered light due to the half-wave plate and the polarizer, or inadequate calibration of the spectrometer to correct for optical effects such as the polarization dependence of the diffraction efficiency of the grating.

When repeating the process for a higher ρ_{set} of 0.7, the variation of both orientation parameters with ρ (green squares on Figure 3.3a and b) is similar to that observed for the case of ρ_{set} = 0.4. When imposing a Δρ of 0.1, the calculated $\langle P_2 \rangle_{DC}$ and $\langle P_4 \rangle_{DC}$ values are 0.27 and -0.022, respectively, and the shape of the ODF (green curve in Figure 3c) is similar to that observed for a ρ_{set} of 0.4. Again, the result is significantly different from the true ODF shown by the black curve. By comparison, the pink circles of Figure 3.3a and b show a drastic variation of both $\langle P_2 \rangle_{DC}$ and $\langle P_4 \rangle_{DC}$ values around ρ_{set} = 0.1, for the same ($\langle P_2 \rangle_{set}$, $\langle P_4 \rangle_{set}$) couple. In this case, a Δρ error as small as 0.03 (ρ = 0.07) has a major impact on the calculated $\langle P_2 \rangle_{DC}$ and $\langle P_4 \rangle_{DC}$, which take values of 0.39 ($\Delta\langle P_2 \rangle$ = 0.09) and -0.19 ($\Delta\langle P_4 \rangle$ = 0.24), respectively. These erroneous coordinates are situated in region III of the $\langle P_2 \rangle\langle P_4 \rangle$ diagram. The pink curve of Figure 3.3c shows that the associated ODF, a narrow unimodal population distribution with a maximum at $\theta_3 \approx 38°$, significantly differs from the most probable one (black curve). If Δρ is further increased to 0.05, the ($\langle P_2 \rangle_{DC}$, $\langle P_4 \rangle_{DC}$) coordinates even fall out of the theoretically acceptable range defined by Eq.3.8.

The variable impact of Δρ on the calculated orientation parameters for the different ρ_{set}, observed in Figure 3.3, can be understood by observing the evolution of the "*a*" parameter with respect to ρ_{set}, as described by Eq. 3.17. It can be observed in Figure 3.4 that the evolution of "*a*" follows an S shape, such that it remains close to zero and varies smoothly for ρ values between 0.2 and 0.6. This reveals that vibrations with similar tensor forms (similar "*a*" values) can lead to a large range of experimental depolarization ratios. When approaching the extremes, especially for ρ < 0.2, the variation of "*a*" becomes more pronounced and it takes larger absolute values. The impact of the same Δρ error on the accuracy of $\langle P_2 \rangle$ and $\langle P_4 \rangle$ is therefore the largest for low ρ values, as noted in Figure 3.3.

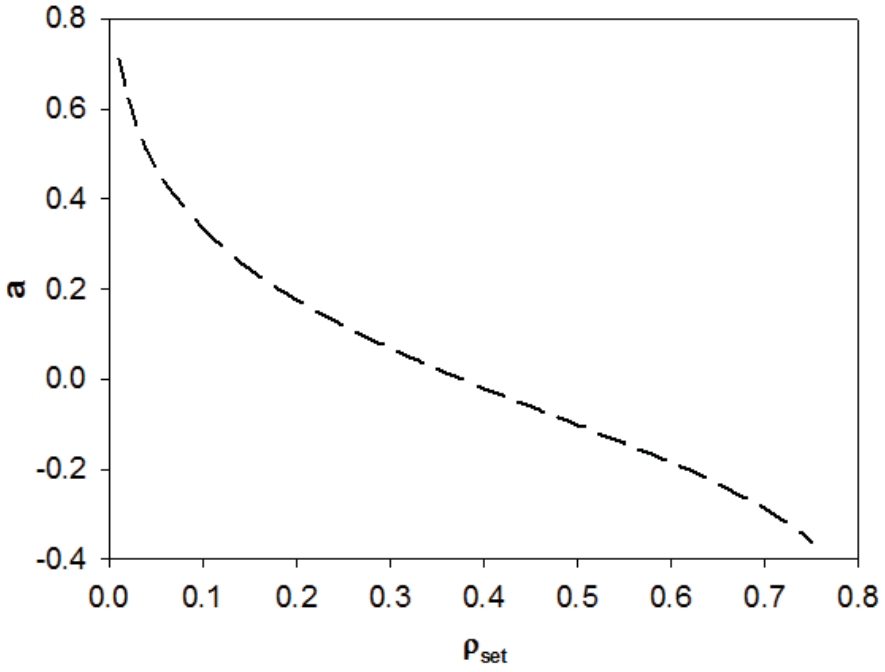

Figure 3.4. Evolution of *a* with respect to ρ according to Eq. 17.

The examples shown in Figure 3.3 were for a specific ($\langle P_2 \rangle_{set}$,$\langle P_4 \rangle_{set}$) couple located on the most probable curve. Similar observations can be made when exploring other couples situated on the most probable curve and in other regions of the diagram. These are shown in Figures 3.S2 to 3.S4 in the Supporting Information for ρ_{set} values of 0.1, 0.4 and 0.7, respectively). These results clearly demonstrate that even small errors on ρ can have a large impact on the $\langle P_2 \rangle$ and $\langle P_4 \rangle$ values determined by the DC method and, consequently, on their associated ODF. The results presented in Figure 3.3c are thus not anecdotic. In fact, they illustrate well the uncertainty that can be expected from experimental errors on ρ in real experimental situations, even if it depends on the specific ($\langle P_2 \rangle$, $\langle P_4 \rangle$) coordinates of the sample. From polarized Raman studies of poly(ethylene terephthalate) using the *complete method*, it can be deduced that the variation of ρ upon orientation can be as high as 0.15 or even more (by calculating ρ from the reported a_1 and a_2 values).[8, 10, 23] The examples shown in Figure 3.3c, with $\Delta\rho \leq 0.1$, are therefore realistic and even underestimate the errors that could be encountered. They highlight the main weakness of the conventional DC method: while the $\langle P_2 \rangle$ value may or may not be accurate, depending on the specific ρ value of the tensor and its experimental error, the combined errors on $\langle P_2 \rangle$ and $\langle P_4 \rangle$ are likely to prevent a proper

description of the ODF for most systems. Indeed, the incorrect quantification of $\langle P_4 \rangle$ can easily lead to the erroneous conclusion that the population distribution does not follow the anticipated most probable behavior.

Based on the two previous sections, several conclusions can be drawn: 1) The DC method is subject to large errors on both orientation parameters due to uncertainty on the depolarization ratio and its unpredictable variation upon orientation. This is true even if the real values are situated on the most probable curve, the most common experimental situation. 2) The MPD method provides $\langle P_2 \rangle$ values with excellent accuracy in the most common conditions and reasonable results for samples across most of the $\langle P_2 \rangle \langle P_4 \rangle$ diagram. 3) The MPD method does not provide the $\langle P_4 \rangle$ value but this sacrifice is negligible when considering the errors on the ODF often generated by the DC method. 4) The MPD method requires more complex calculation than the DC method but it is experimentally more convenient and applicable since it circumvents the issues raised in this section concerning the depolarization ratio.

3.4.2. Simulations of the MPD and DC methods for perpendicular orientations

In this section, we will explore the applicability and limitations of the MPD and DC methods in the case of molecular orientations perpendicular to the reference direction. Figure 3.5 shows the correlation between the $\langle P_2 \rangle_{MPD}$ results from the MPD method and the set values in the negative part of the $\langle P_2 \rangle \langle P_4 \rangle$ diagram for six depolarization ratios. It can be observed that the efficiency of the MPD method is better than for the positive region of the diagram (Figure 3.2). Figure 3.5 was constructed as above, but using Eq. 3.11b to define the most probable $\langle P_4 \rangle_{MPD}$ and limiting the $\langle P_2 \rangle_{MPD}$ values from -0.5 to 0.05. Again, the MPD method often leads to two theoretically acceptable solutions and the one with the largest $\langle P_2 \rangle$ (in absolute values) and ρ couple was systematically rejected. The color scheme is identical to that of Figure 3.2. The absence of symbols for the lowest part of the diagrams indicates a lack of convergence for these coordinates. The MPD method does converge to a solution in the upper part of region IV but these results were eliminated based on an additional criterion (vide infra).

When scanning vertically the diagram with fixed ρ_{set} and $\langle P_2 \rangle_{set}$ values, it can be observed that the $\Delta\langle P_2 \rangle$ are plateauing (close to a perfect agreement) in the most probable section II, as was the case for the positive part of the diagram. The ODFs associated with the different sections of this diagram are shown in the Supporting information (Figure 3.S1) and clearly expose the wide range of population distributions covered. The excellent agreement of the results in the critical region II of the diagrams (the analog of region I for the parallel orientations), where most samples will be found, for all depolarization ratios except $\rho = 0.7$, reinforces the general applicability of the method. In region III of the diagram, the simulations lead to $\langle P_2 \rangle_{MPD}$ results consistent with the fixed $\langle P_2 \rangle_{set}$ until the lowest $\langle P_4 \rangle_{set}$ values or do not converge to any solution. The result is therefore either reliable or non-existent.

The main difference between the simulations in the positive and negative parts of the diagram appears in region IV, for which the aberrant values (red triangles) can be almost completely eliminated in the negative part. Indeed, it was noted that the MPD method converges to aberrant values for all $(\langle P_2 \rangle, \langle P_4 \rangle)$ coordinates associated with simulated spectral ratios $R_1 < R_2$, a situation only observed in region IV of the diagram and associated with an unreasonable experimental behavior (see the red and dark blue curves of Figure 3.S1 in Supporting information). In fact, the elimination of these values is intuitively logical. For uniaxial systems, the XZ and ZX cross-polarized spectra should be equal based on symmetry arguments. They become nonequivalent in Raman microscopy because of out-of-plane contributions due to the use of an objective with a high NA (see Eq. 3.15), but their intensity is generally comparable since the constant B is relatively small. As a consequence, for a band with a perpendicular orientation, the intensity of the XX spectrum should be larger than that of the ZZ spectrum, and therefore $R_1 > R_2$.

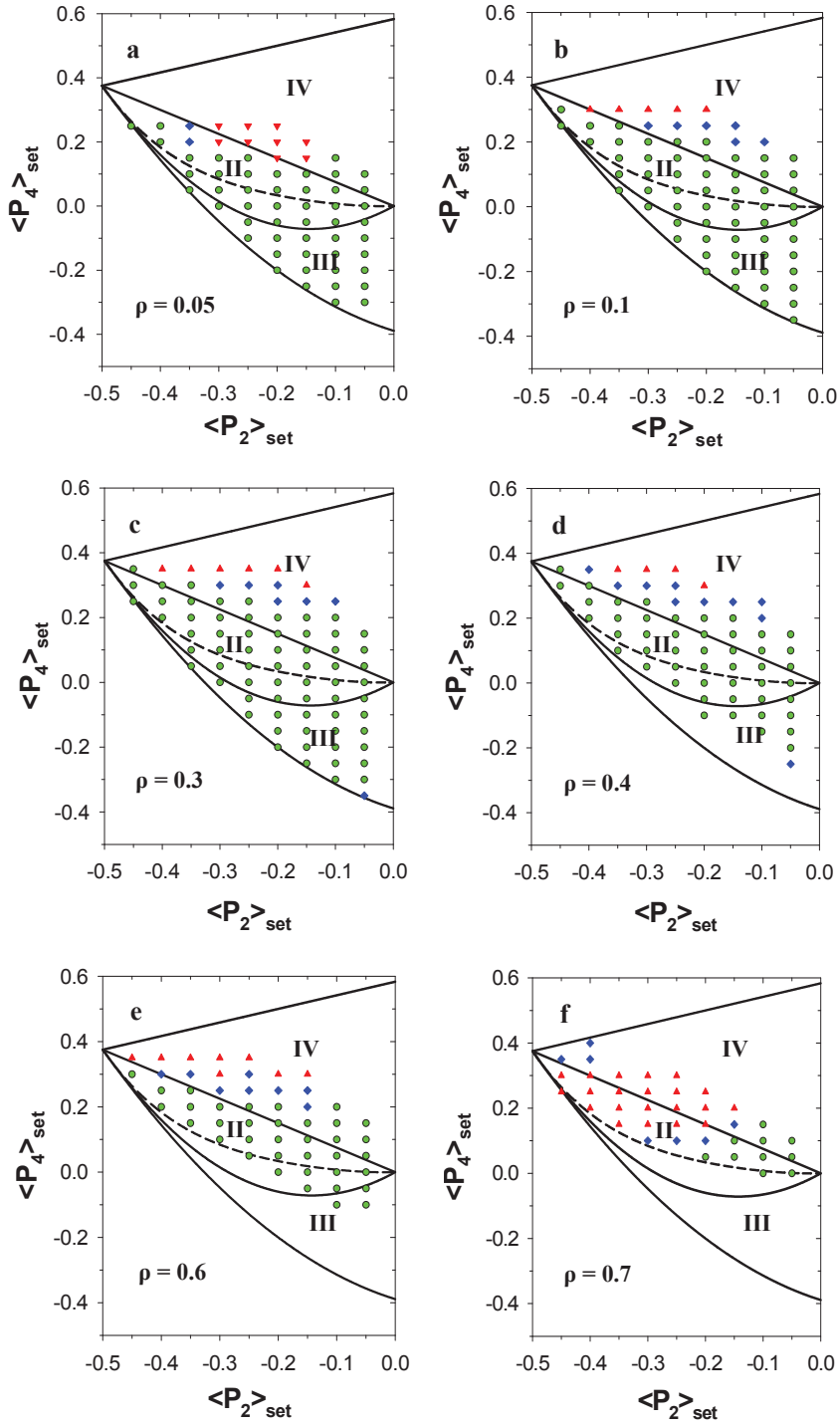

Figure 3.5. Correlation between the $\langle P_2 \rangle_{MPD}$ and $\langle P_2 \rangle_{set}$ values in the negative region of the $\langle P_2 \rangle \langle P_4 \rangle$ diagram. Panels a-f show results for depolarization ratios of 0.05, 0.1, 0.3, 0.4, 0.6 and 0.7, respectively. Red triangles, blue diamonds and green circles are associated with $\Delta\langle P_2 \rangle > 0.1$, $0.05 < \Delta\langle P_2 \rangle < 0.1$ and $\Delta\langle P_2 \rangle \leq 0.05$, respectively. The absence of symbols indicates that the MPD method did not converge to a solution or that it was eliminated based on the criteria described in the text.

Overall, the probability of obtaining under- or overestimated $\langle P_2 \rangle$ values using the MPD method is fairly small for bands with a Raman tensor aligned perpendicular to the long axis of the sample. The only problematic case is again when both the orientation and ρ_{set} reach very high values. In comparison, the DC method suffers from significant limitations, as was the case for the positive part of the $\langle P_2 \rangle \langle P_4 \rangle$ diagram, due to the experimental error on ρ. Following the strategy exposed in the previous section, ($\langle P_2 \rangle_{set}$, $\langle P_4 \rangle_{set}$) coordinates were first chosen directly on the most probable curve, with values of -0.20 and 0.05, respectively. The results of the DC simulations, presented in Figure 3.6, are in fact extremely similar to those shown in Figure 3.3. The emphasis will therefore be placed on the differences between the results obtained for parallel and perpendicular orientations. The $\langle P_2 \rangle_{DC}$ values vary smoothly with ρ when the calculation is based on an intermediate ρ_{set} of 0.4 (blue triangles of Figure 3.6a), but a plateau is not observed as in Figure 3.3a for the positive part of the diagram. Consequently, the impact of a small Δρ error on the calculated $\langle P_2 \rangle_{DC}$ is somewhat larger. Indeed, the same Δρ of 0.05 (ρ = 0.35) induces a change in $\langle P_2 \rangle_{DC}$ from -0.20 to -0.18, while the error was 0.01 in the positive region. The variation of $\langle P_4 \rangle_{DC}$ in Figure 3.6b is significant and is almost identical to that observed in Figure 3.3b. A small Δρ error of 0.05 induces a change of $\langle P_4 \rangle_{DC}$ from 0.05 to -0.06. In practice, these variations convert the resulting ODF from the black (most probable) curve of Figure 3.6c to the blue curve that represents an improbable unimodal ODF with a maximum at $\theta_3 \approx 62.5°$. The discrepancy is clearly more pronounced than for its positive analogue in Figure 3c. In a similar manner, the green squares of Figure 6a illustrate the variation of $\langle P_2 \rangle_{DC}$ with respect to ρ for a ρ_{set} of 0.7. The errors are similar to those discussed for ρ_{set} = 0.4, and also lead to a large discrepancy in the ODF (Figure 3.6c).

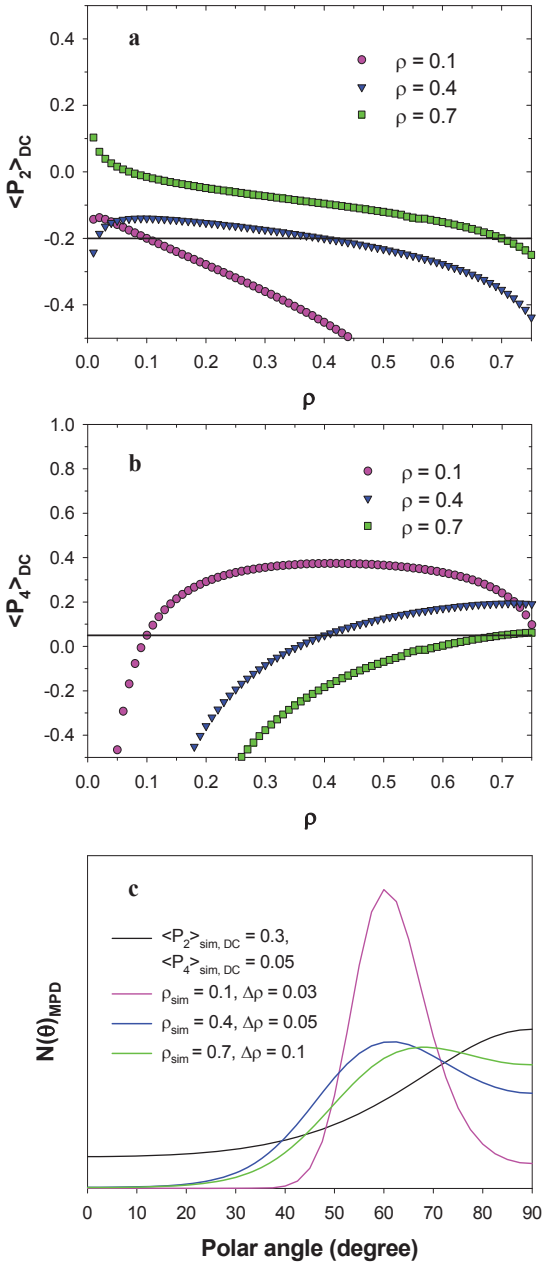

Figure 3.6. a) Variation of the $\langle P_2 \rangle_{DC}$ values calculated by the DC method induced by an incorrect ρ value. The plots were calculated for a ($\langle P_2 \rangle_{set}$, $\langle P_4 \rangle_{set}$) couple of (-0.2, 0.05) and with ρ_{set} values of 0.1 (pink circles), 0.4 (blue triangles) and 0.7 (green squares). The black line indicates the expected $\langle P_2 \rangle$ value. **b)** Variation of the $\langle P_4 \rangle_{DC}$ induced by an incorrect ρ value in the conditions described in a). **c)** ODF resulting from the ($\langle P_2 \rangle_{DC}$, $\langle P_4 \rangle_{DC}$) couples calculated for different Δρ for initial ρ_{set} of 0.1 (pink curve), 0.4 (blue curve) and 0.7 (green curve). The ($\langle P_2 \rangle_{DC}$, $\langle P_4 \rangle_{DC}$) values corresponding to these scenarios are given in the text. The black curve represents the true ODF associated with the ($\langle P_2 \rangle_{set}$, $\langle P_4 \rangle_{set}$) couple of (0.3, 0.05).

The main difference between the results of Figures 3.3 and 3.6 is the shape of the curves describing the variation of $\langle P_2 \rangle_{DC}$ with ρ when simulated with ρ_{set} = 0.1 (pink circles). It is less pronounced in the negative range as compared to the positive section of the $\langle P_2 \rangle \langle P_4 \rangle$ diagram. Consequently, when imposing the same Δρ of 0.03, the $\langle P_2 \rangle_{DC}$ increases less drastically to a value of -0.18 ($\Delta\langle P_2 \rangle$ = 0.02). Meanwhile, the $\langle P_4 \rangle_{DC}$ changes to -0.17 (($\Delta\langle P_2 \rangle$ = 0.22). The significant difference between the results of the DC method and the fixed ($\langle P_2 \rangle_{set}$, $\langle P_4 \rangle_{set}$) coordinates leads to the highly improbable narrow ODF with a maximum at θ_3 = 60° represented by the pink curve of Figure 3.6c.

When exploring other ($\langle P_2 \rangle_{set}$, $\langle P_4 \rangle_{set}$) coordinates situated on the most probable curve or near the extremities of regions III and IV (see the Figures 3.S5-S7 in Supporting information), the patterns observed are essentially the same as those observed for the positive sections of the diagram (Figures 3.S2 to 3.S4 in the Supporting Information), but with respect to the shape of the curves observed in Figure 3.6a and b. The results of these simulations for the negative section of the $\langle P_2 \rangle \langle P_4 \rangle$ diagram reinforce the conclusion that the population distribution cannot be described adequately by the DC method in most cases, mainly because of the large error on the $\langle P_4 \rangle$ value. The quantification of $\langle P_2 \rangle$ appears less problematic but, when considering the experimental error on ρ and its unpredictable evolution with orientation, the variations observed in Figure 3.6a can rapidly lead to inappropriate values. In this context, we believe that the MPD method provides a new and improved way of quantifying the level of orientation, both for parallel and perpendicular orientation of the Raman tensor with respect to the principal axis.

3.5. Conclusion

In this publication, we have proposed a new method for orientation quantification by Raman spectroscopy based on the assumption that the $\langle P_4 \rangle$ value is the most probable one associated with the $\langle P_2 \rangle$ value. We have demonstrated through numerical simulations the efficiency of this new method for quantifying the $\langle P_2 \rangle$ value of samples associated with a large range of $\langle P_4 \rangle$ values around the most probable one, both for parallel and perpendicular orientations. The main advantage of the new MPD method is that it does not require knowledge of the depolarization ratio of the band of interest, a parameter that was shown to

induce large errors when using the conventional DC method. In addition to being experimentally much more convenient, the elimination of this parameter in the quantification procedure enables the analysis of samples for which the depolarization ratio cannot be determined strictly or that evolves upon orientation in an unpredictable manner. This new method greatly simplifies orientation quantification using Raman spectroscopy and should also be applicable, for instance, to polarized fluorescence spectroscopy. The experimental demonstration of the validity and efficiency of the MPD method, in comparison with the conventional DC method, will be the subject of an upcoming manuscript.

3.6. Acknowledgments

This work was supported by a grant and graduate scholarships (MRL) from the Natural Sciences and Engineering Research Council of Canada (NSERC) and the Fonds de recherche du Québec - Nature et technologies (FRQNT).

3.7. References

1. Ward, I. M. *Structure and Properties of Oriented Polymers, 2nd Edition*; Chapman & Hall: London, 1997.
2. Richard-Lacroix, M.; Pellerin, C. *Macromolecules* **2012**, *45*, 1946-1953.
3. Rousseau, M. E.; Lefèvre, T.; Beaulieu, L.; Asakura, T.; Pézolet, M. *Biomacromolecules* **2004**, *5*, 2247-2257.
4. Lagugné-Labarthet, F.; Buffeteau, T.; Sourisseau, C. *J. Phys. Chem. B* **1998**, *102*, 5754-5765.
5. Masic, A.; Bertinetti, L.; Schuetz, R.; Galvis, L.; Timofeeva, N.; Dunlop, J. W.; Seto, J.; Hartmann, M. A.; Fratzl, P. *Biomacromolecules* **2011**, *12*, 3989-3996.
6. Frisk, S.; Ikeda, R. M.; Chase, D. B.; Rabolt, J. F. *Appl. Spectrosc.* **2004**, *58*, 279-286.
7. Pigeon, M.; Prud'homme, R. E.; Pézolet, M. *Macromolecules* **1991**, *24*, 5687-5694.
8. Lesko, C. C. C.; Rabolt, J. F.; Ikeda, R. M.; Chase, B.; Kennedy, A. *J. Mol. Struct.* **2000**, *521*, 127-136.
9. Citra, M. J.; Chase, D. B.; Ikeda, R. M.; Gardner, K. H. *Macromolecules* **1995**, *28*, 4007-4012.

10. Yang, S.; Michielsen, S. *Macromolecules* **2003**, *36*, 6484-6492.
11. Jasse, B.; Koenig, J. L. *J. Polym. Sci. A1* **1980**, *18*, 731-738.
12. Soto, A.; Iconomopoulou, S. M.; Manikas, A. C.; Voyiatzis, G. A. *Appl. Spectrosc.* **2005**, *59*, 1257-1269.
13. Pottel, H.; Herreman, W.; van der Meer, B. W.; Ameloot, M. *Chem. Phys.* **1986**, *102*, 37-44.
14. Lagugné-Labarthet, F.; Buffeteau, T.; Sourisseau, C. *Appl. Spectrosc.* **2000**, *54*, 699-705.
15. Nomura, S.; Asanuma, A.; Suehiro, S.; Kawai, H. *J. Polym. Sci. A-2: Polym. Phys.* **1971**, *9*, 1991-2007.
16. Nomura, S.; Kawai, H.; Kimura, I.; Kagiyama, M. *J. Polym. Sci. A-2: Polym. Phys.* **1970**, *8*, 383-400.
17. Lefèvre, T.; Pellerin, C.; Pézolet, M. In *Comprehensive Analytical Chemistry*; Chalmers, J. M., Meier, R. J., Eds.; Elsevier: 2008; Vol. 53, p 295-335.
18. Lagugné-Labarthet, F.; Buffeteau, T.; Sourisseau, C. *Appl. Spectros.* **2000**, *54*, 699-705.
19. Bower, D. I. *J. Polym. Sci. A-2: Polym. Phys.* **1981**, *19*, 93-107.
20. Park, M. S.; Wong, Y. S.; Park, J. O.; Venkatraman, S. S.; Srinivasarao, M. *Macromolecules* **2011**, *44*, 2120-2131.
21. Bower, D. I. *J. Polym. Sci. A-2: Polym. Phys.* **1972**, *10*, 2135-2153.
22. Turrell, G. *J. Raman Spectros.* **1984**, *15*, 103-108.
23. Tanaka, M.; Young, R. J. *J. Mater. Sci.* **2006**, *41*, 963-991.
24. Yang, S.; Michielsen, S. *Macromolecules* **2002**, *35*, 10108-10113.

,

3.8. Supporting information

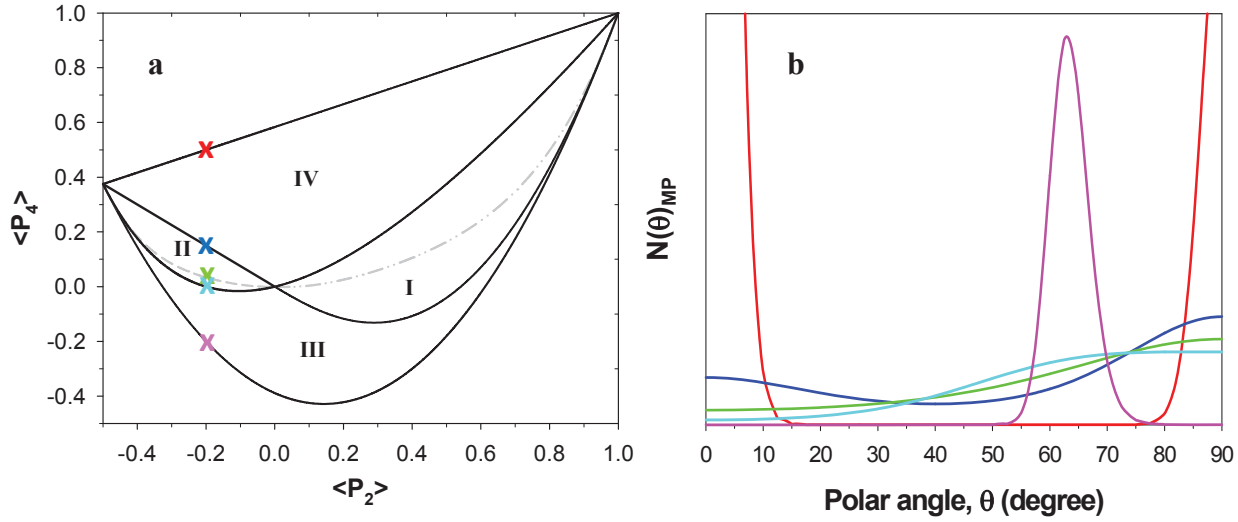

Figure 3.S1. a) $\langle P_2 \rangle \langle P_4 \rangle$ diagram defining four regions with distinct orientation distribution functions (ODF). The maximum and minimum $\langle P_4 \rangle$ curves were plotted according to Eq. 3.8 and represent narrow bimodal ODFs with maxima at 0 and 90°, and narrow unimodal ODFs with a maximum at θ_0 (Eq. 3.9), respectively. The curves delimiting sections I and II were plotted according to Park et al. (Macromolecules. 2011. 44(7): 2120-2131) and define the regions where the ODFs show a monotonic decrease or increase with θ, respectively. The dashed grey curves were plotted according to Eq. 3.11 and represent the most probable $\langle P_4 \rangle_{mp}$ associated with each $\langle P_2 \rangle$ value. **b)** ODFs associated with $\langle P_2 \rangle$ = -0.2 for different values of $\langle P_4 \rangle$ indicated by the X marks in panel a.

Figure 3.S2 a and b shows the variation of $\langle P_2 \rangle_{DC}$ and $\langle P_4 \rangle_{DC}$ for two additional ($\langle P_2 \rangle_{set}$, $\langle P_4 \rangle_{set}$) coordinates at (0.0, 0.0) and (0.6, 0.25). These were selected to cover lower (dark green squares) and higher (red triangles) degrees of orientation than the results already presented in Figure 3.3 of the main manuscript (repeated here as pink circles). The simulations were made by fixing ρ_{set} = 0.1, indicated by black lines, and then calculating the orientation parameters for various erroneous values of ρ. The shape of the curves is almost identical, but they are shifted to the appropriate $\langle P_2 \rangle_{set}$ or $\langle P_4 \rangle_{set}$ values (indicated by dashed lines of the corresponding color). The errors on the calculated ODF (not shown) are therefore similar to those presented in Figure 3.3c of the main manuscript. The same observations can be made by fixing ρ_{set} to 0.4 and 0.7 (see Figures 3.S3 and 3.S4, respectively).

We now consider briefly the case where the ($\langle P_2 \rangle_{set}$, $\langle P_4 \rangle_{set}$) couples are not located on the most probable curve. Figure 3.S2c and d shows the variation of $\langle P_2 \rangle_{DC}$ and $\langle P_4 \rangle_{DC}$ associated with incorrect ρ values for a constant $\langle P_2 \rangle_{set}$ of 0.3, but for $\langle P_4 \rangle_{set}$ values situated near the extremity of region IV (0.5, blue squares), in region I on the most probable curve (0.05, pink circles) and near the extremity of region III (-0.3, green diamonds). Again, the simulations were made by fixing ρ_{set} = 0.1. While a detailed description of these simulations is beyond the scope of this paper, it can be observed in Figure 3.S2c that the variation of $\langle P_2 \rangle_{DC}$ with ρ is significant and that its slope differs for these three coordinates. It becomes increasingly abrupt around ρ_{set} (indicated by the black line) for larger $\langle P_4 \rangle_{set}$ values. The opposite behavior is observed in Figure 3.S2d for $\langle P_4 \rangle_{DC}$: its variation is less abrupt around ρ_{set} for the higher $\langle P_4 \rangle_{set}$ values. Comparable behaviors, although less pronounced, are observed when fixing ρ_{set} to 0.4 and 0.7 (see Figures 3.S3 and 3.S4, respectively). Similar simulations were made for the negative part of the diagram (see Figure 3.S5 to 3.S7).

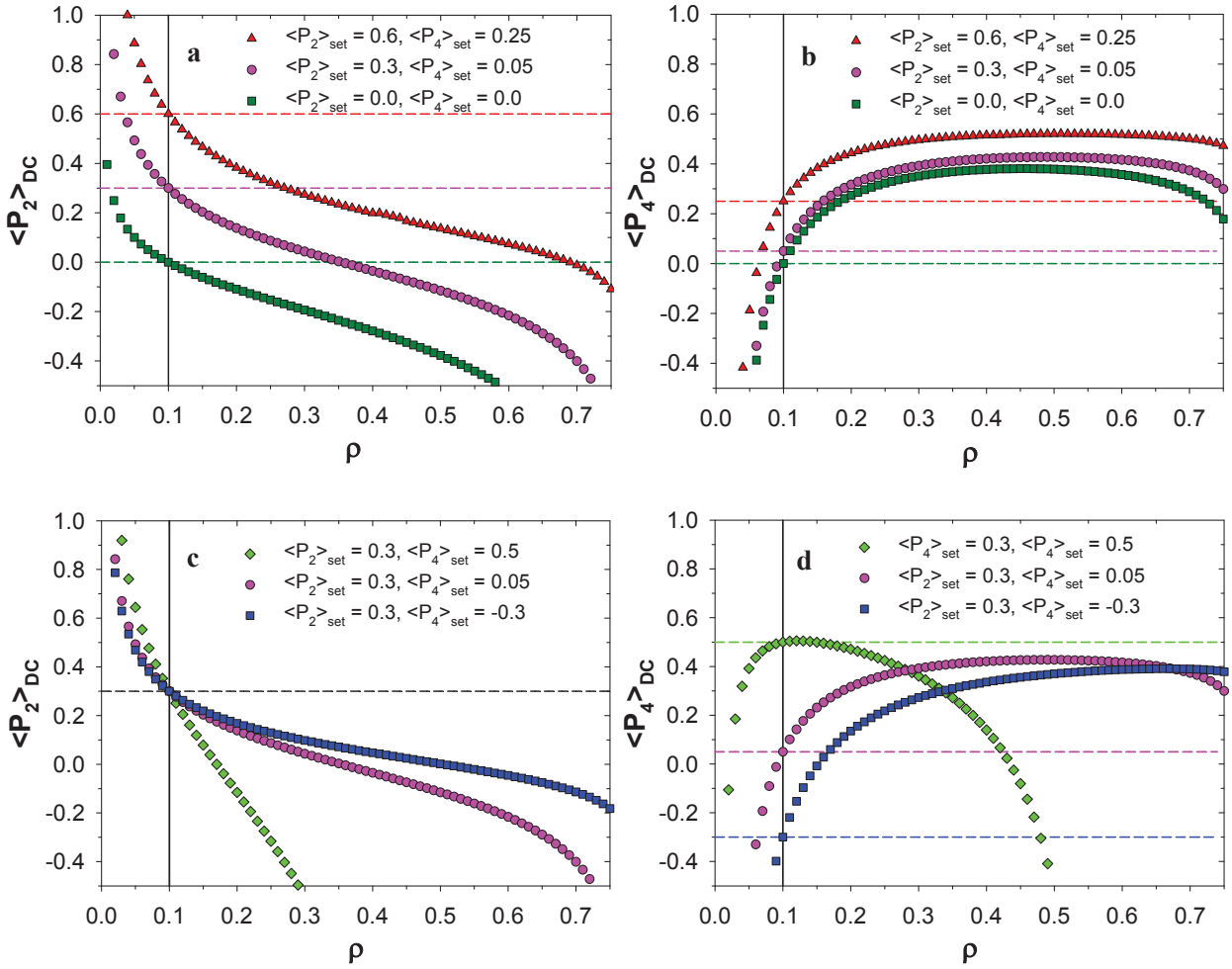

Figure 3.S2 a) Variation of the $\langle P_2 \rangle_{DC}$ values calculated by the DC method induced by an incorrect ρ value. The plots were calculated for fixed ($\langle P_2 \rangle_{set}$, $\langle P_4 \rangle_{set}$) couples of (0.0, 0.0) (dark green squares), (0.3, 0.05) (pink circles) and (0.6, 0.25) (red triangles) and with a ρ_{set} value of 0.1 (indicated by the black line). The dashed lines indicate the true $\langle P_2 \rangle_{set}$ value associated with each curve. **b)** Variation of the $\langle P_4 \rangle_{DC}$ in the conditions described in a). **c)** Variation of the $\langle P_2 \rangle_{DC}$ values calculated by the DC method induced by an incorrect ρ value as described in a) but for fixed ($\langle P_2 \rangle_{set}$, $\langle P_4 \rangle_{set}$) couples of (0.3, 0.5) (green diamonds), (0.3, 0.05) (pink circles) and (0.3, -0.3) (blue squares). **d)** Variation of the $\langle P_4 \rangle_{DC}$ values in the conditions described in c).

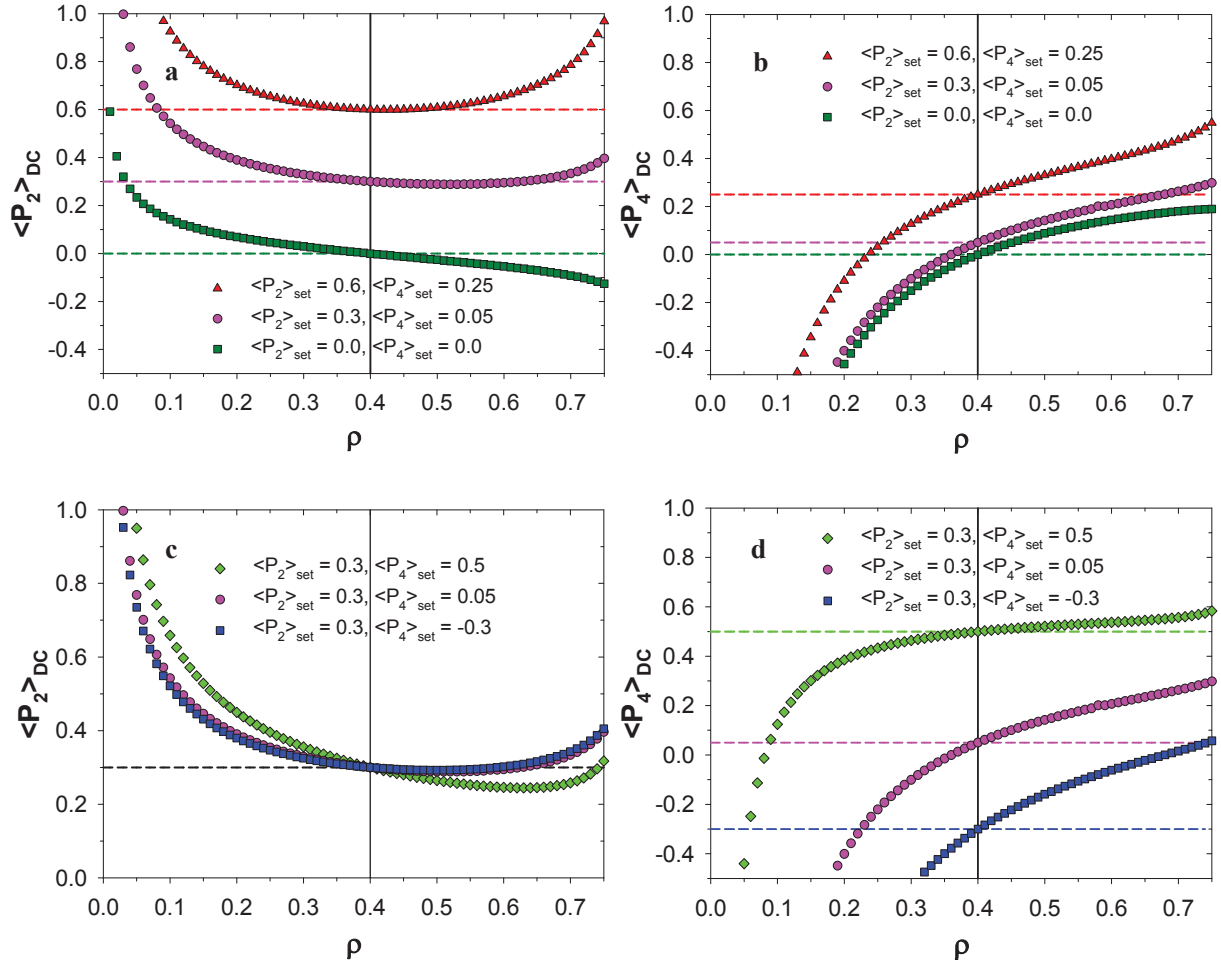

Figure 3.S3. a) Variation of the $\langle P_2 \rangle_{DC}$ values calculated by the DC method induced by an incorrect ρ value. The plots were calculated for ($\langle P_2 \rangle_{set}$, $\langle P_4 \rangle_{set}$) couples of (0.0, 0.0) (dark green squares), (0.3, 0.05) (pink circles) and (0.6, 0.25) (red triangles) and with a ρ_{set} value of 0.4 (indicated by the black line). The dashed lines indicate the true $\langle P_2 \rangle_{set}$ value associated with each curve. **b)** Variation of $\langle P_4 \rangle_{DC}$ in the conditions described in a). **c)** Variation of the $\langle P_2 \rangle_{DC}$ values calculated by the DC method induced by an incorrect ρ value. The plots were calculated for ($\langle P_2 \rangle_{set}$, $\langle P_4 \rangle_{set}$) couples of (0.3, 0.5) (green diamonds), (0.3, 0.05) (pink circles) and (0.3, -0.3) (blue squares) and with a ρ_{set} value of 0.4 (indicated by the black line). The dashed line indicates the true $\langle P_2 \rangle_{set}$ value associated with these curves. **d)** Variation of $\langle P_4 \rangle_{DC}$ in the conditions described in c).

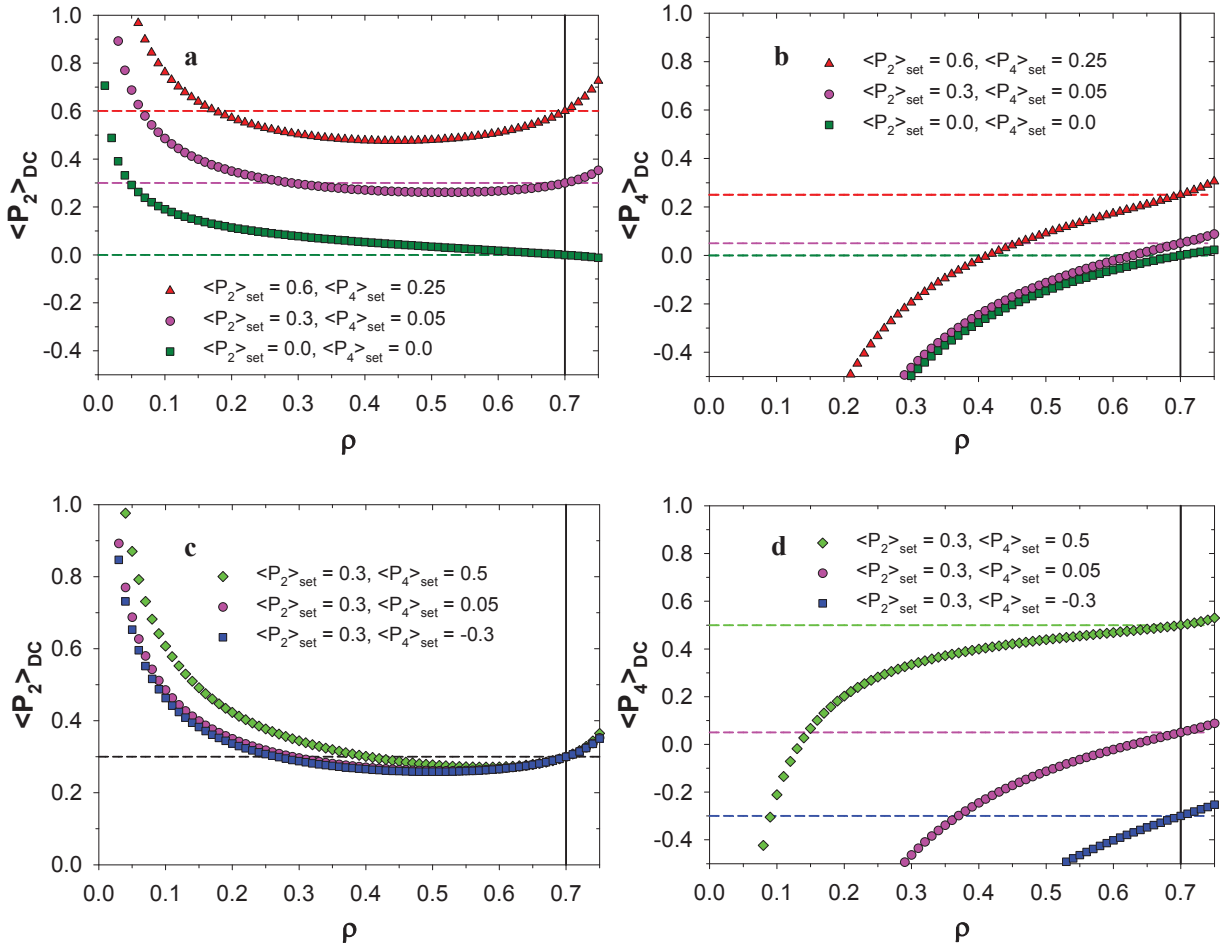

Figure 3.S4. a) Variation of the $\langle P_2 \rangle_{DC}$ values calculated by the DC method induced by an incorrect ρ value. The plots were calculated for ($\langle P_2 \rangle_{set}$, $\langle P_4 \rangle_{set}$) couples of (0.0, 0.0) (dark green squares), (0.3, 0.05) (pink circles) and (0.6, 0.25) (red triangles) and with a ρ_{set} value of 0.7 (indicated by the black line). The dashed lines indicate the true $\langle P_2 \rangle_{set}$ value associated with each curve. **b)** Variation of the $\langle P_4 \rangle_{DC}$ in the conditions described in a). **c)** Variation of the $\langle P_2 \rangle_{DC}$ values calculated by the DC method induced by an incorrect ρ value. The plots were calculated for ($\langle P_2 \rangle_{set}$, $\langle P_4 \rangle_{set}$) couples of (0.3, 0.5) (green diamonds), (0.3, 0.05) (pink circles) and (0.3, -0.3) (blue squares) and with a ρ_{set} value of 0.7 (indicated by the black line). The dashed line indicates the true $\langle P_2 \rangle_{set}$ value associated with these curves. **d)** Variation of the $\langle P_4 \rangle_{DC}$ in the conditions described in c).

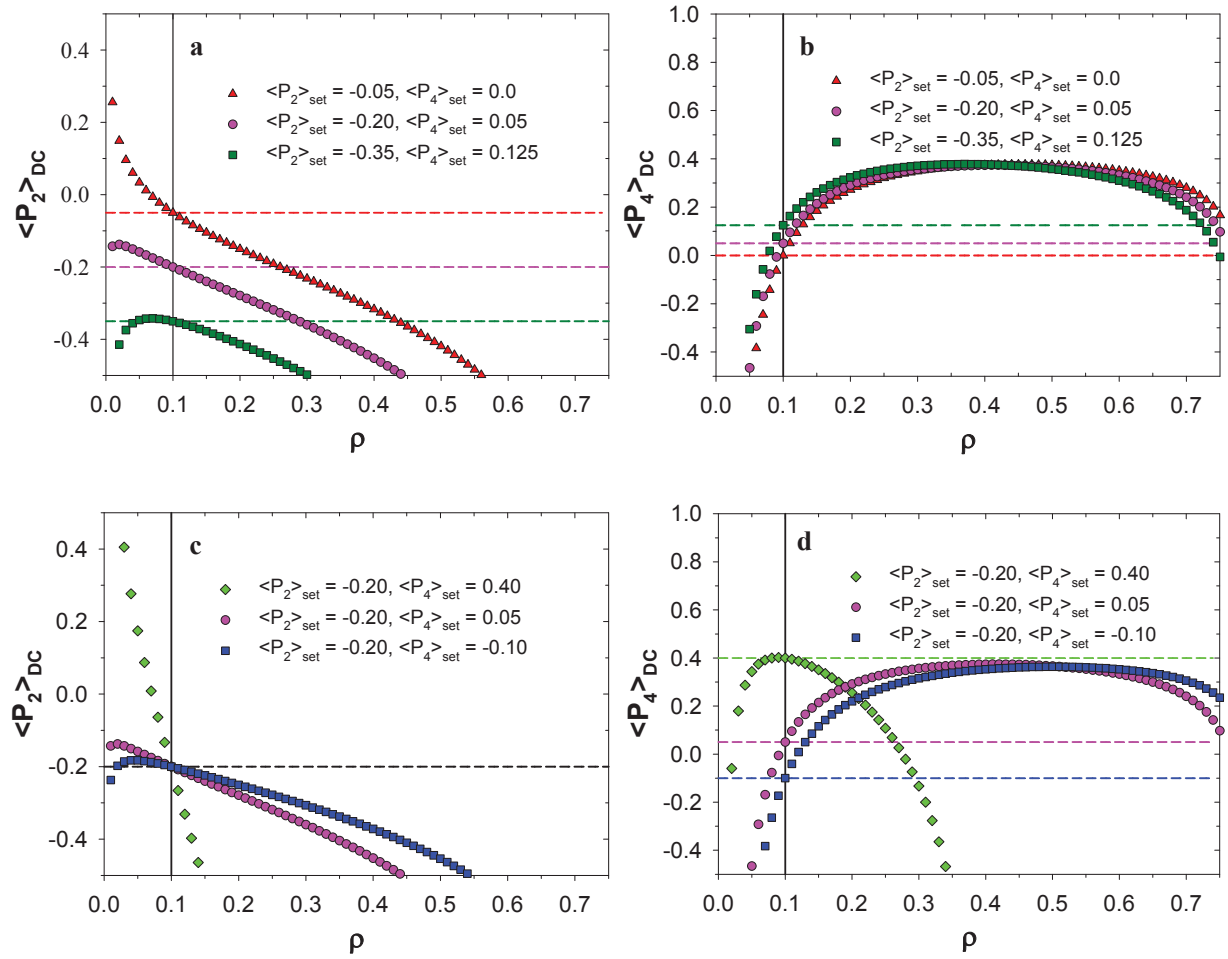

Figure 3.S5. a) Variation of the $\langle P_2 \rangle_{DC}$ values calculated by the DC method induced by an incorrect ρ value. The plots were calculated for ($\langle P_2 \rangle_{set}$, $\langle P_4 \rangle_{set}$) couples of (-0.35, 0.125) (dark green squares), (-0.20, 0.05) (pink circles) and (-0.05, 0.0) (red triangles) and with a ρ_{set} value of 0.1 (indicated by the black line). The dashed lines indicate the true $\langle P_2 \rangle_{set}$ values associated with each curve. **b)** Variation of the $\langle P_4 \rangle_{DC}$ in the conditions described in a). **c)** Variation of the $\langle P_2 \rangle_{DC}$ values calculated by the DC method induced by an incorrect ρ value as described in a) but for ($\langle P_2 \rangle_{set}$, $\langle P_4 \rangle_{set}$) couples of (-0.20, 0.4) (green diamonds), (-0.20, 0.05) (pink circles) and (-0.20, -0.1) (blue squares). **d)** Variation of the $\langle P_4 \rangle_{DC}$ values in the conditions described in c).

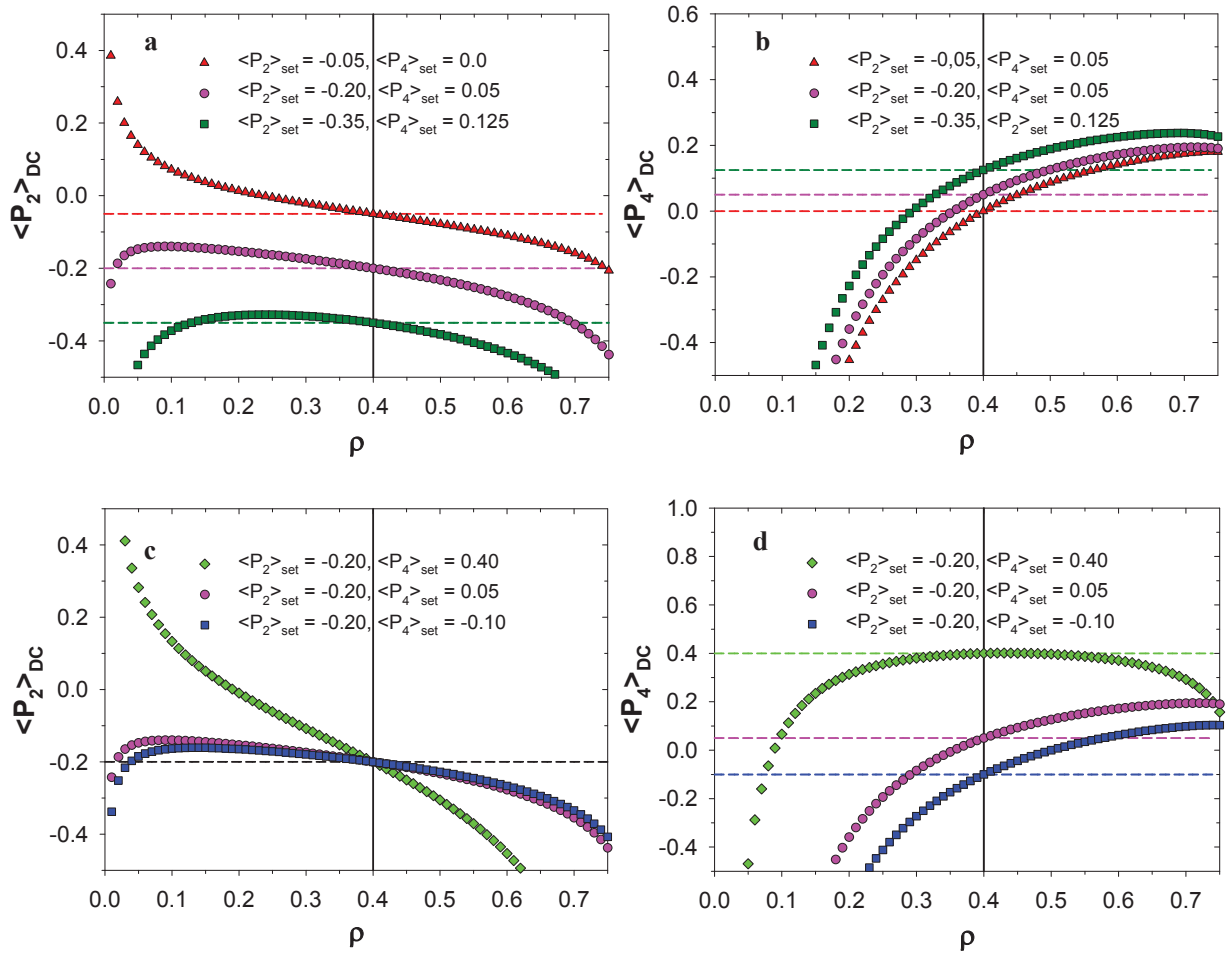

Figure 3.S6. a) Variation of the $\langle P_2 \rangle_{DC}$ values calculated by the DC method induced by an incorrect ρ value. The plots were calculated for ($\langle P_2 \rangle_{set}$, $\langle P_4 \rangle_{set}$) couples of (-0.35, 0.125) (dark green squares), (-0.20, 0.05) (pink circles) and (-0.05, 0.0) (red triangles) and with a ρ_{set} value of 0.4 (indicated by the black line). The dashed lines indicate the true $\langle P_2 \rangle_{set}$ values associated with each curve. **b)** Variation of the $\langle P_4 \rangle_{DC}$ in the conditions described in a). **c)** Variation of the $\langle P_2 \rangle_{DC}$ values calculated by the DC method induced by an incorrect ρ value as described in a) but for ($\langle P_2 \rangle_{set}$, $\langle P_4 \rangle_{set}$) couples of (-0.20, 0.4) (green diamonds), (-0.20, 0.05) (pink circles) and (-0.20, -0.1) (blue squares). **d)** Variation of the $\langle P_4 \rangle_{DC}$ values in the conditions described in c).

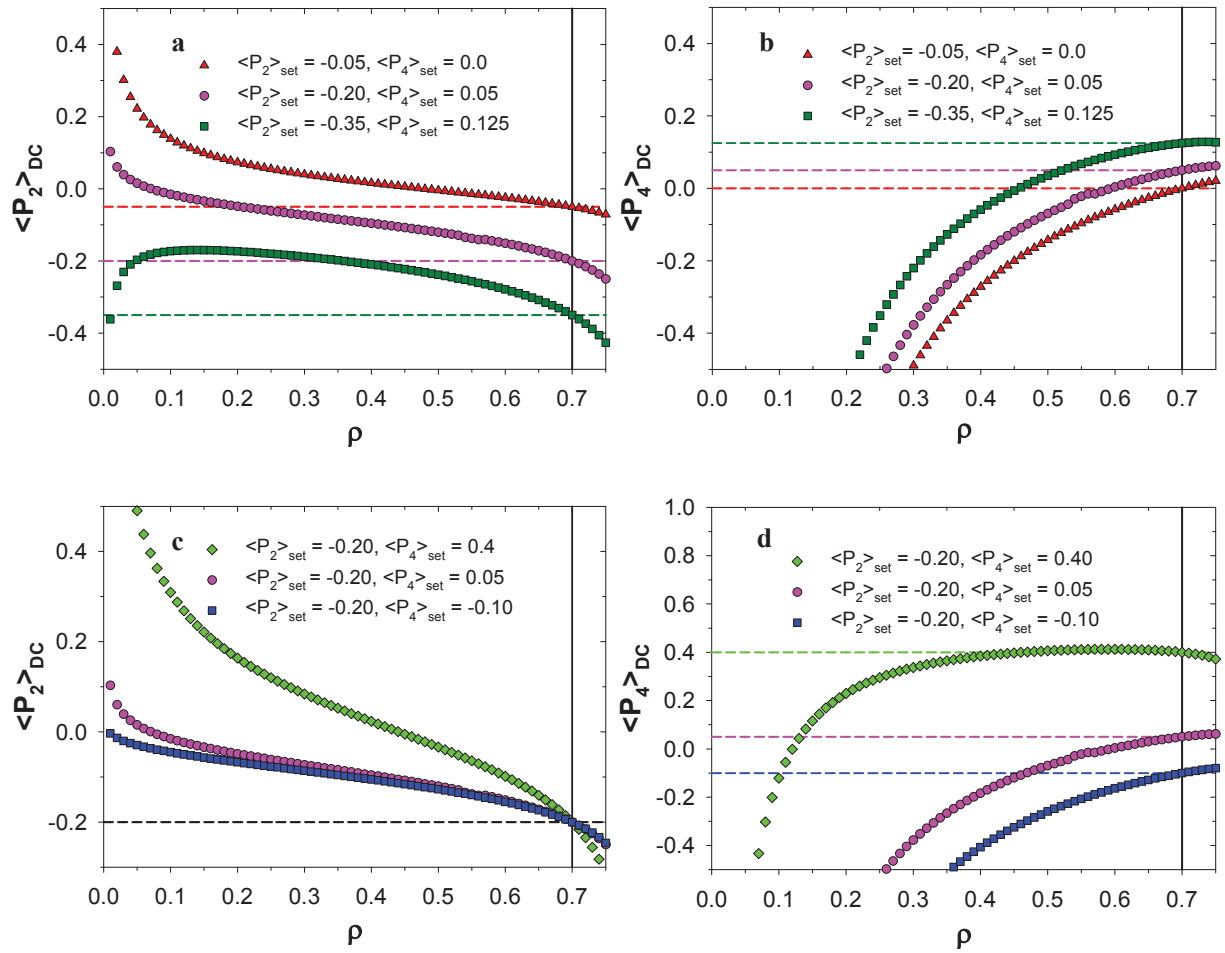

Figure 3.S7. a) Variation of the $\langle P_2 \rangle_{DC}$ values calculated by the DC method induced by an incorrect ρ value. The plots were calculated for ($\langle P_2 \rangle_{set}$, $\langle P_4 \rangle_{set}$) couples of (-0.35, 0.125) (dark green squares), (-0.20, 0.05) (pink circles) and (-0.05, 0.0) (red triangles) and with a ρ_{set} value of 0.7 (indicated by the black line). The dashed lines indicate the true $\langle P_2 \rangle_{set}$ values associated with each curve. **b)** Variation of the $\langle P_4 \rangle_{DC}$ in the conditions described in a). **c)** Variation of the $\langle P_2 \rangle_{DC}$ values calculated by the DC method induced by an incorrect ρ value as described in a) but for ($\langle P_2 \rangle_{set}$, $\langle P_4 \rangle_{set}$) couples of (-0.20, 0.4) (green diamonds), (-0.20, 0.05) (pink circles) and (-0.20, -0.1) (blue squares). **d)** Variation of the $\langle P_4 \rangle_{DC}$ values in the conditions described in c).

Discrimination procedure for the aberrant $\langle P_2 \rangle_{MPD}$ values in region IV of the $\langle P_2 \rangle \langle P_4 \rangle$ diagram

The dashed line of Figure 3.S8 shows the theoretical relation between "a" and ρ_{set} defined by Eq. 3.17. The MPD method rarely converges to this expected value of "a", except for ($\langle P_2 \rangle_{set}$, $\langle P_4 \rangle_{set}$) coordinates directly located on the most probable curve. This behavior is a direct consequence of the good agreement between the $\langle P_2 \rangle_{MPD}$ and $\langle P_2 \rangle_{set}$ values for large sections of the diagram even if the corresponding $\langle P_4 \rangle_{MPD}$ does not match $\langle P_4 \rangle_{set}$. Because of the interdependence of $\langle P_2 \rangle_{MPD}$ and $\langle P_4 \rangle_{MPD}$, the error is necessarily transferred to the only other variable, "a". Its value is consequently not directly usable to deduce information about the form of the Raman tensor. However, it was observed (not shown) that "a" follows a similar decreasing trend with decreasing $\langle P_4 \rangle_{set}$ for all fixed $\langle P_2 \rangle_{set}$. For each panel of Figure 3.2 of the main manuscript, there is a maximum value of "a" (a_{max}) below which the associated $\langle P_2 \rangle_{MPD}$ is acceptable ($\Delta\langle P_2 \rangle \leq 0.05$, green circles) and above which the solution is not acceptable. These a_{max} values are represented by black circles in Figure 3.S8 and can be fitted with a three parameters exponential decay with respect to ρ_{set}.

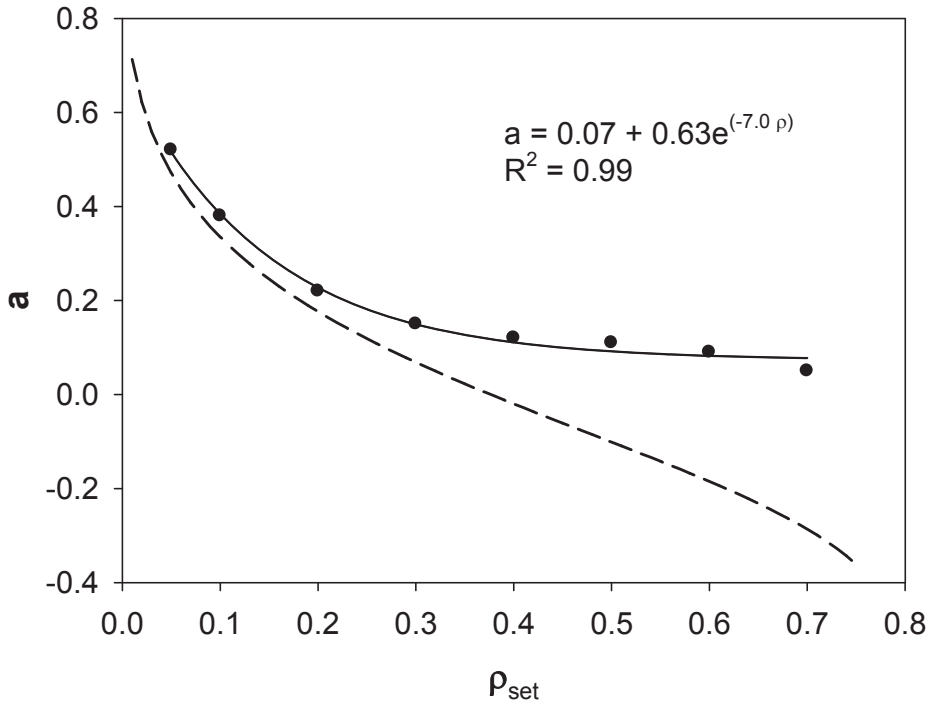

Figure 3.S8. Evolution of a with respect to ρ according to Eq. 17 (dashed curve). The black symbols represent the a_{max} values below which the results of the MPD method are reliable for a given depolarization ratio (see text). The plain curve represents a three parameters exponential fit of a_{max} with respect to ρ.

Therefore, if one possesses a rough estimation of ρ for the band of interest, it is possible discriminate a sample in region IV by comparing the calculated "a" with the a_{max} associated with the roughly approximated ρ. Since the a_{max} values plateau for ρ larger than 0.2, estimation of ρ using a slightly oriented sample or an isotropic sample that does not show the same structure should be sufficient to eliminate aberrant solutions. For example, one could experimentally determine that ρ, for a given band, is on the order of 0.3 to 0.5. If the "a" value generated by the MPD method for an oriented sample is below the a_{max} of ~0.17, it can be concluded with certainty that the associated $\langle P_2 \rangle_{MPD}$ is valid and has an error of less than 0.05 as compared to the one that would have been calculated by the DC method if ρ had been perfectly known. The large errors that can be generated by the DC method if ρ is not correctly estimated are discussed in the main manuscript. The opposite reasoning applies if the calculated "a" is larger than a_{max}. This would automatically mean that the real $(\langle P_2 \rangle, \langle P_4 \rangle)$ coordinates of this sample are in region IV, and that the MPD method is unusable for this

situation. The only exception to this rule is, again, for the case of high values of both ρ (≥ 0.7) and $\langle P_2 \rangle_{set}$, in which case finding an "a" value below the $a_{\max}$ still corresponds to $\Delta\langle P_2 \rangle \leq 0.05$ but for which the $\langle P_2 \rangle_{MPD}$ values located on the most probable curve are underestimated.

Chapitre 4. Accurate new method for molecular orientation quantification using polarized Raman spectroscopy

4.1. Abstract

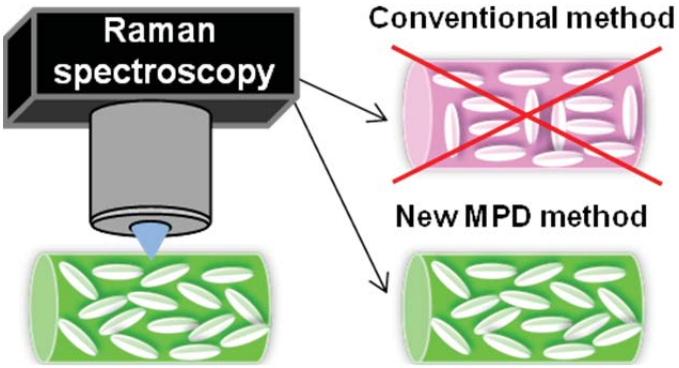

The physical properties of polymers are strongly affected by their molecular orientation. In this paper, we demonstrate for the first time a new and improved Raman spectroscopy method to characterize this key parameter. In recent years, Raman spectroscopy has emerged as an indispensable tool for this purpose, but its widespread use is still largely restricted by the experimental complexity and the limitations imposed by the standard quantification procedure, referred in this article as the depol constant (DC) method. We have very recently proposed and established theoretically a simplified quantification approach that is based on the most probable orientation distribution (MPD method). Herein, we demonstrate its experimental validity and its wide applicability by studying a series of samples from three highly dissimilar polymers (HDPE, PET and PS), and covering the full possible orientation range. We show that the new MPD method overcomes the experimental and theoretical difficulties faced with the current DC method and that it leads to more accurate orientation values. We expect that this method will greatly extend the accessibility of Raman spectroscopy for molecular orientation studies of polymer systems.[3]

---

[3] Publié comme article complet dans *Macromolecules,* **2013**, 46, *14*, 5561-5569 par Marie Richard-Lacroix et Christian Pellerin

4.2. Introduction

Molecular orientation has a significant impact on numerous physical properties of materials and is thus a critical parameter for their characterization. It is well established that it strongly enhances, for example, mechanical properties,[1, 2] hole and electron conductivity[3] and thermal conductivity.[4] Consequently, major research efforts are invested to better control and/or to achieve higher levels of molecular ordering with the objective of optimizing the materials properties and practical applicability, for instance, in optoelectronic and photonic devices.

X-ray diffraction (XRD), selected area electron diffraction (SAED), infrared (IR) spectroscopy and Raman spectroscopy are the most widely used methods for molecular orientation studies. Diffraction techniques give access directly to the orientation distribution function, but they are limited to the study of highly crystalline polymers or small molecules. In contrast, IR and Raman spectroscopies enable probing the order in amorphous, crystalline and mesomorphous phases and provide molecular level specificity. They are therefore also widely applicable to polymer blends, copolymers and composites.

Unfortunately, all these techniques are restrictive with regards to the shape, morphology or thickness of the materials under study. Unless a synchrotron radiation is used, XRD typically requires a sample thickness of at least tens of microns and its spatial resolution is limited to several microns. In contrast, SAED provides nm scale resolution but it necessitates very thin samples, on the order of 50 to 150 nm, that can require thorough preparation. It is also subject to artifacts and quantification limitations due to the sensitivity of most organic materials to electron beam damage.[5] When using IR spectroscopy, the sample thickness is dictated by the absorbance of the bands of interest and can be limited to a few microns. This restriction is aggravated with an increasing the level of orientation.

Accordingly, two strategies are generally employed: 1) using the most appropriate technique that is applicable considering the sample limitations, or 2) modifying the sample in order to meet the requirements of one or more of these techniques to get a better description of its properties. The development of techniques that enable straightforward and accurate quantitative studies of molecular orientation with an appropriate spatial resolution for the

material under study and with minimum (and ideally no) sample preparation is therefore of critical interest in materials science.

In recent years, polarized Raman spectroscopy and, in particular, confocal Raman spectromicroscopy, has become an increasingly popular technique for orientation quantification. It offers the same molecular specificity as IR spectroscopy but it is essentially unaffected by sample thickness. In addition, its submicron resolution is better adapted to a wide variety of material sizes and specific shapes. It has been used first by Lagugné-Labarthet *et al*.[6] to map the orientation in holographic grating, and later shown to be particularly efficient for studying, for instance, thin films of conjugated polymers coated on surfaces[7, 8], silk fibers[9, 10], polymer composites[11] and even individual electrospun nanofibers.[12]

Qualitative orientation information is easily obtained by comparing the intensity of the two parallel-polarized Raman spectra. However, strict quantification of the order parameters, $\langle P_2 \rangle$ and $\langle P_4 \rangle$, is necessary to compare the orientation of different samples, of the components in a complex material, or of different polymer systems. This quantification, to date, remains a challenging task. Indeed, the so-called "complete method", developed in the 1970's by Bower[13], is characterized by its remarkable experimental complexity and is inapplicable for Raman spectromicroscopy.[14] This method has only been applied to a few common polymers for which the Raman spectrum is well understood.[15-20] Apart from these exceptions, the method actually used for orientation quantification is the $a_1 = a_2$ method described by Frisk *et al*.[16] (and referred here as the *depol constant*, DC, method). The DC method requires knowledge of the form of the Raman tensor of the band of interest to extract any quantitative information. This is achieved through the experimental determination of the depolarization ratio of a completely isotropic sample. This is often difficult, if not impossible, to achieve because it implies preparing an isotropic sample (at the submicron level if using spectromicroscopy) that possesses precisely the same chemical and phase composition as the oriented sample. Moreover, we have recently demonstrated by simulation that the DC method often does not adequately describe the level of orientation.[21] In fact, depending on the specific vibrational mode analyzed, very small errors or changes of the depolarization ratio upon orientation can lead to large errors on both $\langle P_2 \rangle$ and $\langle P_4 \rangle$ orientation parameters. These issues greatly limit our capability to characterize a wide variety of materials by Raman spectroscopy.

In this context, we have recently proposed a new method for orientation quantification by Raman spectroscopy, called the *most probable distribution* (MPD) method, that is based on the most probable orientation distribution function.[21] This new method eliminates the restrictive requirement of measuring the depolarization ratio and enables quantifying the level of orientation by recording only four polarized spectra on the oriented sample of interest. In this paper, its practical applicability is demonstrated for the first time by measuring experimental polarized Raman spectra of drawn films of high density polyethylene (HDPE), poly(ethylene terephthalate) (PET), and polystyrene (PS). The $\langle P_2 \rangle$ values obtained from the DC and MPD methods are contrasted with published values using the *complete method* or measured by polarized IR spectroscopy. Our results reveal the great effectiveness of the MPD method for this broad range of samples, even when the DC method results diverge from the expected orientation values.

4.3. Theoretical section

The orientation in a system showing uniaxial symmetry can be described by its orientation distribution function, N(θ), which is an infinite expansion of even Legendre polynomials, $P_l(cos\theta)$.[14]

$$N(\theta) = \sum_{l}^{even} \left(l + \frac{1}{2}\right) \langle P_l \rangle \, P_l(cos\theta) \qquad (4.1)$$

The $\langle P_l \rangle$ coefficients are the averaged value of the l^{th} Legendre polynomials over the distribution and are generally called order parameters.[2] These coefficients are measured experimentally. The first one, $\langle P_0 \rangle$, is 1 by definition. Since Raman spectroscopy is a two photon process, polarized measurements additionally give access to the second and fourth coefficients: [14]

$$\langle P_2 \rangle = \frac{\langle 3cos^2\theta - 1 \rangle}{2} \qquad (4.2a)$$

$$\langle P_4 \rangle = \frac{\langle 35cos^4\theta - 30cos^2\theta + 3 \rangle}{8} \qquad (4.2b)$$

By substitution, the orientation distribution function (ODF) becomes:[9]

$$N(\theta) = \frac{1}{2}\left[1 + \frac{5}{2}\langle P_2 \rangle (3cos^2\theta - 1) + \frac{9}{8}\langle P_4 \rangle (35cos^4\theta - 30cos^2\theta + 3) + \cdots\right] \qquad (4.3)$$

The $\langle P_2 \rangle$ value gives an indication about the level of orientation. Its limiting values are 1 and -0.5 for a perfect alignment of the units along the main axis (Z) and perpendicular to it (X), respectively.[2] The $\langle P_4 \rangle$ coefficient helps to discriminate between different possible ODFs associated to a given $\langle P_2 \rangle$ value. It has limiting values that depend on the specific $\langle P_2 \rangle$, such that:[22, 23]

$$\langle P_4 \rangle_{min} = \frac{1}{18}(35\langle P_2 \rangle^2 - 10\langle P_2 \rangle - 7) \leq \langle P_4 \rangle \leq \frac{1}{12}(5\langle P_2 \rangle + 7) = \langle P_4 \rangle_{max} \qquad (4.4)$$

In Raman spectroscopy, the signal intensity depends on the changes in magnitude (or orientation) of the polarizability ellipsoid associated with a vibration. This can be described by a second rank Raman tensor that can be diagonalized with respect to a chosen reference molecular axis.

$$\alpha = \begin{pmatrix} \alpha_1 & & \\ & \alpha_2 & \\ & & \alpha_3 \end{pmatrix} = \alpha_3 \begin{pmatrix} a_1 & & \\ & a_2 & \\ & & 1 \end{pmatrix} \qquad (4.5)$$

The experimental polarized Raman intensities (I_{ij}, with i and j associated to the incident and scattered polarizations, respectively) are related to quadratic functions of the α_{ij} element of the tensor expressed in the laboratory frame and averaged over the orientation distribution. Bower[13] has developed the theory for Raman orientation quantification (*complete method*). He has shown that, for uniaxial samples, there are 5 independent and non-zero equations of the $\langle (\alpha_{ij})^2 \rangle$ elements of the tensor related to 5 different polarized Raman intensities that must be recorded in three different experimental geometries. These equations are expressed as linear functions of the orientation parameters ($\langle P_2 \rangle$ and $\langle P_4 \rangle$) and of the elements of the Raman tensor (Eq. 4.5).

4.3.1. Depol constant (DC) method

Raman spectromicroscopy is limited to the backscattering geometry and, therefore, to two parallel-polarized (ZZ and XX) and two crossed-polarized (ZX and XZ) spectra. Approximations thus have to be made to reduce the number of unknowns. The standard DC method is based on the approximation that the Raman tensor has a cylindrical symmetry (a_1 =

$a_2 = a$) and a constant form upon orientation.[16] The equations of the complete method can therefore be simplified to 4 $\langle(\alpha_{ij})^2\rangle$ expressions (only 3 are independent) associated to the 4 polarized Raman spectra from the backscattering geometry.[14] The system of equations is solved by doing ratios of the experimental intensities to eliminate common constants, leading to three unknowns, namely a, $\langle P_2\rangle$ and $\langle P_4\rangle$.[9, 14]

$$R_1 = \frac{I_{ZX}}{I_{ZZ}} = \frac{A\langle(\alpha_{ZX})^2\rangle + B\langle(\alpha_{ZY})^2\rangle}{A\langle(\alpha_{ZZ})^2\rangle + B\langle(\alpha_{ZY})^2\rangle} \quad (4.6a)$$

$$R_2 = \frac{I_{XZ}}{I_{XX}} = \frac{A\langle(\alpha_{XZ})^2\rangle + B\langle(\alpha_{XY})^2\rangle}{A\langle(\alpha_{XX})^2\rangle + B\langle(\alpha_{XY})^2\rangle} \quad (4.6b)$$

A and B are optical constants that correct for the relative importance of the in-plane and out-of-plane contributions to the signal and can be easily quantified with knowledge of the numerical aperture of the objective or probe.[24] The a parameter, describing the form of the Raman tensor, must be quantified in a separate experiment by determining the depolarization ratio (ρ) of a perfectly isotropic sample, i.e., a sample for which the $\langle P_2\rangle$ and $\langle P_4\rangle$ values are zero.[9, 14]

$$\rho = R_1 = R_2 = \frac{I_{ZX}}{I_{ZZ}} = \frac{I_{XZ}}{I_{XX}} = \frac{(A+B)(1-a)^2}{A\,(8a^2+4a+3)+B\,(1-a)^2} \quad (4.7)$$

As indicated in the Introduction, resorting to Eq. 4.7 to solve the system of equations often implies serious experimental and theoretical complications because of the unavailability of an isotropic sample and/or because of the evolution of the a parameter upon orientation.

4.3.2. Most probable distribution (MPD) method

The new MPD method is based on the most probable ODF associated to the quantified $\langle P_2\rangle$ value. We first introduce the concept behind this approach by exploring the different possible orientation distributions. Figure 4.1 shows the $\langle P_2\rangle\langle P_4\rangle$ diagram covering all possible combinations of $\langle P_2\rangle$ and $\langle P_4\rangle$ respecting the limits of Eq. 4.4. Knowing $\langle P_2\rangle$ and $\langle P_4\rangle$, one can estimate the most probable ODF associated to each point of this diagram, $N(\theta)_{mp}$, by maximizing the information entropy of the distribution.[22] For any specific $\langle P_2\rangle$ value, there is a single most probable $\langle P_4\rangle$ value ($\langle P_4\rangle_{mp}$), defined by Bower as the one for which the entropy of the distribution is maximized.[22] They are described by the following analytical solutions for

the positive and negative $\langle P_2 \rangle$ values, respectively, and are represented in Figure 4.1 by dashed grey lines.[25]

$$\langle P_4 \rangle_{mp} = -0.083\langle P_2 \rangle + 1.366\langle P_2 \rangle^2 - 1.899\langle P_2 \rangle^3 + 1.616\langle P_2 \rangle^4 \quad (4.8a)$$

$$\langle P_4 \rangle_{mp} = 0.052\langle P_2 \rangle + 1.574\langle P_2 \rangle^2 + 3.968\langle P_2 \rangle^3 + 8.058\langle P_2 \rangle^4 \quad (4.8b)$$

The shape of the ODF greatly varies depending on the specific $\langle P_2 \rangle$, $\langle P_4 \rangle$ couples. The diagram shown in Figure 4.1 can be decomposed into 4 distinct regions. Let us first imagine a fiber for which the $\langle P_2 \rangle$ value is 0. The most probable situation is a completely random distribution of the units, associated to $\langle P_4 \rangle_{mp}$= 0, as schematized by the blue fiber on the left side of Figure 4.1. Keeping the $\langle P_2 \rangle$ value constant at 0, the $\langle P_4 \rangle$ parameter could also theoretically take its minimum value of -0.38, as defined by Eq. 4.4. This $\langle P_2 \rangle$,$\langle P_4 \rangle$ couple would be associated to a narrow unimodal distribution of the units at an angle θ of 55° with respect to the fiber axis. This improbable ODF is illustrated by the orange fiber on the left side of Figure 4.1. At the other extreme, still keeping $\langle P_2 \rangle$ = 0, the maximum $\langle P_4 \rangle$ value is 0.58 (burgundy fiber) and the resulting ODF is a very narrow bimodal distribution of the units at θ angles of 0 and 90°. These two latter ODFs are entropically unfavorable and experimentally seldom observed, unless the samples has been submitted to a very special treatment.[22]

Similarly, if the fiber is stretched to a high draw ratio, inducing a $\langle P_2 \rangle$ value of 0.6, three extreme situations can be theoretically encountered. The most probable case ($\langle P_4 \rangle_{mp}$ = 0.23) is schematized by the light blue fiber on the right side of Figure 4.1, where the units are smoothly distributed with respect to the main axis (θ = 0). This type of Gaussian distribution is encountered for any $\langle P_2 \rangle$,$\langle P_4 \rangle$ couples situated on the most probable curves. More generally, any $\langle P_2 \rangle$,$\langle P_4 \rangle$ couples located in regions I and II are also associated to unimodal distributions centered at θ = 0° or 90° for the positive and negative $\langle P_2 \rangle$ ranges, respectively. The two other, much less probable, ODFs associated with $\langle P_2 \rangle$ = 0.6 are represented by the light orange and light burgundy fibers on the right side of Figure 4.1. They are associated to $\langle P_4 \rangle_{min}$ (narrow unimodal distribution at θ = 32.5°) and $\langle P_4 \rangle_{max}$ (narrow bimodal distribution), respectively. These two types of distributions are found in regions III and IV of the diagram, respectively.

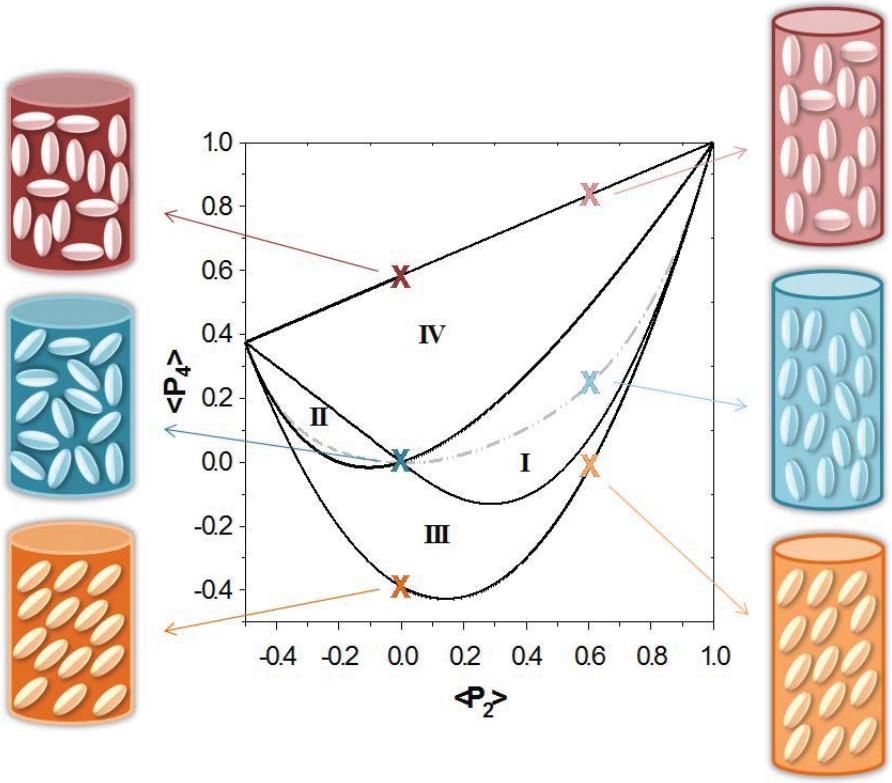

Figure 4.1. $\langle P_2 \rangle \langle P_4 \rangle$ diagram and a schematic representation of different possible ODFs associated with $\langle P_2 \rangle = 0$ (left side of the diagram) and with $\langle P_2 \rangle = 0.6$ (right side). The MPD method assumes that the samples possess the most entropically probable ODF, as represented by the blue fibers.

The new MPD method is similar to the DC method with the significant distinction that it eliminates the problematic use of Eq. 4.7 to quantify the *a* parameter. It is rather replaced by the appropriate Eq. 4.8 (4.8a and 4.8b for positive and negative orientations, respectively) that describes the most probable $\langle P_4 \rangle$ value. Consequently, $\langle P_2 \rangle$ can be quantified using a single set of four polarized spectra, recorded in the backscattering geometry on the oriented sample of interest, by solving Eqs. 4.6 and 4.8 simultaneously. It is experimentally much more convenient since it does not require the preparation of an isotropic sample to determine the depolarization ratio. However, this experimental simplicity implies the loss of the $\langle P_4 \rangle$ value since it is implicitly the most probable one. Our simulations have demonstrated that this sacrifice is negligible since the errors associated with the DC method often make the $\langle P_4 \rangle$ value meaningless.[21] The MPD calculations lead to multiple solutions because of the interdependence of the $\langle P_2 \rangle$ and $\langle P_4 \rangle$ parameters, but criteria for selecting the appropriate solution have been clearly established elsewhere.[21]

4.4. Experimental section

Sample preparation

Atactic PS of 210 000 g/mol (Scientific Polymer Products) was used as received to prepare thin films by solvent casting of a 5% m/v solution in chloroform (Fisher Scientific). Oriented films with different levels of orientation were produced by uniaxial stretching at different draw ratios and drawing rates at temperatures ranging from 110 to 120 °C. They were quickly quenched by blowing the boil off from liquid nitrogen to prevent the relaxation of orientation. The films were further cut into small pieces to take advantage of the non-uniformity of the orientation along the film and to facilitate the comparison of the Raman and IR measurements.

PET films were prepared from flakes with an inherent viscosity of 0.58 (Scientific Polymer Products) by compression molding at 280 °C for 3 min in a Carver Laboratory Press. They were then quenched in iced water to yield amorphous samples. Isotropic HDPE films were generously provided by Prof. A. Ajji from École Polytechnique de Montréal. PET and HDPE films showing different levels of orientation were prepared as described for PS but at 90 and 130 °C, respectively. Additional highly orientated HDPE samples were generously provided by Prof. M. Pézolet from Université Laval.

Raman characterization

Spectra were recorded in the backscattering geometry with a LabRam HR800 spectrometer (Horiba Jobin Yvon) coupled with an Olympus BX41 microscope. The confocal hole and the slit width were fixed at 300 and 350 μm, respectively. A 632.8 nm He-Ne laser was focused on the sample with a 100X long working distance objective (0.8 NA) or with a 10X objective (0.25 NA). A half-wave plate and a polarizer were used to set the polarization of the incident laser beam and to select the X or Z component of the scattered beam, respectively. A scrambler was placed before the 600 groove/mm holographic grating in order to minimize the polarization-dependent response of the spectrograph.

The films were placed with the drawing direction along the Z axis and polarized spectra were recorded in the order: ZZ, ZX, XX, XZ, ZZ(2). The fifth spectrum was recorded to detect any modification in the focus quality and/or deterioration of the system during acquisition.

The depolarization ratios were determined from polarized measurements on isotropic PET, PS and HDPE films. These were only used for calculations based on the standard DC method. Correction factors were applied to all spectra to compensate for the residual polarization dependence of the spectrometer as described previously.[12]

IR Characterization

Polarized IR spectra were recorded in transmission with a 4 cm^{-1} resolution using a Tensor 27 FT-IR spectrometer (Bruker Optics) equipped with a liquid nitrogen-cooled HgCdTe detector. A KRS-5 holographic polarizer (Optometrics) was used to record spectra polarized parallel (p) and perpendicular (s) to the stretching direction. The $\langle P_2 \rangle$ value was determined from the polarized IR absorbance of selected bands as

$$\langle P_2 \rangle_{IR} = \frac{2}{3cos^2\alpha - 1} \frac{A_p - A_s}{A_p + 2A_s} \quad (9)$$

where α is the angle between the polymer chain and the transition dipole moment of the vibration.

4.5. Results and discussion

The objective of the new MPD method is to overcome the experimental and theoretical difficulties faced when using the standard DC method. We have recently demonstrated by numerical simulations that the MPD method should lead to accurate orientation results. In fact, it is expected to be particularly efficient for samples situated in the critical regions (I and II) of the $\langle P_2 \rangle \langle P_4 \rangle$ diagram shown in Figure 4.1, i.e. the region where the real samples are most likely situated. HDPE, PET and PS were selected as proof-of-concept examples because they are among the few polymers that have been deeply studied using the *complete method*. Since it is not based on any approximation other than uniaxial symmetry,[22] the concordance of the $\langle P_2 \rangle_{MPD}$ and $\langle P_2 \rangle_{DC}$ results should give an unambiguous indication of the accuracy of both procedures.

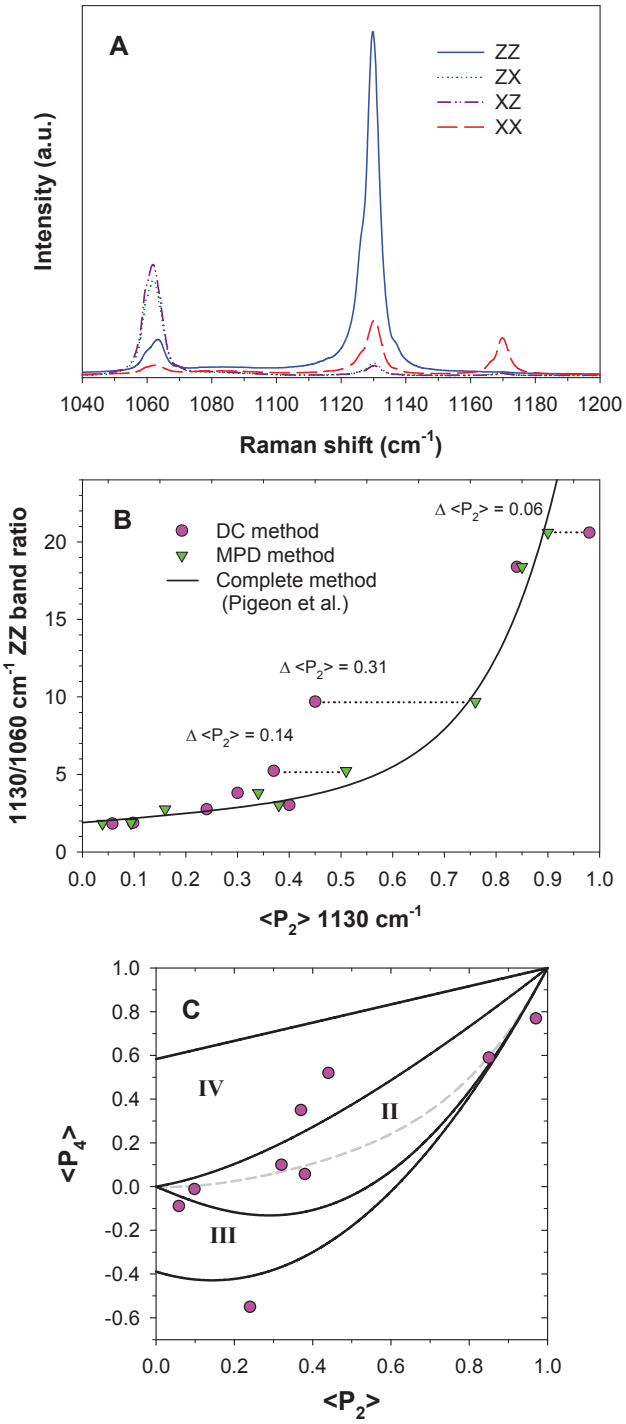

Figure 4.2. A) Polarized Raman spectra of an oriented HDPE sample. **B)** Orientation of HDPE samples quantified with the MPD (green triangles) and DC (pink circles) methods compared to the calibration curve reproduced from Pigeon *et al.* [15] (black curve) using the *complete method*. **C)** Localization in the $\langle P_2 \rangle \langle P_4 \rangle$ diagram of the $\langle P_2 \rangle, \langle P_4 \rangle$ couples quantified using the DC method.

HDPE is first used as a representative example of a highly crystalline polymer. Figure 4.2A shows the four polarized Raman spectra acquired on a HDPE film with a high level of orientation. HDPE crystallizes in an orthorhombic structure in which the chains adopt an all-*trans* conformation, while both *gauche* and *trans* conformations are found in the amorphous phase. The intense 1130 cm^{-1} band is due to the in-phase C-C symmetric stretching in the all-*trans* conformation.[15] It provides the orientation of sequences of *trans* conformers found in the crystalline and amorphous phases. Its Raman tensor is oriented along the chain main axis, as confirmed by its much higher intensity in the ZZ spectrum than in the XX spectrum. It has been used by Pigeon *et al*.[15] and later by Citra *et al*.[19] to quantify the orientation in HDPE films and fibers, respectively, using the *complete method*.

Pigeon *et al*.[15] have established a calibration curve linking $\langle P_2 \rangle$ to the 1130/1060 band ratio in the ZZ spectra for films covering the full orientation range ($0 \leq \langle P_2 \rangle \leq 1$). This curve is reproduced in Figure 4.2B based on Figure 6 of ref. 15. It enables the direct comparison of the $\langle P_2 \rangle$ values quantified by the 3 procedures (MDP, DC and *complete method*) using the same sets of polarized Raman spectra acquired in the backscattering geometry. The green triangles present the relationship between $\langle P_2 \rangle_{MPD}$ and the 1130/1060 band ratio. The correlation between the results of the MPD method and the calibration curve reproduced from Pigeon *et al.* is remarkably good over the whole range of orientation. In contrast, the pink circles of Figure 4.2B show a much worse agreement for the $\langle P_2 \rangle_{DC}$ values quantified with the DC method using the same spectra. These were calculated by fixing a depolarization ratio of 0.19, as determined from the polarized spectral intensities of the 1030 cm^{-1} band measured on an isotropic HPDE film. In fact, the $\langle P_2 \rangle_{DC}$ values are in good agreement with those from the calibration curve and the MPD method for samples showing a low level of orientation ($\langle P_2 \rangle \leq$ 0.3), even though the accuracy is questionable in this orientation range due to the small variation of the band ratio. Nevertheless, they rapidly diverge for higher levels of orientation. The most problematic examples are highlighted in Figure 4.2B. For the sample with $\langle P_2 \rangle_{MPD}$ = 0.77, in good concordance with the calibration curve, $\langle P_2 \rangle_{DC}$ is badly underestimated by 0.31, with a value of 0.46. A similar, although less extreme, example is for the sample with $\langle P_2 \rangle_{MPD}$ = 0.51 as compared to an erroneous $\langle P_2 \rangle_{DC}$ of 0.37. Finally, the results of the DC

method appear more consistent with those of the MPD and *complete method* for the highest levels of orientation.

Pigeon *et al.*[15] have shown that the $\langle P_4 \rangle$ value of HDPE samples stretched to different draw ratios is roughly situated close to the most probable curve of the $\langle P_2 \rangle \langle P_4 \rangle$ diagram shown in Figure 4.1. This conclusion was confirmed by wide angle X-ray diffraction measurements.[15] This is inevitably the case for the MPD method since it assumes that $\langle P_4 \rangle_{MPD}$ is the most probable one associated with the $\langle P_2 \rangle$ value to which the method converges. In fact, the main drawback of the MPD method, when compared to the DC method, is the loss of the information on the population distribution that is brought by the $\langle P_4 \rangle$ value. However, $\langle P_4 \rangle_{DC}$ often leads to erroneous conclusions on the ODF. This was previously shown in our numerical simulations and is observed experimentally, as illustrated in Figure 4.2C. While some $\langle P_2 \rangle_{DC}$,$\langle P_4 \rangle_{DC}$ couples are situated near the most probable curve, a significant proportion are incorrectly located. For instance, the sample with $\langle P_2 \rangle_{DC}$ = 0.24 appeared directly on the curve predicted by the *complete method* in Figure 4.2B, suggesting that the DC method worked well in this case. However, it is in fact associated to an aberrant $\langle P_4 \rangle$ value that falls out of the range defined by Eq. 4.4 and is thus situated outside the diagram in Figure 4.2C. This experimental result is therefore theoretically impossible. A similar conclusion can be drawn for the sample with $\langle P_2 \rangle_{DC}$ = 0.98. These two points must be rejected because they do not lead to any ODF solution and are, consequently, not useful for describing the orientation of the sample. The samples with $\langle P_2 \rangle_{DC}$ = 0.46 and 0.38, which were largely underestimated (Figure 4.2B), are associated to overestimated $\langle P_4 \rangle$ values (Figure 4.2C). Accordingly, these couples both appear to be located in region IV of the diagram and would be incorrectly interpreted as bimodal distributions of the polymer chains. Based on these results, it is clear that the MPD method is both experimentally simpler and more accurate, at least in the context of HDPE samples. In fact, sacrifice of the $\langle P_4 \rangle$ value prevents us of drawing erroneous conclusions about the real behavior of the system upon orientation. It is noteworthy that it might be the case for several published orientation values determined by Raman spectroscopy with the DC method.

The extremely good correlation between the $\langle P_2 \rangle$ values obtained by the MPD and *complete method* is, in fact, somewhat surprising. Indeed, it has been shown that the assumption of a cylindrical tensor is not truly valid for the 1130 cm^{-1} band.[15, 19] The a_1 and a_2 parameters are different both in sign and in magnitude and, furthermore, evolve in opposite ways upon orientation.[15] We have recently shown by simulation that the $\langle P_2 \rangle$ values quantified using the DC method are particularly sensitive to the precise determination of ρ, especially when its value is small such as for the 1130 cm^{-1} band. The MPD method, on the other hand, allows ρ to fluctuate from sample to sample, but the method is still based on the approximation that the form of the Raman tensor is cylindrical. The results of Figure 4.2 reveal that, at least for HDPE, fixing a constant ρ based on the isotropic sample has a much larger detrimental impact on the accuracy of the quantification procedure than postulating cylindrical symmetry of the Raman tensor.

Unfortunately, the origin of the evolution of the a_1 and a_2 parameters of the tensor with orientation has not been established in any study using the *complete method*. A modification of the phase distribution from sample to sample, for instance because of a stress-induced crystallization, would justify changes of the form of the Raman tensor. This is unlikely the case for HDPE samples. Indeed, although the molecular mechanism for crystallite deformation is complex, the crystallinity degree of HDPE is high and has been reported to change only slightly (below 5 %) for samples showing completely different degrees of orientation.[8] Accordingly, HDPE is among the simplest possible systems in the context of this study because one can easily produce samples that span a large orientation range without inducing drastic modification of the phase distribution. It is possible that orientation induces small changes in the molecular interactions that would influence the shape of the polarizability ellipsoid without inducing notable shifts in the band positions. In this context, the variation of ρ cannot be predicted or taken into account by any experimental strategy to improve the accuracy of the DC method. The MPD method, in contrast, is capable of overcoming this issue, at least in the case of HDPE samples.

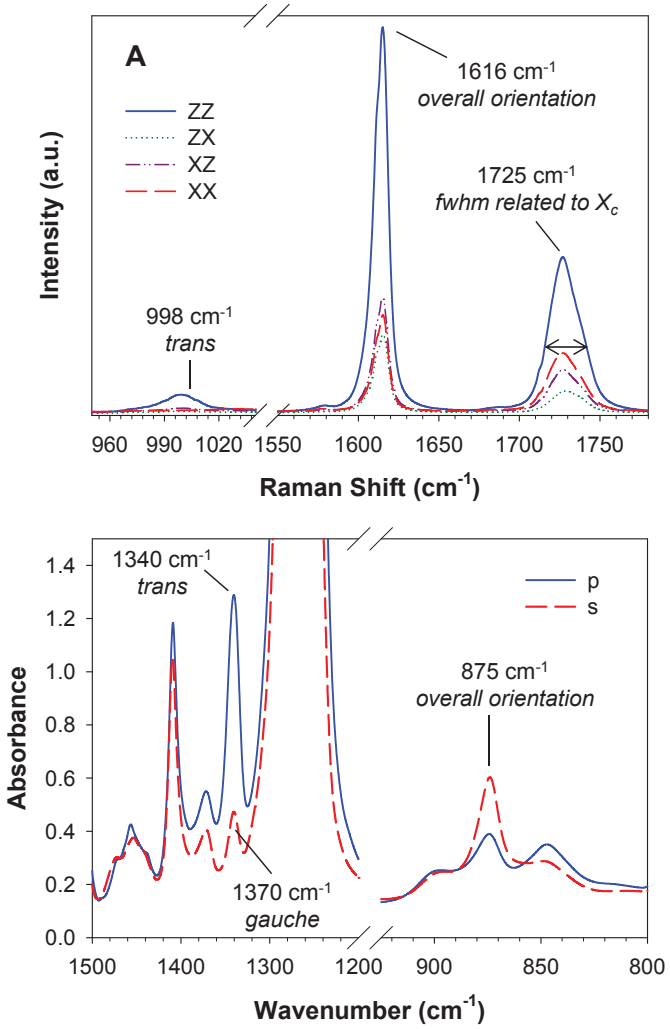

Figure 4.3. A) Polarized Raman spectra and **B)** Polarized IR spectra recorded on the same PET film.

To draw a more general picture of the effectiveness of the new MPD method, PET samples showing different levels of orientation are studied next. As compared to HDPE, PET represents a more complex example since it experiences important phase changes upon orientation. The 4 polarized Raman spectra of a representative PET sample showing an intermediate level of orientation are shown in Figure 4.3A. The 1616 cm^{-1} band is attributed to C=C symmetric stretching of the benzene ring[26] and provides the overall orientation of the PET chains, both in their crystalline and amorphous environments.[18] Its intensity in the ZZ spectrum is higher than in the XX spectrum, showing a preferential orientation of its Raman tensor along the chain axis. This tensor is aligned along the C_1-C_4 axis of the benzene ring,

with a tilt angle of 20° with respect to the main chain.[18] Figure 4.3B shows the polarized IR spectra acquired on the same sample. Everall[27] has shown a good correlation between the 1616 cm^{-1} Raman band and the 875 cm^{-1} IR band, attributed to an out-of-plane C-H deformation of the benzene ring.[28] The absorbance of the 875 cm^{-1} band is higher in the s-polarized spectrum than in the p-polarized spectrum, showing that this vibrational mode is perpendicular to the main chain. The $\langle P_2 \rangle_{IR}$ values were calculated using Eq. 4.9 assuming a tilt angle $\alpha = 86°$.[28]

PET films were stretched at different draw ratios and temperatures in order to cover the broadest possible range of orientation. The $\langle P_2 \rangle_{MPD}$ and $\langle P_2 \rangle_{DC}$ values, quantified from the 1616 cm^{-1} band using the same polarized Raman spectra, are compared in Figure 4.4A to those extracted from IR dichroism measurements on the same samples. A ρ value of 0.54, consistent with previous studies,[17, 18] was determined from an isotropic and amorphous PET sample and used to quantify the $\langle P_2 \rangle_{DC}$ values. The green triangles and pink circles are associated with $\langle P_2 \rangle_{MPD}$ and $\langle P_2 \rangle_{DC}$ values, respectively. Results from both Raman quantification procedures show an impressive correlation with the $\langle P_2 \rangle_{IR}$ results that are used as reference orientation values.

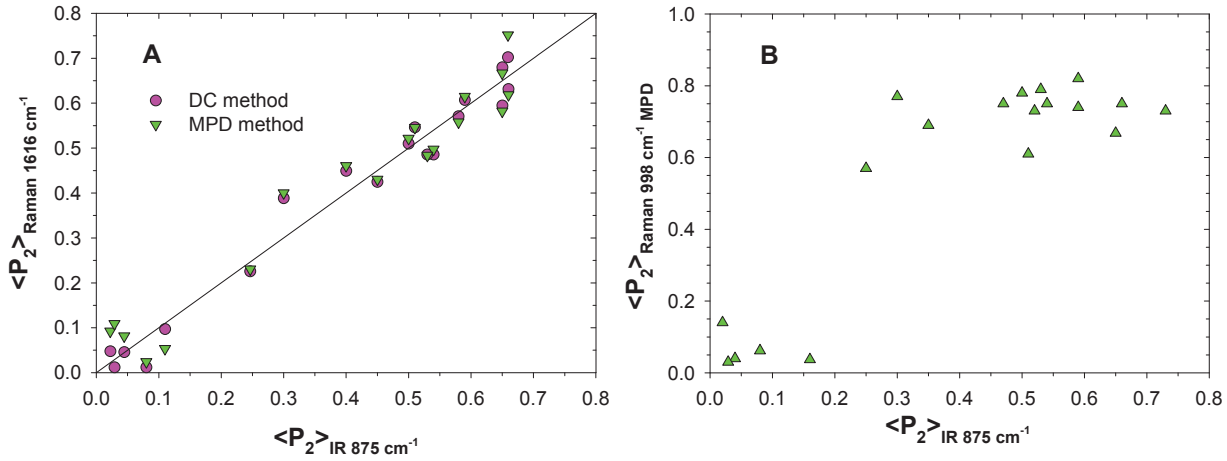

Figure 4.4. A) Comparison of the $\langle P_2 \rangle$ values quantified by Raman with the MPD (green triangles) and DC (pink circles) methods with those obtained by polarized IR spectroscopy on the same PET films. The black line traces a theoretical perfect agreement between the Raman and IR orientation values. **B)** $\langle P_2 \rangle$ values for the *trans* conformers compared with the global $\langle P_2 \rangle$ values obtained by IR spectroscopy.

As in the HDPE case, the non-cylindrical symmetry of the tensor associated to the 1616 cm^{-1} PET band, as well as its significant evolution with orientation, have been highlighted in previous studies using the *complete method*. In particular, Yang and Michielsen[17, 29] and Lesko *et al.*[18] have demonstrated that the tensor components, a_1 and a_2, evolve as a function of crystallinity and spinning speed during PET fiber formation. These results were used to question severely the applicability of the DC method. Clearly, this evolution of the form of the Raman tensor has no impact on the accuracy of the MPD method, justifying the good correlation observed in Figure 4.4A. On the other hand, one would have expected the DC method to be much more affected, as was the case for the HDPE samples. In fact, when using the a_1 and a_2 values published by Yang and Michielsen[17] to calculate depolarization ratios (using the complete equations instead of the simplified Eq. 7), it is observed to decrease with orientation and to plateau around 0.4. The excellent concordance of the $\langle P_2 \rangle_{DC}$ and $\langle P_2 \rangle_{IR}$ results, in spite of this significant variation of ρ, can be explained by our simulation studies. These have revealed that the variation of ρ only has a small impact on $\langle P_2 \rangle_{DC}$ (for positive $\langle P_2 \rangle$ values) when $0.35 < \rho < 0.55$. In line with this, Soto *et al.*[30] have also found a good correlation, within experimental error, between their $\langle P_2 \rangle$ values quantified using the *complete method* and DC method for PET samples stretched to different draw ratios above Tg.

Consequently, the results of Figure 4.4A reinforce the conclusion that the real issue for Raman quantification of orientation is not the assumption of cylindrical symmetry of the Raman tensor. The MPD method, which is, among others, based on this assumption, has led to accurate $\langle P_2 \rangle$ for both HDPE and PET samples. The use of a constant ρ, as additionally required by the DC method, is the main factor justifying the discrepancy of the $\langle P_2 \rangle_{DC}$ results. It has less consequence for intermediate ρ values, as observed for PET samples. However, it causes large errors for smaller and higher ρ, as noted for HDPE and as will be shown for PS samples (vide infra).

The evolution of ρ upon orientation is expected for PET films since it is well known that it undergoes important stress-induced changes in conformation and phase distribution. While the overall chain orientation provided by the 1616 cm^{-1} band is crucial for understanding the system behavior, it is also interesting to have information on the orientation of each phase.

This information is available in the Raman as well as in the IR spectra, but it can be challenging to extract.

In the amorphous phase, PET chains mainly adopt the *gauche* conformation with approximately 10 to 15 % of *trans*.[31, 32] In the crystalline phase, the ethylene glycol units are all in the *trans* conformation and the carbonyls are *trans* to each other. The latter can be observed in the Raman spectra through a reduction of the carbonyl band width at 1725 cm^{-1}.[33] Upon stretching, the chains rotate to adopt the *trans* conformation, as revealed by the appearance of new highly oriented bands at 998 cm^{-1} (assigned to O-CH_2 and C-C stretching vibrations of the ethylene glycol in the *trans* conformation[34]) and 1340 cm^{-1} (assigned to the wagging vibration of the CH_2 groups in the *trans* conformation[31]) in the Raman and IR spectra, respectively. This conformational change eases crystallization by reducing its free energy barrier. However, the reorientation of the carbonyl groups is a slower process that often does not completely happen before the sample solidifies, or before the tension is released. This oriented phase composed of a succession of ethylene glycol units in the *trans* conformation that are not integrated in the crystalline phase is considered as a mesophase. [31, 32, 35]

The crystallinity degree and the *trans* and *gauche* fractions have been quantified, for all samples of Fig. 4.4B, following a procedure described elsewhere.[12] The results are shown in Figure 4.S1 of the Supporting information. Briefly, the crystallinity degree is very low for all samples, around 0 % when $\langle P_2 \rangle_{IR}$ values are smaller than 0.4 and plateauing at 15 % for higher levels of orientation. The *trans* content, on the other hand, increases almost linearly with $\langle P_2 \rangle$ and reaches values up to 50 % for samples showing the highest level of orientation. The orientation of the *trans* conformers, $\langle P_2 \rangle_{trans}$, is much more difficult to extract than the overall orientation of the chains, either from the IR and Raman spectra. The 1340 cm^{-1} IR band often saturates in the p-polarized spectra, as it is the case in Figure 4.3B, unless a very thin sample is used. Raman spectroscopy represents an interesting alternative because it is not affected by the sample thickness. However, most of the *trans* conformers are found in the mesophase, which is anisotropic by nature and cannot be reproduced in the isotropic sample required to quantify the depolarization ratio of the 998 cm^{-1} band. The standard DC method is, therefore, not suitable for quantifying $\langle P_2 \rangle_{trans}$. This is a typical example of the difficulties

that can easily be overcome by the MPD method since it does not rely on the depolarization ratio.

Figure 4.4B shows the $\langle P_2 \rangle_{trans}$ quantified by the MPD method using the 998 cm^{-1} band and compared to the overall orientation of the chains ($\langle P_2 \rangle_{IR}$ from the 875 cm^{-1} band). The orientation is near 0 for slightly oriented samples but it increases rapidly and reaches a plateau at approximately 0.8 for $\langle P_2 \rangle_{IR} > 0.2$. This reveals that the overall orientation of the samples is dominated by a highly anisotropic mesophase (and by a small amount of oriented crystals for the most highly oriented samples). Yang and Michielsen[29] have established a similar comparison using the *complete method* and drawn similar conclusions. The results generated by the much simpler MPD method, shown in Figure 4.4B, are slightly underestimated in comparison to this study. We believe that these small differences are explained by the extremely low intensity of the 998 cm^{-1} band in all polarized spectra other than ZZ.

The formation of new anisotropic phases upon stretching, for which the depolarization ratio is impossible to quantify, is a common phenomenon in polymer science. Several other commercially available polymers, such as poly(lactic acid),[36] poly(vinylidene fluoride),[37] poly(butylene terephthalate)[38] and poly(pivalolactone),[39] can form mesomorphic phases or crystalline polymorphs, depending on the specific processing conditions, that greatly influence their physical properties. The new MPD method proposed in this article enables and greatly simplifies the accurate characterization of these complex events by Raman spectroscopy.

So far, the MPD method has revealed its efficiency for quantifying $\langle P_2 \rangle$ values, over the full possible orientation range, for two polymers with small and intermediate depolarization ratios. As anticipated by our simulation study, these results have also highlighted that the reliability of the DC method greatly differs from sample to sample, depending on the specific value of ρ and its variation. As a last representative example, atactic polystyrene (PS) films showing different levels of orientation are studied. Jasse and Koenig[20] have used the *complete method* to study a series of PS films using the 623 cm^{-1} band. This band is due to a totally anti-symmetric skeletal vibration of the benzene ring and is associated to the highest possible value of ρ of 0.75.[20, 40] They have shown a good correlation between the $\langle P_2 \rangle$ values determined by

Raman measurements and those evaluated by polarized IR spectroscopy on the same films, using the 1028 cm^{-1} band due to an in-plane vibration of the phenyl ring.[41]

An example of the polarized IR and Raman spectra of an oriented PS film is shown in the Supporting Information (Figure 4.S2). Both the IR and Raman bands show perpendicular orientation and all $\langle P_2 \rangle$ values were adjusted for a tilt angle α of 90°.[20, 40, 41] As for PET samples, we compare in Figure 4.5A the $\langle P_2 \rangle$ values quantified by the MDP (green triangles) and DC (pink circles) methods from the same polarized Raman spectra with those obtained by IR spectroscopy. The black squares are the $\langle P_2 \rangle_{Raman}$ and $\langle P_2 \rangle_{IR}$ values reproduced from the Jasse and Koenig study.[20] They are in excellent agreement for a wide range of orientation values and can therefore be used as a reference.

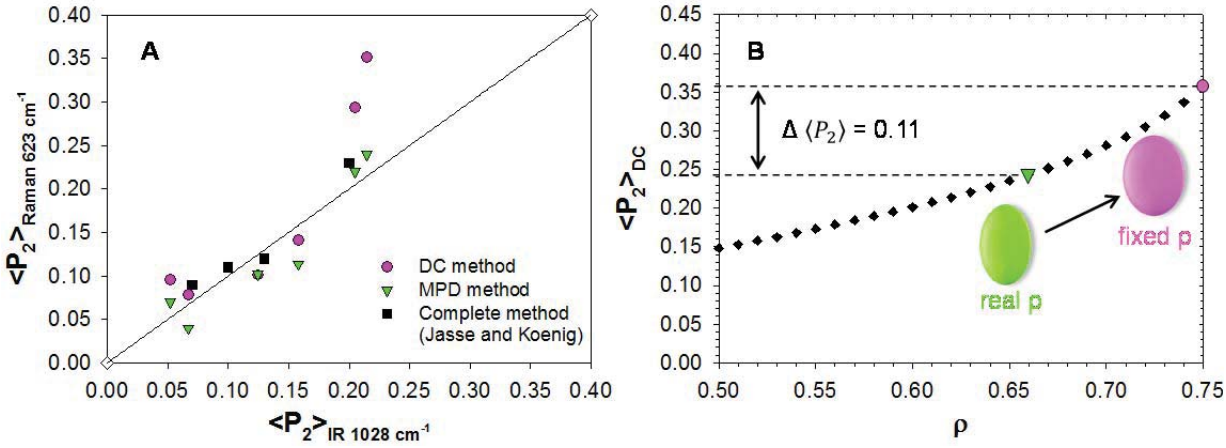

Figure 4.5. A) Comparison of the $\langle P_2 \rangle$ values of a series of PS films quantified by Raman with the MPD method (green triangles) and DC method (pink circles) as a function of the $\langle P_2 \rangle$ values determined by IR spectroscopy on the same films. The black squares are reproduced from the data available in Jasse and Koenig study[20] and quantified using the *complete method*. **B)** Simulation of the impact of the variation of the depolarization ratio on the $\langle P_2 \rangle$ value quantified using the DC method.

As for HDPE and PET, an excellent agreement is observed between $\langle P_2 \rangle_{MPD}$ and $\langle P_2 \rangle_{IR}$ for the series of drawn PS films. This is true even if the 623 cm^{-1} band possesses a very high depolarization ratio. Indeed, our simulation study had revealed that the MPD method may not converge to the appropriate value when both ρ and $\langle P_2 \rangle$ have very high values. However, it should be noted that the $\langle P_2 \rangle_{MPD}$ values reported in Figure 4.5A represent the orientation of the PS chains after taking into account the α angle of 90° between main chain and the

direction of the Raman tensor. The $\langle P_2 \rangle$ values of the vibration itself, which are subject to the above limitation, were all situated in a $\langle P_2 \rangle$ range (smaller and negative) that is not problematic.

In contrast, Figure 4.5A shows a good agreement between $\langle P_2 \rangle_{DC}$ and $\langle P_2 \rangle_{IR}$ only for samples with small or intermediate levels of orientation. The highest $\langle P_2 \rangle_{DC}$ values are largely overestimated, showing the lower efficiency of the DC method to describe properly the orientation of these films. This divergence is obviously caused by a change of the depolarization ratio upon orientation. It can be better understood by simulating the impact of the variation of ρ on the quantified $\langle P_2 \rangle_{DC}$ value.

For this demonstration, we use a sample from Figure 4.5A associated to problematic DC values ($\langle P_2 \rangle_{DC}$ = 0.35 and $\langle P_4 \rangle_{DC}$ = 0.10). These were calculated using the intensity ratios, R_1 and R_2, and ρ = 0.75 following the procedure described in the Theoretical section. R_1 and R_2 are real experimental measurements so their values were kept constant for the simulation and only ρ was varied. Since the initial ρ was fixed at 0.75 (the theoretical maximum), its value can only decrease upon orientation. By decreasing ρ by small increments from 0.75 to 0.50, we can simulate a new $\langle P_2 \rangle$,$\langle P_4 \rangle$ couple for each ρ value. Finally, these couples are adjusted for the α angle of 90° for this Raman band. Figure 4.5B reveals that this simulated fluctuation of ρ leads to a smooth decrease of $\langle P_2 \rangle_{DC}$. As a consequence, if the real value of ρ for the oriented sample decreases from 0.75 to 0.70, the calculated $\langle P_2 \rangle_{DC}$ value will be overestimated by 0.11, as noted directly on Figure 4.5B. This explains the discrepancy of the results in Figure 4.5A for the most highly oriented PS samples. The MPD method, on the other hand, accurately quantified $\langle P_2 \rangle_{MPD}$ as 0.24, since it does not assume a constant ρ value. This evolution of ρ is schematized in Figure 4.5B, assuming that the α_3 component of the tensor is constant, as the transformation from the pink cylindrical tensor (ρ = 0.75) to the green one (ρ = 0.70). It can be observed that the decrease of ρ from 0.75 to 0.70 is associated to a very small reduction of the $\alpha_2 = \alpha_1$ components (the width of the tensor) and, thus, of the *a* parameter ($a = \alpha_1/\alpha_3$). This suggests that a very small variation of the molecular environment can lead to substantial orientation quantification errors when assuming a constant ρ using the DC method.

It is important to stress that the MPD method does not generally allow determining the value of ρ for oriented samples. The ρ generated by the MPD method (ρ_{MPD}) is only accurate when the sample is directly situated on the most probable curve described by Eqs. 4.8 and shown in Figure 4.1. In contrast, our simulation study has revealed that the $\langle P_2 \rangle_{MPD}$ values are correctly quantified for samples situated in a large region around this specific curve of the $\langle P_2 \rangle \langle P_4 \rangle$ diagram.[21] Consequently, the ρ_{MPD} values are not usable to conclude on the specific shape of the tensor. Furthermore, if the initial ρ of the isotropic sample is not at one its extremes (0.75 or 0), it is impossible to predict if it will increase or decrease upon orientation. Only the *complete method* can be used to extract the α_1 and α_2 parameters, but it is often not applicable and always presents significant experimental complications. The example of Figure 4.5B is nevertheless representative of the issues of the DC method raised in this publication.

Finally, it should be emphasized that atactic PS crystallize or experience phase changes upon stretching. In this context, the errors of the DC method must be due to the evolution of ρ caused by the orientation of the polymer chains. This phenomenon is likely to be observed for most polymers and cannot be taken in account by any experimental strategy that relies on measurements on isotropic samples. This problem does not affect the MPD method, since it does not require knowledge of ρ, so that it provides more accurate orientation quantification.

4.6. Conclusion

We have demonstrated experimentally that our new MPD method enables to accurately quantify the orientation of polymers by Raman spectroscopy. In contrast with the standard procedure, a single set of 4 polarized spectra recorded in the backscattering geometry is necessary for orientation quantification. Three polymers showing completely different behaviors upon orientation, HDPE, PET and PS, were studied to cover the full possible ranges of orientation (both parallel and perpendicular to the reference direction) and depolarization ratios. In all cases, the $\langle P_2 \rangle$ values quantified with the MPD method agreed with the ones extracted from published results using the *complete method* or experimentally determined by IR spectroscopy.

This new method eliminates the major experimental complication underneath the standard DC method: the requirement of determining the depolarization on an isotropic sample. It also enables quantifying the level of orientation of intrinsically anisotropic phases, such as mesophases, that are often encountered in polymers and that were impossible to analyze with the DC method. The results unambiguously reveal that the MPD method improves the applicability and accuracy of Raman spectroscopy for orientation studies of polymers and could also be useful for several other types of materials.

4.7. Acknowledgements

This work was supported by grants and graduate scholarships (MRL) from the Natural Sciences and Engineering Research Council of Canada (NSERC) and the Fonds de Recherche du Québec - Nature et technologies (FRQNT). We are grateful to Prof. Abdellah Ajji and Prof. Michel Pézolet for providing HDPE samples.

4.8. References

1. Nakayama, K.; Kaito, A. *Springer Ser. Mater. Sci.* **1999,** *35*, 191-213.
2. Ward, I.M., Structure and Properties of Oriented Polymers, 2nd Edition. Chapman & Hall: London, 1997; pp 1-25.
3. Dong, H.; Li, H.; Wang, E.; Yan, S.; Zhang, J.; Yang, C.; Takahashi, I.; Nakashima, H.; Torimitsu, K.; Hu, W. *J. Phys. Chem. B* **2009,** *113*, 4176-4180; Tseng, H.-R.; Ying, L.; Hsu, B.B.Y.; Perez, L.A.; Takacs, C.J.; Bazan, G.C.; Heeger, A.J. *Nano Lett.* **2012,** *12*, 6353-6357; Yasuda, T.; Han, L.; Tsutsui, T. *J. Photopolym. Sci. Technol.* **2009,** *22*, 713-717.
4. Kurabayashi, K. *Int. J. Thermophys.* **2001,** *22*, 277-288; Schieber, J.D.; Venerus, D.C.; Gupta, S. *Soft Matter* **2012,** *8*, 11781-11785.
5. Sawyer, L.C.; Grubb, D.T., Polymer Microscopy. Chapman and Hall: 1987; pp 1-350.
6. Lagugné-Labarthet, F.; Buffeteau, T.; Sourisseau, C. *Macromol. Symp.* **1999,** *137*, 75-82; Lagugné-Labarthet, F.; Bruneel, J.L.; Buffeteau, T.; Sourisseau, C.; Huber, M.R.; Zilker, S.J.; Bieringer, T. *Phys. Chem. Chem. Phys.* **2000,** *2*, 5154-5167.
7. Cembrola, R.J.; Stein, R.S. *J. Polym. Sci.: Polym. Phys. Ed.* **1980,** *18*, 1065-1085.

8. Jiang, Z.; Tang, Y.; Rieger, J.; Enderle, H.-F.; Lilge, D.; Roth, S.V.; Gehrke, R.; Wu, Z.; Li, Z.; Men, Y. *Polymer* **2009,** *50*, 4101-4111.
9. Rousseau, M.-E.; Lefèvre, T.; Beaulieu, L.; Asakura, T.; Pézolet, M. *Biomacromolecules* **2004,** *5*, 2247-2257.
10. Lefèvre, T.; Paquet-Mercier, F.; Rioux-Dubé, J.-F.; Pézolet, M. *Biopolymers* **2012,** *97*, 322-336.
11. Shin, M.K.; Lee, B.; Kim, S.H.; Lee, J.A.; Spinks, G.M.; Gambhir, S.; Wallace, G.G.; Kozlov, M.E.; Baughman, R.H.; Kim, S.J. *Nat. Commun.* **2012,** *3*, 650.
12. Richard-Lacroix, M.; Pellerin, C. *Macromolecules* **2012,** *45*, 1946-1953.
13. Bower, D.I. *J. Polym. Sci.: Polym. Phys. Ed.* **1972,** *10*, 2135-2153.
14. Lefèvre, T.; Pellerin, C.; Pézolet, M., Characterization of Molecular Orientation. In *Comprehensive Analytical Chemistry*, Chalmers, J. M.; Meier, R. J., Eds. Elsevier: 2008; Vol. 53, pp 295-335.
15. Pigeon, M.; Prud'homme, R.E.; Pézolet, M. *Macromolecules* **1991,** *24*, 5687-5694.
16. Frisk, S.; Ikeda, R.M.; Chase, D.B.; Rabolt, J.F. *Appl. Spectrosc.* **2004,** *58*, 279-286.
17. Yang, S.; Michielsen, S. *Macromolecules* **2003,** *36*, 6484-6492.
18. Lesko, C.C.C.; Rabolt, J.F.; Ikeda, R.M.; Chase, B.; Kennedy, A. *J. Mol. Struct.* **2000,** *521*, 127-136.
19. Citra, M.J.; Chase, D.B.; Ikeda, R.M.; Gardner, K.H. *Macromolecules* **1995,** *28*, 4007-4012.
20. Jasse, B.; Koenig, J.L. *J. Polym. Sci.: Polym. Phys. Ed.* **1980,** *18*, 731-738.
21. Richard-Lacroix, M.; Pellerin, C. *Appl. Spectrosc.* **2013,** *67*, 409-419.
22. Bower, D.I. *J. Polym. Sci.: Polym. Phys. Ed.* **1981,** *19*, 93-107.
23. Nomura, S.; Kawai, H.; Kimura, I.; Kagiyama, M. *J. Polym. Sci. A2* **1970,** *8*, 383-400.
24. Turrell, G. *J. Raman Spectrosc.* **1984,** *15*, 103-108.
25. Lagugné-Labarthet, F.; Buffeteau, T.; Sourisseau, C. *Appl. Spectrosc.* **2000,** *54*, 699-705; Pottel, H.; Herreman, W.; van der Meer, B.W.; Ameloot, M. *Chem. Phys.* **1986,** *102*, 37-44.
26. Štokr, J.; Schneider, B.; Doskočilová, D.; Lövy, J.; Sedláček, P. *Polymer* **1982,** *23*, 714-721.
27. Everall, N.J. *Appl. Spectrosc.* **1998,** *52*, 1498-1504.

28. Cunningham, A.; Ward, I.M.; Willis, H.A.; Zichy, V. *Polymer* **1974,** *15*, 749-756.
29. Yang, S.; Michielsen, S. *Macromolecules* **2002,** *35*, 10108-10113.
30. Soto, A.; Iconomopoulou, S.M.; Manikas, A.C.; Voyiatzis, G.A. *Appl. Spectrosc.* **2005,** *59*, 1257-1269.
31. Cole, K.C.; Ajji, A.; Pellerin, É. *Macromolecules* **2002,** *35*, 770-784.
32. Pellerin, C.; Pézolet, M.; Griffiths, P.R. *Macromolecules* **2006,** *39*, 6546-6551.
33. Melveger, A.J. *J. Polym. Sci. A2* **1972,** *10*, 317-322.
34. Adar, F.; Noether, H. *Polymer* **1985,** *26*, 1935-1943.
35. Kawakami, D.; Hsiao, B.S.; Burger, C.; Ran, S.; Avila-Orta, C.; Sics, I.; Kikutani, T.; Jacob, K.I.; Chu, B. *Macromolecules* **2004,** *38*, 91-103.
36. Stoclet, G.; Seguela, R.; Lefebvre, J.M.; Elkoun, S.; Vanmansart, C. *Macromolecules* **2010,** *43*, 1488-1498.
37. Salimi, A.; Yousefi, A.A. *J. Polym. Sci. B: Polym. Phys.* **2004,** *42*, 3487-3495.
38. Song, K. *J. Appl. Polym. Sci.* **2000,** *78*, 412-423.
39. Prud'homme, R.E.; Marchessault, R.H. *Macromolecules* **1974,** *7*, 541-545.
40. Jasse, B.; Chao, R.S.; Koenig, J.L. *J. Polym. Sci.: Polym. Phys. Ed.* **1978,** *16*, 2157-2169.
41. Pellerin, C.; Prud'homme, R.E.; Pézolet, M. *Macromolecules* **2000,** *33*, 7009-7015.

4.9. Supporting information

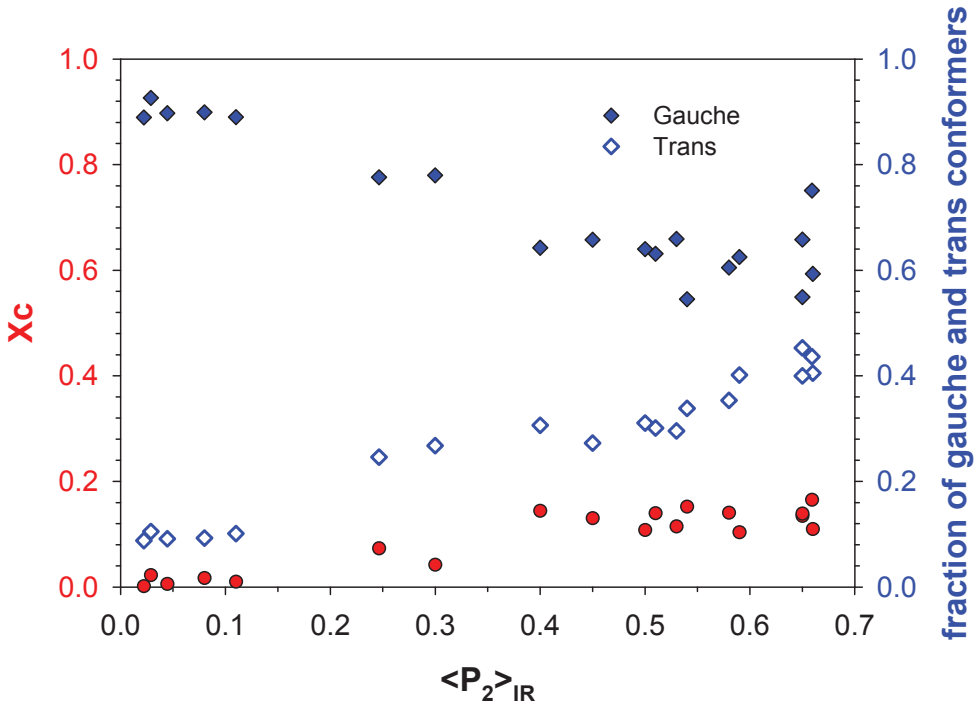

Figure 4.S1. Evolution of the crystallinity degree and *gauche* and *trans* fractions as a function of $\langle P_2 \rangle$ quantified by IR spectroscopy on PET films. The detailed quantification procedures are described in ref. 12 of the main text.

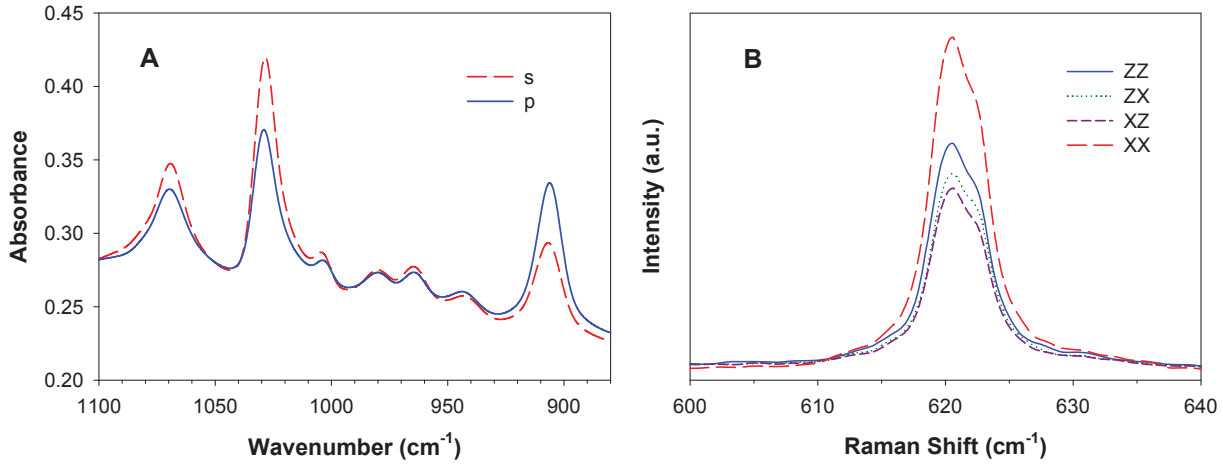

Figure 4.S2. A) Polarized IR spectra and **B)** Polarized Raman spectra recorded on the same PS film.

Chapitre 5. Orientation and structure of single electrospun nanofibers of poly(ethylene terephthalate) by confocal Raman spectroscopy

5.1. Abstract

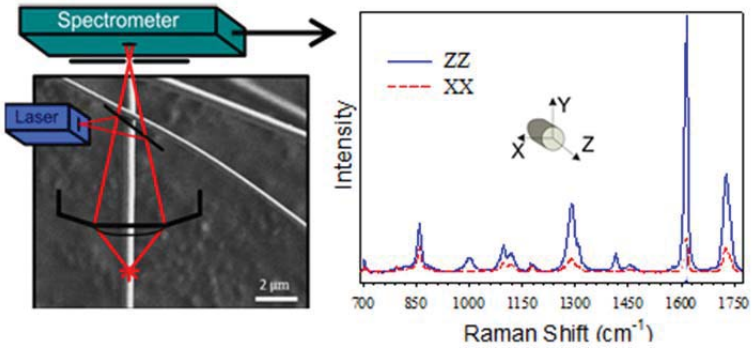

The ability to characterize individual electrospun fibers is essential in order to understand and control this complex process. In this paper, we demonstrate that confocal Raman microscopy is a powerful method to quantify molecular orientation and structure at the individual fiber level using poly(ethylene terephthalate) as a model system. Highly reproducible polarized spectra with an excellent signal-to-noise ratio were measured in one minute or less for fibers with a diameter as little as 500 nm. The orientation of smaller fibers can also be probed using a calibration procedure. Our results reveal a very broad distribution of molecular orientation and structure within the samples: some individual fibers are completely isotropic and amorphous while others present a $<P_2>$ orientation parameter as large as 0.75. The development of this large orientation is accompanied by a *gauche*-to-*trans* structural conversion into the mesomorphous phase. Even the most highly oriented fibers only present a very small degree of crystallinity.[4]

[4] Publié comme article complet dans *Macromolecules*, **2012**, 45, *4*, 1946-1953 par Marie Richard-Lacroix et Christian Pellerin

5.2. Introduction

Electrospinning is a technique that produces continuous fibers of various natural and synthetic polymer systems with typical diameters ranging from a few hundreds of nanometers to a few microns. In the past two decades, it has gained much attention for its versatility, simplicity, and efficiency for producing nanoscale materials for applications in catalysis, tissue engineering, filtration, biosensors, drug delivery, and electronic devices.[1,2] However, the widespread application of electrospun fibers is still limited by a poor understanding and control of their physical properties.[2]

Molecular orientation and crystallinity are parameters that strongly influence properties of nanofibers. Recent studies have demonstrated that the strong elongational forces experienced by the jet during the electrospinning process result in the formation of nanofibers with a high degree of molecular orientation and/or distinct crystal morphology for several highly crystalline polymers.[3,4,5] These fibers are usually characterized by techniques such as X-ray diffraction (XRD) and infrared spectroscopy that require performing measurements on large bundles in order to obtain acceptable signal-to-noise ratios. As a consequence, one must assume a uniform distribution of structural characteristics in the sample and, for molecular orientation, a perfect alignment of fibers within the bundle. In practice, electrospun nanofibers usually present a large distribution of diameters and morphology, are often only partially aligned, and sometimes contain defects such as beads due to jet instabilities during the electrospinning process.[6] The development of characterization techniques adapted to the size of individual nanofibers therefore appears as a critical need.

Selected-area electron diffraction (SAED) has been successfully used to characterize the orientation and crystalline structure within single nanofibers of highly crystalline polymers such as polyethylene,[7] nylon-6,[8] polylactide,[8] and poly(ε-caprolactone).[9] A high degree of orientation along the fiber axis was observed in all cases. However, SAED can require exhaustive sample preparation, depending on the thickness of the fiber, and precise quantification is affected by the sensitivity of most organic polymers to electron beam damage.[10] Another major limitation of diffraction techniques is that they are normally restricted to the analysis of the crystalline phase and are thus of limited use for fibers of

amorphous or low-crystallinity polymers. As a matter of fact, increasing attention has been paid in the past years to the orientation of the amorphous phase in nanofibers. Several atomic force microscopy (AFM) studies of single fibers revealed a sharp increase of Young's modulus with a decreasing fiber diameter.[11,12] This observation was attributed to an anisotropy of the amorphous phase which would be induced by confinement when the fibers reach down a critical diameter.[12,13] This phenomenon still needs to be correlated with direct and quantitative orientation measurements at the single fiber level.

Confocal Raman spectroscopy offers many advantages for the study of individual fibers since it provides molecular level information about conformation, interactions, and crystallinity. Moreover, it enables distinguishing between the molecular orientation of the crystalline and amorphous phases. Bellan and Craighead first proposed using this technique to characterize the orientation of single nylon-6 electrospun nanofibers.[14] Unfortunately, the low signal-to-noise ratio of the four polarized spectra required to quantify orientation lead to values outside the theoretical range, casting a doubt on the applicability of Raman spectroscopy for nanofibers. In fact, to our knowledge, no other successful results were published.

In this paper, we demonstrate that the molecular orientation of single electrospun fibers with diameters down to 500 nm can be quantified using confocal Raman spectroscopy. Nanofibers of poly(ethylene terephthalate) (PET) were used as a model system since its Raman spectrum is well understood. Spectra with an excellent signal-to-noise ratio can be recorded in less than a minute. We finally show that Raman spectroscopy can readily be used to quantify the distribution of conformations and crystallinity within a collection of single nanofibers.

5.3. Theoretical section

The orientation distribution function (ODF) for uniaxially oriented samples such as fibers, N(θ), can be expressed as an expansion of even Legendre polynomials $P_l(\cos\theta)$:[15,16]

$$N(\theta) = \sum_{l}^{even} \left(l + \frac{1}{2}\right) \langle P_l \rangle \, P_l(cos\theta) \qquad (5.1)$$

The $\langle P_l \rangle$ coefficients, called order parameters, are determined experimentally. The brackets indicate that they represent the average value of the l^{th} Legendre polynomial over the complete distribution of orientation. Polarized Raman spectroscopy gives access to the second and fourth coefficients of the series, $\langle P_2 \rangle$ and $\langle P_4 \rangle$, defined as:[15-17]

$$\langle P_2 \rangle = \frac{1}{2}(3\langle cos^2\theta \rangle - 1) \quad (5.2)$$

$$\langle P_4 \rangle = \frac{1}{8}(35\langle cos^4\theta \rangle - 30\langle cos^2\theta \rangle + 3) \quad (5.3)$$

$\langle P_2 \rangle$ is 1 for a perfect orientation along the fiber axis (Z), 0 for an isotropic distribution, and -0.5 for a perfect orientation perpendicular to the fiber axis (X). According to the Schwarz inequalities, the $\langle P_4 \rangle$ values are restricted to a certain range for any given $\langle P_2 \rangle$ value:[15-17]

$$\frac{1}{18}(35\langle P_2 \rangle^2 - 10\langle P_2 \rangle - 7) \leq \langle P_4 \rangle \leq \frac{1}{12}(5\langle P_2 \rangle + 7) \quad (5.4)$$

The maximum and minimum $\langle P_4 \rangle$ values are associated with unimodal and bimodal orientation distributions, respectively.[15-17] With knowledge of the $\langle P_2 \rangle$ and $\langle P_4 \rangle$ coefficients, the most probable ODF can be estimated using the entropy theory.[18]

In Raman spectroscopy, the scattered intensity for a given vibrational mode depends on the shape and orientation of its polarizability ellipsoid, which can be described by a second rank tensor, α, in terms of its principal components α_1, α_2 and α_3.[15,19]

$$\alpha = \begin{pmatrix} \alpha_1 & & \\ & \alpha_2 & \\ & & \alpha_3 \end{pmatrix} = \alpha_3 \begin{pmatrix} a_1 & & \\ & a_2 & \\ & & 1 \end{pmatrix} \quad (5.5)$$

where $a_1 = \alpha_1/\alpha_3$ and $a_2 = \alpha_2/\alpha_3$. Bower[20] developed the theory of orientation quantification by Raman spectroscopy by establishing a linear relationship between the measured polarized spectral intensities (I_s), the principal components of the Raman tensor, and the order parameters ($\langle P_2 \rangle$ and $\langle P_4 \rangle$) according to:

$$I_s = I_0 \langle \sum_{i,j} \left(l_i' l_j \alpha_{ij} \right)^2 \rangle \quad (5.6)$$

where I_0 depends on instrumental factors such as the laser power, l_i' and l_j are the direction cosines of the polarization vector of the incident and scattered beam, respectively, and α_{ij} are the components of the Raman tensor expressed in the laboratory frame. The brackets represent the mean value over the distribution of orientation. Assuming uniaxial symmetry, there are only five independent and nonzero equations that describe this dependency. The so-called "complete method" involves recording twelve different Raman spectra in three different geometries.[21]

In confocal Raman spectroscopy, only the backscattering geometry is accessible so that a limited set of two parallel-polarized (ZZ and XX) and two cross-polarized (ZX and XZ) spectra can be measured. In this notation, the first letter corresponds to the polarization of the incident beam and the second to that of the selected component of the scattered beam. This limitation requires additional approximations to quantify $\langle P_2 \rangle$ and $\langle P_4 \rangle$, as described in detail by Rousseau et al.[19] Common constants can be eliminated by calculating the ratios of the experimental cross- and parallel-polarized spectra.[15,19,22] These two ratios, R_1 and R_2, are related to the α_{ij} elements of the tensor as described by:

$$R_1 = \frac{I_{ZX}}{I_{ZZ}} = \frac{A\langle(\alpha_{ZX})^2\rangle + B\langle(\alpha_{ZY})^2\rangle}{A\langle(\alpha_{ZZ})^2\rangle + B\langle(\alpha_{ZY})^2\rangle} \quad (5.7a)$$

$$R_2 = \frac{I_{XZ}}{I_{XX}} = \frac{A\langle(\alpha_{XZ})^2\rangle + B\langle(\alpha_{XY})^2\rangle}{A\langle(\alpha_{XX})^2\rangle + B\langle(\alpha_{XY})^2\rangle} \quad (5.7b)$$

A and B are constants that take into account the depolarization of the incident and scattered beam in the focal plane associated with the use of a high numerical aperture (NA) objective.[23] B is not negligible when using a high NA objective and requires considering out-of-plane contributions of the Raman tensor to the measured spectral intensity. The $\langle(\alpha_{ij})^2\rangle$ terms in Eq. 5.7 contain four unknown parameters, namely a_1, a_2, $\langle P_2 \rangle$, and $\langle P_4 \rangle$. With the approximation that the Raman tensor has a cylindrical symmetry, that is $a_1 = a_2 = a$, the $\langle(\alpha_{ij})^2\rangle$ terms can be expressed as:[19]

$$\langle(\alpha_{ZZ})^2\rangle = \alpha_3^2\left(\frac{1}{15}(3+4a+8a^2) - \frac{2}{21}(3+a-4a^2)\langle P_2\rangle + \frac{3}{35}(1-a)^2\langle P_4\rangle\right) \quad (5.8a)$$

$$\langle(\alpha_{XX})^2\rangle = \alpha_3^2\left(\frac{1}{15}(3+4a+8a^2) + \frac{4}{21}(3+a-4a^2)\langle P_2\rangle + \frac{8}{35}(1-a)^2\langle P_4\rangle\right) \quad (5.8b)$$

$$\langle(\alpha_{XZ})^2\rangle = \langle(\alpha_{ZX})^2\rangle = \langle(\alpha_{ZY})^2\rangle = \alpha_3^2(1-a)^2\left(\frac{1}{15} + \frac{1}{21}\langle P_2\rangle - \frac{4}{35}\langle P_4\rangle\right) \quad (5.8c)$$

$$\langle(\alpha_{XY})^2\rangle = \alpha_3^2(1-a)^2\left(\frac{1}{15} - \frac{2}{21}\langle P_2\rangle + \frac{1}{35}\langle P_4\rangle\right) \quad (5.8d)$$

The "a" parameter can be determined by measuring the polarized intensities of the band of interest for an isotropic sample. For such sample, R_1 and R_2 are equivalent to the depolarization ratio, ρ, since $\langle P_2\rangle$ and $\langle P_4\rangle$ are equal to zero, and can be expressed as:[19]

$$\rho = R_1 = R_2 = \frac{(A+B)(1-a)^2}{A\,(8a^2+4a+3)+B\,(1-a)^2} \quad (5.9)$$

It should be noted that the use of Eq. 5.9 to obtain "a" implies the approximation of a constant depolarization ratio over the whole range of orientation investigated. With knowledge of "a", one can finally solve Eqs. 5.7 and 5.8 to determine $\langle P_2\rangle$ and $\langle P_4\rangle$.

5.4. Experimental section

Sample preparation

Poly(ethylene terephthalate) (PET) flakes (Scientific Polymer Products) with an inherent viscosity of 0.58, trifluoroacetic acid and dichloromethane (Fisher Scientific) were used without further purification. Fibers were prepared from a 15 % w/w solution of PET in a 50:50 w/w mixture of trifluoroacetic acid and dichloromethane. Solutions were introduced in a glass syringe equipped with a 0.41 mm diameter flat-end needle. A 27 kV positive voltage was applied to the needle tip using a CZE 1000R high-voltage power supply (Spellman High Voltage Electronics) while a 2 kV negative potential (Power Designs) was imposed on two parallel metallic rods to collect the electrospun fibers. The distance between the needle tip and the collector was 15 cm. Small quantities of fibers were then collected on a BaF_2 window and dried under vacuum for at least 4 hours prior to analysis by Raman spectroscopy.

Raman characterization

Spectra were recorded in the backscattering geometry with a LabRam HR800 spectrometer (Horiba Jobin Yvon) coupled with an Olympus BX41 microscope. The confocal hole and the slit width were fixed at 100 and 150 μm, respectively. A 632.8 nm He-Ne laser was focused on the fiber with a 100X long working distance objective (0.8 NA). The power at

the sample was ~10.5 mW. A half wave plate was used to select the polarization of the incident laser beam and a polarizer was used to select the X or Z component of the scattered beam. A scrambler was placed before the 600 groove/mm holographic grating in order to minimize its polarization-dependent response.

Individual nanofibers isolated by several microns from their nearest neighbors were aligned with their long axis along the Z direction and polarized spectra were recorded in the order: ZZ, ZX, XX, XZ, ZZ(2). The fifth spectrum was recorded to detect any drift of the system during acquisition. Any series showing more than a 5% difference in the absolute intensity of the 1616 cm^{-1} band in the ZZ and ZZ(2) spectra was rejected. The depolarization ratio was determined with polarized measurements on isotropic amorphous PET films. Correction factors were applied to all spectra to compensate for the residual polarization dependence of the spectrometer. They were determined by recording polarized spectra of isotropic amorphous films of PET and polystyrene for a series of bands with known depolarization ratio.

5.5. Results and discussion

5.5.1. Orientation quantification at the single nanofiber level

The bottom of Figure 5.1 presents an example of a full set of parallel- and cross-polarized Raman spectra for a ~500 nm electrospun PET fiber in the 1575-1775 cm^{-1} spectral region. No smoothing or baseline corrections were applied. An excellent signal-to-noise ratio can be observed, on the order of 200:1 for the 1616 cm^{-1} band in the ZZ spectrum and of 100:1 in the cross-polarized spectra (XZ and ZX). This high spectral quality was achieved with a short acquisition time of only 30 s per spectrum. In fact, acceptable polarized spectra could be acquired with an integration time as short as 5 to 10 s, depending on samples, but six acquisitions were averaged in order to improve the signal-to-noise ratio.

The molecular orientation of this nanofiber was quantified using the intensity of the 1616 cm^{-1} band, which is assigned to the symmetric C=C stretching of the benzene ring.[24] The principal axis of its tensor is aligned along the C_1-C_4 axis with a tilt angle of 20° with respect to the main chain.[25] This band is of particular interest since it is reported to be representative

of the overall orientation of the system thanks to its constant bandwidth and position upon orientation and/or crystallization.[26,27] In contrast, the 1725 cm^{-1} band, which is due to symmetric stretching of the carbonyl groups, shifts and narrows with increasing crystallinity.[24,28,29] The orientation of this nanofiber is small with a $<P_2>$ value of 0.08 after adjustment for the 20° tilt angle of the 1616 cm^{-1} band. This result appears consistent with previous XRD studies on electrospun PET nonwovens that reported a small degree of orientation.[30]

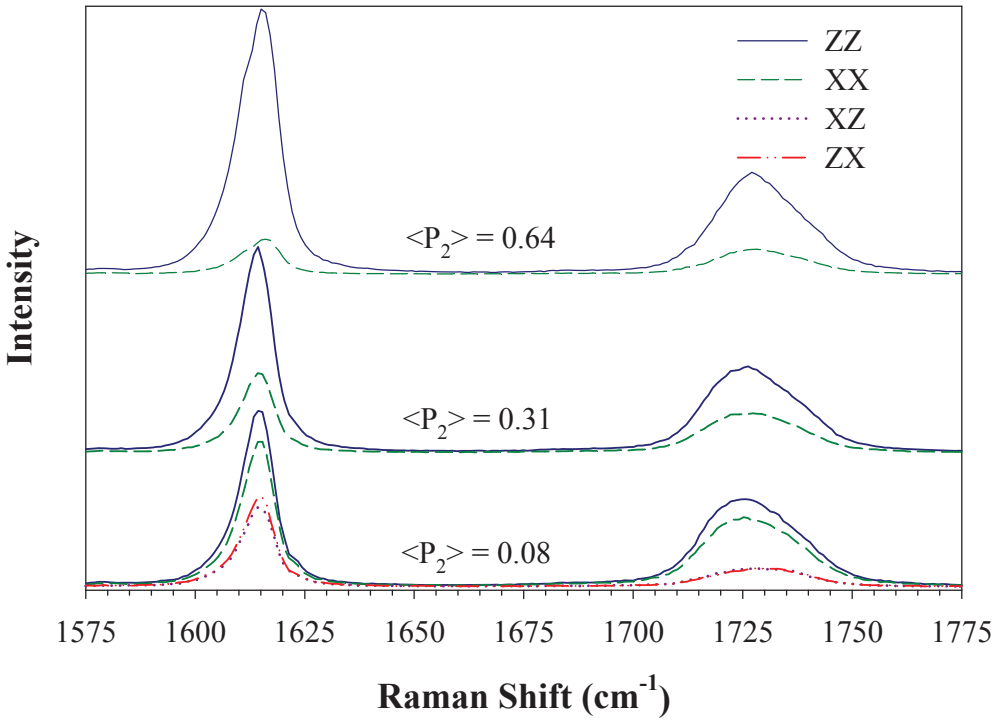

Figure 5.1. Polarized Raman spectra for three representative individual electrospun PET fibers in the 1580-1780 cm^{-1} spectral region. For clarity, the cross-polarized spectra (XZ and ZX) are only shown for one fiber.

Figure 5.1 also presents examples of polarized Raman spectra obtained for two other nanofibers with a ~500 nm diameter. For clarity, only the parallel-polarized Raman spectra (ZZ and XX) are shown. The spectra clearly demonstrate the non-uniformity of the orientation from fiber to fiber within the sample. Indeed, some nanofibers show a surprisingly high degree of orientation with $<P_2>$ values as high as 0.75. Such high values have never been reported for PET nanofibers and are unexpected for nanofibers composed of a low-crystallinity polymer.

To our knowledge, $<P_2>$ values of this order of magnitude have only been observed for fibers composed of highly crystalline polymers such as poly(ε-caprolactone),[5] poly(ethylene oxide) (PEO)[3] and PEO complexes with urea.[31] The non-uniformity of orientation within the sample is consistent with the recent SAED study of Yoshioka et al.[7] on individual electrospun polyethylene nanofibers. In their case, a direct correlation was established between the molecular orientation and the diameter of the fibers. Such a clear dependence was not observed in this study for PET nanofibers, possibly because the diameter of most fibers was close to the spatial resolution of the optical microscope and could not be determined with high accuracy. This limited spatial resolution is the main weakness of Raman microscopy as compared to TEM-based electron diffraction.

As mentioned in the theoretical section, the calculation of these $<P_2>$ values assumes that the tensor of the 1616 cm^{-1} band is cylindrical and is not affected by changes in orientation and/or crystallinity, as first proposed by Purvis and Bower.[25] These assumptions have been questioned by Lesko *et al*.[26] and later by Yang and Michelson[32] who reported that the shape of this Raman tensor is not perfectly cylindrical and evolves with structural changes, leading to a larger error in the magnitude of $<P_2>$ and $<P_4>$ with increasing orientation. However, the consequence is a slight underestimation of $<P_2>$ so that the large values reported here for highly oriented PET nanofibers are not overestimated and comparisons from fiber to fiber are still reliable.

Figure 5.2 shows the polarized Raman spectra of the same three fibers in the 675-1175 cm^{-1} spectral region. The bands are considerably weaker, especially in the cross-polarized spectra since most of them have a small depolarization ratio[25], but their signal-to-noise ratio is still sufficient to allow quantitative analysis. These spectra strongly support the quantitative nature of our orientation results. In particular, the 795 cm^{-1} band, which is due to a combination of C=O and ring ester C-C out-of-plane bending and ring torsion[33] is well known for its insensitivity to orientation.[29] Its equivalence in both parallel-polarized spectra (ZZ and XX) for all samples demonstrates that the distribution of $<P_2>$ values observed from fiber to fiber is real and not an artifact due to incorrect focusing.

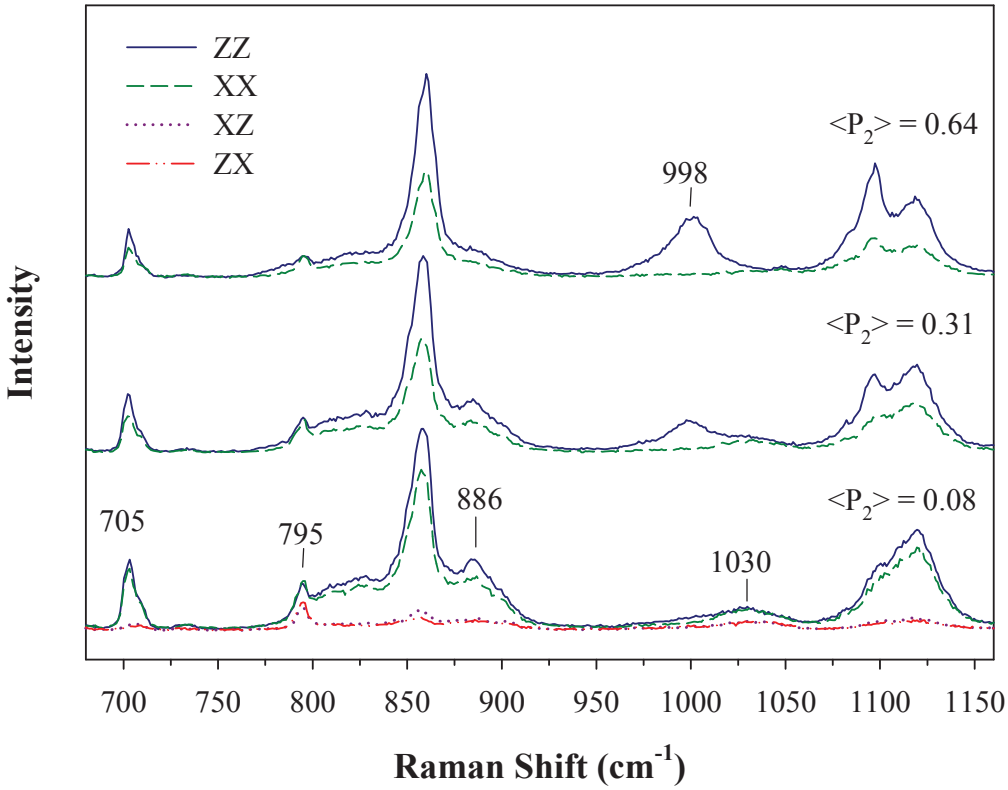

Figure 5.2. Polarized Raman spectra of single electrospun PET fibers in the 675-1175 cm^{-1} spectral region. For clarity, the cross-polarized spectra (XZ and ZX) are only shown for one fiber.

The 998 cm^{-1} band, which is associated with O-CH_2 and C-C stretching of the ethylene glycol unit in the *trans* conformation,[29] appears only in the ZZ spectra of oriented nanofibers and its intensity increases with orientation. A similar but more complicated behavior is observed for the 1096 cm^{-1} band which is also associated to the *trans* conformation.[24] This is in agreement with the *gauche*-to-*trans* rotational isomerization of the ethylene glycol units upon orientation.[34] These results indicate that the population of *trans* conformer increases with the overall orientation of the polymer chains and that their degree of orientation is extremely high in all cases. In contrast, the bands associated with *gauche* conformers[24] show the opposite behavior. In particular, the 1030 cm^{-1} band does not show any polarization dependence and only appears in the spectra of weakly oriented fibers while the 886 cm^{-1} band shows a drastic decrease in intensity in both parallel-polarized spectra upon orientation. These results suggest

that the *gauche* conformers are essentially isotropic and that their fraction decreases with the overall orientation of the system. Similar behaviors were observed by Adar and Noether[29] and by Yang and Michelson[32,35] in their studies of spin-oriented PET fibers.

Over fifteen PET nanofibers showing the intensity equivalence for the 795 cm^{-1} band and a high reproducibility between the ZZ and ZZ(2) spectra were analyzed. The $<P_2>$ and $<P_4>$ values were always found to be in the acceptable range defined by the limiting values of Eq. 5.4. These two order parameters were used to calculate the most probable orientation distribution of the polymer chains within nanofibers using the entropy theory.[18] Figure 5.3 shows the ODF determined for the three fibers shown as examples in Figures 5.1 and 5.2. For weakly oriented samples, the distribution is almost constant for all polar angles. For more oriented samples, both $<P_2>$ and $<P_4>$ follow a similar increasing trend. This leads in all cases to a unimodal ODF with its maximum along the fiber axis (polar angle of 0°). For the most highly oriented samples, the ODF is significantly narrowed as compared to the one associated with smaller $<P_2>$ values.

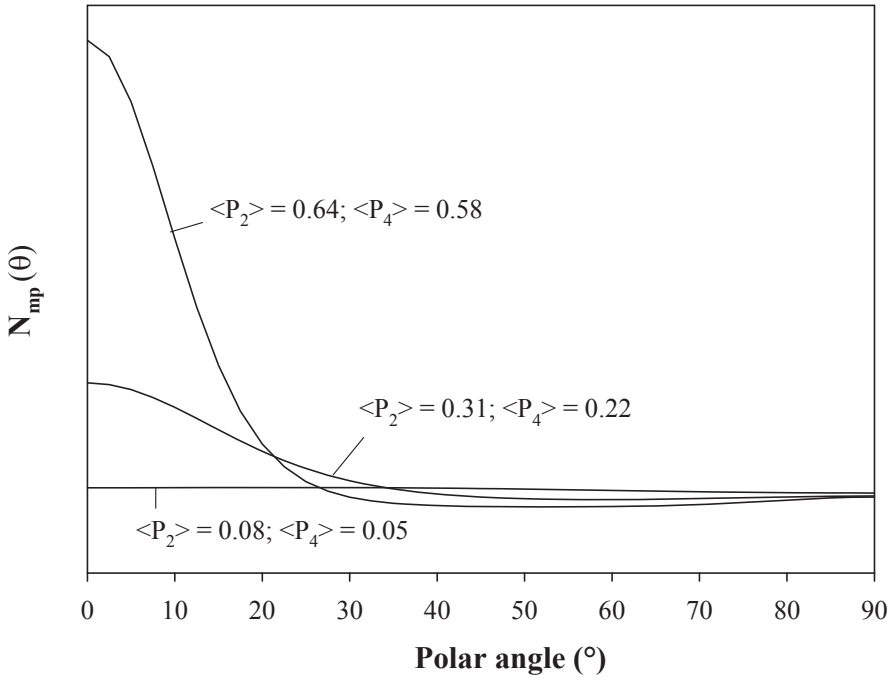

Figure 5.3. Most probable orientation distribution function determined for three single electrospun PET nanofibers.

The results obtained here show a significant improvement in spectral quality as compared to those previously reported,[14] leading to a much better confidence in the validity of the quantitative analysis. We believe this is mainly due to the differences in sample handling and in the objective used. Indeed, even imperceptible fiber movements during the experiment are detrimental to the reproducibility between the ZZ and ZZ(2) spectra. The relationship between the absolute band intensities of the four polarized spectra, which is required to perform orientation quantification, therefore becomes compromised. To overcome this problem, small quantities of fibers were electrospun between two parallel rod collectors and carefully transferred on a BaF_2 window, a planar and Raman-inactive substrate in the spectral regions of interest. The samples were further dried under vacuum for a few hours in order to eliminate the residual solvent before measurement. It was found that if the fibers are allowed to completely dry before their transfer on the substrate, the focus equivalence is impossible to achieve. We believe that traces of solvent that are always trapped in nanofibers immediately after electrospinning, even when using volatile solvents, helped to initially adsorb the fibers on the substrate. This prevented any motion after the subsequent drying and enabled reproducible measurements, even a month after the fiber deposition. Attempts to use transmission electron microscopy grids were unsuccessful because the points of contact between the nanofibers and the substrate were not sufficient to prevent movements. The size of the laser spot on the sample is also a key factor in obtaining high signal-to-noise ratios. The diameter of the laser spot was approximately 700 nm with our 100X objective as compared with a 4 μm spot reported by Bellan and Craighead with a 50X objective.[14] As a consequence, the signal-to-noise ratio was drastically improved even if the total acquisition time was reduced from 600 s to less than 60 s for each polarized spectrum.

The very broad distribution of orientation level observed from fiber to fiber within the same electrospun sample reveals the need of characterizing a large number of fibers to properly describe these heterogeneous systems. In order to reduce the time necessary to perform such analysis, we established a calibration curve relating the orientation parameters to the intensity ratio of bands in a single polarized spectrum. The ZZ spectra appeared as the best option because of their larger signal-to-noise ratio. Figure 5.4 presents the linear relationship

established between the 1616/705 cm^{-1} band ratio and the $<P_2>$ and $<P_4>$ parameters. Both calibration curves show an excellent linearity with a correlation coefficient of 0.98. Interestingly, $<P_2>$ and $<P_4>$ evolve collinearly and $<P_4>$ is systematically slightly smaller than $<P_2>$. These order parameters result in unimodal ODFs that become narrower with increasing $<P_2>$ as shown in Figure 5.3 for selected examples. These calibration curves eliminate the need of recording the full set of polarized spectra and, importantly, to achieve spectral quality equivalence between the spectra before the measurement, which is the most time consuming step of the experiment. Semi-quantitative orientation information can therefore be obtained in less than 1 min based on the acquisition of a single ZZ spectrum. To our knowledge, such short measurement time for individual electrospun nanofibers has not been achieved by any other technique.

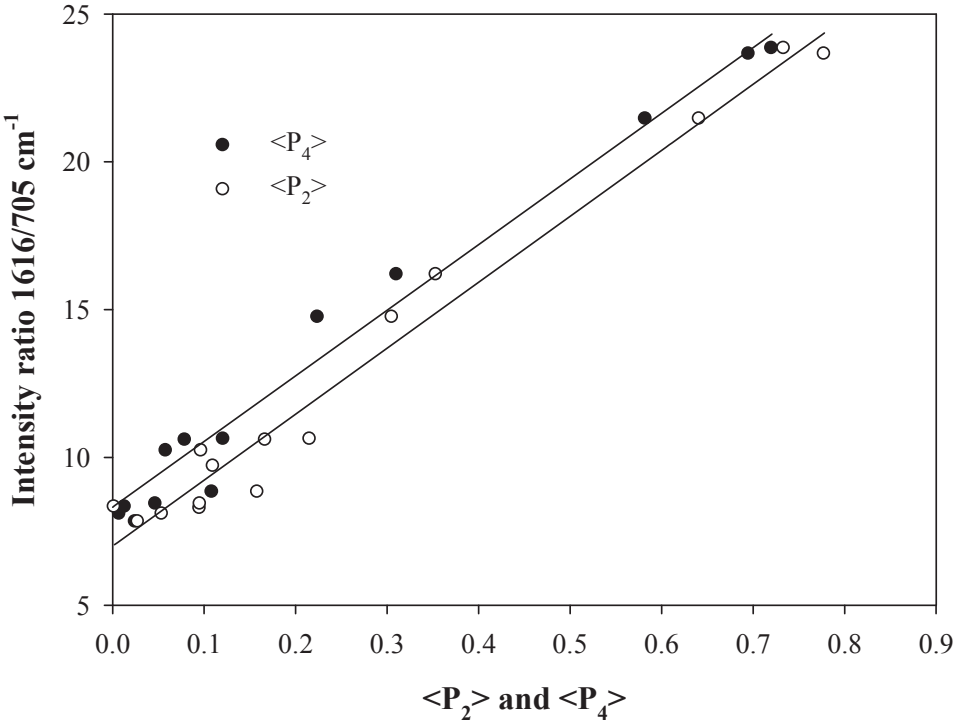

Figure 5.4. Calibration curve relating the 1616/705 cm^{-1} intensity ratio in the ZZ spectra to the $<P_2>$ and $<P_4>$ orientation parameters. Fifteen PET nanofibers with diameters between 500 nm and 1 μm were used to establish these calibration curves.

The orientation of thirty five additional individual nanofibers from five independent samples (from different sample depositions) was quantified using this strategy in order to

evaluate the distribution of orientation of the PET sample from a statistical point of view. The fibers appeared to separate into three non-overlapping clusters: approximately 70% of the fibers were only slightly oriented with an average $<P_2>$ value of 0.09 and a standard deviation of 0.04, 20% were very highly oriented with $<P_2> = 0.70 \pm 0.04$, and only 10 % of the fibers had an intermediate level of orientation between these two extremes ($<P_2> = 0.32 \pm 0.08$). It should also be pointed out that large variations of orientation were also observed when analyzing points separated by tens of micrometers along some single fibers. It is clear that orientation quantification on bundles would have missed this fundamental information about the heterogeneity of the system.

In addition to enabling statistically meaningful studies, this calibration procedure enables evaluating the orientation of fibers with diameters smaller than 500 nm. Even if a very good signal-to-noise ratio can be obtained by increasing the acquisition time, we were not able to perform strict molecular orientation quantification for fibers with a size comparable to or smaller than the diffraction limit of the laser: the intensity equivalence for the 795 cm^{-1} band in the ZZ and XX spectra was no longer achievable. The calibration curves of Figure 5.4 enable to overcome this diameter limitation and to study orientation in thinner fibers. These calibrations curves should remain valid even if the behavior of ultrathin fibers departs from that of the larger ones since the two bands are well known for their insensitivity to morphological changes.

5.5.2. Structural analysis at the single nanofiber level

In addition to orientation, rich structural information can be obtained at the single nanofiber level using confocal Raman spectroscopy. It is well known that PET chains can be organized into three distinct phases: the amorphous, the crystalline, and the mesomorphous phases. The amorphous phase is largely dominated by the *gauche* conformers of the ethylene glycol units while the *trans* conformation is adopted in the crystalline and mesomorphous phase.[36] These two phases are mainly differentiated by the organization of the terephthalate groups, which are randomly oriented in the mesomorphous phase and coplanar in the crystalline phase.[37] Cold-drawn PET films[38] and spin-oriented fibers[29] were shown to be dominated by the mesomorphous phase. On the other hand, samples stretched above Tg or

annealed after the drawing process additionally give rise to crystallization.[39] This microstructure has a large impact on the physical properties of the samples. It is therefore interesting to evaluate the nature and the relative importance of the phases formed during the electrospinning process, as well as their homogeneity from fiber to fiber.

As mentioned when discussing Figure 5.2, the evolution of the 998 cm^{-1} and 886 cm^{-1} bands clearly show an increase in *trans* conformers when going from slightly to highly oriented fibers. Rodriguez-Cabello *et al.*[40] proposed quantifying the *gauche* and *trans* fractions (F_T and F_G) using these two bands and the 795 cm^{-1} band as an internal reference, which was later replaced by the 705 cm^{-1} band:[41]

$$F_T = p_1 \left(\frac{I_{998}}{I_{705}}\right)_{iso} \qquad F_G = p_2 \left(\frac{I_{886}}{I_{705}}\right)_{iso} \tag{5.10}$$

where p_1 and p_2 are coefficients that express the relative weight of the 998 and 886 cm^{-1} bands, respectively. To perform this calculation on oriented samples, one needs to eliminate the effect orientation from the measured spectral intensity. Frisk *et al*.[42] developed a strict method to evaluate an "orientation insensitive" spectrum and Lefèvre *et al*.[43] later adapted it to Raman micro-spectroscopy. This method is hardly applicable here because using the cross-polarized spectra for three of the weakest bands of the spectrum leads to large errors. As a first approximation, the analog of the infrared structural absorbance was calculated using only the parallel-polarized spectra:[41]

$$\left(\frac{I_{band}}{I_{705}}\right)_{iso} = \left(\frac{I_{band}}{I_{705}}\right)_{ZZ} + 2\left(\frac{I_{band}}{I_{705}}\right)_{XX} \tag{5.11}$$

Since the band intensities are normalized in Eq. 5.11, it is not necessary to obtain the focus equivalence between the XX and ZZ spectra so that *trans* and *gauche* fractions can be calculated even for fibers smaller than 500 nm. The coefficients p_1 and p_2 were determined experimentally by rearranging Eq. 5.10 and were found to be 0.30 and 0.32, respectively, in excellent agreement with the reported ones.[40,41,44] It should be noted that the 705 cm^{-1} band, used for normalization, shows a small polarization dependence and that band fitting was not used to quantify the intensity of the 886 cm^{-1} band. These two factors did not have a significant influence on the determined coefficients.

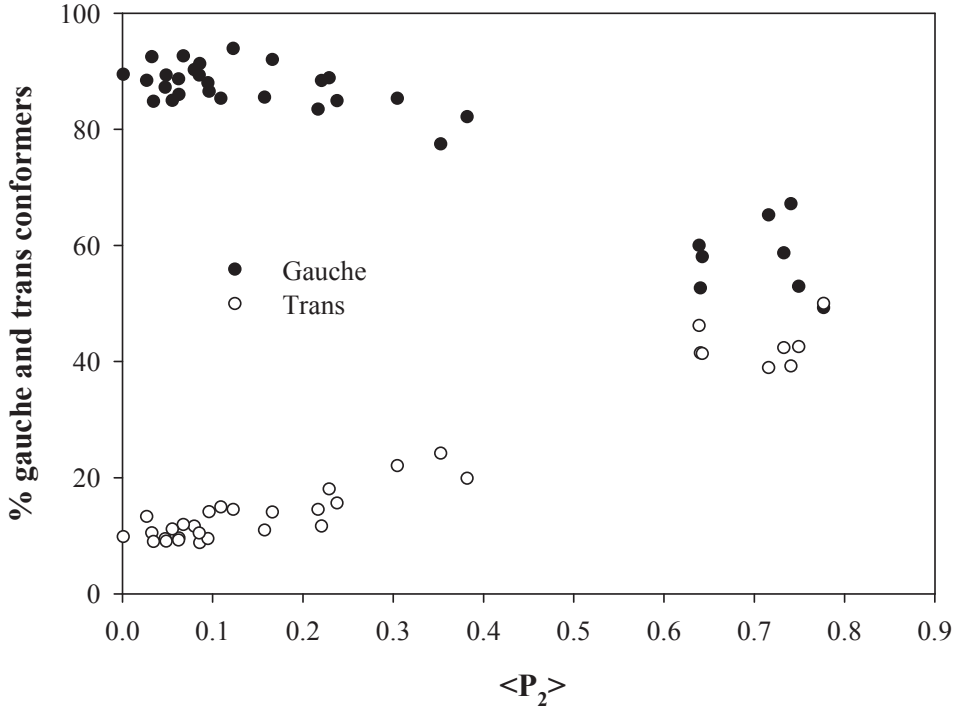

Figure 5.5. Evolution of the *gauche* and *trans* fractions as function of $\langle P_2 \rangle$ in electrospun PET fibers.

Figure 5.5 shows the evolution of the *trans* and *gauche* fractions determined independently using Eq. 5.10 as a function of $\langle P_2 \rangle$ for a series of nanofibers covering the complete range of orientation obtained. Results show that unoriented or slightly oriented nanofibers contain 10-15 % of *trans* conformers, which is consistent with the conformation distribution of totally amorphous and isotropic PET samples.[37,40] The population of *trans* conformers gradually increases with orientation and reaches 40-50 % for the nanofibers with the highest $\langle P_2 \rangle$ values. The population of *gauche* conformers follows the opposite trend. This increase in *trans* fraction with orientation is in agreement with studies of fibers formed at high wind-up speed[34] and of films stretched to high draw ratios.[38,44] While this method is only semi-quantitative because of the approximations associated with Eq. 5.11, it demonstrates very well the capability of Raman spectroscopy to follow small structural changes in individual nanofibers. It should also be pointed out that Figure 5.5 includes $\langle P_2 \rangle$ values that were calculated strictly or using the calibration curve shown in Figure 5.4. No distinction can observed between these two series, reinforcing the validity of the calibration method.

This increase in *trans* content with orientation can be either due to crystallization or to the formation of the mesomorphous phase. Crystallinity degrees must therefore be determined at the single fiber level to discriminate between these two possibilities. The simplest and most commonly used method is to follow the full width at half-maximum (FWHM) of the C=O stretching band at 1725 cm^{-1}. The carbonyl groups are randomly oriented in the amorphous and mesomorphous phases but are coplanar with the phenyl ring and *trans* to one another in the crystalline phase, resulting in a reduction of the bandwidth. Melveger[28] reported a linear relationship between the FWHM of this band and the density (d) of the polymer, which can then be related to crystallinity through:

$$d = \frac{-FWHM_{1725}+305}{209} \quad (5.12a)$$

$$X_c = (d - d_a)/(d_c - d_a) \quad (5.12b)$$

where d_a = 1.335 g/cm^3 and d_c = 1.445g/cm^3 are the density of the amorphous and crystalline phases, respectively.[32]

Figure 5.6 shows the evolution of the degree of crystallinity (labeled as Model 1) as a function of $<P_2>$ for the series of electrospun fibers presented in Figure 5.5. All crystallinity values are very small but two behaviors can be distinguished: nanofibers with a $<P_2>$ value smaller than 0.5 are almost totally amorphous ($X_c < 0.05$), while only the most highly oriented nanofibers show a non-negligible degree of crystallinity. X_c remains small, below 14 %, for nanofibers with a *trans* content as high as 50 %, suggesting that the overall orientation is mainly due to the formation of a highly oriented mesomorphous phase. By comparison, XRD patterns recorded on PET bundles (not shown) did not show any crystalline peaks. Kim et al.[30] also concluded to totally amorphous PET nanofibers using XRD when studying PET nonwovens formed under similar electrospinning conditions. This apparent discrepancy is due to the fact that the highly oriented fibers only accounts for ~20% of the sample. Crystallinity can hardly be detected for bundles because the ensemble measurement averages out the nanofibers characteristics.

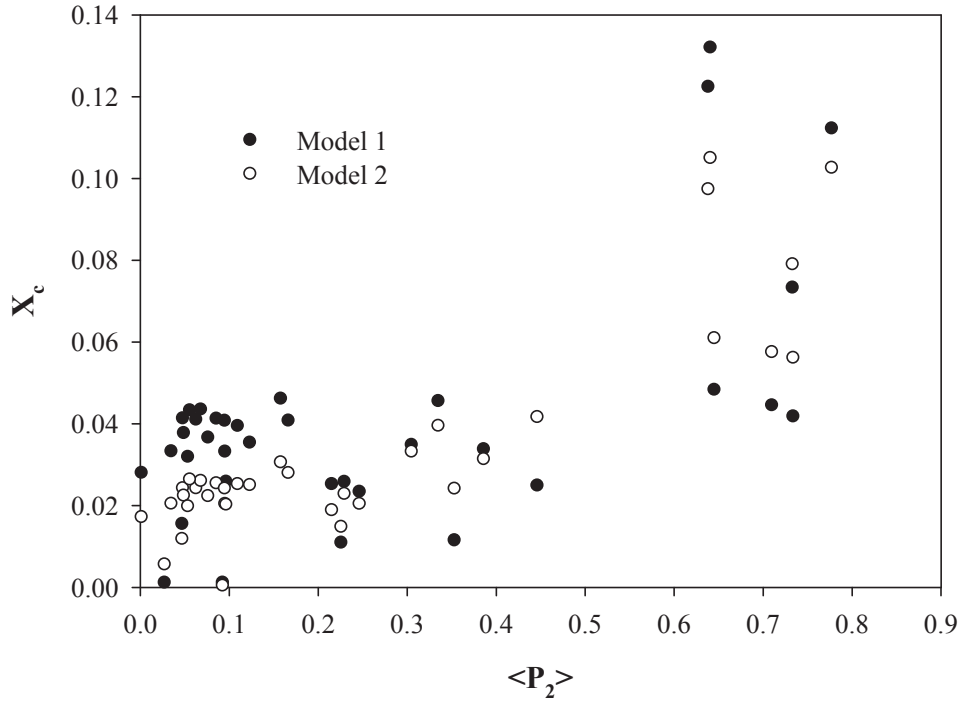

Figure 5.6. Evolution of the degree of crystallinity of PET nanofibers as function of their $\langle P_2 \rangle$. The results of Models 1 and 2 were calculated with Eqs. 5.12 and 5.13, respectively.

For this simple quantification, only the ZZ spectra were used since the FWHM of the 1725 cm^{-1} was reported to be unaffected by orientation.[28] This approximation has been questioned for highly oriented samples.[45,46] To confirm these conclusions, crystallinity degrees were also determined using a more elaborate method proposed by Natarajan *et al*.[46] These authors showed that an improved correlation between the ZZ spectra and density can be obtained by combining the bandwidth of the 1725 cm^{-1} band with the intensity the 998 cm^{-1} band (normalized to the 705 cm^{-1} band):

$$d = 1.390 - 0.0023\mathrm{FWHM}_{ZZ1725} + 0.00305\left(\frac{I_{ZZ998}}{I_{ZZ705}}\right) + 0.00072\left(\frac{I_{ZZ998}}{I_{ZZ705}}\right)^2 \qquad (5.13)$$

The results are shown in Figure 5.6 as Model 2 and correlate very well with those of the simpler Model 1. Differences can be attributed to a polarization dependence of the bandwidth of the 1725 cm^{-1} band and to small changes in the numerical coefficients of Eq. 5.13 since they depend on the NA of the objective.[46] It should be noted that both models rely on the assumption that the mesomorphous phase (largely dominated by *trans* conformers) has the

same density as the amorphous phase (largely dominated by *gauche* conformers). This approximation leads to an overestimation of the crystallinity degree[47] so the conclusion that the significant increase in *trans* fraction with orientation (Figure 5.5) is mostly due to the formation of the mesomorphous phase is unaffected. Both models are experimentally simple since they only require one polarized spectrum and are therefore applicable to fibers with a diameter smaller than 500 nm.

It is possible to draw a general picture of the structure in the electrospun PET fibers. Results indicate that the largest fraction (~70%) of the fibers possess a weak orientation ($<P_2>$ below 0.2) and are essentially amorphous, as shown in Figure 5.5. Some fibers develop a much higher orientation that is almost completely due to *trans* conformers. Indeed, even if the 1616 cm^{-1} band provides the overall orientation of the system, the spectra of Figure 5.2 indicate that the orientation of the *trans* conformers is very high while the *gauche* conformers are essentially isotropic. Accordingly, Figure 5.5 shows that the increase in overall orientation and in the fraction of the *trans* conformers are closely related. These *trans* conformers are mostly found in the mesomorphous phase. The strong elongational forces experienced by the polymer chains during the electrospinning process enable the formation of this oriented phase, but the fast solvent evaporation limits the chains mobility and prevents the formation of the better organized crystalline phase. Figure 5.6 suggests that some nuclei can form by a stress induced crystallization process along the fiber axis for the most highly oriented nanofibers, but that they did not have the opportunity to grow. This behavior is similar to that observed for fibers and films drawn at room temperature[29,38] but is highly heterogeneous from fiber to fiber. It is plausible that this heterogeneity originates from a broad distribution of effective elongational forces experienced by fibers (or fiber sections) during the whipping process.

5.6. Conclusion

In this work, we demonstrated the great efficiency of Raman spectroscopy for characterizing molecular orientation and structural characteristics of individual electrospun nanofibers. Highly reproducible polarized Raman spectra of single PET nanofibers were obtained in less than a minute with an excellent signal-to-noise ratio. With the establishment of a calibration curve, a single polarized spectrum was shown to be sufficient to perform

orientation quantification on a large number of nanofibers, including those with a diameter smaller than 500 nm. Quantitative orientation parameters ($<P_2>$ and $<P_4>$), *gauche* and *trans* isomer fractions, and crystallinity degrees were obtained on several individual PET nanofibers. A broad distribution of all these parameters was observed from fiber to fiber. It was shown that the mesomorphous phase rather than the crystalline phase was mainly dominant.

We believe that confocal Raman spectroscopy will become a major tool for the characterization of single nanofibers. This technique should improve our understanding of the parameters that control the molecular orientation and structural organization of polymer chains in electrospun nanofibers.

5.7. Acknowledgments

This work was supported by a grant and a graduate scholarship (MRL) from the Natural Sciences and Engineering Research Council of Canada (NSERC). We are grateful to T. Lefèvre for useful discussions.

5.8. References

1. Sill, T. J.; von Recum, H. A. *Biomaterials* **2008,** 29, 1989; Agarwal, S.; Wendorff, J. H.; Greiner, A. *Polymer* **2008,** 49, 5603; Bhardwaj, N.; Kundu, S. C. *Biotechnol. Adv.* **2010,** 28, 325; Greiner, A.; Wendorff, J. H. *Angew. Chem. Int. Ed.* **2007,** 46, 5670; Wang, Z.-G.; Wan, L.-S.; Liu, Z.-M.; Huang, X.-J.; Xu, Z.-K. *J. Mol. Catal. B: Enzym.* **2009,** 56, 189; Kumbar, S. G.; James, R.; Nukavarapu, S. P.; Laurencin, C. T. *Biomed. Mater.* **2008,** 3
2. Baji, A.; Mai, Y.-W.; Wong, S.-C.; Abtahi, M.; Chen, P. *Comp. Sci. technol.* **2010,** 70, 703.
3. Kakade, M. V.; Givens, S.; Gardner, K.; Lee, K. H.; Chase, D. B.; Rabolt, J. F. *J. Am. Chem. Soc.* **2007,** 129, 2777.
4. Fennessey, S. F.; Farris, R. J. *Polymer* **2004,** 45, 4217; Kongkhlang, T.; Tashiro, K.; Kotaki, M.; Chirachanchai, S. *J. Am. Chem. Soc.* **2008,** 130, 15460.
5. Edwards, M. D.; Mitchell, G. R.; Mohan, S. D.; Olley, R. H. *Eur. Polym. J.* **2010,** 46, 1175.

6. Zuo, W.; Zhu, M.; Yang, W.; Yu, H.; Chen, Y.; Zhang, Y. *Polym. Eng. Sci.* **2005,** 45, 704; Deitzel, J. M.; Kleinmeyer, J.; Harris, D.; Beck Tan, N. C. *Polymer* **2001,** 42, 261; Lim, C. T.; Tan, E. P. S.; Ng, S. Y. *Appl. Phys. Lett.* **2008,** 92, 141908; Tripatanasuwan, S.; Zhong, Z.; Reneker, D. H. *Polymer* **2007,** 48, 5742.
7. Yoshioka, T.; Dersch, R.; Tsuji, M.; Schaper, A. K. *Polymer* **2010,** 51, 2383.
8. Dersch, R.; Liu, T.; Schaper, A. K.; Greiner, A.; Wendorff, J. H. *J. Polym. Sci., Part A: Polym. Chem.* **2003,** 41, 545.
9. Chen, X.; Dong, B.; Wang, B.; Shah, R.; Li, C. Y. *Macromolecules* **2010,** 43, 9918.
10. Williams, D. B.; Carter, C. B., *Transmission Electron Microscopy*. 2nd ed.; Springer: New York, 2009; Vol. 1.
11. Ji, Y.; Li, B.; Ge, S.; Sokolov, J. C.; Rafailovich, M. H. *Langmuir* **2005,** 22, 1321; Liu, Y.; Chen, S.; Zussman, E.; Korach, C. S.; Zhao, W.; Rafailovich, M. *Macromolecules* **2011,** 44, 4439.
12. Burman, M.; Arinstein, A.; Zussman, E. *EPL-Europhys. Lett.* **2011,** 96, 16006.
13. Arinstein, A.; Burman, M.; Gendelman, O.; Zussman, E. *Nat. Nanotechnol.* **2007,** 2, 59.
14. Bellan, L. M.; Craighead, H. G. *Polymer* **2008,** 49, 3125.
15. Lefèvre, T.; Pellerin, C.; Pézolet, M., Characterization of molecular orientation. In *Molecular Characterization and Analysis of Polymers*, Chalmers, J. M.; Meier, R. J., Eds. Elsevier: Amsterdam, 2008; Vol. 53, p 295.
16. Tanaka, M.; Young, R. *J. Mater. Sci.* **2006,** 41, 963.
17. Bower, D. I. *J. Polym. Sci.: Polym. Phys. Ed.* **1981,** 19, 93.
18. Nomura, S.; Kawai, H.; Kimura, I.; Kagiyama, M. *J. Polym. Sci. Part A-2: Polym. Phys.* **1970,** 8, 383.
19. Rousseau, M.-E.; Lefèvre, T.; Beaulieu, L.; Asakura, T.; Pézolet, M. *Biomacromolecules* **2004,** 5, 2247.
20. Bower, D. I. *J. Polym. Sci.: Polym. Phys. Ed.* **1972,** 10, 2135.
21. Pigeon, M.; Prud'homme, R. E.; Pézolet, M. *Macromolecules* **1991,** 24, 5687.
22. Lagugné-Labarthet, F.; Buffeteau, T.; Sourisseau, C. *J. Phys. Chem. B* **1998,** 102, 5754.
23. Turrell, G. *J. Raman Spectrosc.* **1984,** 15, 103.
24. Štokr, J.; Schneider, B.; Doskočilová, D.; Lövy, J.; Sedláček, P. *Polymer* **1982,** 23, 714.
25. Purvis, J.; Bower, D. I. *J. Polym. Sci.: Polym. Phys. Ed.* **1976,** 14, 1461.

26. Lesko, C. C. C.; Rabolt, J. F.; Ikeda, R. M.; Chase, B.; Kennedy, A. *J. Mol. Struct.* **2000,** 521, 127.
27. Jarvis, D. A.; Hutchinson, I. J.; Bower, D. I.; Ward, I. M. *Polymer* **1980,** 21, 41.
28. Melveger, A. J. *J. Polym. Sci. Part A-2: Polym. Phys.* **1972,** 10, 317.
29. Adar, F.; Noether, H. *Polymer* **1985,** 26, 1935.
30. Kim, K.; Lee, K.; Khil, M.; Ho, Y.; Kim, H. *Fibers Polym.* **2004,** 5, 122.
31. Liu, Y.; Antaya, H.; Pellerin, C. *J. Polym. Sci. B: Polym. Phys.* **2008,** 46, 1903.
32. Yang, S.; Michielsen, S. *Macromolecules* **2003,** 36, 6484.
33. Boerio, F. J.; Bailey, R. A. *J. Polym. Sci.: Polym. Lett. Ed.* **1974,** 12, 433.
34. Garton, A.; Carlsson, D. J.; Holmes, L. L.; Wiles, D. M. *J. Appl. Polym. Sci.* **1980,** 25, 1505.
35. Yang, S.; Michielsen, S. *Macromolecules* **2002,** 35, 10108; Yang, S.; Michielsen, S. *J. Polym. Sci. B: Polym. Phys.* **2004,** 42, 47.
36. Manley, T. R.; Williams, D. A. *Polymer* **1969,** 10, 339.
37. Cole, K. C.; Ajji, A.; Pellerin, É. *Macromolecules* **2002,** 35, 770.
38. Pellerin, C.; Pézolet, M.; Griffiths, P. R. *Macromolecules* **2006,** 39, 6546.
39. Ajji, A.; Guèvremont, J.; Cole, K. C.; Dumoulin, M. M. *Polymer* **1996,** 37, 3707; Cole, K. C.; Ajji, A.; Pellerin, É. *Macromol. Symp.* **2002,** 184, 1.
40. Rodríguez-Cabello, J. C.; Quintanilla, L.; Pastor, J. M. *J. Raman Spectrosc.* **1994,** 25, 335.
41. Kawakami, D.; Hsiao, B. S.; Burger, C.; Ran, S.; Avila-Orta, C.; Sics, I.; Kikutani, T.; Jacob, K. I.; Chu, B. *Macromolecules* **2004,** 38, 91.
42. Frisk, S.; Ikeda, R. M.; Chase, D. B.; Rabolt, J. F. *Appl. Spectrosc.* **2003,** 57, 1053.
43. Lefèvre, T.; Rousseau, M.-E.; Pézolet, M. *Appl. Spectrosc.* **2006,** 60, 841.
44. Rodríguez-Cabello, J. C.; Merino, J. C.; Quintanilla, L.; Pastor, J. M. *J. Appl. Polym. Sci.* **1996,** 62, 1953.
45. Everall, N.; Tayler, P.; Chalmers, J. M.; MacKerron, D.; Ferwerda, R.; van der Maas, J. H. *Polymer* **1994,** 35, 3184.
46. Natarajan, S.; Michielsen, S. *J. Appl. Polym. Sci.* **1999,** 73, 943.
47. Lin, S.-B.; Koenig, J. L. *J. Polym. Sci.: Polym. Phys. Ed.* **1982,** 20, 2277.

Chapitre 6. Partial disentanglement in continuous polystyrene electrospun fibers

6.1. Abstract

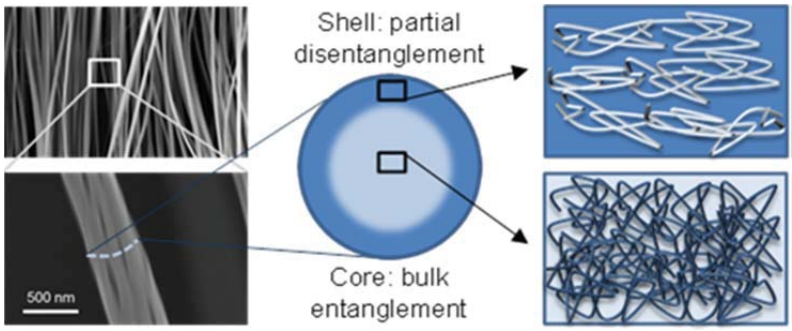

Electrospun fibers show a rich and complex variety of diameter-dependent properties. Chain orientation, confinement, and partial disentanglement are the three main factors that have been proposed to explain these phenomena. While molecular orientation is currently the subject of intensive study, the others are more challenging to probe experimentally. Here, we provide support for partial disentanglement in continuous polystyrene electrospun fibers on the basis of infrared spectroscopy measurements. We show that the fiber's capability to remain partially disentangled, and ours to detect it, is highly dependent on the initial polymer concentration and on the time the fibers are allowed to accumulate on the collector. A model, based on the core-shell morphology observed for the fibers, is proposed to explain the experimental observations.[5]

[5] Publié comme article complet dans *Macromolecules*, **2015**, 48, *1*, 37-42 par Marie Richard-Lacroix et Christian Pellerin

6.2. Introduction

Electrospinning is a widely used technique to produce nano- to microscale continuous fibers from semidilute entangled or concentrated polymer solutions. These materials have been integrated in various electronic and optical devices and find application in domains such as tissue engineering, membrane filtration and energy storage.[1-3] Despite more than two decades of intensive fundamental research, controlling properties of these fibers remains a major challenge due to our limited understanding of their internal microstructure. One of the most exciting recent discoveries is the apparently systematic exponential increase of their modulus with a decreasing diameter.[4-6] Such studies open the door to a fine tuning of fiber properties through a precise control of their diameter. However, the factors giving rise to this unusual behavior remain unclear. Several research groups have proposed models which, although fundamentally different and sometimes in contradiction, all involve the orientation of the polymer chains.[4-12]

In a series of recent publications, it was proposed that the properties of electrospun fibers are also influenced by a lower level of entanglement as compared to bulk materials.[13-19] The Zussman group has modeled theoretically (and corroborated experimentally) that the chains are already fully extended in the first millimeters of the jet and that partial disentanglement takes place.[13,14] One must however keep in mind that the orientation of the chains is never perfect in the collected fibers. Relaxation would therefore occur in the subsequent stages of their formation, although theoretical studies of the electrospinning jet have shown that the stretching forces are even higher in the whipping region that follows the straight part of the jet.[20] In any case, the presence of residual orientation, as well as the formation of metastable crystalline phases for some polymers, provide direct experimental evidence that the conformation of the chains is indeed frozen in an out-of-equilibrium state in electrospun fibers due to the combination of high stretching forces and rapid solvent evaporation.[4] In this context, the complete re-entanglement of the chains, from the lower entanglement density present in the initial solution toward the bulk value, should at least be partly hindered throughout the whole process. Besides its possible impact on modulus, this partial disentanglement would explain the melting point reduction that has been observed for several highly crystalline polymers when decreasing the fiber diameter.[16-18,21] Disentanglement

has also been recently shown to lead to exceptionally improved properties such as thermal conductivity[22] and electron conductivity.[23] It is thus expected to have strong consequences on the properties of electrospun fibers. To date, the only experimental demonstrations of partial disentanglement are based on X-ray phase contrast imaging of the first few millimeters of the jet[13,14] and on the formation of short fibers when the axial stress is high enough to cause jet fragmentation.[15] Experimental evidence that the phenomenon persists until the very last stage of fiber formation, i.e., until their collection as continuous fibers, is still lacking.

Freeze-drying is a well-established technique to produce samples in which the density of chain entanglements is lower than in the equilibrium bulk state (down to the limit of individual chains).[24-34] This method involves the extremely rapid freezing of the solvent from highly diluted polymer solutions followed by its removal by sublimation, thereby preventing the chain reptation that is necessary for re-entanglement to occur. When freeze-dried from a solution in a good solvent, the chains are obtained in a partially disentangled state with an expanded macroconformation that is similar to their state in the initial solution.[25-30] It was shown that disentanglement in freeze-dried samples can be probed by infrared (IR) or Raman spectroscopy for polymers such as poly(vinyl chloride) (PVC) and polystyrene (PS).[25-28] Disentanglement (or re-entanglement) implies long-range cooperative chain motion, while IR and Raman spectroscopies probe molecular vibrations affected by local conformations and interactions (with the exception of low-frequency phonons due to lattice modes). In this context, the presence of new bands in the spectra of several partially disentangled polymers implies that the chains can adopt conformations that are not favored in the bulk and/or that partial disentanglement affects short-range inter- or intra-chain interactions. It has been shown, for instance, that partial disentanglement significantly affects the crystallization kinetics of PVC[28], polypropylene[30] and poly(ethylene terephthalate)[29] samples, upon annealing, due to chains adopting specific local conformations.

The case of atactic PS is especially interesting since its inability to crystallize reduces complications in interpreting the spectral features. Sasaki et al.[25,26] have reported a series of new bands in the IR spectra of freeze-dried PS samples and shown that they are a good, although indirect, probe to evaluate the amplitude of the disentanglement phenomenon. The same bands were later observed in ultrathin spin-coated films by Tretinikov et al.[35] and again

attributed to a conformation made possible by partial chain disentanglement. This technique also involves rapid solvent extraction as compared to the chain relaxation time and can lead to a reduced entanglement density under specific conditions.[31,36,37] To the best of our knowledge, these three bands have never been reported, in any other context, for atactic PS.

Knowing that electrospinning also involves extremely fast solvent evaporation, and based on the literature reports[13-19] suggesting that a lower degree of entanglement should be observed in electrospun fibers, we hypothesized that the additional IR bands should also be observable in the spectra of electrospun PS fibers. Here, we present the first experimental evidence suggesting partial disentanglement in continuous electrospun fibers using IR spectroscopy. We validate that the new bands in the spectra of PS fibers are related to a conformation allowed by chain disentanglement by eliminating other possibilities, identify some of the main electrospinning parameters governing their appearance, and propose a model justifying the specific conditions in which the phenomenon is observed.

6.3. Experimental section

Atactic polystyrene (Pressure Chemical) with a weight-average molecular weight of 929 000 g/mol (PDI of 1.10) and chloroform (Fisher Scientific) were used as received. Solutions with 8, 10, 12.5 and 15% of PS (w/v) in chloroform, well above the overlap concentration, were prepared by stirring for at least 6 hours at room temperature. Electrospun fibers were produced by introducing the solutions in a 5 ml glass syringe equipped with a 0.41 mm needle on which a 15 kV voltage was applied using a CZE 1000R high-voltage power supply (Spellman High Voltage Electronics). A flow rate of 0.4-0.8 ml/h was imposed with a PHD 2000 syringe pump (Harvard Apparatus). A voltage of -2 kV was imposed on a static aluminum foil or on a rotating disk collector (rotating at a linear velocity of 29.4 m/s), acting as a counter electrode. Scanning electron microscopy (SEM) pictures of the resulting fibers are shown in Figure S1 of the Supporting Information. Solvent-cast films were prepared from the 10% solution and allowed to dry at room temperature.

Infrared spectra with a 4 cm^{-1} resolution were recorded on agglomerates of fibers (minimum of 256 scans) with a Tensor 27 FT-IR spectrometer from Bruker Optics with a liquid nitrogen-cooled HgCdTe detector and a Golden Gate (Specac) diamond attenuated total

reflection (ATR) accessory. An extended ATR correction for a 45° incidence angle, a concave rubberband baseline correction and 4 levels of zero-filling were applied on the spectra using OPUS. For the temperature-controlled experiments, a ramp of 1 °C/min was applied using the same ATR accessory and 56 scans were averaged per spectrum.

SEM images were recorded using a Quanta 200 FEG environmental SEM (FEI) under high vacuum mode and with an acceleration voltage of 20kV. A thin gold layer was deposited on the fibers prior to their observation.

6.4. Results and discussion

Figure 6.1 compares the IR spectra of a solvent-cast PS film (spectrum a) and of electrospun fibers produced from the same 10% solution. While the spectra of most fibers are essentially identical to that of the film (spectrum b), new bands at 1262, 1098 and 803 cm^{-1} are clearly observable for fibers electrospun in specific conditions (spectrum c). These three bands, which are even more intense for fibers produced from an 8% solution (spectrum d), have the same frequency and relative intensity as those observed for partially disentangled freeze-dried PS samples.[25,26] It must be stressed that they are completely absent from the spectra of chloroform, PS solutions, and films cast directly on the ATR crystal. It is thus excluded that they are due to residual solvent or other sources of contamination.

Sasaki et al.[25,26] concluded, based on IR and X-ray scattering studies, that the spectral changes are associated to an expanded chain conformation. An analogous situation was reported for freeze-dried PVC samples.[27,30] They evaluated the possibility of a 3/1 helical conformation similar to that in crystalline isotactic PS due to the common presence of the 1262 cm^{-1} band and made possible by the lower entanglement density. However, due to the inability of atactic PS to crystallize, the other bands associated to this conformation and/or to the specific interactions in the crystalline phase are absent from the spectra. Nonetheless, the conclusion of an expanded macroconformation was supported by the observation of more intense bands for samples produced from solutions in a good solvent (benzene) than from solutions in cyclohexane under theta conditions.[26] In contrast, the additional IR bands were not

reported in disentangled single-chain Pauci particles of atactic PS, possibly because their preparation method leads to a more compact globular conformation.[38] The bands are also absent from our infrared spectra of solvent-cast films of PS with a molecular weight of 1650 g/mol, well below its molecular weight between entanglements of 18000 g/mol. These results indicate that partial (or even complete) disentanglement is not a sufficient condition for the additional bands to appear and that a specific local conformation is required.

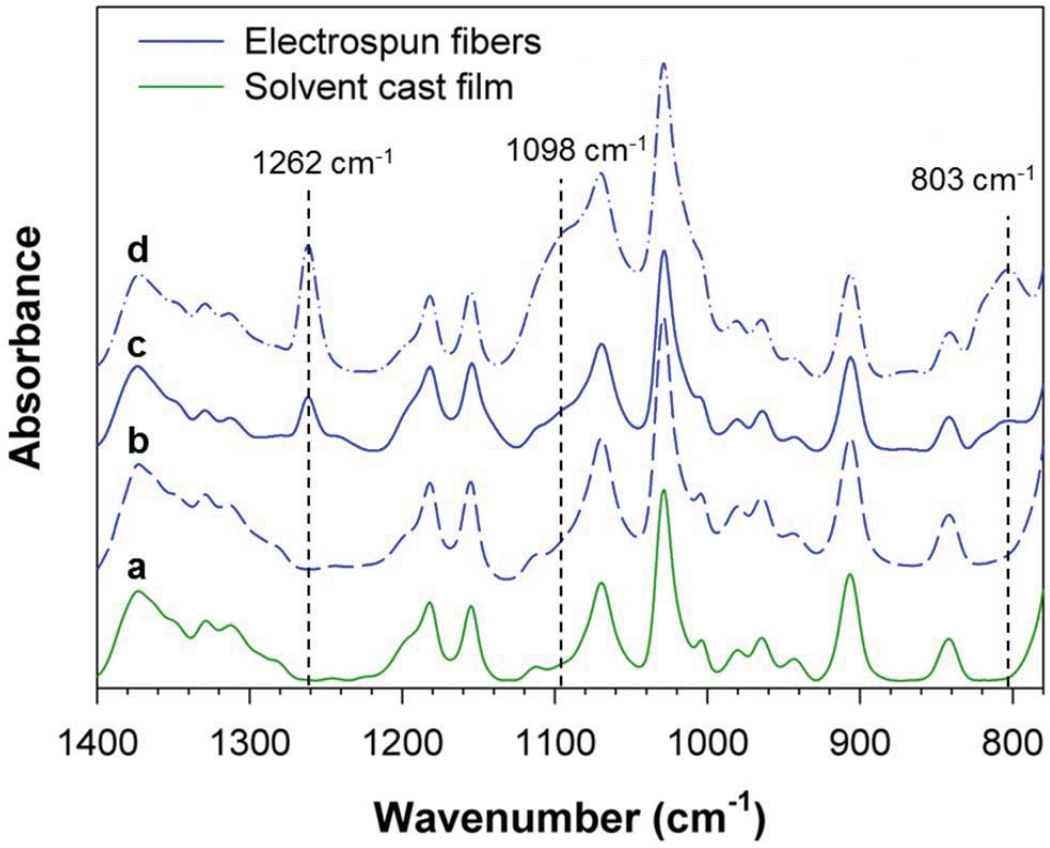

Figure 6.1. IR spectra of a solvent-cast PS film produced from a 10% chloroform solution **(a)** and of fibers electrospun from the same solution without **(b)** and with **(c)** additional bands associated to a conformation made possible by partial disentanglement of the polymer chains. **d)** IR spectrum of fibers electrospun from an 8% solution.

To validate the association of these bands to a conformation allowed by partial disentanglement in fibers, we examined two other possibilities: 1) an orientation-induced conformational change, since the extremely large elongational forces experienced by the jet

could lead to high molecular orientation in the fibers,[4] and 2) a simple conformational change not related to disentanglement or to orientation that would give rise to the same new bands.

The first hypothesis can be eliminated based on the IR spectrum (shown in Figure 6.S2) of a very highly oriented PS film with an orientation parameter, $\langle P_2 \rangle$, of 0.22, close to the highest values reachable for atactic PS samples.[39] The 1262 cm^{-1} band is barely discernable while the 1098 and 803 cm^{-1} bands are completely absent. When compared to the spectra of electrospun fibers showing these additional bands, it is clear that the orientation contribution must be small, at best.

The thermal behavior of the fibers further eliminates the second possibility. Figure 6.2A shows the spectra of fibers initially containing the additional bands measured at different temperatures, up to 200 °C, at a rate of 1 °C/min. As expected, multiple spectral changes occur with temperature, including band broadening and shifting. However, the 1262 cm^{-1} band maintains a strong absorbance even when the sample reaches 200 °C. It is also clear that the bands at 1098 and 803 cm^{-1} are still present. Figure 6.2B shows the evolution with temperature of the 1262 cm^{-1} band for two representative fiber samples. This band was selected as a probe because it is the most intense and the best isolated of the three new bands. Its absorbance was normalized with respect to the 3026 cm^{-1} band, which is known to be insensitive to conformation.[35] It can be observed that the band intensity only slightly decreases before reaching 120 °C, 15 °C above Tg, and that around 50% of the original intensity is maintained at 200 °C for both samples.

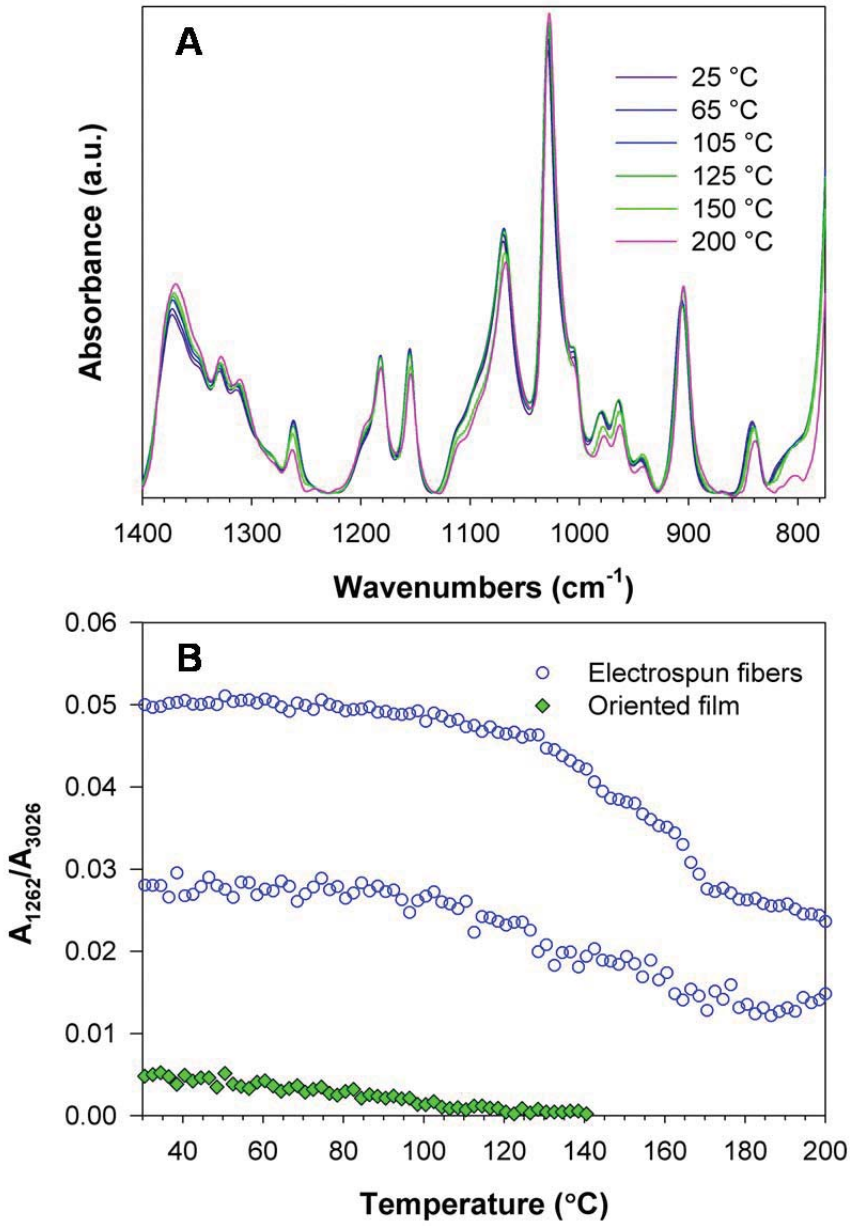

Figure 6.2. A) Temperature-controlled infrared spectra of electrospun fibers, collected from a 10% chloroform solution, during a heating ramp at 1 °C/min. The bands due to a conformation associated to disentanglement remain clearly present at 200 °C, 95 °C above Tg. **B)** Temperature evolution of the normalized absorbance of the 1262 cm^{-1} band for electrospun fibers and for a highly oriented film ($<P_2> = 0.22$).

This high thermal stability is consistent with the observations of Sasaki et al.[25] on their freeze-dried samples, which revealed that the 1262 cm^{-1} band decreases with time but remains clearly present in the spectra of samples annealed for 72 h at 130 °C. It also supports the

association with partial disentanglement from a theoretical point of view. Indeed, chains must undergo reptation in order to re-entangle, a process that is much slower than the relaxation of local conformations.[31,40-42] If the additional bands in our spectra were simply due to a conformational change or to an orientation-induced phenomenon that does not require partial disentanglement, one would have expected them to completely disappear when heating a free sample (without constraint) above its Tg. To further demonstrate this, a temperature-controlled experiment was conducted for the highly oriented film showing a weak band at 1262 cm^{-1}. As shown in Figure 6.2B, the band completely disappeared on reaching Tg, as expected. Overall, these results reinforce the conclusion that the new bands in the spectra of PS electrospun fibers are related to the partial disentanglement of the chains.

As observed in Figure 6.1, the additional IR bands do not appear for all samples electrospun from the 10% solution, even though the electrospinning conditions such as the applied voltage and the velocity of the collector were identical. This lack of reproducibility probably explains the absence of earlier reports in the literature in spite of the fact that electrospun PS fibers have been extensively studied. It is noteworthy that these bands are also observed, with the same sample-to-sample variability, for fibers collected directly on a static aluminum foil. In this context, the supplementary stretching imposed by the collector rotation may contribute to, but cannot completely induce, the partial disentanglement process.

We identified that one of the main factors influencing the results is the electrospinning time, i.e. the time we allow fibers to accumulate on the collector before stopping their production. Figure 6.3A shows representative spectra, in the region of the 1262 cm^{-1} band, measured for PS fibers collected for electrospinning times ranging from 1 to 10 min. For long collection times (10 min or more), the spectrum is always identical to that of a solvent-cast film. Reducing the collection time leads to a gradual increase of the normalized intensity of the 1262 cm^{-1} band, which becomes more prominent in the spectrum of fibers collected for 1 min. Figure 6.3B shows the range of 1262/3026 cm^{-1} absorbance ratios observed for at least three independent samples for fibers electrospun from 10, 12.5 and 15% w/v chloroform solutions (results from the 8% solutions are not included due to difficulties in collecting sufficient amounts of sample for short electrospinning times). While it should be emphasized that the relative intensity of the 1262 cm^{-1} band is rather variable (within the bar height) for

any given experimental condition, the results clearly reveal its gradual decrease for longer electrospinning times at all three concentrations.

Figure 6.3B also shows that the initial solution concentration is also a critical factor: increasing concentration significantly decreases the amplitude of the disentanglement-related bands. In fact, the absence of bars for an electrospinning time of 10 min for the 12.5 and 15% solutions signifies that the 1262 cm^{-1} band was never observed in these conditions. Similarly, attempts to electrospin more concentrated PS solutions never led to the observation of the additional bands. These results are in excellent agreement with those of Sasaki et al.[25,26] who also reported a gradual increase of these IR bands for freeze-dried samples when reducing the initial concentration of PS in either benzene or cyclohexane. Tretinnikov et al.[35] observed a similar phenomenon when decreasing the thickness of their spin-coated films to less than 200 nm.

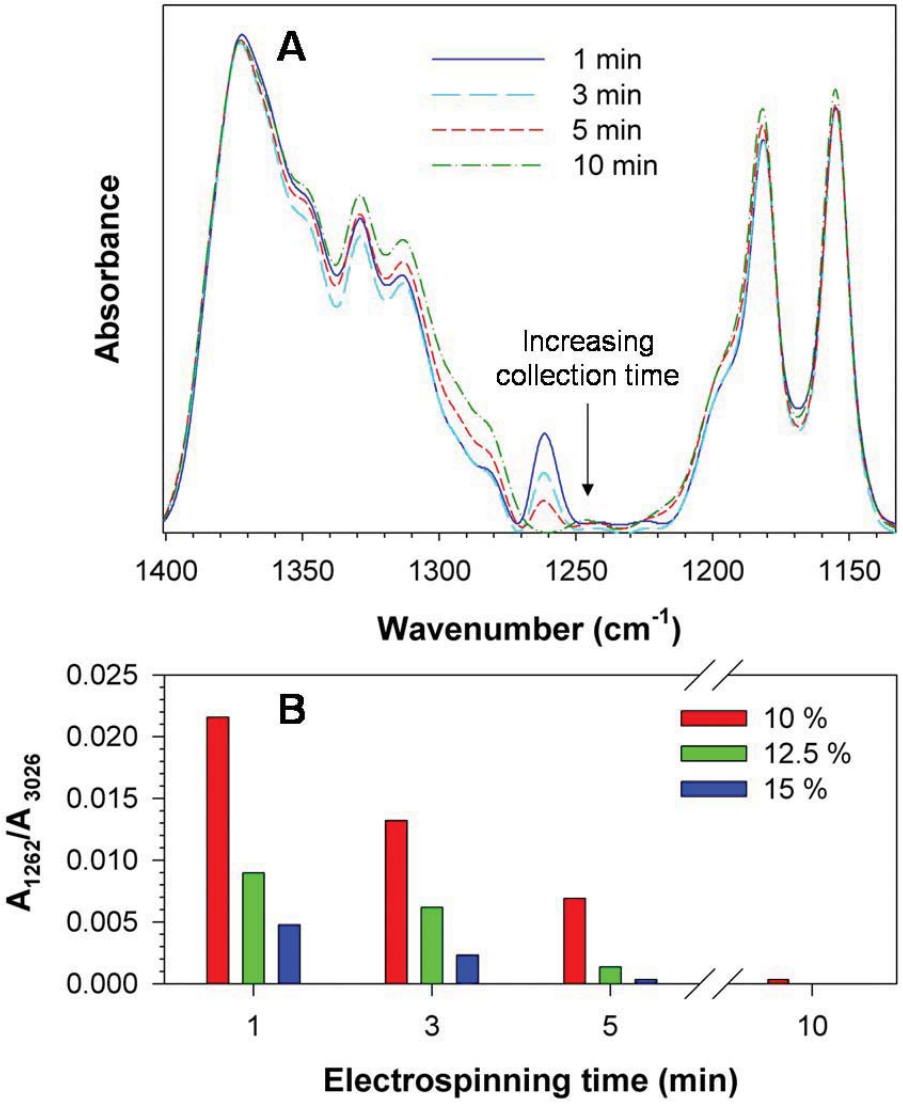

Figure 6.3. A) Representative IR spectra of fibers produced from a 10% chloroform solution and collected for different electrospinning times. **B)** Evolution of the 1262/3026 cm^{-1} absorbance ratio as a function of the collection time for PS fibers electrospun from 10, 12.5 and 15% chloroform solutions. The bars represent the range of values observed for at least three independent experiments.

The SEM images shown in Figures 6.S1 (in Supporting Information) and 6.4A help understanding the effects of concentration and collection time on partial disentanglement. First, they show the expected reduction of diameter when decreasing the solution concentration, with average diameters of 2.1, 1.9 and 0.8 μm for fibers prepared from 15, 12.5 and 10% solutions, respectively. The standard deviation on these values is fairly large,

especially for fibers prepared from 10 and 15 % solutions where the distribution is bimodal, such that these values should be interpreted as rough estimations. Most importantly, Figure 6.4A reveals a wrinkled morphology in all conditions, which was associated by Pai et al.[43] to the formation of a core-shell morphology when no phase separation is involved. The initial solvent evaporation is extremely fast during the electrospinning process, in particular when using a low boiling point solvent such as chloroform. The outer part of the jet solidifies rapidly a few mm away from the spinneret, creating a shell enriched in polymer and leading to a polymer density gradient (see Figure 6.4B).[44] The residual solvent entrapped in the fiber core evaporates at a much lower rate and its gradual removal, combined with the jet stretching that would cause a contraction of the core network,[13,14] leads to the collapse of the shell and to the observed wrinkled morphology. A detailed investigation of the kinetics of solvent evaporation leading to buckling of the shell for tubular fibers (an extreme case of the core-shell morphology) was reported by Arinstein et al.[45] Stachewicz et al.[8] have shown by AFM imaging of fiber cross-sections that the thickness of the shell remains essentially constant when reducing the fiber diameter.

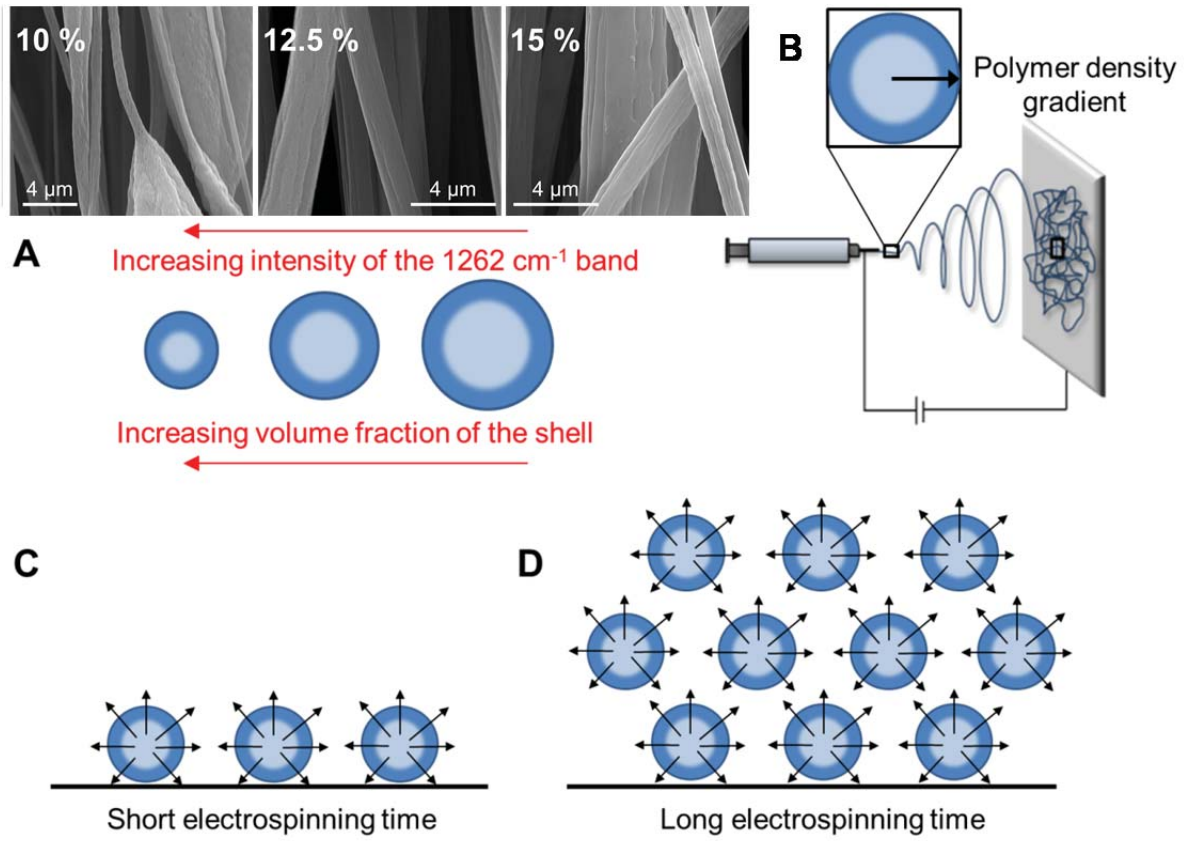

Figure 6.4. A) SEM pictures of PS fibers electrospun from 10, 12.5 and 15% chloroform solutions and schematic representation of a core-shell morphology as a function of the average fiber diameter. Schematic representations of the electrospinning process **(B)** and of the solvent evaporation from the fibers core for short **(C)** and long **(D)** collection times.

We thus hypothesize that two factors play an important role in the partial disentanglement of PS fibers. First, they are produced from semidilute solutions in which, by definition, entanglements are present but their density is lower than in the bulk polymer. Second, the formation of a distinct shell is fast enough to partially preserve the level of chain entanglement found in the initial solution and to prevent the system from reaching its equilibrium state. The phenomenon would thus be comparable to the events leading to partial disentanglement in freeze-dried samples or spin-coated films.[25,26,35] As illustrated at the bottom of Figure 6.4A, the volume fraction of the shell is expected to increase (assuming a constant thickness) when decreasing the fibers diameter, thereby leading to the increase of the 1262/3026 cm^{-1} band ratios observed in Figure 6.3B when decreasing the solution concentration.

This model would also explain the effect of the collection time on the disentanglement-related bands. As illustrated in Figure 6.4C, the evaporation of the solvent that remains trapped in the core of the fibers, during and after their collection, must proceed through the shell over the course of at least several seconds[44,46] (in practice, our IR spectra revealed the presence of a small amount of residual chloroform in the fibers several minutes after their collection). This residual solvent could act as a plasticizer and ease the re-entanglement of the chains. The vapor pressure generated by the ensemble of accumulated fibers can also cause the penetration of solvent in the shell of neighboring fibers. For short electrospinning times (Figure 6.4C), fibers are almost isolated and only affected by the solvent evaporation from a few neighbors. In contrast, a much closer packing is expected for longer electrospinning times (Figure 6.4D) so that fibers are subjected to a higher local solvent vapor pressure. In this situation, the solvent evaporation is slower and can contribute to a much greater extent to chain re-entanglement, as observed in Figure 6.3B when collecting fibers for 10 min or more. Thus, this model implies that it is the capability of the fibers to remain partially disentangled after their deposition on the collector (and consequently ours to detect it) that is collection time-dependent. It also helps explaining the results variability because the surface area occupied by the fibers is highly variable from one experiment to the other and is impossible to control with conventional electrospinning setups due to complications such as charge accumulation on the collector or variations in relative humidity.

We have considered here the simplest case where the fibers would deposit parallel to each other and form multiple layers for long collection times. The experimental situation is more complex due to the imperfect alignment of the fibers that diminishes their contact area and the density of the collected mat. It may therefore be possible to maximize the residual disentanglement by optimizing the fiber organization in the collected mats. It must also be emphasized that electrospinning with the lower solution concentrations (8 and 10%) leads to beaded fibers, which was not considered in the model but influences the results from different points of view. First, the core of a bead, which can be considered as a giant fiber, is expected to consist of chains with a bulk-like conformation and to occupy a significantly larger volume fraction (as compared to the shell) for beads than for thin fibers. Second, beads are expected to contain a much greater amount of residual solvent that can plasticize the shell of the bead itself

and those of the surrounding fibers, therefore allowing re-entanglement to a greater extent. Third, the formation of beads may favor chain re-entanglement during the electrospinning process. Finally, from a spectroscopic point of view, beads occupy a larger volume than thinner fibers and may dominate the overall signal, especially for long collection times. Fortunately, this effect is attenuated by the fact that the penetration depth of the ATR evanescent wave, which is approximately 2 μm in the experimental conditions for the 1262 cm^{-1} band, is much smaller than the bead diameter. These four effects should all to lead to a decrease of the relative intensity of the conformation-sensitive bands associated with partial disentanglement, and reduce our capacity to detect it, in beaded fibers. It is therefore interesting to notice that, in spite of this, the additional bands are the most intense in samples obtained from the 8 and 10% solutions, suggesting that the phenomenon is even more pronounced then revealed by our results.

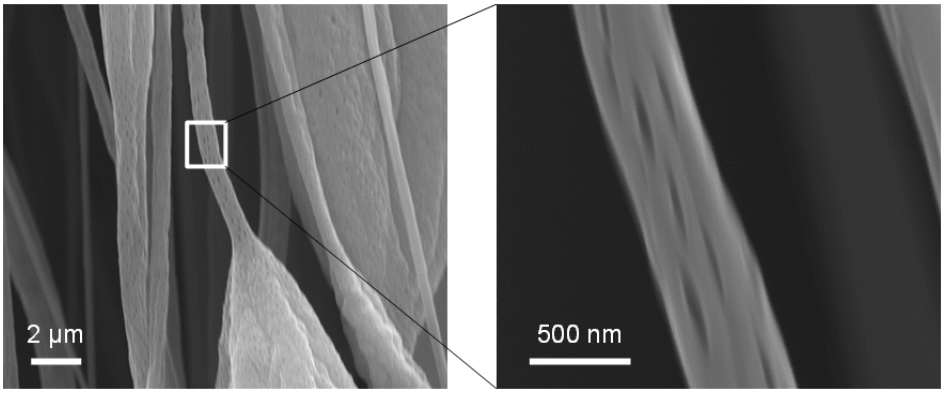

Figure 6.5. SEM pictures of PS fibers electrospun from a 10% chloroform solution showing the presence of elongated pores on the surface.

Overall, our results are in general agreement with the propositions of Zussman et al.[13-18] since they support the hypothesis of partial disentanglement in electrospun fibers. However, these authors have reported that the formation of a shell would reduce the subsequent stretching of the fiber and, thus, prevent stretching-induced chain disentanglement. The observation of partial disentanglement for fibers clearly showing a wrinkled morphology thus challenges this hypothesis. It must, however, be noted that elongated pores, which most likely originate from water vapor condensation,[47] are clearly visible on the surface of the fibers (see Figure 6.5) and constitute a direct evidence for fiber elongation after the shell formation, but

possibly before its complete solidification. In this context, we cannot exclude that the stretching of the jet could have played a role in the partial disentanglement, but our results reveal that additional aspects, especially shell formation, must be taken into account to fully understand this phenomenon.

6.5. Conclusion

Infrared spectroscopy enabled detecting and quantifying conformation-sensitive bands associated to partial disentanglement in polystyrene electrospun fibers. To our knowledge, this constitutes the first experimental support for the phenomenon in continuous electrospun fibers. Our results reveal that a low polymer solution concentration is necessary to observe partial disentanglement and that the electrospinning time is a critical factor, with long collection times systematically leading to bulk-like spectra. Based on the wrinkled fiber morphology revealed by SEM and associated in the literature to a core-shell structure, we hypothesize that a lower entanglement density should be found in the shell. We are currently using Raman spectroscopy, at the single fiber scale,[11] to better understand the spatial distribution of the disentanglement in these fibers.

Our observations are important from a larger perspective because they imply that the properties of electrospun fibers that are influenced by their level of entanglement could be directly affected by the electrospinning time. This may have important implications for studies of individual fibers since they are normally produced with short collection times to prepare isolated fibers. Upon the impressively large number of factors that are known to influence electrospun fibers, it is, to the best of our knowledge, the first time that collection time is raised as a possible key parameter.

6.6. Acknowledgements

This work was supported by a grant and a graduate scholarship (MRL) from the Natural Sciences and Engineering Research Council of Canada (NSERC). We are grateful to F. Byette for his assistance for the SEM imaging.

6.7. References

1. Sill, T. J.; von Recum, H. A. *Biomaterials* **2008,** 29, 1989; Agarwal, S.; Wendorff, J. H.; Greiner, A. *Polymer* **2008,** 49, 5603; Bhardwaj, N.; Kundu, S. C. *Biotechnol. Adv.* **2010,** 28, 325; Greiner, A.; Wendorff, J. H. *Angew. Chem. Int. Ed.* **2007,** 46, 5670; Wang, Z.-G.; Wan, L.-S.; Liu, Z.-M.; Huang, X.-J.; Xu, Z.-K. *J. Mol. Catal. B: Enzym.* **2009,** 56, 189; Kumbar, S. G.; James, R.; Nukavarapu, S. P.; Laurencin, C. T. *Biomed. Mater.* **2008,** 3, 034002.
2. Baji, A.; Mai, Y.-W.; Wong, S.-C.; Abtahi, M.; Chen, P. *Comp. Sci. technol.* **2010,** 70, 703.
3. Kakade, M. V.; Givens, S.; Gardner, K.; Lee, K. H.; Chase, D. B.; Rabolt, J. F. *J. Am. Chem. Soc.* **2007,** 129, 2777.
4. Fennessey, S. F.; Farris, R. J. *Polymer* **2004,** 45, 4217; Kongkhlang, T.; Tashiro, K.; Kotaki, M.; Chirachanchai, S. *J. Am. Chem. Soc.* **2008,** 130, 15460.
5. Edwards, M. D.; Mitchell, G. R.; Mohan, S. D.; Olley, R. H. *Eur. Polym. J.* **2010,** 46, 1175.
6. Zuo, W.; Zhu, M.; Yang, W.; Yu, H.; Chen, Y.; Zhang, Y. *Polym. Eng. Sci.* **2005,** 45, 704; Deitzel, J. M.; Kleinmeyer, J.; Harris, D.; Beck Tan, N. C. *Polymer* **2001,** 42, 261; Lim, C. T.; Tan, E. P. S.; Ng, S. Y. *Appl. Phys. Lett.* **2008,** 92, 141908; Tripatanasuwan, S.; Zhong, Z.; Reneker, D. H. *Polymer* **2007,** 48, 5742.
7. Yoshioka, T.; Dersch, R.; Tsuji, M.; Schaper, A. K. *Polymer* **2010,** 51, 2383.
8. Dersch, R.; Liu, T.; Schaper, A. K.; Greiner, A.; Wendorff, J. H. *J. Polym. Sci., Part A: Polym. Chem.* **2003,** 41, 545.
9. Chen, X.; Dong, B.; Wang, B.; Shah, R.; Li, C. Y. *Macromolecules* **2010,** 43, 9918.
10. Williams, D. B.; Carter, C. B., *Transmission Electron Microscopy*. 2nd ed.; Springer: New York, 2009; Vol. 1.
11. Ji, Y.; Li, B.; Ge, S.; Sokolov, J. C.; Rafailovich, M. H. *Langmuir* **2005,** 22, 1321; Liu, Y.; Chen, S.; Zussman, E.; Korach, C. S.; Zhao, W.; Rafailovich, M. *Macromolecules* **2011,** 44, 4439.
12. Burman, M.; Arinstein, A.; Zussman, E. *EPL-Europhys. Lett.* **2011,** 96, 16006.
13. Arinstein, A.; Burman, M.; Gendelman, O.; Zussman, E. *Nat. Nanotechnol.* **2007,** 2, 59.

14. Bellan, L. M.; Craighead, H. G. *Polymer* **2008,** 49, 3125.
15. Lefèvre, T.; Pellerin, C.; Pézolet, M., Characterization of molecular orientation. In *Molecular Characterization and Analysis of Polymers*, Chalmers, J. M.; Meier, R. J., Eds. Elsevier: Amsterdam, 2008; Vol. 53, p 295.
16. Tanaka, M.; Young, R. *J. Mater. Sci.* **2006,** 41, 963.
17. Bower, D. I. *J. Polym. Sci.: Polym. Phys. Ed.* **1981,** 19, 93.
18. Nomura, S.; Kawai, H.; Kimura, I.; Kagiyama, M. *J. Polym. Sci. Part A-2: Polym. Phys.* **1970,** 8, 383.
19. Rousseau, M.-E.; Lefèvre, T.; Beaulieu, L.; Asakura, T.; Pézolet, M. *Biomacromolecules* **2004,** 5, 2247.
20. Bower, D. I. *J. Polym. Sci.: Polym. Phys. Ed.* **1972,** 10, 2135.
21. Pigeon, M.; Prud'homme, R. E.; Pézolet, M. *Macromolecules* **1991,** 24, 5687.
22. Lagugné-Labarthet, F.; Buffeteau, T.; Sourisseau, C. *J. Phys. Chem. B* **1998,** 102, 5754.
23. Turrell, G. *J. Raman Spectrosc.* **1984,** 15, 103.
24. Štokr, J.; Schneider, B.; Doskočilová, D.; Lövy, J.; Sedláček, P. *Polymer* **1982,** 23, 714.
25. Purvis, J.; Bower, D. I. *J. Polym. Sci.: Polym. Phys. Ed.* **1976,** 14, 1461.
26. Lesko, C. C. C.; Rabolt, J. F.; Ikeda, R. M.; Chase, B.; Kennedy, A. *J. Mol. Struct.* **2000,** 521, 127.
27. Jarvis, D. A.; Hutchinson, I. J.; Bower, D. I.; Ward, I. M. *Polymer* **1980,** 21, 41.
28. Melveger, A. J. *J. Polym. Sci. Part A-2: Polym. Phys.* **1972,** 10, 317.
29. Adar, F.; Noether, H. *Polymer* **1985,** 26, 1935.
30. Kim, K.; Lee, K.; Khil, M.; Ho, Y.; Kim, H. *Fibers Polym.* **2004,** 5, 122.
31. Liu, Y.; Antaya, H.; Pellerin, C. *J. Polym. Sci. B: Polym. Phys.* **2008,** 46, 1903.
32. Yang, S.; Michielsen, S. *Macromolecules* **2003,** 36, 6484.
33. Boerio, F. J.; Bailey, R. A. *J. Polym. Sci.: Polym. Lett. Ed.* **1974,** 12, 433.
34. Garton, A.; Carlsson, D. J.; Holmes, L. L.; Wiles, D. M. *J. Appl. Polym. Sci.* **1980,** 25, 1505.
35. Yang, S.; Michielsen, S. *Macromolecules* **2002,** 35, 10108; Yang, S.; Michielsen, S. *J. Polym. Sci. B: Polym. Phys.* **2004,** 42, 47.
36. Manley, T. R.; Williams, D. A. *Polymer* **1969,** 10, 339.
37. Cole, K. C.; Ajji, A.; Pellerin, É. *Macromolecules* **2002,** 35, 770.

38. Pellerin, C.; Pézolet, M.; Griffiths, P. R. *Macromolecules* **2006,** 39, 6546.
39. Ajji, A.; Guèvremont, J.; Cole, K. C.; Dumoulin, M. M. *Polymer* **1996,** 37, 3707; Cole, K. C.; Ajji, A.; Pellerin, É. *Macromol. Symp.* **2002,** 184, 1.
40. Rodríguez-Cabello, J. C.; Quintanilla, L.; Pastor, J. M. *J. Raman Spectrosc.* **1994,** 25, 335.
41. Kawakami, D.; Hsiao, B. S.; Burger, C.; Ran, S.; Avila-Orta, C.; Sics, I.; Kikutani, T.; Jacob, K. I.; Chu, B. *Macromolecules* **2004,** 38, 91.
42. Frisk, S.; Ikeda, R. M.; Chase, D. B.; Rabolt, J. F. *Appl. Spectrosc.* **2003,** 57, 1053.
43. Lefèvre, T.; Rousseau, M.-E.; Pézolet, M. *Appl. Spectrosc.* **2006,** 60, 841.
44. Rodríguez-Cabello, J. C.; Merino, J. C.; Quintanilla, L.; Pastor, J. M. *J. Appl. Polym. Sci.* **1996,** 62, 1953.
45. Everall, N.; Tayler, P.; Chalmers, J. M.; MacKerron, D.; Ferwerda, R.; van der Maas, J. H. *Polymer* **1994,** 35, 3184.
46. Natarajan, S.; Michielsen, S. *J. Appl. Polym. Sci.* **1999,** 73, 943.
47. Lin, S.-B.; Koenig, J. L. *J. Polym. Sci.: Polym. Phys. Ed.* **1982,** 20, 2277.

6.8. Supporting information

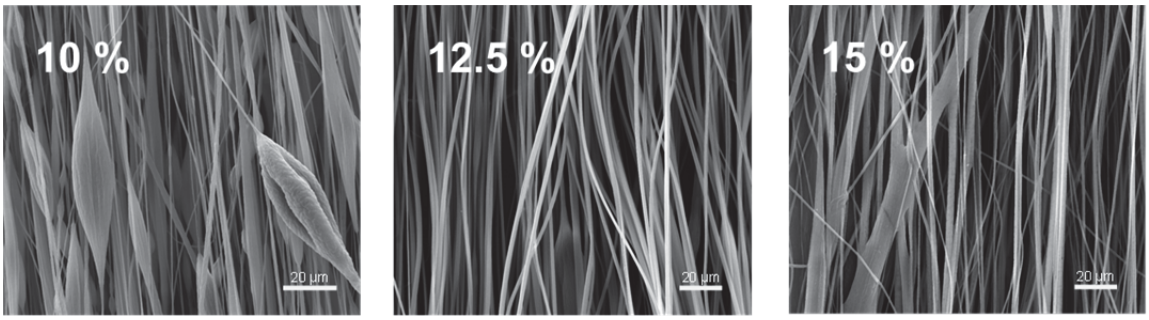

Figure 6.S1. SEM pictures of PS fibers electrospun from 10, 12.5 and 15% PS/chloroform solutions.

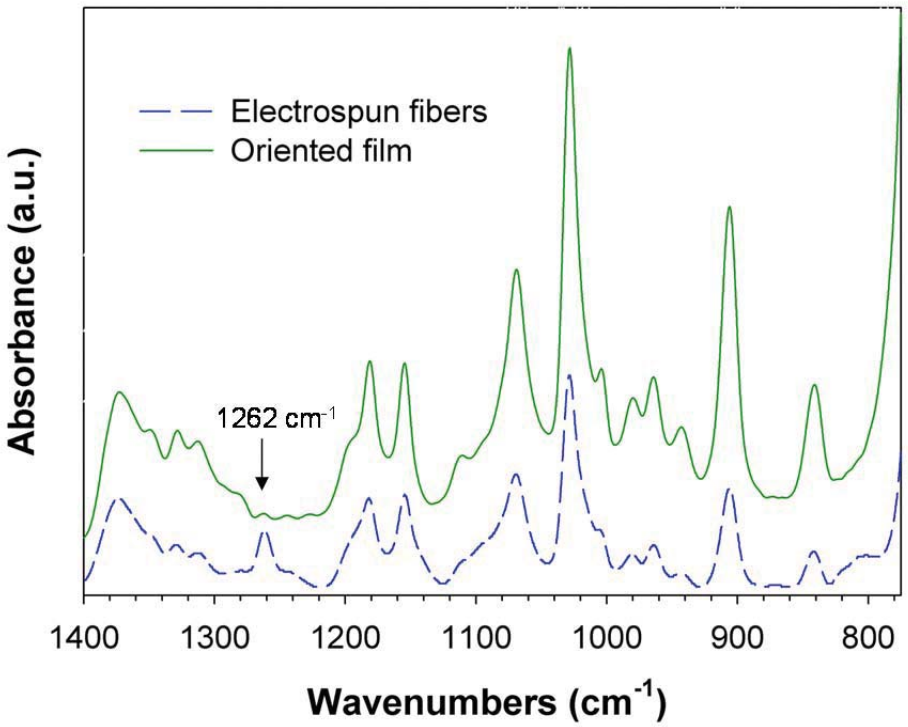

Figure 6.S2: Infrared spectra of electrospun fibers collected from a 10% chloroform solution (blue) and of a highly oriented PS film with $\langle P_2 \rangle = 0.22$ (green).

Chapitre 7. Orientation and partial disentanglement in individual electrospun fibers: diameter dependence and correlation with mechanical properties

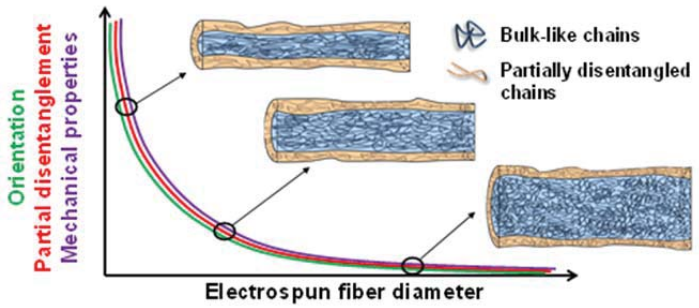

7.1. Abstract

Electrospun fibers are versatile materials that exhibit unusual and tunable properties when studied at the single fiber level, including an exponential increase in modulus with a decreasing diameter toward the nanoscale. Understanding the detailed molecular organization giving rise to this behavior is a key for reaching the ultimate goal of controlling their properties and realizing their full potential as 1D materials. In particular, molecular orientation and chain disentanglement are thought to play a critical role but their study in individual fibers has proven extremely challenging. Here, we quantify molecular orientation in more than 100 individual fibers of atactic polystyrene (PS) from the micro- to the nanoscale by polarized Raman spectroscopy and we probe for the first time a disentanglement-related conformation in the same spectra. We observe an exponential increase of both parameters when decreasing the fiber diameter below an impressively large onset of 2.5 μm, much larger than the typical onset values. The orientation quantified for 500 nm fibers is among the highest values ever reported for PS samples. A clear correlation is found with the previously published diameter dependence of modulus measured in individual PS fibers. Our results also highlight the longitudinal and radial structural heterogeneity of electrospun fibers and suggest separate mechanisms for molecular orientation and disentanglement, which is shown to be mainly situated in the fiber shell. Finally, we combine our observations in a model describing the evolution of chain organization with fiber diameter.[6]

---

[6] Publié comme article complet dans *Macromolecules*, **2015**, 48, *13*, 4511-4519 par Marie Richard-Lacroix et Christian Pellerin

7.2. Introduction

Electrospinning is widely used to produce continuous nanofibers through the application of a high voltage on an entangled polymer solution. Electrospun fibers raise an increasing interest because their small diameter, from tens of nm to a few μm, often leads to unusual or improved physical properties as compared to bulk materials.[1-3] In particular, AFM and nano-tensile testing studies of individual fibers have led to the exciting discovery of a drastic increase in modulus when reducing the fiber diameter below an onset diameter typically around 500-600 nm.[4-7] This observation was repeated for several semi-crystalline and amorphous polymers and is now considered as a general phenomenon.[5-9] The incorporation of electrospun nanofibers in electronic and photonic devices has also led to impressive performance improvements as compared to their thin film counterparts.[10-19] Nevertheless, the controlled production of highly ordered fibers with improved and tunable properties is hampered by our limited comprehension of the structural factors leading to these unusual properties.[8]

The foremost hypothesis to explain the exponential diameter dependence of modulus is a higher molecular orientation in smaller fibers. Modulus and orientation may be directly correlated, in the simplest scenario, but orientation studies on bundles of fibers have led to conflicting results. For instance, Pai et al. have shown a direct orientation/modulus correlation for poly(trimethyl hexamethylene terephthalamide) fibers,[20] while Arinstein et al. have observed a linear increase of orientation, rather than exponential, for Nylon 6.6 fibers.[9] Various models have been proposed to describe the chains organization in oriented fibers, including the formation of confined and oriented nanoscale supramolecular structures,[4,9] of a core-shell fiber morphology in which the oriented chains would be located either in the shell[21] or in the core[22-25], and of mechanically coupled oriented surfaces.[5,6] The heterogeneous distribution of density and molecular organization in fiber cross-sections has recently been highlighted, in agreement with the core-shell model, although the results were again contradictory.[21-23]

Adding to the complexity of the system, it has recently been proposed that the polymer chains are less entangled in electrospun fibers than in the bulk polymer due to the extremely high stretching forces acting on the jet during the fiber formation process.[22-26] The hypothesis

of a lower entanglement density was supported by the formation of short fibers and by X-ray phase contrast imaging of the first few mm of the electrospinning jet.[24-26] We have recently shown that partial disentanglement can last until fiber collection, for bundles of continuous atactic polystyrene (PS) fibers,[27] based on the observation of infrared (IR) bands previously associated to a disentanglement-enabled conformation in PS samples prepared by freeze-drying or by spin-coating diluted solutions.[27-30] In contrast to the above hypothesis, and based on the core-shell morphology of the fibers, we suggested that chains in the shell are kinetically frozen in an incompletely re-entangled state due to the fast solvent evaporation at the jet boundaries. Partial disentanglement is known to increase the thermal and electric conductivities of bulk polymers[31,32] and was suggested to have a large influence on the modulus[22] and the melting point[33-35] of electrospun fibers. The disentanglement hypothesis must therefore be incorporated in models relating the unusual properties of electrospun fibers to their molecular-level organization.

The conflicting results and models explaining the chain organization in electrospun fibers originate, at least in part, from our limited ability to characterize the molecular structure of individual nanofibers. Conventional tools such as X-ray diffraction and IR spectroscopy require studying bundles composed of hundreds of aligned fibers, which often show a broad diameter distribution, in order to achieve an appropriate signal-to-noise ratio. The response is thus a convolution of the true molecular characteristics of each fiber with the macroscopic organization and diameter distribution in the mat. To date, structural studies of single fibers have been mainly conducted using selected area electron diffraction (SAED)[36-39] and scanning near-field optical microscopy (SNOM).[22,23] Unfortunately, SAED only probes the crystalline phase, limiting the range of polymers and parameters that can investigated, while SNOM is limited to conjugated polymers when used in the visible wavelength range. The experimental complexity of these techniques has also restricted previous studies to a few individual fibers, preventing from drawing a statistical picture of the evolution of structural parameters with fiber diameter. We have recently shown that confocal Raman spectroscopy provides rich molecular information (including quantitative molecular orientation) at the single fiber scale for semi-crystalline and amorphous polymers and that it enables studying larger quantities of single fibers within a reasonable time.[40]

Here, we study the diameter dependence of molecular orientation and partial disentanglement in individual electrospun fibers of atactic PS. This system is ideal since complications associated to crystallization are avoided. By studying more than 100 fibers with diameters ranging from 500 to 5000 nm, we establish a direct correlation between the orientation and the exponential increase in modulus (using published data[6] for PS single fibers produced in similar conditions) when decreasing fiber diameter. We further confirm that partial disentanglement is located in the shell and that its amplitude follows the same exponential diameter-dependence as orientation and modulus. Based on these results, we propose a schematic model describing the radial distribution of orientation and partial disentanglement as a function of fiber diameter.

7.3. Experimental

Electrospinning. Atactic polystyrene (Pressure Chemicals) with a weight-average molecular weight of 900 kg/mol (PDI of 1.10) and chloroform (Fisher Scientific) were used as received. Fibers were prepared from 10, 12.5 and 15% w/v solutions in a glass syringe equipped with a 0.41 mm diameter flat-end needle. A flow rate of 0.4-0.8 ml/h was imposed with a PHD 2000 syringe pump (Harvard Apparatus). A 15 kV positive voltage was applied to the needle tip using a CZE 1000R high-voltage power supply (Spellman High Voltage Electronics) while a 2 kV negative potential (Power Designs) was imposed on a rotating disk acting as a counter electrode. The distance between the needle tip and the collector was 15 cm. Small quantities of fibers were carefully transferred on BaF_2 windows and dried under vacuum for at least 12 h prior to analysis by Raman spectroscopy.

Raman spectroscopy. Spectra were recorded in the backscattering geometry using the 632.8 nm He-Ne laser of a LabRam HR800 spectrometer (Horiba Jobin Yvon) coupled with an Olympus BX41 microscope. The confocal hole and the slit were fixed at 100 and 150 μm, respectively. The protocol for preparing oriented PS films[41] and the detailed experimental procedures for Raman measurements on electrospun fibers40 and for quantifying the orientation parameter ($\langle P_2 \rangle$) values[41,42] are provided elsewhere. The polarization of the laser and of the Raman scattering, parallel (Z) and perpendicular (X) to the fiber axis, were selected with the help of a half-wave plate and a polarizer, respectively, such that a complete set of two

parallel-polarized spectra (ZZ and XX) and two crossed-polarized spectra (ZX and XZ) could be recorded (first and second letters referring to the incident and scattered polarizations, respectively). A scrambler was inserted in the optical path before the 600 grooves/mm holographic grating to minimize its polarization dependence. The acquisition time for each spectrum was fixed between 10 s to 2 min, averaged 5 to 10 times.

7.4. Results and discussion

7.4.1. Diameter dependence of orientation in individual PS fibers

PS fibers were electrospun from chloroform solutions at three concentrations in order to produce fibers covering a large diameter range from 500 to 5000 nm. Figure 7.1 shows the four polarized spectra required for quantifying molecular orientation by confocal Raman spectroscopy for two representative PS fibers with diameters of approximately 3 μm and 700 nm. The most commonly used band to probe PS orientation is the totally anti-symmetric skeletal vibration of the benzene ring at 620 cm^{-1}.[43,44] The signal-to-noise ratio is extremely good although the scattering cross-section of this band is weak and the diameter of the smaller fiber is similar to the laser wavelength. The intensity of the parallel-polarized spectra (ZZ and XX) is identical for the 3 μm fiber, indicating that it is completely isotropic. In contrast, the intensity of the XX spectrum is higher than that of the ZZ spectrum for the 700 nm fiber, revealing significant chain orientation. The perpendicular orientation of this band (XX > ZZ) indicates a global orientation of the PS chains along the fiber axis since the Raman tensor associated with this vibrational mode is perpendicular to the main chain.[43,44] As expected when dealing with samples with uniaxial symmetry (a valid approximation for fibers), the cross-polarized spectra (ZX and XZ) are almost identical in both cases.

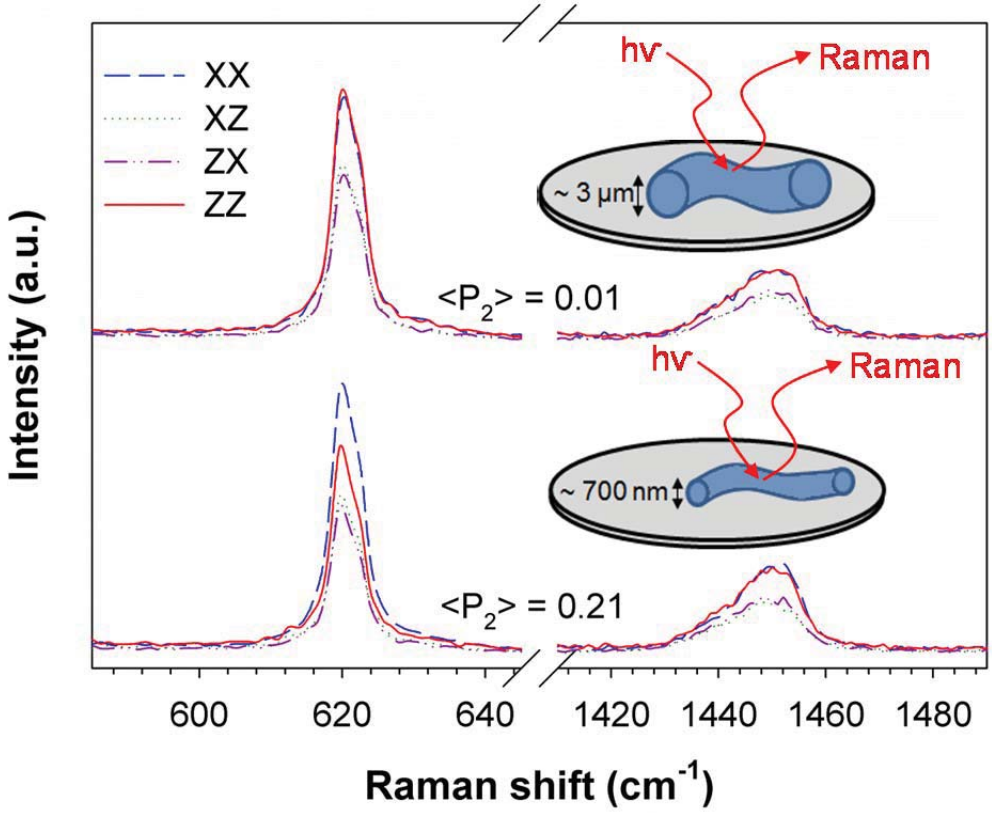

Figure 7.1. Representative sets of four polarized Raman spectra (required for orientation quantification) recorded for individual PS electrospun fibers with a diameter of ~3 μm (top) and 700 nm (bottom) showing no orientation ($\langle P_2 \rangle$ = 0.01) and a high level of orientation ($\langle P_2 \rangle$ = 0.21), respectively.

Quantifying molecular orientation strictly requires calculating the orientation parameter, $\langle P_2 \rangle$, which takes limiting values of 0 for a totally isotropic distribution and 1 for a perfect alignment of the polymer chains along the fiber axis. $\langle P_2 \rangle$ values of 0.01 and 0.21 are found for the 3 μm and 700 nm fibers, respectively, taking into account the tilt angle of 90° of the Raman tensor with respect to the chain axis. These values suggest a strong diameter dependence of molecular orientation, as will be demonstrated below. They were quantified using our simplified method which eliminates restrictive experimental procedures that often induce errors in the calculation of orientation parameters.[42] In particular, the most commonly used procedure leads to an overestimation of molecular orientation in the specific case of oriented PS samples.[41] The accuracy of the $\langle P_2 \rangle$ values is reinforced by the intensity

equivalence of the XX and ZZ spectra for the 1450 cm^{-1} band for both the isotropic and oriented fibers. This behavior, although not previously reported, was also observed for stretched films covering the full range of orientation for PS samples (data not shown). It strongly supports the absence of any drift during (or between) the acquisition of the 4 polarized spectra and confirms the equivalence of the focus quality for both polarizations. Nevertheless, acquiring 4 polarized spectra on micro- or nanoscale fibers is extremely time consuming considering the numerous experiments that must be rejected based on previously described criteria.[40] Not respecting these stringent conditions could induce large errors in the $\langle P_2 \rangle$ values of individual fibers. To circumvent this issue, a calibration curve enabling the quantification of $\langle P_2 \rangle$ using a single polarized Raman spectrum was established using 35 fibers and validated by 7 oriented films (see Figures 7.S1 and 7.S2 in the supporting information).

The molecular orientation of 100 additional PS fibers covering the 500 – 5000 nm diameter range was quantified using the calibration procedure. Figure 7.2A shows the evolution of $\langle P_2 \rangle$ as a function of diameter, averaged over ranges of ~200 nm. The largest fibers, with diameters from 5000 to approximately 2500 nm, are essentially isotropic with $\langle P_2 \rangle$ = 0 within experimental error. In sharp contrast, reducing the diameter below 2500 nm clearly leads to an exponential increase of the average $\langle P_2 \rangle$ values, as supported by the high correlation coefficient associated to this fit. Some of the smallest fibers (diameter ~500 nm) reach unexpectedly high orientation for PS samples with $\langle P_2 \rangle$ values as high as 0.3. Such large values have only been reported for PS films cold drawn in the Tg region[45] and for stretched blends of PS with a miscible polymer,[46] emphasizing the extremely large stretching forces to which these smallest fibers must have been submitted during their formation. To the best of our knowledge, the only other study of orientation in PS electrospun fibers (using small angle neutron scattering) led to moderate orientation values ($\langle P_2 \rangle < 0.15$), even after considering the alignment of fibers within the studied bundles.[47]

It can be observed in Figure 7.2A that the standard deviation increases strongly for fibers with a diameter below 2.5 μm. In fact, Figure 7.S3 reveals that a broad distribution of orientation (with $\langle P_2 \rangle$ of 0 vs. 0.21) exists for small fibers with a very similar diameter in spite of a good signal-to-noise ratio and identical XX and ZZ intensities for the orientation-

insensitive band at 1450 cm^{-1}. We thus associate this observation to a real distribution of $\langle P_2 \rangle$ values rather than to experimental uncertainty. We also observed an analogous broad distribution in a previous study of poly(ethylene terephthalate) electrospun fibers. In that case, the $\langle P_2 \rangle$ values were quantitatively correlated with the fraction of *trans* conformers associated to the formation of a mesophase made possible by the orientation of the chains.[40] These results highlight the reality of the distribution of structural characteristics for fibers of a given diameter and, thus, the requirement of probing large quantities of fibers for an accurate diameter–orientation correlation to emerge. It should be stressed that the large distribution of $\langle P_2 \rangle$ values in Figure 7.2A is highly reminiscent of that observed for mechanical properties measured at the single fiber level, suggesting that they share the same origin in the chaotic nature of jet elongation in the whipping zone during the electrospinning process.[9,20] In the context of this study, the use of a rotating collector might have induced additional stretching of the fibers and contributed to the extremely large orientation in the smallest fibers. Further investigations are necessary to discriminate the relative contributions of the collector and of the fiber formation process.

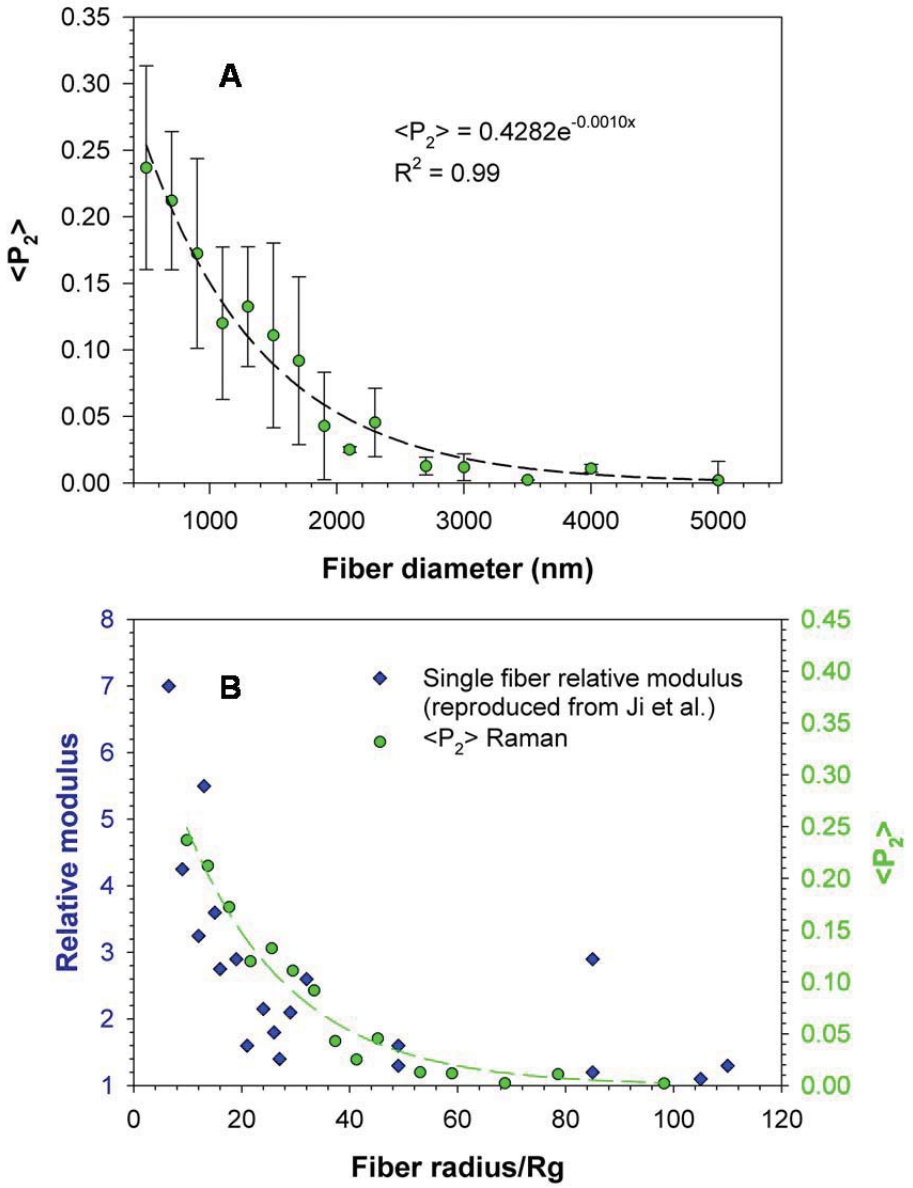

Figure 7.2. A) Exponential dependence of molecular orientation ($\langle P_2 \rangle$) as a function of the fiber diameter for PS electrospun fibers. The results for n = 135 fibers are averaged over ~200 nm ranges. **B)** Demonstration of the direct correlation between the diameter dependence of relative modulus and molecular orientation. The modulus values were obtained by Ji et al.[6] using shear modulation force microscopy at the single fiber level. The fiber radii are normalized by their radius of gyration (Rg) to take into account the use of PS samples with different molecular weights.

Interestingly, the onset point for the beginning of the exponential increase in orientation is situated at approximately 2500 nm, much larger than the 500-600 nm range often reported in studies of the modulus evolution with the fiber diameter.[8] This impressively large onset

diameter can be explained by the high molecular weight of the PS used in this work. Ji et al. have studied the mechanical properties of single fibers of PS (produced in conditions similar to this study) over a large range of molecular weights using AFM-based shear modulation force microscopy and three-point bending techniques. They observed an exponential increase of modulus with a decreasing fiber diameter in all cases and found that, when normalizing the fiber radius with the radius of gyration (Rg) of the chains, the diameter-dependence of the modulus becomes essentially independent of molecular weight.[6] Their relative moduli (normalized with respect to the bulk value) are reproduced in Figure 7.2B (blue diamonds) as a function of normalized fiber radius. The orientation values of Figure 7.2A are also reproduced (green circles) after normalizing the fiber radius with a Rg of 25.45 nm for our 900 kg/mol PS.[48] Figure 7.2B clearly shows an extremely strong correlation between the modulus and the molecular orientation. To the best of our knowledge, it is the first time that such direct correlation is established between mechanical properties and molecular orientation measured both at the single fiber scale. Since atactic PS cannot crystallize, these results strongly support the hypothesis that the several-fold increase in modulus observed in the past years for several polymers is mainly due to molecular orientation. This does not exclude, however, that stress-induced crystallization can amplify the phenomenon for crystallizable polymers. In addition, as discussed in the following sections, the molecular orientation and chain organization are not necessarily homogeneous throughout the fiber.

The fact that the onset for the exponential increase of molecular orientation occurs at a large diameter for a polymer with a high molecular weight (2.5 μm for PS of 900 kg/mol) offers interesting possibilities in the field of electrospinning. Indeed, it avoids the need of producing fibers with extremely small diameters in order to achieve some of their exceptional properties caused by high orientation and/or to take advantage of their diameter-dependent properties. Based on the results of Figure 7.2B, the usual 500-600 nm diameter onset would be expected, in first approximation, for a PS with Mw ~ 40 kg/mol, a typical molecular weight for many polymers. The onset could reach values as large as 3.7 μm for fibers produced from solutions of PS with Mw ~ 2000 kg/mol. In this mindset, it should be possible to transpose the nanoscale properties of electrospun fibers to the micron scale, when appropriate, for any polymer by simply selecting a sample with a higher molecular weight. This would allow

producing larger fibers that are much more convenient to manipulate and to characterize by techniques with a limited spatial resolution while preserving an unusually high orientation and improved diameter-dependent properties.

7.4.2. Partial disentanglement in individual polystyrene fibers

We have recently shown that PS fibers prepared in the same conditions as here present "new" IR bands that indicate the presence of chains adopting an out-of-equilibrium conformation associated with a level of chain entanglement lower than in the bulk.[27] The same bands were previously reported only for freeze-dried samples and for ultrathin spin-coated films,[28-30] samples for which it is well accepted that the chains are kinetically frozen in a partially disentangled state.[28,29,49,50] Sasaki et al.[29] concluded that partial disentanglement enables an expanded conformation, much less probable in the bulk, due to the presence of at least one of these bands in the spectrum of crystalline isotactic PS.

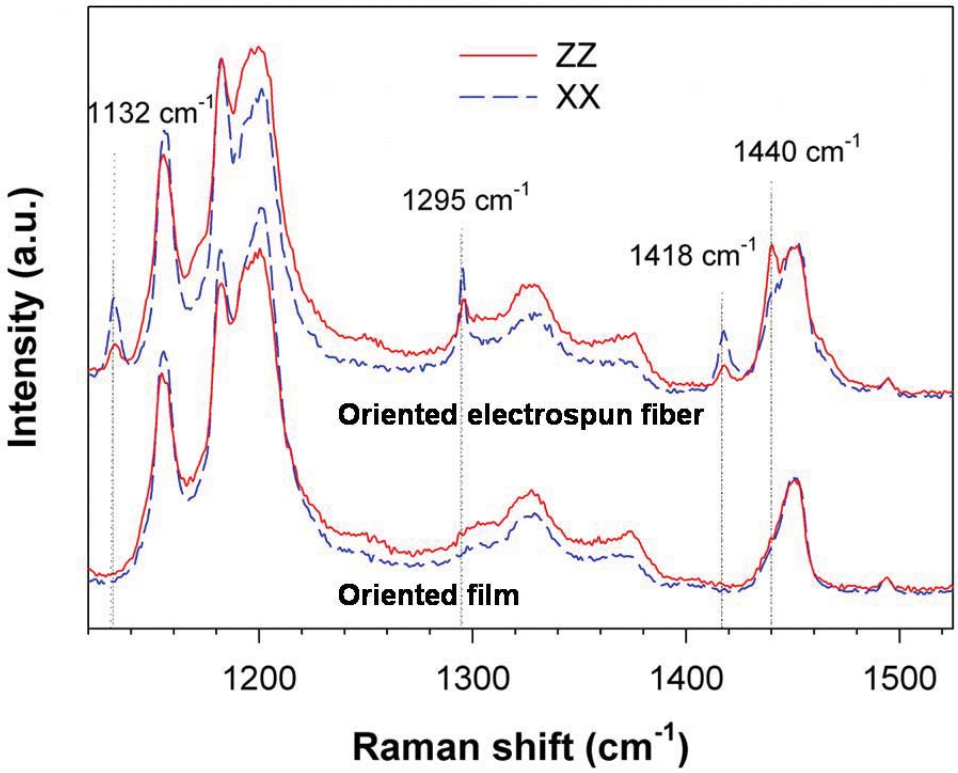

Figure 7.3. Comparison of the parallel-polarized Raman spectra of an electrospun PS fiber of 500 nm ($\langle P_2 \rangle$ = 0.17) with those of an oriented PS film ($\langle P_2 \rangle$ = 0.20). New bands in the fiber spectra are highlighted and are associated to a conformation made possible by partial chain disentanglement.

In a similar way, we observed for the first time unexpected bands in the Raman spectra of some PS fibers. Figure 7.3 highlights the differences between the ZZ and XX spectra of a 500 nm PS fiber (top) in the 1120-1520 cm^{-1} spectral range with those of an oriented film (bottom). These samples have similar $\langle P_2 \rangle$ values, 0.20 for the film and 0.17 for the fiber. New bands at 1132, 1295, 1418 and 1440 cm^{-1} are clearly discernable in the spectra of the fiber, in addition to a new shoulder around 1230 cm^{-1} and the possible presence of other bands overlapped with the intense bands around 1200 cm^{-1}. Interestingly, two of these new bands (1295 and 1440 cm^{-1}) are also present in the Raman spectra of crystalline isotactic PS adopting a 3/1 helix conformation.[51,52] It is noteworthy that chloroform does not share these Raman bands and that no traces of contamination were noticed in the IR spectra of the fibers. The absence of the new bands in the spectra of oriented films confirms that bulk orientation does not lead to this specific conformation. Consequently, we associate these new Raman bands to a conformation made possible by partial chain disentanglement in electrospun fibers.

Our previous IR study suggested that partial disentanglement is related to the formation of a shell, as revealed by a wrinkled fiber morphology in the SEM pictures of Figure 7.S4. When using a highly volatile solvent such as chloroform, a polymer-rich region is created at the edges of the electrospinning jet due to the fast solvent evaporation.[25,53] This limits the mobility of the polymer chains and hinders their complete re-entanglement. The final level of entanglement should therefore be intermediate between the bulk value and that in the partially entangled semi-diluted initial solution.[27] The shell is denser than the core when it forms and acts as a wall that severely slows the evaporation of the solvent remaining in the core. Its eventual evaporation induces a buckling that gives rise the wrinkled morphology observed in Figure 7.S4.[54,55]

Confocal Raman spectroscopy enables mapping the longitudinal and radial distribution of the new bands in fibers. The intensity of the 1295 cm^{-1} band was chosen for this purpose due to its common characteristics with the 1262 cm^{-1} IR band (used in our previous work) in terms of position and association with crystalline isotactic PS. However, it is not perfectly isolated and appears as a very weak shoulder in the spectra of films. One must eliminate this bulk contribution to compare quantitatively fibers produced in different conditions and/or at different positions on a single fiber. The orientation effects (further discussed below) on its

intensity must also be taken into account. For this purpose, we calculated an “isotropic” intensity using the ZZ and XX spectra[40] and used oriented PS films as a baseline comparison. This led to the evaluation of the "EID" value, the Excess of isotropic Intensity associated to a conformation made possible by Disentanglement. The procedure is described in more details in the supporting information. EID values higher than 20 % will be associated to partial disentanglement (for comparison, the largest value obtained for a highly oriented film was 15%).

Figure 7.4A shows the optical microscopy image of a PS fiber, for which the core-shell morphology is clearly discernible, along with the EID values quantified at three radial locations using the ZZ and XX spectra shown in Figure 7.4B. The much higher EID on the edges, as compared to the center of the fiber, supports the hypothesis that partial disentanglement mainly appears in the shell. The spatial resolution of Raman spectroscopy (~1 μm, represented by the colored circles) is much larger than the expected thickness of the shell[21,22] such that the shell cannot be fully isolated from the core and the EID values result from their combined contributions. They nevertheless clearly expose the heterogeneity of the radial distribution and the primary localization of the partially disentangled chains.

According to the core-shell model, large beads should be composed of chains in their bulk-like state (i.e. fully entangled and isotropic) since the evaporation of the massive quantity of solvent entrapped in this enormous core, after the shell solidification, should induce the relaxation of molecular orientation and the loss of any conformation associated to partial disentanglement. Indeed, all large beads analyzed (not shown) were found to be isotropic and to possess an EID similar to that of films. However, Figure 7.4C shows that the case of elongated beads is more complex. The EID values at the left edge of this bead are comparable to those at the edges of the fiber shown in Figure 7.4A, but those on the right edge of the bead are much smaller. Since the core of this specific bead is thicker close to its right edge, it occupies a larger fraction of the sampled volume and dominates the Raman signal, leading to low EID values.

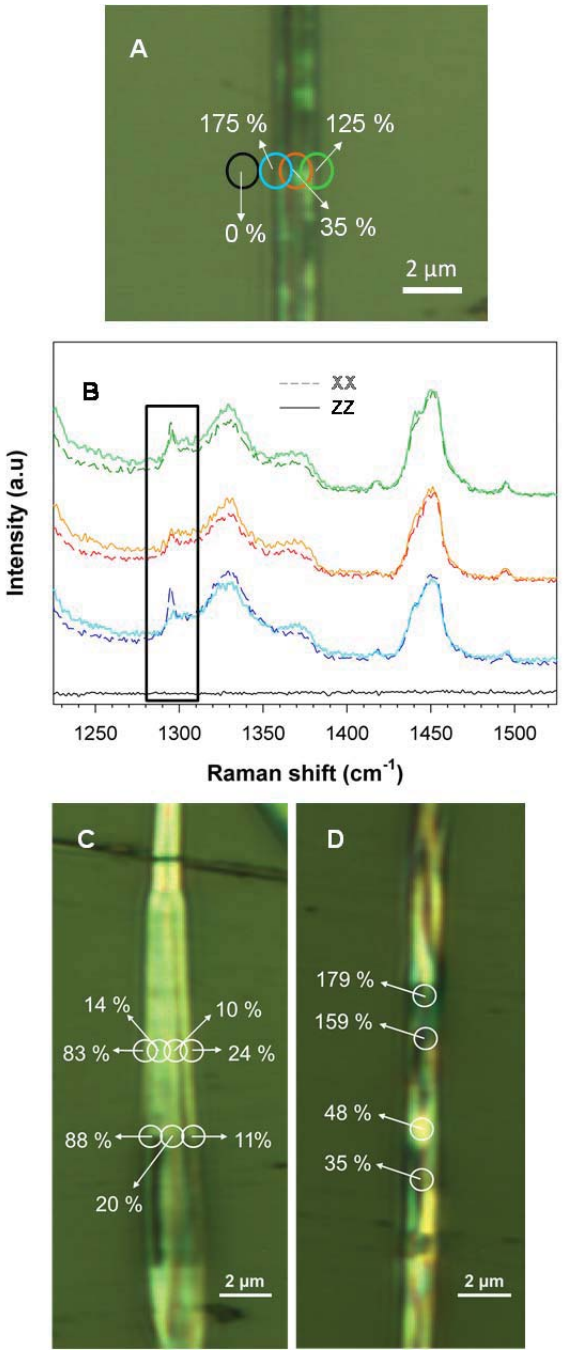

Figure 7.4. A) Radial Raman mapping of the Excess of isotropic Intensity of the 1295 cm^{-1} band associated to partial Disentanglement of the chains (EID) for a fiber showing a wrinkled morphology on the micrometer scale. **B)** Parallel-polarized Raman spectra recorded at the similarly-colored mapping positions shown in panel A. **C)** Raman mapping of the EID of an elongated bead showing a core-shell morphology. **D)** Longitudinal Raman mapping of a fiber showing a wrinkled morphology.

Most fibers (and beads) do not show a core-shell morphology as apparent as those in Figure 7.4A and C (i.e. with a thick core surrounded by a collapsed shell) when observed by optical microscopy. Most fibers, such as the one shown in Figure 7.4D, rather exhibit a wrinkled morphology which is also associated with a core-shell organization in the fiber. In such cases, the EID values are highly heterogeneous along the fiber axis: some sections appear to be dominated by the shell (EID > 100%) while others show core-like values, although the fiber does not show any clear diameter variation. This is analogous to the case of molecular orientation for which a large distribution of $\langle P_2 \rangle$ values was observed for fibers of a similar diameter.

The EID values were quantified for 135 fibers and are plotted as a function of diameter in Figure 5. For fibers larger than the laser spot (or with the type of morphology shown in Figure 7.4A), the measurements were made in the center of the fiber. Figure 7.5A reveals an exponential increase of the EID values with a decreasing fiber diameter which is extremely similar to the diameter-dependence of orientation (reproduced as green circles). The average EID values remain below 20 % (close to the 15% bulk value) for fibers larger than 2 μm but it increases sharply for smaller fibers. The EID results are more scattered than their orientation counterpart, especially for the smallest diameters. Based on the results of Figure 7.4D, which show a large EID distribution for a given diameter, we believe that this scatter exposes a real distribution of the presence of the conformation made possible by a lower level of entanglement in fibers. However, the results are affected by a much larger uncertainty caused by the low intensity of the 1295 cm^{-1} band.

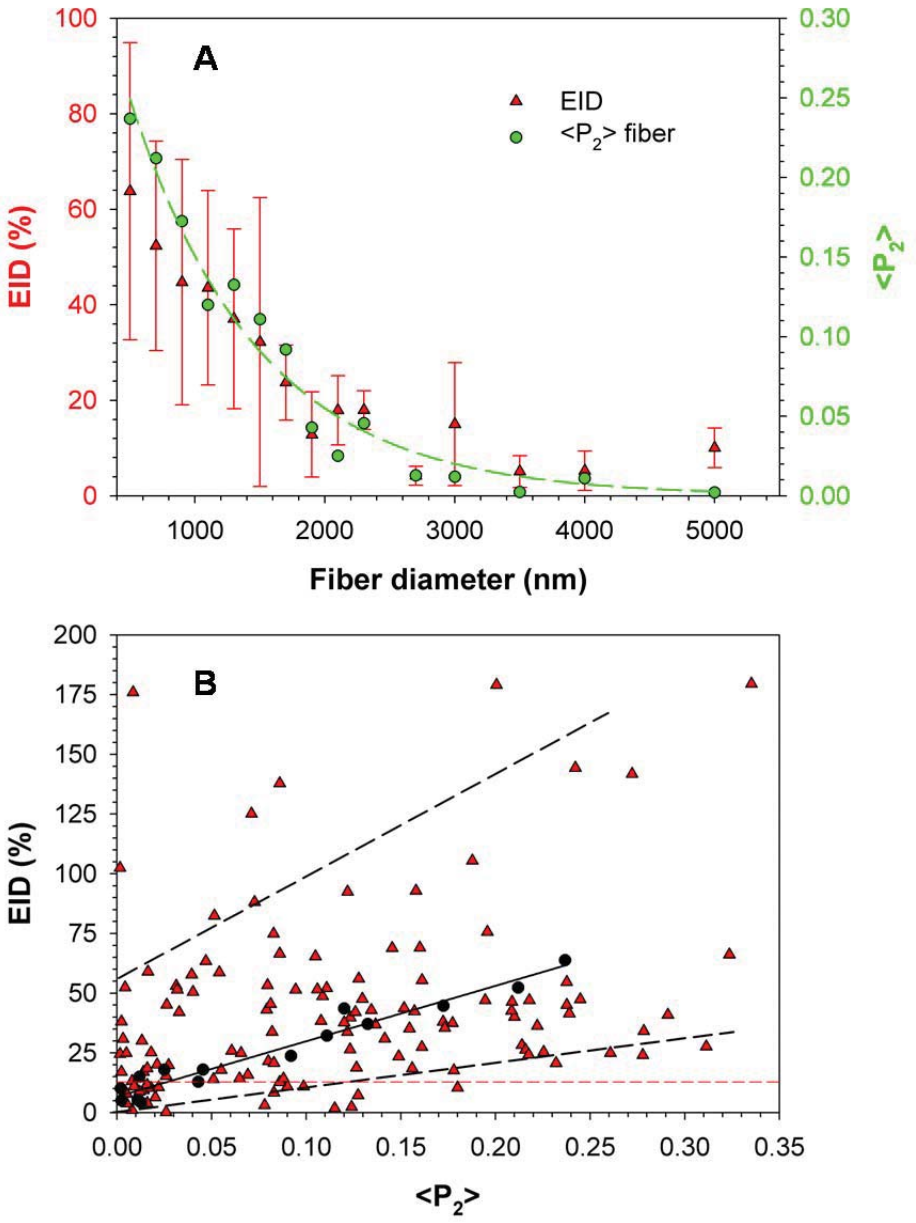

Figure 7.5. A) Diameter dependence of the Excess of isotropic Intensity of the 1295 cm^{-1} band associated to partial Disentanglement of the chains (EID) (red triangles). The orientation results are reproduced (green circles) to highlight the similarity of their diameter dependence. **B)** Orientation dependence of the EID values determined for 135 individual fibers (red triangles). The black circles and plain black line show the linear relationship between the average values of EID and $\langle P_2 \rangle$ while the dashed black lines approximately delimit the range of the distribution. The dashed red line indicates the largest EID value observed in oriented films and represents a bulk-like state of entanglement.

The results of Figure 7.5A appear to suggest a direct orientation / disentanglement correlation due to the close similarity of their diameter dependence. Indeed, Figure 7.5B demonstrates that the average EID values increase approximately linearly as a function of $\langle P_2 \rangle$ (black circles and plain black line). However, Figure 7.5B also shows as red triangles the individual EID / $\langle P_2 \rangle$ couples for each of the 135 fibers analyzed, along with additional results obtained when mapping the edges of some fibers (such as in Figure 7.4). A general increase of EID with orientation can still be observed but it is clear that the spread of the values is extremely large, for any given $\langle P_2 \rangle$. In some cases, a high level of orientation is associated with a fairly low amplitude of the disentanglement phenomenon. The opposite is also true, some fibers showing a large EID in spite of a moderate $\langle P_2 \rangle$ value. Accordingly, although they share an average diameter dependence that is remarkably similar, orientation and disentanglement are therefore only indirectly correlated. As a consequence, Figure 7.5B provides key information on the organization of the system by revealing the absence of a causal relationship between these two parameters.

These results are in partial disagreement with the model proposed by Zussman et al. according to which chain orientation and partial disentanglement occur in the core of the fiber due to the large stretching forces acting on the jet.[23-26,33-35] As a consequence, disentanglement and orientation should be directly correlated because the first occurs as a consequence of the second. In this model, the rapid solvent evaporation leading to the complete solidification of the shell would restrict the occurrence of both phenomena.[23-26,33-35] This does not correspond to our observations for PS fibers, for which a lower apparent entanglement density is rather found in the shell due to the rapid solvent evaporation that would prevent complete re-entanglement. The different origins for stress-induced orientation and for solvent evaporation-induced incomplete re-entanglement would therefore enable the decoupling of the orientation and EID values observed in Figure 7.5B. Our results do not exclude that stretching-induced disentanglement could also take place and lead to an increase of the amplitude of the phenomenon in the shell while simultaneously inducing it in the core. However, they strongly suggest that this mechanism is not the main driving force for the lower level of chain entanglement in these fibers.

Another important information on the chain organization in PS fibers is provided by the anisotropy of the Raman bands associated to a lower degree of entanglement. So far, we have only considered the $\langle P_2 \rangle$ values quantified using the 620 cm^{-1} band representing the overall state of f the most probable organization of the chains consistent with the diameter dependence observed here for orientation and partial disentanglement molecular orientation in the fibers. However, Figures 7.3 and 7.4B clearly show that the intensity in the XX spectrum is significantly and systematically higher than in the ZZ spectrum for three of the four new bands (the opposite is observed for the 1440 cm^{-1} band). This implies that the chains adopting this conformation are highly oriented, most likely along the fiber axis.

7.4.3. Schematic representation of chains organization in PS fibers

Our aim is now to draw an overall picture o and reported by Ji et al.[6] for the mechanical properties. For this purpose, four main conclusions must be taken into consideration: 1) from Figure 7.2A, the global molecular orientation increases exponentially when decreasing the fiber diameter, following extremely well the trend reported for the modulus[6]; 2) from the SEM pictures, it can be concluded that the fibers possess a core-shell morphology; 3) from Figure 7.5A, the average volume fraction of chains showing the conformation enabled by partial disentanglement (the EID values) also increases exponentially with diameter reduction; and 4) from Figure 7.4, these partially disentangled chains are mainly found in the shell and they are systematically highly oriented whenever observed. Taken together, these factors lead to the schematic representation in Scheme 7.1 of core-shell fibers larger (top), close to (middle) and smaller (bottom) than the onset diameter of ~2.5 μm.

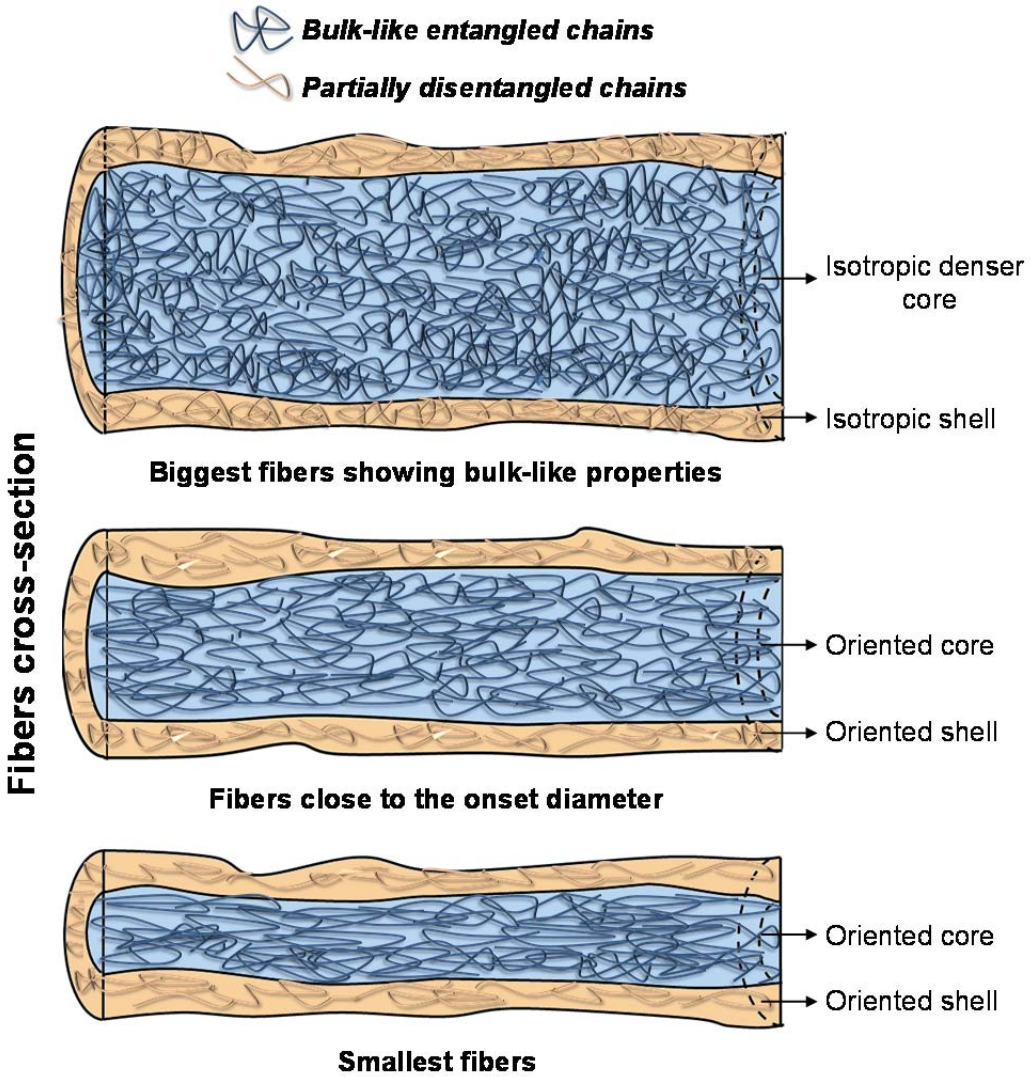

Scheme 7.1. Schematic representation of the chain organization in PS electrospun fibers showing a core-shell morphology with a constant shell thickness. Fibers are composed of bulk-like entangled chains in the core (blue) and of partially disentangled chains in the shell (orange). For the largest fibers (top), the orientation distribution is isotropic in the core. When reducing the fiber diameter close to or below the onset diameter for exponential increase of the modulus, chains in both the shell and the core show a significant level of orientation (middle fiber). Further reducing the fiber diameter toward the nanoscale leads to an increasingly high level of orientation and to an increasing apparent level of disentanglement (EID) due the increasing volume fraction of the shell.

The largest fibers show bulk-like mechanical properties and molecular structure with no orientation and no measurable disentanglement. The core (blue section) is thus composed of isotropic chains with a bulk-like degree of entanglement. Based on the SEM pictures (Figure 7.S4), the shell (orange section) is preserved even for large fibers but, due to its extremely

small volume fraction as compared to the core, the 1295 cm^{-1} band (whose intensity is always small) is not detectable in the Raman spectra. Depending on the fiber diameter, the shell can therefore contain either incompletely or totally re-entangled chains. The orientation of chains in the shell cannot be estimated directly but, knowing that orientation relaxation is a much faster process than chain re-entanglement,[56-58] we speculate that the slow evaporation of the large amount of solvent trapped in the core of large fibers enables an almost complete orientation relaxation. It is noteworthy that this description of large fibers is also applicable to most beads.

As the fiber diameter is reduced close to and below (middle and bottom of Scheme 7.1, respectively) the onset value, the situation in the shell becomes more explicit. The spectral markers for the conformation associated to partially disentangled chains are now clearly present and they increase drastically with a decreasing fiber diameter. Since the shell forms at the early stage of the electrospinning process (less than a few mm from the spinneret), its thickness should be independent of diameter (for fibers produced from solutions at the same concentration). This is in line with the AFM observation by Stachewicz et al.[21] of a constant average shell thickness of ~30 nm for poly(vinyl alcohol) fibers over a large range of diameters. The increase in EID when reducing the fiber diameter is therefore mainly a simple consequence of the increasing volume fraction of the shell.

It is well established that the polymer density is higher in the shell than in the core, at the moment when it forms, due to the rapid solvent evaporation during the electrospinning process.[25,53] In contrast, it has been proposed in the literature that the shell is either more[21] or less[22] dense than the core once the fiber has reached its final state and the solvent is completely removed. Although the shell density has never been measured for PS fibers, our results point toward a less dense shell since it would contain polymer chains that are kinetically frozen by rapid solvent evaporation into an incompletely re-entangled state.

The fibers with a diameter below the onset also show an exponentially increasing molecular orientation that is highly correlated with the increasing modulus. It has been suggested in the literature, in the context of a core-shell morphology, that an increasing orientation could be due to 1) a highly oriented shell surrounding an essentially isotropic core

(due to slow solvent evaporation enabling orientation relaxation in the core), or 2) an oriented core surrounded by a more or less isotropic shell (because its fast drying would prevent its deformation during the later stages of the electrospinning process). Our results clearly show that the chains in the shell (at least those presenting the Raman conformational markers for incomplete entanglement) are oriented, which is more in line with the first proposition. However, it is very unlikely that the core of the PS fibers remains isotropic. Indeed, the $\langle P_2 \rangle$ values quantified for the smallest fibers using the 620 cm^{-1} band, which reflect the global orientation in the sample, are sometimes close to the maximum value that has ever been reached for PS samples. To mathematically reproduce these results in an oriented shell / isotropic core model, one would need to assume unrealistic $\langle P_2 \rangle$ values as compared to the highest $\langle P_2 \rangle$ values reported for atactic PS stretched films. In addition, the results of Figure 7.5B revealed that a large $\langle P_2 \rangle$ value is sometimes found in spite of a bulk-like EID value, which appears inconsistent with the scenario of an isotropic core.

We thus conclude that the core and the shell both present a significant level of orientation along the fiber axis for fibers below the onset diameter. The core orientation increases for smaller fibers since they must experience a larger overall stretching during their travel towards the collector. The early solidification of the shell implies that all fibers initially entrapped a similar amount of solvent whose presence and eventual evaporation favors orientation relaxation and chain re-entanglement. However, the solvent removal process is sped up for thinner fibers by their stretching-induced diameter reduction, leading to an increasingly larger residual orientation (and to a reduced tendency toward re-entanglement in the shell). According to Zussman et al.,[22-26] stretching could also lead to additional disentanglement either in the shell or in the core of the fiber. Accordingly, reducing the fiber diameter below the onset, as represented at the bottom of Scheme 7.1, leads to an increase of the volume fraction of the partially disentangled shell and to an exponential increase of orientation in the core (and most likely in the shell). In this scenario, the modulus in the shell should be reduced by the presence of partially disentangled chains and by a lower density, as proposed by Camposeo et al. based on polarized SNOM measurements of poly[2-methoxy-5-(2-ethylhexyloxy)-1,4-phenylenevinylene] fibers. In practice, this effect on the overall modulus is clearly compensated by the increasingly higher orientation of the chains forming

the denser core (and possibly by an increasing orientation of the chains in the shell) as the diameter is reduced, leading to the commonly observed exponential increase of modulus.

It is noteworthy that Scheme 7.1 represents the general tendencies for the averaged $\langle P_2 \rangle$ and EID values quantified in this study. As discussed above and shown explicitly in Figure 7.4, the longitudinal and radial distributions of $\langle P_2 \rangle$ and EID can be extremely large and they do not necessarily correlate at each point of a fiber. The strength of this model resides in the large number of individual fibers that could be probed by Raman spectroscopy, allowing us to draw statistically meaningful conclusions about the chain organization in amorphous electrospun fibers.

7.5. Conclusion

We have established the first orientation / mechanical properties correlation for individual electrospun fibers using atactic polystyrene as a model amorphous system. The results show a direct correlation that supports the controlling role of molecular orientation on the increasing mechanical properties of electrospun fibers when reducing their diameter toward the nanoscale. Probing large quantities of fibers allowed demonstrating the heterogeneity of the distribution for a given diameter while still providing a statistically meaningful diameter correlation for the averaged values. We also observed for the first time Raman bands associated to a conformation made possible by partial disentanglement of the chains. Mapping of the radial distribution of these bands shows that partially disentangled chains are mainly situated in the shell of the fiber, suggesting that they mainly originate from incomplete re-entanglement rather than from stress-induced disentanglement. The average excess intensity of these bands nevertheless follows the same exponential increase as orientation when reducing the diameter due to the increasing volume fraction of the shell. The capability of Raman to simultaneously probe incomplete re-entanglement and orientation in a single set of spectra enabled highlighting the absence of direct correlation between these phenomena. A model describing the radial chain organization as a function of fiber diameter is proposed in the context of electrospinning fibers using a volatile solvent that enables shell formation, which represents a very common situation. Our aim is now to generalize and refine

this model by studying the impact of different solvent parameters and of molecular weight on the chain organization.

7.6. Acknowledgments

This work was supported by a grant and a graduate scholarship (MRL) from the Natural Sciences and Engineering Research Council of Canada (NSERC). We are grateful to F. Byette for his assistance for the SEM imaging.

7.7. References

1. Luo, C.J.; Stoyanov, S.D.; Stride, E.; Pelan, E.; Edirisinghe, M. *Chem. Soc. Rev.* **2012,** *41*, 4708-4735.
2. Agarwal, S.; Wendorff, J.H.; Greiner, A. *Adv. Mater.* **2009,** *21*, 3343-3351.
3. Persano, L.; Camposeo, A.; Tekmen, C.; Pisignano, D. *Macromol. Mater. Eng.* **2013,** *298*, 504-520.
4. Arinstein, A. *J. Polym. Sci. Part B* **2013,** *51*, 756-763.
5. Ji, Y.; Li, B.; Ge, S.; Sokolov, J.C.; Rafailovich, M.H. *Langmuir* **2006,** *22*, 1321-1328.
6. Ji, Y.; Li, C.; Wang, G.; Koo, J.; Ge, S.; Li, B.; Jiang, J.; Herzberg, B.; Klein, T.; Chen, S.; Sokolov, J.C.; Rafailovich, M.H. *Europhys. Lett.* **2008,** *84*, 56002.
7. Papkov, D.; Zou, Y.; Andalib, M.N.; Goponenko, A.; Cheng, S.Z.; Dzenis, Y.A. *ACS nano* **2013,** *7*, 3324-3331.
8. Richard-Lacroix, M.; Pellerin, C. *Macromolecules* **2013,** *46*, 9473-9493.
9. Arinstein, A.; Burman, M.; Gendelman, O.; Zussman, E. *Nat. Nanotechnol.* **2007,** *2*, 59-62.
10. Pu, J.; Yan, X.; Jiang, Y.; Chang, C.; Lin, L. *Sensor Actuat. A-Phys.* **2010,** *164*, 131-136.
11. Canesi, E.V.; Luzio, A.; Saglio, B.; Bianco, A.; Caironi, M.; Bertarelli, C. *ACS Macro Letters* **2012,** *1*, 366-369.
12. Liu, H.; Reccius, C.H.; Craighead, H.G. *Appl. Phys. Lett.* **2005,** *87*, 253106.
13. Lee, S.W.; Lee, H.J.; Choi, J.H.; Koh, W.G.; Myoung, J.M.; Hur, J.H.; Park, J.J.; Cho, J.H.; Jeong, U. *Nano Letters* **2009,** *10*, 347-351.

14. Shin, M.; Song, J.H.; Lim, G.-H.; Lim, B.; Park, J.-J.; Jeong, U. *Adv. Mater.* **2014,** *26*, 3706-3711.
15. Tu, D.; Pagliara, S.; Camposeo, A.; Persano, L.; Cingolani, R.; Pisignano, D. *Nanoscale* **2010,** *2*, 2217-2222.
16. Chen, J.-Y.; Kuo, C.-C.; Lai, C.-S.; Chen, W.-C.; Chen, H.-L. *Macromolecules* **2011,** *44*, 2883-2892.
17. Lin, C.J.; Hsu, J.C.; Tsai, J.H.; Kuo, C.C.; Lee, W.Y.; Chen, W.C. *Macromol. Chem. Physic* **2011,** *212*, 2452-2458.
18. Ding, B.; Wang, M.; Wang, X.; Yu, J.; Sun, G. *Mater. Today* **2010,** *13*, 16-27.
19. Huang, C.; Soenen, S.J.; Rejman, J.; Lucas, B.; Braeckmans, K.; Demeester, J.; De Smedt, S.C. *Chem. Soc. Rev.* **2011,** *40*, 2417-2434.
20. Pai, C.-L.; Boyce, M.C.; Rutledge, G.C. *Polymer* **2011,** *52*, 2295-2301.
21. Stachewicz, U.; Bailey, R.J.; Wang, W.; Barber, A.H. *Polymer* **2012,** *53*, 5132-5137.
22. Camposeo, A.; Greenfeld, I.; Tantussi, F.; Pagliara, S.; Moffa, M.; Fuso, F.; Allegrini, M.; Zussman, E.; Pisignano, D. *Nano Lett.* **2013,** *13*, 5056-5062.
23. Camposeo, A.; Greenfeld, I.; Tantussi, F.; Moffa, M.; Fuso, F.; Allegrini, M.; Zussman, E.; Pisignano, D. *Macromolecules* **2014,** *47*, 4704-4710.
24. Greenfeld, I.; Arinstein, A.; Fezzaa, K.; Rafailovich, M.H.; Zussman, E. *Phys. Rev. E* **2011,** *84*, 041806.
25. Greenfeld, I.; Fezzaa, K.; Rafailovich, M.H.; Zussman, E. *Macromolecules* **2012,** *45*, 3616-3626.
26. Greenfeld, I.; Zussman, E. *J. Polym. Sci. Part B* **2013,** *51*, 1377-1391.
27. Richard-Lacroix, M.; Pellerin, C. *Macromolecules* **2015,** *48*, 37-42.
28. Sasaki, T.; Tanaka, M.; Takahashi, T. *Polymer* **1997,** *38*, 4765-4768.
29. Sasaki, T.; Tanaka, M.; Takahashi, T. *Polymer* **1998,** *39*, 3853-3857.
30. Tretinnikov, O.N.; Zbankov, R.G. *Macromolecules* **2004,** *37*, 3543-3545.
31. Noriega, R.; Rivnay, J.; Vandewal, K.; Koch, F.P.V.; Stingelin, N.; Smith, P.; Toney, M.F.; Salleo, A. *Nat. Mater.* **2013,** *12*, 1038-1044.
32. Shen, S.; Henry, A.; Tong, J.; Zheng, R.; Chen, G. *Nat. Nano.* **2010,** *5*, 251-255.
33. Arinstein, A.; Liu, Y.; Rafailovich, M.; Zussman, E. *Europhys. Lett.* **2011,** *93*, 46001.
34. Arinstein, A.; Zussman, E. *J. Polym. Sci. Part B* **2011,** *49*, 691-707.

35. Liu, Y.; Chen, S.; Zussman, E.; Korach, C.S.; Zhao, W.; Rafailovich, M. *Macromolecules* **2011,** *44*, 4439-4444.
36. Yoshioka, T.; Dersch, R.; Greiner, A.; Tsuji, M.; Schaper, A.K. *Macromol. Mater. Eng.* **2010,** *295*, 1082-1089.
37. Yoshioka, T.; Dersch, R.; Tsuji, M.; Schaper, A.K. *Polymer* **2010,** *51*, 2383-2389.
38. Ma, X.; Liu, J.; Ni, C.; Martin, D.C.; Chase, D.B.; Rabolt, J.F. *ACS Macro Letters* **2012,** *1*, 428-431.
39. Tosaka, M.; Yamaguchi, K.; Tsuji, M. *Polymer* **2010,** *51*, 547-553.
40. Richard-Lacroix, M.; Pellerin, C. *Macromolecules* **2012,** *45*, 1946-1953.
41. Richard-Lacroix, M.; Pellerin, C. *Macromolecules* **2013,** *46*, 5561-5569.
42. Richard-Lacroix, M.; Pellerin, C. *Appl. Spectrosc.* **2013,** *67*, 409-419.
43. Jasse, B.; Chao, R.S.; Koenig, J.L. *J. Polym. Sci. A1* **1978,** *16*, 2157-2169.
44. Jasse, B.; Koenig, J.L. *J. Polym. Sci. A1* **1980,** *18*, 731-738.
45. Jasse, B.; Koenig, J.L. *J. Polym. Sci. A1* **1979,** *17*, 799-810.
46. Pellerin, C.; Prud'homme, R.E.; Pézolet, M. *Macromolecules* **2000,** *33*, 7009-7015.
47. Mohan, S.D.; Mitchell, G.R.; Davis, F.J. *Soft Matter* **2011,** *7*, 4397.
48. Shin, K.; Pu, Y.; Rafailovich, M.H.; Sokolov, J.; Seeck, O.H.; Sinha, S.K.; Tolan, M.; Kolb, R. *Macromolecules* **2001,** *34*, 5620-5626.
49. Chen, J.; Xue, G.; Li, Y.; Wang, L.; Tian, G. *Macromolecules* **2001,** *34*, 1297-1301.
50. Sun, Q.; Zhou, D.; Wang, X.; Xue, G. *Macromolecules* **2002,** *35*, 7089-7092.
51. Cornell, S.W.; Koenig, J.L. *J. Appl. Phys.* **1968,** *39*, 4883-4890.
52. Painter, P.C.; Koenig, J.L. *J. Polym. Sci. A1* **1977,** *15*, 1885-1903.
53. Guenthner, A.J.; Khombhongse, S.; Liu, W.; Dayal, P.; Reneker, D.H.; Kyu, T. *Macromol. Theor. Simul.* **2006,** *15*, 87-93.
54. Arinstein, A.; Avrahami, R.; Zussman, E. *J. Phys. D Appl. Phys.* **2009,** *42*, 015507.
55. Pai, C.-L.; Boyce, M.C.; Rutledge, G.C. *Macromolecules* **2009,** *42*, 2102-2114.
56. Teng, C.; Gao, Y.; Wang, X.; Jiang, W.; Zhang, C.; Wang, R.; Zhou, D.; Xue, G. *Macromolecules* **2012,** *45*, 6648-6651.
57. Huang, Q.; Alvarez, N.J.; Matsumiya, Y.; Rasmussen, H.K.; Watanabe, H.; Hassager, O. *ACS Macro Letters* **2013,** *2*, 741-744.
58. Napolitano, S.; Capponi, S.; Vanroy, B. *Eur. Phys. J. E* **2013,** *36*, 1-37.

7.8. Supporting information

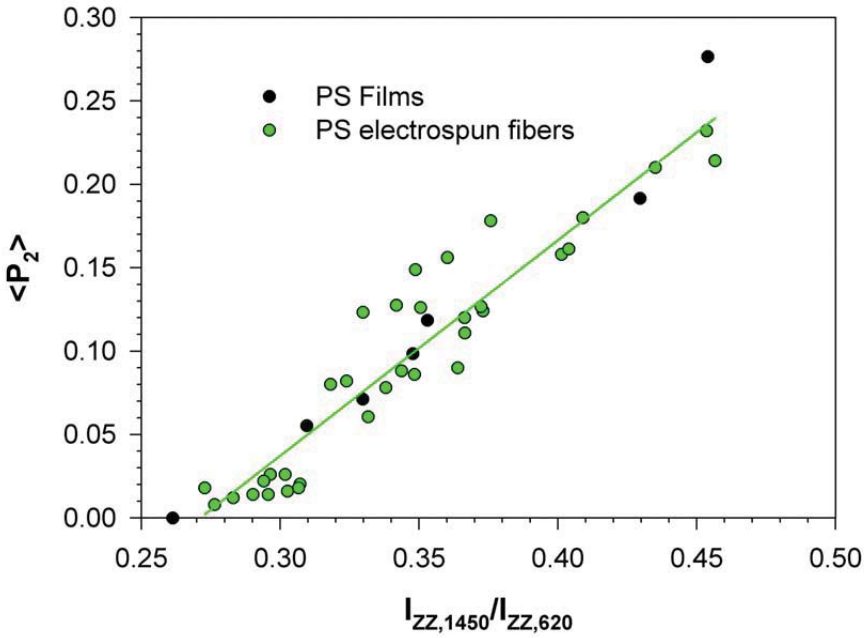

Figure 7.S1. Calibration curve linking the $\langle P_2 \rangle$ value to the 1450/620 cm^{-1} band ratio of the ZZ spectra for fibers (green circles) and films (black circles) covering the accessible orientation range for PS samples.

Figure 7.S1 shows the linear relationship between $\langle P_2 \rangle$ and the 1450/620 cm^{-1} band ratio in ZZ spectra quantified on 35 individual PS fibers (green circles). The reliability of the orientation quantification on these fibers was confirmed by measurements on oriented PS films (black circles) and by the observation of a linear relationship between $\langle P_2 \rangle$ and the XX/ZZ ratio of the 620 cm^{-1} band for the fibers and the films (Figure 7.S2).

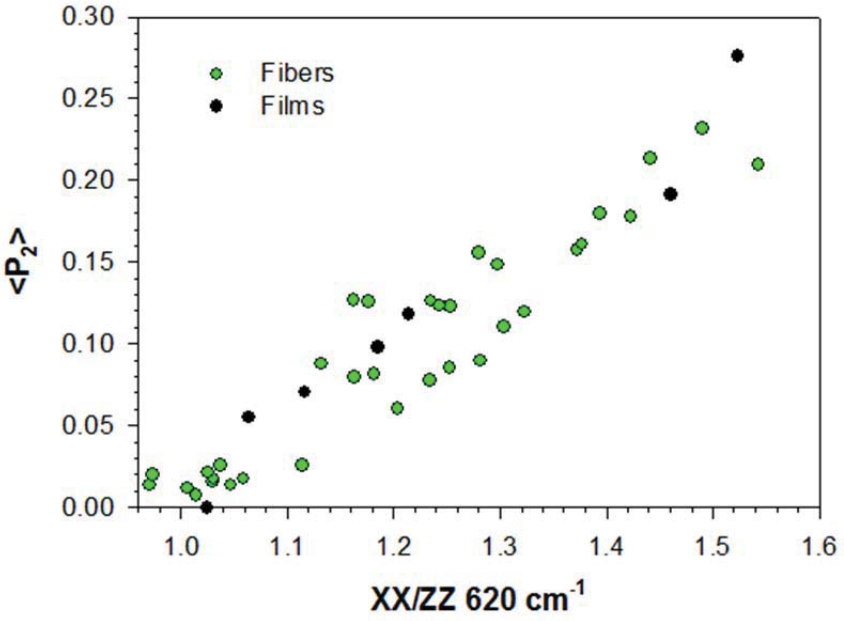

Figure 7.S2. Calibration curve relating the orientation parameter ($\langle P_2 \rangle$) to the ratio of the parallel-polarized spectra (XX/ZZ) of the 620 cm^{-1} band for oriented films and electrospun fibers.

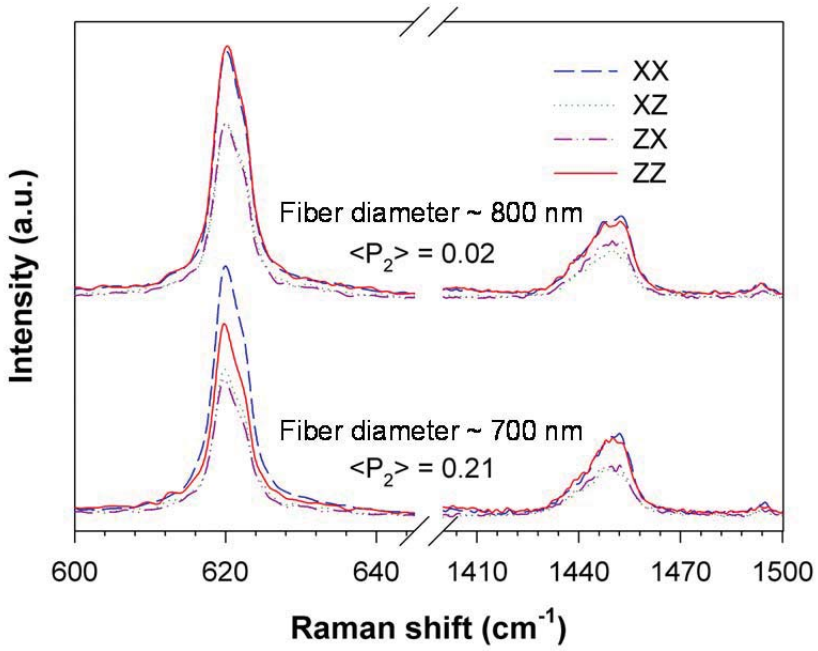

Figure 7.S3. Representative series of the four polarized Raman spectra recorded for PS electrospun fibers with similar diameters (~800 and 700 nm for the top and bottom spectra,

respectively). The very large heterogeneity of the orientation for fibers of similar diameter is revealed by the absence of orientation ($\langle P_2 \rangle$ = 0.01) and the high level of orientation ($\langle P_2 \rangle$ = 0.21) calculated from the top and bottom spectra, respectively.

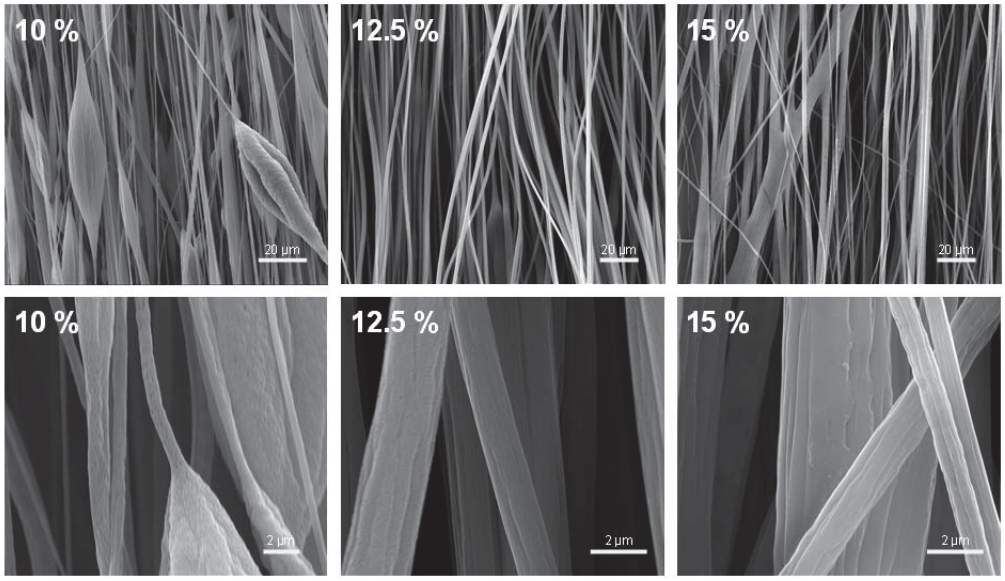

Figure 7.S4. SEM images of polystyrene fibers produced from 10, 12.5 and 15 % w/v solutions in chloroform.

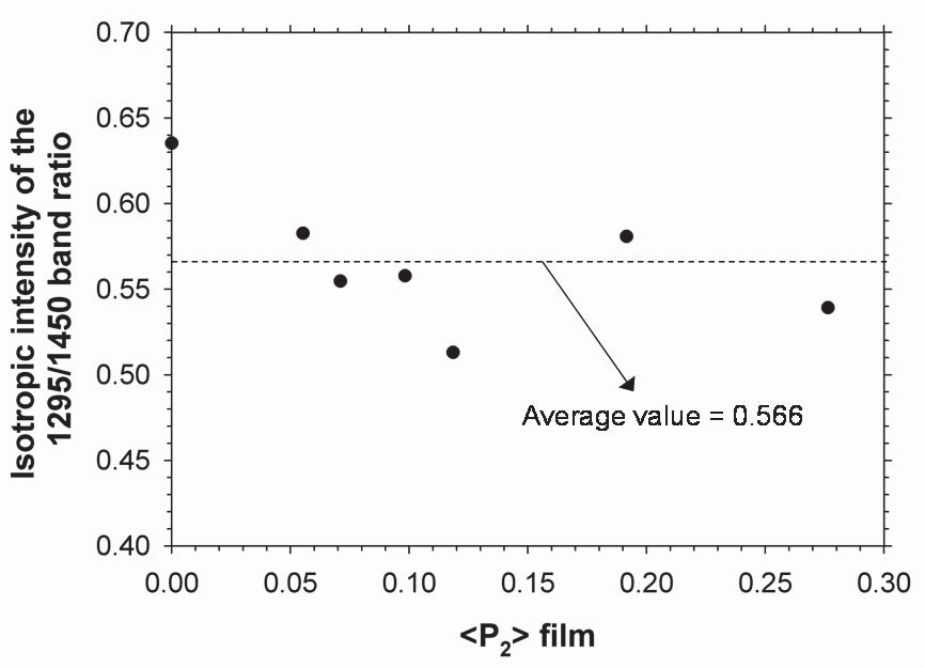

Figure 7.S5. Isotropic intensity of the 1295 cm^{-1} quantified according to Equation 1 for PS films showing a wide range of orientation.

In order to calculate the Excess of isotropic Intensity associated to partial Disentanglement of the chains (EID), it is necessary to eliminate the bulk contribution to the 1295 cm^{-1} band and to correct for the orientation effects. The intensity of the 1295 cm^{-1} was first normalized with the 1450 cm^{-1} band, which we have shown to be insensitive to orientation both in films and in fibers, to take into account the sampled volume. The isotropic normalized intensity was then calculated using the infrared structural absorbance equation, i.e. using only the intensity of XX and ZZ spectra. A more accurate procedure to quantify isotropic Raman intensities has been demonstrated by Lefèvre et al.[1] and involves using the four polarized spectra available in the backscattering geometry as well as the depolarization ratio of the band of interest. However, the 1295 cm^{-1} band is weak and juxtaposed to another weak band, such that band fitting is prone to a large uncertainty, especially for the crossed-polarized spectra. The alternative approach used here is only semi-quantitative as it does not take into account the possible impact of $<P_4>$ variations (which are expected to be small in the $<P_2>$ range observed for PS samples based on the most probable orientation distribution function) but it provides a reliable relative EID scale. The method was shown to be effective for quantifying the *gauche* and *trans* conformer fractions in poly(ethylene terephthalate) fibers and to provide results correlating well with previous studies.[2]

$$I_{iso} = \left(\frac{1295}{1450}\right)_{ZZ} + 2\left(\frac{1295}{1450}\right)_{XX} \quad (7.1)$$

These quantities were then normalized with the average value quantified for oriented films (0.566, see Figure 7.S5), covering a large range of orientation values, and transformed in percentage. 100 % was finally subtracted with the aim of quantifying the excess of isotropic intensity as compared to oriented films (Equation 7.2).

$$I_{iso\ 1295\ cm^{-1},\ excess} = \left(\left(\frac{I_{iso}}{0.566}\right) x\ 100\right) - 100\ \% \quad (7.2)$$

Because the average isotropic intensity of the films was used for this calculation, most of the films show either small negative or positive excess percentages. The maximum observed in a film is 15% and defines the maximum value that could be reached for a bulk oriented sample. To take into account the uncertainty due to noise in the Raman spectra, only EID

value larger than 20% are associated to the presence of the conformation made possible by partial disentanglement of the chains.

References.

1. Lefèvre, T.; Rousseau, M. E.; Pézolet, M. *Appl. Spectrosc.* **2006**, *60*, 841-846.
2. Richard-Lacroix, M.; Pellerin, C. *Macromolecules* **2012**, *45*, 1946-1953.

8. Conclusions et perspectives

8.1. Conclusion

Dans le contexte actuel qui tend vers un contrôle de plus en plus fin des propriétés des matériaux et vers la constante miniaturisation de multiples types de dispositifs, les études structurales à l'échelle des fibres électrofilées individuelles sont rapidement devenues critiques pour l'avenir de ces matériaux. Des méthodologies de spectroscopie Raman confocale permettant l'atteinte de cet objectif ont été développées dans le cadre de cette thèse, puis appliquées sur des systèmes simples qui ont révélé certains aspects surprenants des fibres électrofilées. Une emphase importante a été mise sur l'étude de l'orientation moléculaire, un paramètre important et influençant plusieurs propriétés des fibres telles que leurs propriétés mécaniques, leur conductivité électrique et leur conductivité thermique.

Dans un premier temps, les Chapitres 3 et 4 visaient le développement d'une méthode de quantification de l'orientation moléculaire par spectroscopie Raman polarisée dans l'optique d'en simplifier l'utilisation expérimentale, d'élargir la gamme des matériaux pouvant être étudiés et de réduire considérablement les erreurs pouvant être commises par les approximations se cachant derrière les méthodes généralement utilisées. L'idée générale consiste à remplacer une des approximations de la méthode couramment utilisée (appelée ici DC pour « depol constant ») par une autre, expérimentalement moins contraignante et en accord avec la réalité de la plupart des échantillons à l'étude. Plus spécifiquement, la méthode DC est basée sur la quantification expérimentale du ratio de dépolarisation de la bande d'intérêt à partir de mesures polarisées sur un échantillon parfaitement isotrope. Elle suppose que le tenseur Raman est cylindrique et que sa forme est constante sur tout le domaine possible d'orientation. La nouvelle méthode (nommée MPD pour « most probable distribution »), développée au Chapitre 3, montre qu'il est possible de conserver l'approximation du tenseur cylindrique mais d'éliminer la quantification expérimentale du paramètre lui-même. L'équation décrivant la forme du tenseur est remplacée par une équation décrivant la distribution d'orientation la plus probable associée à un paramètre d'ordre ($<P_2>$) donné. Cette méthode implique toutefois le sacrifice de la quantification du $<P_4>$, dont le rôle est principalement le raffinement de la description de la distribution d'orientation.

Le potentiel de la méthode sur une vaste gamme de matériaux a d'abord été démontré à partir de simulations sur l'ensemble des distributions d'orientation pouvant théoriquement être rencontrées. Il a été démontré que la méthode MPD permet de quantifier le paramètre d'ordre $<P_2>$ avec très peu d'erreur (un écart-type équivalent ou inférieur à 0.05) pour des échantillons dont la distribution d'orientation est relativement éloignée de la courbe de la distribution la plus probable dans le diagramme $<P_2><P_4>$. Dans ce même chapitre, il a été démontré par simulation que l'amplitude des erreurs générées par la méthode conventionnelle DC dépend du ratio de dépolarisation de la bande d'intérêt : pour des ratios de dépolarisation faibles ou élevés, une petite erreur lors de la détermination expérimentale de ce paramètre entraîne des erreurs importantes sur la valeur de $<P_2>$ extraite; en revanche, pour un mode dont ratio de dépolarisation est « intermédiaire », de grandes erreurs expérimentales sur sa quantification et/ou son évolution avec l'orientation n'ont que très peu d'influence sur le $<P_2>$ quantifié.

Armé de ces résultats, le Chapitre 4 démontre la puissance de la méthode MPD par son application expérimentale sur des films et/ou des fibres de trois polymères différents, soit le polyéthylène de haute densité (HDPE), le poly(éthylène téréphtalate) (PET) et le polystyrène (PS), couvrant toute la gamme des orientations qui leurs sont accessibles. La quantification d'orientation à partir de mesures Raman polarisées a permis la comparaison des méthodes DC et MPD. Les $<P_2>$ obtenus ont également été comparés avec des étalonnages Raman provenant de la littérature (HDPE) ou avec des valeurs quantifiées par spectroscopie infrarouge polarisée (PET et PS). Pour le HDPE, les résultats ont démontré que, pour des valeurs d'orientation faibles, les méthodes DC et MPD sont toutes deux en relativement bon accord avec la courbe d'étalonnage. Par contre, pour des valeurs d'orientation plus élevées, la méthode DC mène à une sous-estimation du paramètre d'ordre alors que la méthode MDP demeure en très bon accord avec l'étalonnage. De manière cohérente avec les simulations du Chapitre 3, ces erreurs sont associées au faible ratio de dépolarisation du mode utilisé pour quantifier l'orientation. Il a également été démontré que l'utilisation du $<P_4>$, quantifié par la méthode DC, mène fréquemment à des conclusions erronées sur l'organisation moléculaire du système. Par la suite, deux bandes du spectre du PET ont été analysées. L'une d'elle est associée à l'orientation globale des chaînes en englobant les parties amorphe et cristalline. Son ratio de dépolarisation étant intermédiaire, les méthodes DC et MPD s'accordent toutes deux

particulièrement bien avec la quantification effectuée en IR sur les mêmes échantillons, et ce, sur toute la gamme d'orientation à l'étude. Une autre bande du spectre Raman du PET, associée aux conformations *trans* des chaînes, a également été analysée. Le ratio de dépolarisation de cette bande ne peut pas être quantifié puisqu'il a été démontré qu'elle est associée à une mésophase formée principalement par étirement. Cette phase intrinsèquement orientée peut difficilement être reproduite sous une forme isotrope à l'échelle du micromètre, ou même de quelques micromètres, rendant ainsi impossible la quantification du ratio de dépolarisation et l'utilisation de la méthode DC. À l'inverse, la méthode MDP a permis une quantification de l'orientation moléculaire de cette mésophase et montré des résultats cohérents avec la haute orientation anticipée. Finalement, l'analyse d'échantillons de PS, en comparaison avec des mesures par spectroscopie IR, a également permis de confirmer que, aux basses orientations, les méthodes DC et MPD sont en bon accord et cohérentes avec les résultats quantifiés par IR alors que, aux plus hautes orientations accessibles à ces échantillons, la méthode DC montre une nette déviation par rapport à la méthode MPD et aux résultats IR. Encore ici, ces déviations sont associées à l'évolution du ratio de dépolarisation avec l'orientation pour une bande dont le ratio de dépolarisation est près de la valeur la plus élevée possible. Au global, au-delà de l'applicabilité de la méthode MPD elle-même, ces résultats ont mis en évidence l'évolution du ratio de dépolarisation avec l'orientation, sa conséquence sur les valeurs de $<P_2>$ quantifiées, ainsi que l'impact plus important de l'approximation que le ratio de dépolarisation est constant, par rapport à l'approximation de la forme cylindrique du tenseur, sur les valeurs d'orientation.

Par la suite, au Chapitre 5, un protocole expérimental permettant les mesures d'orientation sur des fibres électrofilées individuelles, de manière stricte et crédible, a été développé et validé en utilisant le PET comme système modèle. Les limites expérimentales de ce protocole, dont principalement l'impossibilité d'effectuer la mesure d'orientation sur une fibre de diamètre inférieur à 500 nm, ont été mises en évidence. De même, une méthodologie d'étalonnage, basée sur la mesure d'un seul spectre polarisé, a été proposée pour réduire significativement le temps nécessaire à l'étude d'une quantité statistiquement représentative de fibres. Cette stratégie permet notamment d'évaluer l'orientation de fibres de diamètre inférieur à 500 nm. La validité de la mesure a été démontrée par l'équivalence des intensités des

spectres polarisés parallèles (XX et ZZ) pour une bande rapportée comme étant insensible à l'orientation des fibres mesurées. La fraction de conformères *trans* a également été quantifiée à partir des spectres Raman parallèles. Il a été démontré que la fraction de ces conformères augmente significativement avec l'orientation, de manière cohérente avec d'autres études spectroscopiques ayant démontré que l'orientation du PET se produit par un changement de *gauche* vers *trans* de la conformation des chaînes. Le taux de cristallinité a également été quantifié à l'aide des spectres Raman et évalué comme étant faible pour l'ensemble des fibres individuelles étudiées, menant à la conclusion que les fibres orientées sont principalement composées de mésophases, soit un état pré-cristallin. Cette étude a également mis en évidence pour la première fois la distribution très importante des valeurs d'orientation pour un diamètre moyen d'environ 500 nm: certaines fibres étaient pratiquement isotropes alors que d'autres montraient des valeurs d'orientation aussi élevées que 0.70. Cette étude est ainsi la première à démontrer que de très hautes valeurs d'orientation peuvent être atteintes par des fibres composées d'un polymère dont la vitesse de cristallisation est relativement lente et donc, dont le taux de cristallinité est généralement faible

Au Chapitre 6, un autre aspect structural a été étudié, soit le taux d'enchevêtrement plus faible dans les fibres de polystyrène que ce qui est typiquement retrouvé dans la masse. Bien que cette hypothèse ait été soulevée par un autre groupe de recherche et que le phénomène ait été proposé comme étant potentiellement responsable de certaines propriétés des fibres (Chapitre 2), aucun résultat expérimental n'avait permis de confirmer directement la présence de chaînes partiellement désenchevêtrées. Les résultats du Chapitre 6 montrent que la spectroscopie infrarouge permet de sonder le phénomène dans le cas du PS atactique par l'apparition de bandes associées à une conformation rendue possible par un taux d'enchevêtrement plus faible que dans la masse. Il a également été démontré que l'absorbance relative de ces bandes (par rapport à une bande insensible à la conformation des chaînes) augmente significativement avec la diminution du temps alloué à la collection des fibres et avec la diminution de la concentration initiale de la solution. De même, la morphologie des fibres, observée par microscopie électronique à balayage, suggère que ces dernières possèdent une « gaine » provenant de la solidification rapide de la partie externe du jet dû à l'utilisation de solvants très volatils pour la production des fibres. Dans ce contexte, un modèle regroupant

les résultats experimentaux et extrapolant le comportement réel des amas de fibres a été proposé. Ces conclusions soulèvent également un point important : si la capacité des fibres à conserver le désenchevêtrement partiel des chaînes est corrélée au temps de collection et si ce phénomène a lui-même des conséquences sur les propriétés des fibres, tel que suggéré par plusieurs autres études, alors les propriétés des fibres dépendent, dans une certaine mesure, du temps de collection.

Au Chapitre 7, les méthodologies Raman développées aux Chapitres 3, 4 et 5 ont tout d'abord été utilisées pour étudier l'évolution de l'orientation moléculaire avec le diamètre des fibres pour des fibres de PS. L'étude de plus d'une centaine de fibres individuelles a mis en évidence une augmentation exponentielle de l'orientation moléculaire avec la réduction du diamètre ainsi qu'une forte augmentation de la dispersion des résultats à partir du diamètre critique d'environ 2.5 μm, c'est-à-dire le diamètre à partir duquel cette évolution est observable. Ces résultats ont été corrélés à des valeurs de module d'élasticité, mesurées à l'échelle de la fibre unique par un autre groupe de recherche, mettant en évidence des évolutions extrêmement similaires avec le diamètre. Ils ont également permis de constater les valeurs d'orientation élevées pouvant être atteintes dans les fibres électrofilées de systèmes amorphes, comparé aux valeurs modestes obtenues par étirement de films. De plus, des bandes associées à une conformation des chaînes rendue possible lorsque le degré d'enchevêtrement est plus faible que dans la masse et montrant clairement une orientation élevée (le plus probablement dans l'axe de la fibre) ont été identifiées dans le spectre Raman. En faisant un calcul simple et approximatif pour éliminer l'effet de l'orientation dans le signal associé à ces bandes, il a été possible de comparer l'amplitude du phénomène d'une fibre à l'autre et d'en déterminer la distribution axiale et longitudinale dans une même fibre. Cette étude a permis de mettre en évidence la distribution fortement hétérogène du désenchevêtrement le long de l'axe des fibres et de le situer principalement dans la gaine, en accord avec le modèle présenté au Chapitre 6. Il a également été démontré que l'évolution de l'amplitude du phénomène avec la réduction du diamètre est similaire à celle de l'orientation moléculaire et du module d'élasticité. En couplant ces informations, un modèle expliquant l'évolution de l'ensemble de ces paramètres avec la réduction du diamètre a été présenté. Ce modèle propose notamment que la gaine soit d'épaisseur moyenne similaire, peu importe le diamètre des fibres, de

manière à ce que sa fraction volumique par rapport à l'ensemble de la fibre augmente avec la diminution du diamètre. Cette gaine serait partiellement composée de chaînes très orientées et montrant un degré d'enchevêtrement plus faible que celui dans la masse. Finalement, l'orientation de plus en plus prononcée du cœur de la fibre permet de justifier l'évolution globale de l'orientation et du module avec la diminution du diamètre des fibres. Cette étude présente la toute première relation structure/propriétés établie à l'échelle de la fibre électrofilée individuelle.

Au global, il est primordial de souligner que les études reliées à la caractérisation des nanofibres électrofilées rapportées dans cette thèse ne font qu'effleurer la surface de ce qui pourra dorénavant être exploré grâce aux nouvelles méthodologies développées. Ces travaux ont très certainement tracé la voie vers des études à la fois plus accessibles et plus approfondies de ces matériaux. Plusieurs des perspectives présentées dans la prochaine section évoquent des exemples de projets rendus possibles dorénavant. Dans ce contexte, les différentes méthodologies développées, loin de représenter une fin en soi, constituent en fait une ouverture permettant l'étude raffinée des nanofibres électrofilées et pouvant s'étendre à d'autres types de matériaux.

8.2. Perspectives

8.2.1. Études fondamentales sur les fibres électrofilées individuelles par spectroscopie Raman confocale

En faisant une analyse détaillée de la littérature des fibres electrofilées, en particulier celle des fibres individuelles, plusieurs aspects surprenants, dont l'origine moléculaire apparaît plus que complexe, ressortent. Tel que soulevé dans la perspective présentée au Chapitre 2, il est par exemple fascinant de constater que les mesures de propriétés mécaniques à l'échelle de la fibre individuelle mènent toutes à une conclusion conceptuellement identique : une augmentation exponentielle du module avec la réduction du diamètre des fibres et ce, peu importe la nature du polymère, le taux de cristallinité, la méthode de collection utilisée ou la nature du solvant.[1-6] D'autres propriétés, telles que la conductivité thermique, ont récemment montré des évolutions similaires avec la réduction du diamètre.[7]

En revanche, plusieurs modèles tentant d'expliquer le comportement des fibres avec la réduction du diamètre font appel à des concepts divergents et suggèrent une distribution radiale des caractéristiques structurales des chaînes en désaccord évident.[5,8-10] La première étude montrant que différentes formes d'évolution des propriétés mécaniques en fonction du diamètre peuvent être obtenues en modifiant simplement la distance seringue /collecteur n'a été publiée que récemment.[11] De même, il a été démontré que la masse molaire influence la valeur du diamètre critique pour des fibres de PS,[9] éliminant par le fait même l'idée longtemps véhiculée que la taille de la fibre (soit un diamètre critique universel de 500 nm) était le facteur principal influençant les propriétés. À notre connaissance, ces deux études sont les seules ayant suggéré que la forme de la courbe d'évolution de module avec le diamètre peut être modifiée et, donc, qu'elle dépend de d'autres paramètres expérimentaux.

La littérature nous offre plusieurs indications sur les facteurs susceptibles d'influencer les propriétés. Il est par exemple connu que la morphologie des fibres est reliée, au moins en partie, à des paramètres tels que la volatilité du solvant.[12,13] Cette morphologie est elle-même associée à des distributions radiales de densité qui diffèrent d'un système à l'autre. Par exemple, les solvants volatils sont connus pour mener à la formation d'une gaine (ou plus

spécifiquement à la conservation de la gaine jusqu'au moment de la collection).[14-17] En parallèle à l'étude présentée au Chapitre 7, d'autres groupes ont récemment démontré une relation entre la présence d'une gaine et la distribution hétérogène de caractéristiques structurales des chaînes en fonction de la position radiale, que ce soit en terme d'orientation et de densité[18,19] ou de distribution spatiale de formes cristallines polymorphes.[10]

Somme toute, les effets du solvant, des caractéristiques du polymère lui-même (telles que sa capacité à cristalliser) et de la méthode de collection, pour n'en nommer que quelques-uns, sur l'orientation moléculaire et sur certaines propriétés des fibres sont essentiellement inexplorés, en particulier à l'échelle de la fibre unique. Dans l'optique de prédire les propriétés des fibres, de les optimiser et/ou de les moduler à partir d'une simple sélection du diamètre pour un système donné, de telles études sont incontournables. Les six sous-sections suivantes présentent des projets détaillés, dont certains sont entamés, qui visent essentiellement l'atteinte de ces objectifs.

8.2.1.1. Effet de solvant sur l'orientation et le désenchevêtrement des fibres

L'objectif principal de ce premier projet est de pousser l'établissement des relations structure/propriétés des fibres jusqu'aux relations structure/propriétés/morphologie. Dans cette optique, deux paramètres sont prioritairement à étudier, soit 1) l'effet de la volatilité du solvant et 2) l'effet de l'affinité relative du polymère avec le solvant (χ) sur l'orientation et sur le désenchevêtrement. L'effet de l'humidité relative est un paramètre supplémentaire qui, par le biais de l'affinité du solvant avec l'eau, peut influencer les propriétés[20] ainsi que la morphologie des fibres.[12,21]

Plus spécifiquement, on cherche à créer des conditions expérimentales dans lesquelles différentes morphologies sont formées pour comprendre l'influence de la morphologie sur l'orientation (l'orientation retenue). Ces études peuvent également donner des indices sur les mécanismes de formation de la fibre, donnant lieu à différentes distributions longitudinales et radiales de l'orientation. Ces études peuvent également s'étendre au désenchevêtrement pour les polymères où le phénomène peut être observé spectroscopiquement. L'ensemble de ces effets de solvant peut ensuite être comparé pour différentes masses molaire pour déterminer

simultanément son effet sur l'orientation, sur le désenchevêtrement et, ultimement, sur le diamètre critique.

Dans cette optique, le polystyrène atactique apparait comme un premier système idéal : il ne peut pas cristalliser, ce qui simplifie l'interprétation des résultats d'orientation et il donne lieu à des bandes clairement identifiées, autant en spectroscopie IR qu'en spectroscopie Raman, comme étant associées à une conformation rendue possible par le désenchevêtrement. Des fibres de PS de différentes tailles peuvent être préparées à partir de solutions dans le chloroforme (température d'ébullition de ~ 62 °C, χ avec le PS d'environ 0.42 à la température ambiante)[22], le tétrahydrofurane (THF) ($T_{ébu}$ ~ 66 °C, χ = 0.38)[23], le butan-2-one (MEK) ($T_{ébu}$ ~ 80 °C, χ = 0.47),[22,24] et le N,N-diméthylformamide (DMF) ($T_{ébu}$ ~ 153 °C, χ = 0.48) [22] et être étudiées par spectroscopie Raman confocale en utilisant les stratégies développées aux Chapitres 3, 4, 5 et 7. Ces solvants ont été sélectionnés de manière à couvrir différentes volatilités et affinités par rapport au PS, mais également pour donner lieu à différentes morphologies connues. Le chloroforme, tel que démontré aux Chapitres 6 et 7, permet clairement d'observer l'effet de la formation d'une gaine. Le THF, au contraire, donne lieu à une morphologie extrêmement poreuse à cause de la séparation de phases causée par le mélange du THF avec l'eau de l'atmosphère.[25] Le DMF, grâce à sa très faible volatilité, devrait mener à une distribution uniforme de densité radiale.[16] Nos récentes photos de microscopie électronique à balayage permettent de confirmer la morphologie des fibres formées, tel qu'anticipé par les études antérieures. Les conclusions pourront ensuite être étendues et raffinées en reproduisant l'étude pour trois masses molaires commercialement disponibles, soit le 210, 900 (tel qu'utilisé au Chapitre 7) et le 2000 kg/mol.

Des corrélations entre les études à l'échelle des fibres individuelles peuvent également être faites avec des mesures sur des amas de fibres, par spectroscopie IR, par calorimétrie différentielle à balayage (DSC) et par diffusion des rayons X aux grands angles (WAXS). Nos résultats préliminaires montrent, par exemple, qu'une transition exothermique ayant lieu sous la Tg est systématiquement présente dans les échantillons de fibres de PS électrofilées et ce, peu importe le solvant ou la masse molaire. De même, les mesures par DSC modulée d'échantillons de fibres ayant subi un recuit sous la Tg montrent deux transitions endothermiques, probablement toutes deux associées à des relaxations enthalpiques. La

présence même de ces deux transitions illustre de manière flagrante l'hétérogénéité de la distribution de caractéristiques dans les fibres. Dans cette même optique, les halos de diffusion associés aux distances interchaines observables en WAXD se déplacent, pour plusieurs de ces échantillons, à des plus petits angles (et donc à des distances plus grandes) que ce qui est observé pour des échantillons massiques.

Somme toute, les importantes différences de comportement des fibres électrofilées par rapport à d'autres matériaux tels que les films minces et/ou les films orientés illustrent leur complexité, même pour un polymère aussi simple que le PS. Ces comportements doivent faire l'objet d'études afin d'en comprendre la provenance et de corréler les observations à l'échelle des amas de fibres aux mesures de fibres uniques. En augmentant de manière importante la quantité de fibres individuelles pouvant être étudiées en un temps raisonnable par l'établissement de droites d'étalonnage reliant l'orientation moléculaire à un ratio de bandes (tel que présenté aux Chapitres 5 et 7) il devient également possible de comparer de manière statistiquement représentative les distributions de caractéristiques en fonction du diamètre et ainsi de tirer des informations qui deviennent comparables aux résultats observés pour des amas de fibres.

8.2.1.2. Effets du solvant sur l'orientation des polymères semi-cristallins et hautement cristallins

La suite logique de ces projets est l'étude de polymères plus complexes, soit des polymères semi-cristallins ou hautement cristallins dont on peut déterminer simultanément l'orientation et le taux de cristallinité par spectroscopie Raman polarisée. En plus des corrélations mentionnées à la section précédente, on cherchera avant tout à connaître l'orientation relative des cristaux formés par rapport à la phase amorphe, leur évolution en fonction du diamètre, ainsi que l'influence du solvant et de la morphologie adoptée sur le taux de cristallinité.

Concrètement, il est plus simple dans un premier temps d'utiliser des polymères dont le spectre Raman est bien connu. Une première étape serait de comparer les résultats observés pour le PS dans divers solvants avec des fibres de PET (dont l'analyse spectrale est facilitée par les méthodologies développées au Chapitre 5) dans l'optique d'une première évaluation de

l'effet de la cristallisation sur les courbes d'orientation en fonction du diamètre. Des fibres de PET de différentes tailles peuvent être préparées à partir de solutions de différentes concentration dans des solvants tels que l'hexafluoropropan-2-ol (HFIP) (un solvant extrêmement volatil avec une T_{ebu} de ~58 °C), l'acide trifluoroacétique (TFA) (moins volatil que le HFIP avec une température d'ébullition de ~72 °C) et un mélange de TFA et de dichlorométhane (le mélange de solvant utilisé au Chapitre 5, qui pourrait agir à titre d'intermédiaire entre le HFIP et le TFA). Le PET est idéal pour cette comparaison puisqu'il est relativement simple de quantifier son taux de cristallinité ainsi que la proportion de mésophase à partir de seulement deux spectres polarisés parallèles. En utilisant la méthode développée aux Chapitres 2 et 3, il est également possible de quantifier l'orientation des conformères *trans* (associés à la mésophase ou à la phase cristalline), en plus de l'orientation globale, d'une manière qui n'était pas possible lors de la publication de l'étude du Chapitre 5.

Dans l'optique d'étendre certaines de ces conclusions, il est également possible d'étudier d'autres polymères semi-cristallins tels que la poly(ε-caprolactone) (PCL) ou le poly(chlorure de vinyle) (PVC) et ce, dans plusieurs solvants, de manière à tenir compte des facteurs influençant le plus fortement l'orientation et la cristallisation du PET. Il sera également intéressant d'évaluer l'influence de la Tg sur le comportement en cristallisation des fibres et leur rétention d'orientation globale en comparant le PET (Tg ~ 80 °C) avec le PCL (Tg ~ 60 °C) et le PVC (Tg ~ 90 °C). Bien que la littérature « spectrale » de ces deux polymères soit moins riche en information structurale facile à extraire, il devrait être possible d'établir des étalonnages par une analyse fine des spectres d'échantillons dont on comprend mieux le comportement que celui des fibres. Concrètement, il est possible de préparer des films montrant différents taux de cristallinité (par recuit) et/ou différents degrés d'orientation (par étirement) et d'établir des étalonnages reliant l'évolution de certaines bandes à l'orientation de différents groupements et/ou au taux de cristallinité. Ces informations extraites pourront par la suite être appliquées directement pour l'étude des fibres.

Le cas du PVC est également d'intérêt accru puisqu'il permet de sonder et d'étendre le concept du désenchevêtrement partiel des chaînes largement étudié aux Chapitres 6 et 7. Il est important de rappeler que, dans le contexte de cette thèse, le concept du désenchevêtrement dans les fibres électrofilées n'a été démontré à partir de résultats expérimentaux que pour un

seul système simple, soit le polystyrène atactique. Malheureusement, ce concept est difficile à généraliser, car l'apparition de bandes reliées à une conformation rendue possible par le désenchevêtrement est un fait assez peu commun et/ou documenté. Le cas du PVC est une seconde exception intéressante, puisque l'étude spectroscopique d'échantillons produits par lyophilisation a permis d'observer au moins une bande associée au désenchevêtrement des chaines.[26] Ce polymère offre donc la possibilité de valider les conclusions tirées avec le PS, tout en étant un polymère semi-cristallin dont le comportement pourrait également être comparable à celui du PET.

Il serait également intéressant de pousser la comparaison à des polymères dont le taux de cristallinité est généralement très élevé, tel que le poly(oxyde d'éthylène) (PEO) et le polyéthylène (PE). Bien que représentant un défi potentiellement plus imposant, leur étude est toutefois d'un intérêt particulier. En effet, une étude de Papkov et al. a récemment démontré que le taux de cristallinité du PEO (mesuré sur des amas de fibres), diminue de manière importante avec le diamètre et ce, malgré le fait les fibres conservent un module très élevé, qui évolue de manière exponentiel avec le diamètre.[27] L'hypothèse de ces auteurs pour justifier ce comportement hautement inhabituel est une orientation élevée et croissante de la phase amorphe avec la diminution du diamètre. Ce phénomène mérite d'être exploré et corrélé par des mesures directes et quantitatives. À l'inverse, Ma et al.[28] ont récemment étudié par spectroscopie Raman des fibres uniques de PE produites par électrofilage et montrant un diamètre inférieur à 100 nm. Leur conclusion était que, bien que peu d'effets de diamètre soient observés, le taux de cristallinité, l'orientation, ainsi que la conductivité thermique augmentent simultanément avec l'augmentation du voltage (qui tend à réduire le diamètre des fibres).

Le PEO est un polymère particulièrement facile à électrofiler et très soluble dans divers solvants : des fibres peuvent donc être préparées dans le HFIP, le méthanol et l'eau ou, à l'extrême, le DMF, pour évaluer l'effet des caractéristiques du solvant sur un polymère hautement cristallin. Ces résultats pourrait par la suite être comparés à ceux du PS (amorphe) et du PVC ou du PET (semi-cristallins). Par contre, la plupart des bandes du spectre Raman du PEO sont très peu intenses. De plus, comme le PEO cristallise, sous sa forme thermodynamiquement la plus stable, sous forme d'hélices composées de séquences de

conformères *trans-gauche-trans*, l'évaluation directe du taux de cristallinité par méthode spectroscopique est complexe. Nos études préliminaires nous ont tout de même permis d'observer l'apparition de bandes dans les spectres qui sont généralement associées à la phase amorphe. L'amplitude relative de cette dernière par rapport à d'autres bandes du spectre Raman pourrait donner certaines indications sur le taux de cristallinité des échantillons. À l'inverse, le spectre du PE est beaucoup mieux connu et permet une quantification relativement facile du taux de cristallinité.[29,30] Par contre, c'est un polymère très difficile à électrofiler à cause de sa faible solubilité dans la plupart des solvants organiques communs. Une stratégie fréquemment utilisée dans la littérature pour les polymères peu solubles est le « melt spinning » (où la seringue est chauffée par une source IR de manière à ce que le polymère soit en fondu) et ses différentes variantes.[31,32] Par contre, l'absence de solvant rend la comparaison moins directe avec les résultats des études sur les différents polymères préalablement mentionnés.

8.2.1.3. Effet du taux de cristallinité et de l'orientation sur la température de fusion

Au cours des dernières années, plusieurs études ont porté sur la température de fusion des fibres qui, lorsqu'étudiées individuellement, montrent des comportements inhabituels. L'effet de la taille des fibres est un sujet de débat récurrent mais deux comportements « typiques » semblent se distinguer : 1) les polymères considérés comme étant hautement cristallins, tel que le PE et le PEO, voient leur température de fusion diminuer avec la diminution du diamètre[33-36] et 2) les polymères semi-cristallins, tel que le polylactide, montrent une température de fusion anormalement élevées suite à un recuit.[37-39] Dans les deux cas, ces effets sont associés, sous une forme ou une autre, à l'orientation des chaînes, mais sans que des mesures directes en fonction de la température, à l'échelle de la fibre individuelle, n'aient permis de valider ces hypothèses. Encore une fois ici, la spectroscopie Raman confocale apparait comme une technique de choix pour élucider le comportement réel des fibres électrofilées.

Idéalement, ces études suivront celles précédemment décrites, c'est-à-dire qu'elles devraient prioritairement être effectuées sur des systèmes dont on comprend bien l'évolution de l'orientation et du taux de cristallinité avec la réduction du diamètre. Ces mesures

requièrent de l'équipement relativement complexe, une solide expertise expérimentale des méthodologies développées dans cette thèse et du developpement expérimental, qui a été effectué dans les dernières années. La distance focale de la plupart des objectifs à grand grossissement (requis pour les mesures d'orientation sur fibres uniques) étant très courte, l'objectif lui-même doit être refroidi à l'aide d'un dispositif simultanément au chauffage de l'échantillon. De même, le moindre mouvement dans la pièce est nuisible à la mesure Raman sur fibre unique. Un porte-échantillon a été construit sur mesure pour stabiliser une pastille de BaF_2 (sur laquelle les fibres doivent être déposées, tel que démontré au Chapitre 2), refermé avec un couvercle très fin (puisque la distance focale est courte) et avec un thermocouple directement relié à la surface de BaF_2 pour permettre une évaluation précise de la température.

La température de fusion et la cinétique de la relaxation d'orientation (ou de cristallisation à froid) peuvent donc être évaluées spectroscopiquement en effectuant des mesures Raman sur fibre unique en fonction de la température et/ou du temps. Pour ce faire, il est essentiel de travailler sur des systèmes pour lesquels des étalonnages, reliant un ou plusieurs ratios de bandes à l'orientation et au taux de cristallinité, à partir d'un seul spectre polarisé, ont été préalablement établies. Ici encore, le PET est d'intérêt particulier, notamment grâce à l'accessibilité et à la richesse de l'information pouvant être extraite à partir d'un ou de deux spectres polarisés. On note également le cas du PVC qui, suite à un travail d'étalonnage, permettrait simultanément d'accéder à une compréhension de l'effet du désenchevêtrement sur la cinétique et la mécanistique de cristallisation à froid des fibres formées de polymères semi-cristallins. Une hypothèse plausible est que le plus faible degré d'enchevêtrement des chaînes pour un polymère pouvant cristalliser, couplé à une forte orientation de ces chaînes moins enchevêtrées, pourrait promouvoir la formation cinétiquement rapide de cristaux de grande taille et très orientés, à des températures très près de la Tg, qui fondraient à des températures anormalement élevées.

Un autre aspect d'intérêt serait la comparaison de résultats obtenus pour des fibres avec des mesures sur des films formés par la « technique de la tournette » (« spin-coating ») sur les mêmes pastilles de BaF_2. Comme l'électrofilage, cette technique implique une évaporation très rapide du solvant et potentiellement une certaine orientation locale. Nos travaux non-inclus dans cette thèse ont montré que ces films mènent parfois à des résultats similaires à

ceux observés en utilisant l'électrofilage, notamment pour la préparation de complexes dont la formation est rendue cinétiquement possible par l'évaporation rapide du solvant.[40] Finalement, les mêmes mesures peuvent être effectuées sur des films isotropes ou orientés par étirement (de manière à couvrir tout le domaine d'orientation), produits par évaporation lente de solvant. Ce type de mesures comparatives devrait permettre d'établir plus précisément les causes du comportement inhabituel des fibres électrofilées ainsi que l'effet relatif des différents paramètres qui sont associées à l'électrofilage.

8.2.1.4. Effet du collecteur sur l'orientation moléculaire

Une quantité impressionnante de types de collecteurs, mais également des méthodes d'électrofilages modifiées, ont été développés dans l'optique, entre autres, d'un contrôle accru de l'alignement des fibres, ou en vue d'un dépôt ciblé, qui est cruciale pour plusieurs applications telles que l'ingénierie tissulaire et le relargage de médicaments.[41] Les trois types de collecteurs les plus communs demeurent toutefois: 1) les surfaces planes conductrices, tel qu'un simple papier d'aluminium, 2) les collecteurs métalliques rotatifs, dont la vitesse de rotation est variable, et 3) les tiges métalliques, entre lesquelles les fibres se déposent et qui peuvent être séparées par des distances plus ou moins importantes. Tel que soulevé au Chapitre 2, l'orientation moléculaire dans les fibres électrofilées a, par le passé, été considérée comme provenant principalement de l'effet des collecteurs.[42-44] Depuis, des fibres collectées dans de multiples conditions ont montré une orientation moléculaire forte, mais l'impact réel du collecteur demeure largement incompris. Deux stratégies principales sont utilisées pour évaluer l'effet de ce paramètre. La plus commune est de miser sur une organisation macroscopique similaire des fibres préparées dans différentes conditions pour évaluer l'effet global sur l'orientation moléculaire des fibres.[45] L'autre consiste à quantifier l'alignement macroscopique des fibres et à en tenir compte dans le calcul de l'orientation moléculaire de fibres préparées par différentes techniques.[46,47] Dans tous les cas, des effets de collecteurs notables sur l'orientation ont été rapportés. Les quelques études effectuées sur des fibres uniques, principalement par mesures de diffraction électronique par aire sélectionnée (SAED) sur des fibres composées de polymères semi-cristallins tels que le poly(fluorure de vinylidène) PVDF[45,48] et le poly[(R)-3-hydroxybutyrate-co-(R)-3-hydroxyhexanoate] (PHBHx)[10] ont également révélé que de minimes changements au niveau des collecteurs, tels qu'un

changement de la distance entre les tiges de métal, peuvent engendrer des changements importants au niveau de l'orientation moléculaire. Il est par contre important de noter que ces études sont limitées à un nombre très restreint de fibres et que peu de paramètres ont été étudiés à ce jour.

Dans cette optique, nous avons étudié par spectroscopie Raman des fibres de PEO préparées à partir de solution de méthanol (un solvant très volatil) et collectées par les trois modes principaux précédemment décrits. L'orientation moléculaire quantifiée à partir des méthodologies développées dans cette thèse est pratiquement identique dans les trois cas, très élevée ($<P_2>$ ~ 0,85), et montre une faible dispersion. Ces résultats contredisent les conclusions de Kakade et al.[43] selon lesquelles l'orientation des fibres de PEO serait causée par l'étirement de la fibre lors du passage d'une tige métallique à l'autre.

L'hypothèse la plus probable est que cette totale absence d'effet de collecteur sur l'orientation moléculaire est causée par la cristallisation très rapide du PEO, couplée à la relaxation lente d'orientation de la phase cristalline formée pendant l'évaporation rapide du solvant. On s'attend donc à ce que les polymères dont la vitesse de cristallisation est significativement plus faible que celle du PEO, ainsi que les polymères amorphes tels que le PS, soient beaucoup plus influencés par ce paramètre. Encore une fois ici, la Tg du polymère et la nature du solvant peuvent donner lieu à plusieurs types de comportements en fonction du collecteur. Si, par exemple, l'évaporation du solvant est tellement rapide qu'une gaine épaisse se forme sans que plus d'étirement ne soit possible, il est probable que l'effet du collecteur soit minime. À l'inverse, dans le cas d'un solvant très peu volatil tel que le DMF, il est probable que du solvant résiduel demeure plus longtemps et que les dernières étapes de la formation de la fibre (soit sa déposition sur un collecteur en rotation, par exemple), aient un impact beaucoup plus grand sur l'orientation finale mesurée.

8.2.1.5. Les mélanges polymères

L'étude des mélanges polymères sous forme de fibres électrofilées est également d'intérêt, autant d'un point de vue fondamental qu'en vue de différentes applications des fibres. De manière générale, les mélanges miscibles peuvent donner lieu à des matériaux aux propriétés montrant une certaine synergie par rapport à ceux composés des polymères

individuels. À l'inverse, les mélanges immiscibles donnent généralement lieu à des matériaux ayant des propriétés médiocres suite à la formation de domaines distincts de phases riches en chacun des constituants individuels. Les fibres électrofilées de mélanges immiscibles, quant à elles, donnent lieu à une distribution spatiale de domaines composés de chacun des polymères (ou des phases enrichies en l'un et l'autre des polymères) qui peut s'avérer particulièrement intéressante. L'organisation des différentes phases peut être modulée en exploitant l'effet de l'affinité relative du solvant (ou d'un mélange de solvant) par rapport aux deux polymères. Une étude réalisée par notre groupe de recherche a démontré que l'électrofilage d'un mélange PS/ poly(vinyl méthyl éther) (PVME) à partir d'une solution composée d'un solvant menant à un film immiscible mène à la formation d'une gaine de PVME entourant un cœur de PS.[49] Le PVME peut ensuite être facilement retiré en solution aqueuse sans détruire le matériau, qui conserve sa forme de fibre (composée pratiquement exclusivement de PS). D'autres groupes ont étudié différents mélanges donnant lieu à une morphologie gaine/cœur, tel que les mélanges de polyvinylpyrrolidone (PVP)/PVDF,[50] PS/poly(méthyl méthacrylate) (PMMA),[51] et PLA/PCL,[52] pour ne donner que quelques exemples.

Récemment, la formation de nanodomaines dispersés de l'ordre de quelques dizaines de nm (plutôt que de quelques µm lorsque formés par évaporation lente de solvant) dans les fibres électrofilées pour des systèmes immiscible ou présentant des miscibilités partielles a été démontrée comme étant extrêmement efficace en vue du relargage contrôlé de médicaments.[53-56] Pourtant, notre compréhension actuelle de l'influence de différents paramètres d'électrofilage sur des aspects tels que la miscibilité des polymères, la dispersion et/ou la taille des domaines (en situation de séparation de phases) ainsi que sur les propriétés des matériaux formés est limitée à quelques études isolées.

Dans cette optique, on s'intéresse tout d'abord à un système miscible dont le PS est l'un des constituants de manière à établir des comparables avec les études présentées dans cette thèse et avec l'étude antérieure de notre groupe. Les mélanges PS/poly(2,6-dimethyl-1,4-phenylene oxide) (PPO) comportent plusieurs avantages. La Tg du PPO étant relativement élevée, les mélanges PS/PPO miscibles possèdent une Tg supérieure à celle du PS pur, contribuant à augmenter sa capacité à conserver une orientation induite par l'élongation. L'un des objectifs de ce projet est d'établir une corrélation entre la dynamique de relaxation

d'orientation du PS et du PPO et l'orientation mesurée à l'échelle de la fibre électrofilée individuelle par spectroscopie Raman. L'idée est tout d'abord d'effectuer des mesures dynamiques sur des films, par dichroïsme linéaire infrarouge avec modulation de polarisation (PM-IRLD) et en spectroscopie infrarouge à matrice à plan focal (PAIRS) pour étudier la relaxation des deux polymères avec une résolution temporelle de quelques millisecondes[57,58] lorsque le matériau est déformé à très haute vitesse. On cherche à reproduire, de la manière la plus fidèle possible, le processus de formation des fibres lors de l'électrofilage, puis à coupler l'information obtenue sur les temps de relaxation de chacun des polymères avec l'orientation moléculaire mesurée sur les fibres. Ces comparatifs peuvent être effectués pour différents ratios de PS/PPO et pour différentes tailles de fibres, pour chacun de ces ratios. Outre l'orientation, d'autres paramètres peuvent être étudiés afin de comprendre l'impact des conditions d'électrofilage ainsi que les similitudes et/ou différences de comportement par rapport à des films préparés par évaporation lente de solvant. La position de différentes bandes du spectre, par exemple, donne de l'information sur la qualité de la séparation de phases et/ou sur la force d'interaction de différents groupements des deux polymères. De plus, des études précédentes sur la dynamique de relaxation de ce système ont proposé que, aux faibles fractions massiques de PPO, la présence de PPO augmente le degré d'enchevêtrement du PS.[59] Cette hypothèse pourra donc être explorée et, s'il y a lieu, les résultats pourront être comparés pour différents ratios PS/PPO et différentes tailles de fibres. On cherche donc, au global, à évaluer les points suivants : comment la présence du PPO influence le degré d'enchevêtrement des chaînes de PS dans les fibres électrofilées? Comment la présence du PPO influence l'orientation du PS (par rapport aux fibres de PS pur), pour différents ratios de PS/PPO, par comparaison avec des films? Quel est l'effet de la taille des fibres sur l'ensemble de ces paramètres?

Dans une autre optique, en changeant les conditions de formation des fibres pour diminuer la miscibilité du PS et du PPO, il devient possible de répondre aux interrogations suivantes : comment peut-on moduler la miscibilité et/ou la distribution spatiale (ainsi que la taille des domaines formés) et/ou l'amplitude de la séparation de phases en changeant les propriétés du solvant? Comment l'orientation moléculaire de chacun des polymères varie-t-

elle dans ces circonstances? Peut-on systématiquement retirer la totalité (ou la quasi-totalité) de la phase minoritaire en utilisant un solvant sélectif?

8.2.1.6. Formation de phases cristallines polymorphes

Tel que soulevé à plusieurs occasions dans cette thèse, les fibres électrofilées sont produites dans des conditions extrêmes, c'est-à-dire sous l'effet de forces d'élongation importantes et avec une vitesse rapide d'évaporation du solvant. Ces effets couplés donnent fréquemment lieu à des formes cristallines polymorphes inhabituelles et difficiles à former avec d'autres techniques que l'électrofilage. La présence de ces polymorphes confère fréquemment aux matériaux des propriétés différentes. Typiquement, l'électrofilage donne lieu à trois types de polymorphes : 1) la phase thermodynamiquement stable, 2) la phase qui se forme prioritairement par effet de trempe, et 3) la phase qui se forment prioritairement sous tension. Fréquemment, les fibres donnent lieu à des mélanges de ces différents polymorphes, sans qu'on en comprenne la provenance, la distribution spatiale et les facteurs affectant leur formation. Pourtant, tel que soulevé dans la perspective du Chapitre 2, ces fibres ont pratiquement uniquement été étudiées sous forme d'amas de fibres.

Le cas les plus largement étudié est celui du PVDF, puisque la phase β, principalement formée par l'application d'une tension, est ferro et piézoélectrique et que l'électrofilage est reconnu comme étant l'une des techniques permettant d'obtenir les plus hauts pourcentages atteignables de cette phase cristalline. Dans ce contexte, les méthodologies développées ici peuvent être utilisées pour tenter de répondre aux questions suivantes : lorsque les fibres sont composées d'un mélange de polymorphes, leur distribution est-elle uniforme d'une fibre à l'autre? Quelle est la distribution longitudinale? Y-a-il un effet de diamètre? L'orientation relative des polymorphes est-elle homogène d'une fibre à l'autre? Ultimement, dans le même esprit que pour les projets précédemment décrits, quelle corrélation structures/propriétés/morphologies peut-on en extraire? Évidemment, l'ensemble des points soulevés dans le présent chapitre entre également en ligne de compte pour ce qui concerne, par exemple, l'influence différents paramètres sur les températures de fonte et, s'il y a lieu, des transitions d'une phase cristalline à une autre.

Le poly(pivalolactone) (PPL) est un bon exemple de polymère possédant plusieurs polymorphes : la phase α thermodynamiquement stable se forme spontanément sous recuit ou par évaporation lente du solvant, la phase γ, se forme uniquement par effet de trempe, et la phase β est formée sous contrainte à partir de la phase α.[60,61] Les transitions de la forme β vers α (ou l'inverse) se font sous la forme d'une transition solide-solide.[60,61] Nos résultats préliminaires sur le PPL nous ont permis d'observer la formation d'un mélange des phases α et γ lorsque les fibres sont produites à partir de solutions dans le HFIP ($T_{ébu}$ ~58 °C) alors que seule la phase α est détectable à partir d'une solution dans le TFA ($T_{ébu}$ ~72 °C). La phase β, si elle se forme, n'a pas été expérimentalement observée. On s'intéresse également ici aux cinétiques et mécanismes de transition de phases, à l'échelle de la fibre unique, en comparaison aux fibres commerciales. La formation de la phase β est-elle possible à partir de la phase α de fibres électrofilées? Si tel est le cas, comment la cinétique de la transition de β vers α se compare-t-elle avec celle observée pour des fibres commerciales? Peut-on former la phase β en étirant la forme γ?

8.2.2. Caractérisation des fibres électrofilées à l'aide de méthodes spectroscopiques émergentes

8.2.2.1. Brève description de techniques spectroscopiques émergentes

L'un des objectifs principaux de cette thèse était l'étude de nanofibres électrofilées par des méthodologies simples et rapides, à l'échelle de la fibre individuelle. Le succès de ces études provient de la résolution spatiale accessible en microcopie Raman confocale couplée à la richesse des informations structurales accessibles par spectroscopie vibrationnelle. Au cours des deux dernières décennies, les techniques de spectroscopie vibrationnelles en champ proche tel que la spectroscopie Raman à effet de pointe (TERS, en anglais « tip enhanced Raman spectroscopy »), la microscopie en champ proche à sonde diffusante dans l'IR (IR s-SNOM, en anglais « scattering-type scanning near-field optical microscopy ») ou les techniques photothermiques couplées avec un microscope à force atomique (AFM-IR et ses différentes variantes) ont connu un essor important et ont repoussé les limites de la résolution spatiale accessible à la spectroscopie vibrationnelle. Leur utilisation se restreint principalement à des applications biologiques, de détection analytique, à des matériaux inorganiques ou organique

(principalement sous forme de graphite et de nanotube de carbone) et elles sont donc peu utilisées pour la caractérisation des matériaux polymères. Actuellement, à cause de leur coût et de leur complexité technique (ou théorique), elles sont également confinées à un petit nombre de laboratoires et/ou ne sont accessibles commercialement que dans des versions qui ne reflètent que peu leur réelle puissance. Leur utilisation pour l'étude des nanofibres électrofilées pourrait toutefois permettre une variété impressionnante d'études approfondies de la distribution spatiale de caractéristiques structurales et ainsi contribuer à notre compréhension de ces matériaux. La présente section explique brièvement les bases de ces techniques ainsi que certaines de leurs limites actuelles en vue de l'étude de fibres.

À ce jour, la technique de spectroscopie vibrationnelle en champ proche de loin la plus accessible est la spectroscopie Raman à effet de pointe (TERS) qui est basée sur la diffusion Raman exaltée de surface (SERS). En SERS, un champ électrique local est fortement amplifié à la surface d'une particule métallique (typiquement l'or ou l'argent) dû au couplage de la résonance des plasmons avec le champ électromagnétique de la lumière incidente et diffusée. La diffusion Raman est donc fortement amplifiée par rapport au Raman conventionnel, augmentant ainsi la sensibilité de la technique.[62] Le TERS est une variation du SERS, en ce sens que la surface métallique prend la forme d'une pointe ultra fine qui agit comme une antenne pour créer un « site chaud » où l'intensité irradiée, c'est-à-dire l'intensité de la diffusion Raman et de la fluorescence, est fortement amplifiée. Les plasmons étant confinés à l'extrémité de la pointe, l'utilisation du TERS donne accès à une résolution spatiale exceptionnelle (5-20 nm) par rapport au Raman conventionnel, qui est limité par la limite de diffraction (typiquement quelques centaines de nm). En TERS, elle est déterminée principalement par la courbure de la pointe et le type de matériaux qui la compose.[63] Le TERS permet donc le couplage de l'information moléculaire et structurale pouvant être typiquement extraite par spectroscopie vibrationnelle avec la résolution spatiale et les capacités d'imagerie d'un AFM. Par contre, de légères modifications des règles de sélection des modes vibrationnels impliqués, couplé avec la polarisation intrinsèque de la technique, peuvent modifier de manière significative l'intensité relative des bandes par rapport au spectre Raman conventionnel, compliquant l'interprétation des spectres.

Le IR *s*-SNOM, comme le TERS, utilise le couplage plasmonique entre l'extrémité d'une pointe AFM et l'échantillon et offre les mêmes capacités d'imagerie au-delà de la limite de diffraction qui, dans l'IR, est de quelques micromètres. Dans ce cas-ci, l'échantillon est irradié directement avec la longueur d'onde d'intérêt pour exciter un mode donné. La diffusion IR est fortement amplifiée par le couplage des plasmons et c'est cette diffusion qui est mesurée et comparée pour différentes longueurs d'onde. Ultimement, ce sont les constantes optiques sont mesurées, puis transformées en absorbance pour effectuer des comparaisons avec l'IR conventionnelle. Les fréquences doivent être mesurées individuellement, à l'aide de lasers accordables ou à partir d'une source de synchrotron permettant la mesure simultanée de plusieurs fréquences à la fois.[64,65] La complexité de la technique provient des artéfacts importants causés par la topologie de l'échantillon et les signaux parasites provenant du champ lointain, qui sont éliminés par de multiples stratégies complexes de traitement de signal, requérant un équipement sophistiqué (coûteux) et des détecteurs extrêmement sensibles dans l'IR. À ce jour, les spectromètres IR *s*-SNOM commercialisés ne sont pas équipés de la technologie adéquate permettant de tels traitements de signal.

L'AFM-IR fait appel à des concepts relativement différents de ceux des deux techniques précédentes. Elle est basée sur la photo-expansion de l'échantillon, détectée par une pointe AFM, lorsqu'un mode vibrationnel est excité par un laser infrarouge.[66] Elle mène à des résultats qui, d'un point de vue spectral, sont comparables aux mesures FT-IR conventionnelles.[67] Plutôt que d'être limitée à la taille de la pointe, la résolution spatiale est, cette fois-ci, principalement déterminée par les coefficients de diffusion thermique. De fait, l'AFM-IR, tel qu'actuellement commercialisé, donne accès à une résolution d'une centaine de nm, de sorte que seules les distributions spatiales des fibres dont le diamètre est quelques fois supérieur à 100 nm peuvent être étudiées.

Pour chacune de ces techniques, une problématique cruciale pour l'étude des fibres électrofilées est la préparation des échantillons permettant d'analyser des coupes transversales des fibres avec la certitude de ne pas en avoir altéré ou modifié la nature chimique ou la structure. Une stratégie est de placer une petite quantité de fibres relativement bien alignées dans une résine époxy, qui est par la suite réticulée par chauffage, durcie et coupée. Pour contrôler les coupes, qui doivent être parfaites du point de vue de l'imagerie AFM, on utilise

un faisceau d'électrons[5] ou des couteaux de diamant. Dans tous les cas, les effets de bords ou la dénaturation chimique (ou physique) par effet de chauffage ou de frottement peuvent interférer dans l'interprétation des résultats.

8.2.2.2. Exemples d'études de fibres avec les techniques de spectroscopie émergentes

Par extension des résultats présentés dans cette thèse, on peut d'abord s'intéresser à l'étude plus précise de la localisation du désenchevêtrement des chaînes observé dans le polystyrène atactique aux Chapitres 6 et 7. La spectroscopie Raman a permis de démontrer que, lorsque les conditions expérimentales mènent à la formation d'une gaine, le désenchevêtrement s'y situe principalement. Par contre, l'épaisseur de cette gaine et l'absence de chaînes désenchevêtrées dans le cœur ne peuvent être démontrées qu'en effectuant une étude à l'échelle nanométrique de la distribution radiale des caractéristiques. Ces études peuvent également être étendues à des conditions expérimentales menant à d'autres types de morphologie, ainsi qu'à des fibres composées d'autres polymères, tel que le PVC. Le IR *s*-SNOM n'est pas suffisamment sensible pour que ce type de mesure soit possible, puisque seules les bandes les plus intenses du spectres sont détectables. L'AFM-IR pourrait permettre de localiser clairement le phénomène, mais le succès à court terme de ce projet dépend du coefficient d'absorption de ces bandes. Par contre, seules les grosses fibres peuvent être analysées et il serait impossible d'établir clairement la taille de la gaine à cause de la résolution spatiale limitée. En théorie, le TERS devrait donner accès à une meilleure résolution et donc, être plus efficace, tout dépendant de la section efficace associée à ce mode en Raman.

Pour les polymères formant des polymorphes, plusieurs questions fondamentales intéressantes peuvent être résolues par de telles études. La phase cristalline adoptant la conformation la plus étendue se situe-t-elle dans la gaine ou au cœur du cœur de la fibre? De même, la phase cristalline se formant prioritairement lors d'une trempe se situe-t-elle nécessairement dans la gaine ou est-elle en compétition (et donc en mélange) avec la phase la plus étendue? La distribution spatiale peut-elle changer en modifiant la volatilité du solvant, et donc la morphologie des fibres? Nos résultats sur les fibres de PS présentés au Chapitre 7 (suggérant que le désenchevêtrement, fortement orienté dans l'axe de la fibre, se situe

principalement dans la gaine à cause de l'évaporation extrêmement rapide du solvant), nous mènent à l'hypothèse que les formes cristallines se formant prioritairement lors d'une trempe ou sous élongation se situeraient probablement dans la gaine de la fibre, alors que la forme thermodynamiquement stable, composerait le cœur. De même, l'étude récente par AFM-IR de Gong et al. de fibres de poly[(R)-3-hydroxybutyrate-co-(R)-3-hydroxyhexanoate], un polymère montrant deux polymorphes (la forme α thermodynamiquement stable qui cristallise sous forme d'hélices et la phase β qui adopte une conformation zig-zag étendue) a démontré que la forme étendue, lorsque présente, se situe principalement dans la gaine.[10] Ces résultats s'opposent par contre à ceux des groupes de Zussman et Pisignano[18,19] qui suggèrent que le cœur serait sujet à des forces d'élongation plus grandes que la partie extérieure de la fibre. Leurs résultats suggèrent donc au contraire la formation d'un cœur composé d'une phase cristalline à conformation étendue, et d'une gaine composée d'une phase plus stable thermodynamiquement.

Encore une fois, ces études peuvent être perçues sous différents angles. D'un point de vue appliqué, en premier lieu, on se demande comment et jusqu'à quel point il est possible de contrôler les propriétés à la surface des fibres versus celles du le cœur. On peut facilement imaginer des applications pour lesquelles on souhaiterait, par exemple, que la conduction d'électrons ou que la piézo électricité ait lieu au cœur de la fibre, alors que l'extérieur agirait comme isolant. De même, dans certains cas, il est préférable que les électrons, les trous ou les photons puissent voyager en surface uniquement pour se propager facilement d'une fibre à l'autre, tout en évitant les recombinaisons dans le cœur. L'optimisation des propriétés des fibres est fonction de l'orientation moléculaire, mais également de la distribution spatiale, à l'échelle nanométrique, des caractéristiques structurales des fibres.

D'un point de vue fondamental, en deuxième lieu, il est primordial de s'intéresser à la taille précise de la gaine, lorsqu'elle se forme, et de comprendre comment elle évolue avec l'utilisation de différents types de solvant. Ceci peut être fait principalement à partir de mesures par TERS d'une caractéristique structurale précise, tel que la présence d'un polymorphe ou de désenchevêtrement. L'un des objectifs est, entre autres, d'évaluer la taille de la gaine par rapport à la taille d'une (ou quelques) pelote statistique. Peut-on réellement parler d'effet de confinement des chaînes tel que suggéré par le groupe de Zussman[2,68-70]

depuis plusieurs années ou doit-on considérer ce concept comme étant un abus de langage extrêmement présent dans la littérature des fibres électrofilées? Ces questionnements sont d'un intérêt particulièrement puissant puisqu'ils soulèvent un point de litige important dans ce domaine : les propriétés et/ou les comportements inhabituels des fibres électrofilées sont-ils 1) causés par effet de confinement (donc généralisable à tout matériau pour lequel les mêmes effets de confinement sont observés) ou 2) uniquement causés par le mode très spécifique de formation des fibres (donc généralisable à d'autres matériaux pour lesquels des conditions de formations sont similaires, tel qu'une évaporation rapide du solvant et des forces d'élongation importantes sont en jeu et ce, peu importe leur taille).

Dans l'état actuel des choses, aucune des techniques présentées n'offre une solution parfaite pour l'étude des fibres. L'AFM-IR montre une résolution spatiale insuffisante pour certaine des applications proposées et le IR *s*-SNOM n'offre pas une sensibilité suffisante puisque seules les bandes très intenses peuvent être détectées. De plus, à cause des méthodes de détection et de traitement de signal employées, la forme des bandes ainsi que leur position exacte demeurent difficilement comparables à celles obtenues par spectroscopie IR conventionnelle. Le TERS est certainement très prometteur pour l'étude de petites fibres, mais pourrait également souffrir de problèmes de sensibilité puisque les études suggérées requièrent des mesures dans des configurations expérimentales qui nuisent à l'intensité du signal.[71] Actuellement, une combinaison du TERS et de l'AFM-IR apparaît comme la meilleure option envisageable pour la caractérisation de fibres électrofilées.

Il est essentiel de mentionner que, la science et la technologie évoluant sans cesse, il est extrêmement probable que ces techniques (ou leurs différentes variantes) nous apparaitront incontournables pour la caractérisation des nanomatériaux dans un futur relativement rapproché et nous forceront, encore une fois, à revoir notre vision globale des relations structures/propriétés des fibres électrofilées et donc, de notre capacité à les moduler.

8.3. Références

1. Lim, C. T.; Tan, E. P. S.; Ng, S. Y. *Appl. Phys. Lett.* **2008**, *92*, 141908.
2. Arinstein, A.; Burman, M.; Gendelman, O.; Zussman, E. *Nat. Nanotechnol.* **2007**, *2*, 59-62.
3. Liao, C.-C.; Wang, C.-C.; Chen, C.-Y.; Lai, W.-J. *Polymer* **2011**, *52*, 2263-2275.
4. Pai, C.-L.; Boyce, M. C.; Rutledge, G. C. *Polymer* **2011**, *52*, 2295-2301.
5. Stachewicz, U.; Bailey, R. J.; Wang, W.; Barber, A. H. *Polymer* **2012**, *53*, 5132-5137.
6. Shin, M. K.; Kim, S. I.; Kim, S. J.; Kim, S.-K.; Lee, H.; Spinks, G. M. *Appl. Phys. Lett.* **2006**, *89*, 231929-231923.
7. Zhong, Z.; Wingert, M. C.; Strzalka, J.; Wang, H.-H.; Sun, T.; Wang, J.; Chen, R.; Jiang, Z. *Nanoscale* **2014**, *6*, 8283-8291.
8. Arinstein, A. *J. Polym. Sci. B: Polym. Phys.* **2013**, *51*, 756-763.
9. Ji, Y.; Li, C.; Wang, G.; Koo, J.; Ge, S.; Li, B.; Jiang, J.; Herzberg, B.; Klein, T.; Chen, S.; Sokolov, J. C.; Rafailovich, M. H. *Europhys. Lett.* **2008**, *84*, 56002.
10. Gong, L.; Chase, D. B.; Noda, I.; Liu, J.; Martin, D. C.; Ni, C.; Rabolt, J. F. *Macromolecules* **2015**, *48*, 6197-6205.
11. Naraghi, M.; Arshad, S. N.; Chasiotis, I. *Polymer* **2011**, *52*, 1612-1618.
12. Pai, C.-L.; Boyce, M. C.; Rutledge, G. C. *Macromolecules* **2009**, *42*, 2102-2114.
13. Wang, L.; Pai, C.-L.; Boyce, M. C.; Rutledge, G. C. *Appl. Phys. Lett.* **2009**, *94*, 151916.
14. Greenfeld, I.; Arinstein, A.; Fezzaa, K.; Rafailovich, M. H.; Zussman, E. *Phys. Rev. E* **2011**, *84*, 041806.
15. Greenfeld, I.; Fezzaa, K.; Rafailovich, M. H.; Zussman, E. *Macromolecules* **2012**, *45*, 3616-3626.
16. Guenthner, A. J.; Khombhongse, S.; Liu, W.; Dayal, P.; Reneker, D. H.; Kyu, T. *Macromol. Theor. Simul.* **2006**, *15*, 87-93.
17. Greenfeld, I.; Zussman, E. In *Electrospinning for High Performance Sensors*; Macagnano, A., Zampetti, E., Kny, E., Eds.; Springer International Publishing: Cham, 2015, p 35-64.

18. Camposeo, A.; Greenfeld, I.; Tantussi, F.; Moffa, M.; Fuso, F.; Allegrini, M.; Zussman, E.; Pisignano, D. *Macromolecules* **2014**, *47*, 4704-4710.
19. Camposeo, A.; Greenfeld, I.; Tantussi, F.; Pagliara, S.; Moffa, M.; Fuso, F.; Allegrini, M.; Zussman, E.; Pisignano, D. *Nano Lett.* **2013**, *13*, 5056-5062.
20. Fasano, V.; Moffa, M.; Camposeo, A.; Persano, L.; Pisignano, D. *Macromolecules* **2015**, *48*, 7803-7809.
21. Casper, C. L.; Stephens, J. S.; Tassi, N. G.; Chase, D. B.; Rabolt, J. F. *Macromolecules* **2004**, *37*, 573-578.
22. Orwoll, R. A.; Arnold, P. A. In *Physical Properties of Polymers Handbook*; Mark, J. E., Ed.; Springer New York: New York, NY, 2007, p 233-257.
23. Tan, H.; Moet, A.; Hiltner, A.; Baer, E. *Macromolecules* **1983**, *16*, 28-34.
24. Flory, P. J.; Hocker, H. *T. Faraday Soc.* **1971**, *67*, 2258-2269.
25. Dayal, P.; Liu, J.; Kumar, S.; Kyu, T. *Macromolecules* **2007**, *40*, 7689-7694.
26. Chen, J.; Xue, G.; Li, Y.; Wang, L.; Tian, G. *Macromolecules* **2001**, *34*, 1297-1301.
27. Papkov, D.; Zou, Y.; Andalib, M. N.; Goponenko, A.; Cheng, S. Z.; Dzenis, Y. A. *ACS Nano* **2013**, *7*, 3324-3331.
28. Ma, J.; Zhang, Q.; Mayo, A.; Ni, Z.; Yi, H.; Chen, Y.; Mu, R.; Bellan, L. M.; Li, D. *Nanoscale* **2015**, *7*, 16899-16908.
29. Strobl, G. R.; Hagedorn, W. *J. Polym. Sci.: Polym. Phys.* **1978**, *16*, 1181-1193.
30. Lagaron, J. M.; Dixon, N. M.; Reed, W.; Pastor, J. M.; Kip, B. J. *Polymer* **1999**, *40*, 2569-2586.
31. Cheng, Y.-W.; Lu, H.-A.; Wang, Y.-C.; Thierry, A.; Lotz, B.; Wang, C. *Macromolecules* **2010**, *43*, 2371-2376.
32. Yoshioka, T.; Dersch, R.; Greiner, A.; Tsuji, M.; Schaper, A. K. *Macromol. Mater. Eng.* **2010**, *295*, 1082-1089.
33. Wang, W.; Barber, A. H. *Nanotechnology* **2010**, *21*, 225701.
34. Wang, W.; Peijs, T.; Barber, A. H. *Nanotechnology* **2010**, *21*, 035705.
35. Liu, Y.; Li, C.; Chen, S.; Wachtel, E.; Koga, T.; Sokolov, J. C.; Rafailovich, M. H. *J. Polym. Sci. B: Polym. Phys.* **2009**, *47*, 2501-2508.
36. Liu, Y.; Chen, S.; Zussman, E.; Korach, C. S.; Zhao, W.; Rafailovich, M. *Macromolecules* **2011**, *44*, 4439-4444.

37. Tsuji, H.; Nakano, M.; Hashimoto, M.; Takashima, K.; Katsura, S.; Mizuno, A. *Biomacromolecules* **2006**, *7*, 3316-3320.
38. Zhang, X.; Nakagawa, R.; Chan, K. H. K.; Kotaki, M. *Macromolecules* **2012**, *45*, 5494-5500.
39. Ma, Q.; Pyda, M.; Mao, B.; Cebe, P. *Polymer* **2013**, *54*, 2544-2554.
40. Richard-Lacroix, M.; Pellerin, C. *Macromol. Symp.* **2011**, *303*, 42-47.
41. Li, H.; Xu, Y.; Xu, H.; Chang, J. *J. Mater. Chem. B* **2014**, *2*, 5492-5510.
42. Fennessey, S. F.; Farris, R. J. *Polymer* **2004**, *45*, 4217-4225.
43. Kakade, M. V.; Givens, S.; Gardner, K.; Lee, K. H.; Chase, D. B.; Rabolt, J. F. *J. Am. Chem. Soc.* **2007**, *129*, 2777-2782.
44. Kongkhlang, T.; Tashiro, K.; Kotaki, M.; Chirachanchai, S. *J. Am. Chem. Soc.* **2008**, *130*, 15460-15466.
45. Ma, X.; Liu, J.; Ni, C.; Martin, D. C.; Chase, B. D.; Rabolt, J. F. *J. Polym. Sci. B: Polym. Phys.* **2016**, *54*, 617-623.
46. Edwards, M. D.; Mitchell, G. R.; Mohan, S. D.; Olley, R. H. *Eur. Polym. J.* **2010**, *46*, 1175-1183.
47. Mohan, S. D.; Mitchell, G. R.; Davis, F. J. *Soft Matter* **2011**, *7*, 4397.
48. Ma, X.; Liu, J.; Ni, C.; Martin, D. C.; Chase, D. B.; Rabolt, J. F. *ACS Macro Letters* **2012**, *1*, 428-431.
49. Valiquette, D.; Pellerin, C. *Macromolecules* **2011**, *44*, 2838-2843.
50. Wang, M.; Fang, D.; Wang, N.; Jiang, S.; Nie, J.; Yu, Q.; Ma, G. *Polymer* **2014**, *55*, 2188-2196.
51. Wei, M.; Kang, B.; Sung, C.; Mead, J. *Macrom. Mater. Eng.* **2006**, *291*, 1307-1314.
52. Lu, L.; Wu, D.; Zhang, M.; Zhou, W. *Ind. Eng. Chem. Res.* **2012**, *51*, 3682-3691.
53. Tipduangta, P.; Belton, P.; Fábián, L.; Wang, L. Y.; Tang, H.; Eddleston, M.; Qi, S. *Mol. Pharm.* **2016**, *13*, 25-39.
54. Choi, J. S.; Kim, H. S.; Yoo, H. S. *Drug Deliv. Trans. Res.* **2013**, *5*, 137-145.
55. Weng, L.; Xie, J. *Curr. Pharm. Design* **2015**, *21*, 1944-1959.
56. Chou, S.-F.; Carson, D.; Woodrow, K. A. *J. Control. Release* **2015**, *220, Part B*, 584-591.
57. Farbos, B.; Mauran, D.; Pellerin, C. *Vib. Spectros.* **2009**, *51*, 34-38.

58. Pellerin, C.; Snively, C. M.; Chase, D. B.; Rabolt, J. F. *Appl. Spectrosc.* **2004**, *58*, 639-646.
59. Zhao, Y.; Prud'homme, R. E.; Bazuin, C. G. *Macromolecules* **1991**, *24*, 1261-1268.
60. Prud'homme, R. E. *J. Polym. Sci.: Polym. Phys. Ed.* **1974**, *12*, 2455-2463.
61. Prud'homme, R. E.; Marchessault, R. H. *Macromolecules* **1974**, *7*, 541-545.
62. Kneipp, K.; Moskovits, M.; Kneipp, H. *Phys. Today* **2007**, *60*, 40.
63. Bailo, E.; Deckert, V. *Chem. Soc. Rev.* **2008**, *37*, 921-930.
64. Hermann, P.; Hoehl, A.; Patoka, P.; Huth, F.; Rühl, E.; Ulm, G. *Opt. Express* **2013**, *21*, 2913-2919.
65. Bechtel, H. A.; Muller, E. A.; Olmon, R. L.; Martin, M. C.; Raschke, M. B. *PNAS* **2014**, *111*, 7191-7196.
66. Dazzi, A.; Prater, C. B.; Hu, Q.; Chase, D. B.; Rabolt, J. F.; Marcott, C. *Appl. Spectrosc.* **2012**, *66*, 1365-1384.
67. Mastel, S.; Govyadinov, A. A.; de Oliveira, T. V. A. G.; Amenabar, I.; Hillenbrand, R. *Appl. Phys. Lett.* **2015**, *106*, 023113.
68. Boas, M.; Gradys, A.; Vasilyev, G.; Burman, M.; Zussman, E. *Soft Matter* **2015**, *11*, 1739-1747.
69. Alhazov, D.; Burman, M.; Arinstein, A.; Zussman, E. *J. Polym. Sci. B: Polym. Phys.* **2015**, *53*, 1254-1259.
70. Arinstein, A.; Zussman, E. *J. Polym. Sci. Part B* **2011**, *49*, 691-707.
71. Stadler, J.; Schmid, T.; Zenobi, R. *Nano lett.* **2010**, *10*, 4514-4520.